UNIWERSYTET JAGIELLOŃSKI
W KRAKOWIE

Wydział Fizyki, Astronomii i Informatyki Stosowanej

Instytut Fizyki im. Mariana Smoluchowskiego

Spektroskopia wzbudzenia i emisji stanów rydbergowskich dwuatomowych molekuł van der Waalsa zawierających metale 12. grupy układu okresowego

Joanna Sobczuk

Rozprawa doktorska

wykonana pod opieką

prof. dr. hab. Jarosława Koperskiego

oraz dr. Tomasza Urbańczyka

w Zakładzie Fotoniki

Oświadczenie

Ja, niżej podpisana, Joanna Sobczuk (nr indeksu: 1091304), doktorantka Wydziału Fizyki, Astronomii i Informatyki Stosowanej Uniwersytetu Jagiellońskiego oświadczam, że przedłożona przeze mnie rozprawa doktorska pt. „Spektroskopia wzbudzenia i emisji stanów rydbergowskich dwuatomowych molekuł van der Waalsa zawierających metale 12. grupy układu okresowego" jest oryginalna i przedstawia wyniki badań wykonanych przeze mnie osobiście, pod kierunkiem prof. dr. hab. Jarosława Koperskiego oraz dr. Tomasza Urbańczyka. Pracę napisałam samodzielnie.

Oświadczam, że moja rozprawa doktorska została opracowana zgodnie z Ustawą o prawie autorskim i prawach pokrewnych z dnia 4 lutego 1994 r. (Dziennik Ustaw 1994 nr 24 poz. 83 wraz z późniejszymi zmianami).

Jestem świadoma, że niezgodność niniejszego oświadczenia z prawdą ujawniona w dowolnym czasie, niezależnie od skutków prawnych wynikających z ww. ustawy, może spowodować unieważnienie stopnia nabytego na podstawie tej rozprawy.

Kraków, ……. ……
(data) (podpis doktorantki)

Streszczenie

Celem głównym, w oparciu o który powstała niniejsza praca, jest wnikliwe zrozumienie natury najsłabszych oddziaływań spajających atomy w stany związane, tzw. oddziaływań van der Waalsa (vdW). Temat rozprawy: *Spektroskopia wzbudzenia i emisji stanów rydbergowskich dwuatomowych molekuł van der Waalsa zawierających metale 12. grupy układu okresowego* w sposób naturalny dzieli tematykę, o której będą rozważania, na dwie części: spektroskopię wzbudzenia oraz spektroskopię emisji. Przedmiotem badań są natomiast stany rydbergowskie molekuł, czyli - zgodnie z definicją IUPAC - takie, których asymptoty stanowią stany atomowe o głównej liczbie kwantowej większej, niż główna liczba kwantowa asymptoty stanu podstawowego [1]. W rozprawie tej będzie mowa o niskich stanach rydbergowskich.

W pierwszym rozdziale czytelnik będzie mógł dowiedzieć się więcej na temat natury oddziaływań van der Waalsa, w szczególności dyspersyjnych (Londona), oraz najprostszych obiektów, w których owe oddziaływania występują – dwuatomowych molekuł vdW. Została również poruszona problematyka różnic między modelami teoretycznymi i wynikami doświadczalnymi kształtów krzywych potencjału (ang. *Potential Energy Curves,* PECs) oddziaływań międzyatomowych w molekułach vdW, która skłania do nieustannego ulepszania zarówno modelu teoretycznego, jak i eksperymentu. Naturalną rzeczą jest, iż różnice te pogłębiają się dla stanów rydbergowskich. Jest to związane zarówno z większą ilością poprawek, które należy brać pod uwagę przy modelach *ab initio*, jak i większą złożonością eksperymentu, wynikającą z konieczności wzbudzenia molekuł do wysokich stanów energetycznych. Praca ta koncentruje się na eksperymentalnym podejściu do wyznaczania kształtu PEC stanów rydbergowskich w dwuatomowych molekułach vdW.

Rozdziały: drugi, trzeci i czwarty stanowią podsumowanie badań wykonanych w ramach rozprawy doktorskiej. Każdy z tych rozdziałów opatrzony jest krótkim wstępem opisującym wkład doktorantki w opublikowane prace. W drugim rozdziale została poruszona problematyka spektroskopii wzbudzenia. Przedstawiono wyniki eksperymentalne dotyczące spektroskopii wzbudzenia molekuł CdRg (Cd – atom kadmu, Rg – atom gazu szlachetnego): efekt selektywnego wzbudzania izotopologów w metodzie podwójnego wzbudzenia optyczno – optycznego (ang. *Optical-Optical Double Resonance,* OODR) charakterystykę poziomów rotacyjnych stanu rydbergowskiego $E^3\Sigma_1^+(6^3S_1)$ molekuły CdNe oraz eksperymentalne wyznaczenie kompletnego, dwudołkowego kształtu PEC stanu rydbergowskiego $E^3\Sigma_1^+(6^3S_1)$ molekuły CdAr uwzględniające kształt bariery potencjału między dwiema studniami.

Zagadnienie spektroskopii wzbudzenia molekuł CdRg stanowi główną oś rozprawy doktorskiej, a wyniki eksperymentalne opisane są w trzech pracach wchodzących w skład rozprawy: [A], [E] i [F].

Trzeci rozdział poświęcony jest spektroskopii emisyjnej molekuł vdW Cd_2, CdRg, Zn_2 i ZnRg. Zostały w nim zawarte przewidywania co do dalszego rozwoju badań doświadczalnych. Propozycja eksperymentu umożliwiającego badanie widm emisyjnych ze stanów rydbergowskich tych molekuł wraz z niezbędnymi symulacjami została zawarta w [C]. Ponadto, opracowano model teoretyczny umożliwiający przewidywanie liczby molekuł wzbudzonych metodą OODR oraz liczbę fotonów pochodzących z emisji ze stanów rydbergowskich molekuł, które mogą być zarejestrowane przez detektor. Te badania umożliwiają przewidywanie, czy widma emisji z nowo eksplorowanych stanów rydbergowskich mogą zostać zarejestrowane. Model, o którym mowa, został opublikowany w [D].

W czwartym rozdziale przedstawiono problematykę badań stanów rydbergowskich molekuł Zn_2 i ZnRg. Poczyniono kroki w kierunku eksperymentalnego wyznaczenia kształtu ich potencjałów. W tym celu został zaprojektowany i wykonany nowy moduł źródła umożliwiający wytwarzanie tego typu molekuł. Opis tego urządzenia, wraz ze wstępnymi wynikami spektroskopowymi wzbudzenia przejść bound ← bound między stanami $b^3 0_u^+(4^3P_1) \leftarrow X^1 0_g^+(4^1S_0)$ dla molekuły Zn_2 zostały opisane w [B].

Abstract

The main goal of the presented thesis is a thorough understanding of the weakest interactions that bond atoms into bound states, i.e. van der Waals interactions (vdW). The thesis, as suggested by the title: *Excitation and emission spectroscopy of Rydberg states of diatomic van der Waals molecules containing 12. group elements* is divided into two parts: excitation and emission spectroscopy. The research is focused on Rydberg states of molecules which are defined by IUPAC as excited molecular states which are composed primarily of atomic orbitals with principal quantum numbers greater than that of the ground state [1]. In this work, only low-lying Rydberg states were investigated.

The first chapter provides information about the principles of van der Waals interactions, especially dispersive (London), and about the simplest objects containing such interactions – diatomic vdW molecules. Moreover, discrepancy between theoretically - and experimentally - resolved potential energy curves (PECs) in vdW molecules that leads to the ongoing enhancement of both theoretical and experimental tools is described. Naturally, the discrepancy is particularly marked in the case of Rydberg states. It is due to both: a large number of corrections that must be taken into account in *ab initio* calculations and the higher complexity of experimental design required to excite molecules to Rydberg states. This work focuses on the experimental determination of PECs of Rydberg states for diatomic vdW molecules.

The second, third, and fourth chapters contain a summary of research performed within the PhD thesis. Each of them begins with a short description of the contribution of the PhD student to published works. The second chapter contains results regarding excitation spectroscopy of CdRg molecules (Cd – cadmium atom, Rg - rare gas atom): isotopologue selection in optical – optical double resonance (OODR) method, characteristics of rotational profiles of the $E^3\Sigma_1^+(6^3S_1)$ Rydberg state of CdNe molecule, and experimental determination of a complete, double-well PEC of the $E^3\Sigma_1^+(6^3S_1)$ in CdAr including the shape of a potential barrier between two wells. The study of excitation spectroscopy is a main part of the presented thesis, and the experimental results were described in three articles being a part of the thesis: [A], [E], and [F].

In the third chapter a study on emission spectroscopy of Cd_2, CdRg, Zn_2 and ZnRg is described. An experiment that enables to record emission spectra from Rydberg states of vdW molecules was proposed and simulations of emission from ZnAr and CdAr Rydberg states were performed. The results were published in [C]. Furthermore, a theoretical model for an estimation of the number of excited molecules in OODR approach and the number of detected

photons was proposed in [D]. The calculations enable to predict whether emission spectra from newly-explored Rydberg states can be detectable.

In the fourth chapter the experimental study of Rydberg states of Zn_2 and ZnRg and its future prospective is described. A new source – module of molecular beam for zinc has been designed and built. A description of the source – module along with spectroscopic results of the $b^3 0_u^+(4^3P_1) \leftarrow X^1 0_g^+(4^1S_0)$ bound←bound excitation in Zn_2 were published in [B].

Podziękowania

Serdecznie dziękuję promotorowi mojej rozprawy doktorskiej, prof. dr. hab. Jarosławowi Koperskiemu za czas poświęcony na wprowadzenie mnie do tematyki molekuł van der Waalsa, za pracę nad poprawkami do publikacji, wniosków grantowych i rozprawy, oraz za cenne dyskusje, podczas których zafascynowałam się tematyką spektroskopii molekularnej. Dziękuję również Profesorowi za danie przykładu godnej podziwu etyki pracy naukowca oraz za wsparcie okazane w najtrudniejszym etapie doktoratu.

Pragnę podziękować również mojemu promotorowi pomocniczemu, dr. Tomaszowi Urbańczykowi, za wiele wspólnych godzin spędzonych w laboratorium, za cierpliwe przekazanie mi cennej wiedzy dotyczącej optyki, elektroniki, aparatury próżniowej oraz analizy danych.

Dziękuję także wszystkim osobom zaangażowanym w powstanie i koordynowanie projektem „Kartezjusz", szczególnie prof. Andrzejowi Sitarzowi z Uniwersytetu Jagiellońskiego w Krakowie oraz prof. Piotrowi Mucha z Uniwersytetu Warszawskiego, za realną pomoc w poszerzaniu moich horyzontów, szczególnie przez umożliwienie odbycia stażów zagranicznych. Ponadto, podziękowania kieruję do opiekunów stażów: prof. Asena Pashova z Uniwersytetu Sofijskiego oraz prof. Weidonga Chena z Uniwersytetu Opalowego Wybrzeża (fr. Université du Littoral Côte d'Opale) w Dunkierce we Francji, za przekazaną wiedzę i okazaną gościnność.

Podziękowania składam także mojemu Mężowi, Franciszkowi Sobczukowi, za wsparcie okazane podczas powstawania niniejszej rozprawy, nie tylko duchowe, lecz również merytoryczne. Zdecydowanie mogę przyznać, że nasze długie rozmowy dotyczące fizyki toczące się nieraz do późnej nocy ukształtowały mnie jako naukowca.

Dziękuję również moim Rodzicom za trud wychowania mnie, bycia moimi pierwszymi nauczycielami oraz za ich serdeczne wsparcie na drodze mojej edukacji.

Ponadto, dziękuję lekarzom: Tomaszowi Wojewodzie z Oddziału Chirurgii Ogólnej, Onkologicznej i Naczyniowej 5. Wojskowego Szpitala Klinicznego z Poliklinika w Krakowie oraz Karolowi Wójcikowi z Oddziału Hematologii i Chorób Wewnętrznych Szpitala Specjalistycznego im. Ludwika Rydygiera w Krakowie, a także pielęgniarkom i wszystkim pracownikom służby zdrowia z ww. oddziałów, bez których pracy niniejsza rozprawa nie mogłaby powstać.

Na końcu, dziękuję dobremu Bogu za niezwykłe piękno i złożoność Wszechświata, który możemy badać.

Spis treści

Wykaz prac wchodzących w skład pracy doktorskiej

[A] T. Urbańczyk, J. Dudek, J. Koperski, *Isotopologue – selective excitation studied via optical – optical double resonance using* $E^3\Sigma_1^+(6^3S_1)\leftarrow A^3\Pi_{0^+}(5^3P_1)\leftarrow X^1\Sigma_{0^+}(5^1S_0)$ *transitions in CdAr and CdKr van der Waals complexes*, J. Quant. Spectrosc. Radiat. Transf. **212**, 32 (2018). https://doi.org/10.1016/j.jqsrt.2018.03.013

[B] J. Dudek, K. Puczka, T. Urbańczyk, J. Koperski, *High – temperature molecular beam source for aggressive elements*: *An example of zinc*, Rev. Sci. Instrum. **90**, 115109 (2019). https://doi.org/10.1063/1.5127809

[C] J. Dudek, A. Kędziorski, J.P. Zobel, M. Krośnicki, T. Urbańczyk, K. Puczka, J. Koperski, *Bound→free and bound→bound multichannel emission spectra from selectively excited Rydberg states in the ZnAr and CdAr van der Waals complexes*, J. Mol. Struc. **1222**, 128840 (2020). https://doi.org/10.1016/j.molstruc.2020.128840

[D] J. Sobczuk, T. Urbańczyk, J. Koperski, *Optical-optical double resonance process in free-jet supersonic expansion of van der Waals molecules: characteristics of the expansion, number of excited molecules and emitted photons*, Mol. Phys. **120**, e2024614 (2022). https://doi.org/10.1080/00268976.2021.2024614

[E] T. Urbańczyk, J. Sobczuk, J. Koperski, *Rotational characterization of the* $E^3\Sigma_1^+(5s6s^3S_1)$ *Rydberg state of CdNe van der Waals complex via selective J-excitation in OODR process*, Spectrochim. Acta A: Mol. Biomol. Spectrosc. **264**, 120248 (2022). https://doi.org/10.1016/j.saa.2021.120248

[F] J. Sobczuk, T. Urbańczyk, J. Koperski, *The lowest-lying Rydberg state of CdAr van der Waals complex: The improved characterization of the interatomic potential*, Spectrochim. Acta A: Mol. Biomol. Spectrosc. **282**, 121655 (2022). https://doi.org/10.1016/j.saa.2022.121655

Lista skrótów

IPA	ang. ***I**nverted **P**erturbative **A**pproach*, metoda odwróconego rachunku perturbacynego
LIF	ang. ***L**aser **I**nduced **F**luorescence*, emisja indukowana laserem
Me	metal 12. grupy Układu Okresowego Pierwiastków (Zn, Cd, Hg)
OODR	ang. ***O**ptical – **O**ptical **D**ouble **R**esonance*, podwójny rezonans optyczno – optyczny
PEC	ang. ***P**otential **E**nergy **C**urve*, krzywa energii potencjalnej
Rg	ang. ***R**are **G**as*, gaz szlachetny
TDM	ang. ***T**ransition **D**ipole **M**oment*, dipolowy moment przejścia
vdW	van der Waalsa (kompleks/molekuła, oddziaływanie)
UOP	**U**kład **O**kresowy **P**ierwiastków

1. Molekuły van der Waalsa

1.1 Oddziaływania dyspersyjne

O oddziaływaniach dyspersyjnych (Londona) między atomami (cząsteczkami) mówimy wtedy, gdy oddziałujące obiekty nie posiadają trwałego momentu dipolowego, a przyciąganie elektrostatyczne zachodzi dzięki niezerowej polaryzowalności dwóch oddziałujących obiektów [2]. W praktyce oddziaływania dyspersyjne występują również w przypadku atomów lub cząsteczek posiadających trwały moment dipolowy, lecz są one pomijalnie małe w porównaniu z przyciąganiem między stałymi dipolami (Keesoma) lub między dipolem stałym i indukowanym (Debye'a) [2]. Oddziaływania te maleją wraz z odległością R między atomami jak $1/R^6$, co zostanie pokazane dla prostego jednowymiarowego modelu [3].

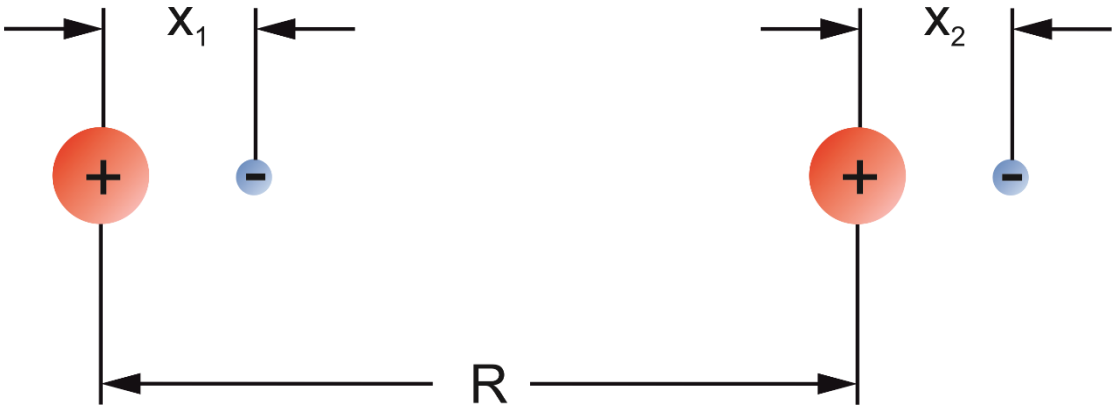

Rysunek 1. Prosty jednowymiarowy model atomów wodoru oddziałujących dyspersyjnie [3].

Dane są dwa atomy, których jądra (rdzenie atomowe) są w odległości R od siebie (rys.1). Każdy z atomów opisany jest modelem oscylatora harmonicznego składającego się z ciężkiego jądra (rdzenia atomowego) i lekkiego elektronu. Uwzględniając ponadto oddziaływania kulombowskie między czterema ładunkami, hamiltonian tego układu można zapisać jako:

$$\mathcal{H} = \mathcal{H}_0 + \mathcal{H}_1, \tag{1}$$

gdzie część $\mathcal{H}_0$ opisuje oddziaływania związane z oscylatorem harmonicznym, a $\mathcal{H}_1$ – oddziaływania elektrostatyczne. Człony $\mathcal{H}_0$ i $\mathcal{H}_1$ można rozwinąć jako:

$$\begin{aligned} \mathcal{H}_0 &= \frac{1}{2m}p_1^2 + \frac{1}{2}m\omega_0^2 x_1^2 + \frac{1}{2m}p_2^2 + \frac{1}{2}m\omega_0^2 x_2^2, \\ \mathcal{H}_1 &= \frac{e^2}{4\pi\epsilon_0}\left(\frac{1}{R} + \frac{1}{R + x_1 - x_2} - \frac{1}{R + x_1} - \frac{1}{R - x_2}\right), \end{aligned} \tag{2}$$

gdzie $p_1(p_2)$ – pęd pierwszego (drugiego) atomu, m – masa atomu, ω_0 – częstość drgań atomu w stanie podstawowym, $x_1(x_2)$ – odległość między jądrem (rdzeniem atomowym) a elektronem w pierwszym (drugim) atomie. Ponieważ $R \gg x_1, x_2$, rozwinięcie $\mathcal{H}_1$ w szereg do wyrazów 2. stopnia daje przybliżenie:

$$\mathcal{H}_1 \approx -2\frac{e^2 x_1 x_2}{4\pi\epsilon_0 R^3}. \tag{3}$$

Równanie (3) bardzo obrazowo przedstawia naturę oddziaływań dyspersyjnych. Otóż $\mathcal{H}_1$ opisuje energię atomu 2. jako dipola znajdującego się w polu elektrycznym pochodzącym od momentu dipolowego atomu 1.:

$$\mathcal{H}_1 \sim -d_2 E_2(d_1) = e x_2 \frac{-e x_1}{4\pi\epsilon_0 R^3} = -\frac{e^2 x_1 x_2}{4\pi\epsilon_0 R^3}, \tag{4}$$

gdzie $d_1(d_2)$ – moment dipolowy atomu pierwszego (drugiego), $E_2(d_1)$ – pole elektryczne pochodzące od dipola d_1 w położeniu atomu drugiego. Postać równania (4) analogiczna do równania (3) pod względem zależności od R, x_1 i x_2.

Przedstawmy teraz ten układ używając rachunku zaburzeń. Ponieważ atomy pozbawione są trwałego momentu dipolowego, poprawki perturbacyjne pierwszego rzędu ΔE_1 nie wnoszą wkładu w energię układu:

$$\Delta E_1 = \langle \psi_0 | \mathcal{H}_1 | \psi_0 \rangle = 0, \tag{5}$$

gdzie ψ_0 – funkcja falowa układu.

Zmiana energii związana z oddziaływaniem dyspersyjnym jest zatem związana z poprawkami drugiego rzędu ΔE_2:

$$\Delta E_2 = V(R) = \sum_{n \neq 0} \frac{\langle 0 | \mathcal{H}_1 | n \rangle \langle n | \mathcal{H}_1 | 0 \rangle}{E_0 - E_n}. \tag{6}$$

Dla jednowymiarowego oscylatora harmonicznego:

$$\langle l | x | 0 \rangle = \delta_{l,1} \sqrt{\frac{1}{2m\omega_0}}, \tag{7}$$

gdzie $\delta_{l,1}$ oznacza funkcję delta Diraca. Wówczas z równania (6) otrzymujemy:

$$V(R) = \left(\frac{2e^2}{4\pi\epsilon_0 R^3}\right)^2 \sum_{n_1,n_2} \frac{\delta_{n_1,1}\delta_{n_2,1}|\langle 1,1|x_1x_2|0,0\rangle|^2}{(n_1+n_2)\omega_0}$$

$$= \left(\frac{2e^2}{4\pi\epsilon_0 R^3}\right)^2 \left(\sqrt{\frac{1}{2m\,\omega_0}}\right)^4 \frac{1}{(-2\omega_0)} \qquad (8)$$

$$= -\frac{e^4}{32\pi^2\epsilon_0^2 m^2 \omega_0^3 R^6}.$$

Równanie (8) pokazuje, że potencjał oddziaływań dyspersyjnych rzeczywiście maleje jak $1/R^6$. Wynik uzyskany w równaniu (8) można zapisać, używając polaryzowalności oddziałującego atomu α_E. Jeżeli do układu przyłożone jest zewnętrzne pole elektryczne E_0, hamiltonian tego systemu jest następujący:

$$\mathcal{H} = \mathcal{H}_0(x_1, x_2) + eE_{0x_1} + eE_0x_2 = \mathcal{H}_0(z_1, z_2) - \frac{e^2E_0^2}{m\omega_0^2}, \qquad (9)$$

gdzie $z_i = x_i + \frac{eE_0}{m\omega_0^2}$. Indukowany moment dipolowy d_{ind} wynosi wówczas:

$$d_{ind} = \frac{\delta\mathcal{H}}{\delta\, E_0} = \frac{2e^2E_0}{m\omega_0^2}. \qquad (10)$$

Polaryzowalność elektryczna α_E jest wielkością opisującą zdolność układu do tworzenia dipola elektrycznego pod wpływem zewnętrznego pola elektrycznego. Zgodnie z definicją można więc zapisać, że:

$$d_{ind} = 4\pi\epsilon_0\alpha_E E_0. \qquad (11)$$

Z równań (10) i (11) wynika natomiast:

$$\alpha_E = \frac{2e^2}{4\pi\epsilon_0 m\omega_0^2}. \qquad (12)$$

Na końcu, potencjał dyspersyjny w równaniu (8) można wyrazić przez polaryzowalność w równaniu (12), otrzymując:

$$V(R) = \frac{\alpha_E^2\omega_0}{8R^6}. \qquad (13)$$

Jest to „tradycyjna” forma potencjału zaproponowana przez Londona [4].

W powyższym wyprowadzaniu przyjęto założenie, że czas propagacji oddziaływań elektrostatycznych jest nieskończenie krótki. Jednak dla dużych odległości międzyatomowych, dla których czas propagacji sygnału jest zbliżony lub większy od czasu charakteryzującego ewolucję atomu, tzn. $\omega_0 R \geq 1$, należy uwzględnić relatywistyczny efekt retardacji. Zatem dla

dużych odległości oddziaływania dyspersyjne opisywane są przez oddziaływanie Casimira-Poldera i maleją wraz z odległością jak $1/R^7$ [5].

1.2 Właściwości molekuł van der Waalsa

Molekułami (kompleksami) van der Waalsa nazywane są kompleksy utworzone przez atomy lub molekuły, związane nie przez wiązania chemiczne, lecz przez przyciągające oddziaływania międzyatomowe (międzymolekularne) [6], w szczególności: Keesoma, Debye'a lub Londona. Przykładowo, gazy szlachetne, wodór, tlen czy benzen zawierają śladowe ilości molekuł vdW typu Rg_2 [6], $(H_2)_2$, $(O_2)_2$ czy $(C_6H_6)_2$ [7]. Atomy mogą natomiast tworzyć kompleksy vdW wtedy, gdy posiadają zapełnione powłoki elektronowe, tj. atomy gazu szlachetnego lub atomy 2. i 12. grupy Układu Okresowego Pierwiastków (UOP) [8]. W tej pracy będzie mowa o dwuatomowych kompleksach typu MeRg lub Me_2 (Me – atom 12. grupy UOP).

Zgodnie z nomenklaturą IUPAC molekułą określa się neutralną elektrycznie grupę dwóch lub więcej atomów, których powierzchnia energii potencjału posiada studnię na tyle głęboką, aby zawierała co najmniej jeden poziom oscylacyjny. Natomiast kompleksami nazywane są grupy atomów, jonów lub molekuł otrzymane przez oddziaływania słabsze, niż kowalencyjne [1]. Ponieważ Me_2 i MeRg spełniają definicję zarówno kompleksu, jak i molekuły, w niniejszej pracy oba terminy używane są zamiennie.

Aby w pełni opisać potencjał oddziaływania między atomami posiadającymi zamkniętopowłokową strukturę elektronową, oprócz przyciągających oddziaływań dyspersyjnych należy wziąć również pod uwagę oddziaływania odpychające, wynikające z zakazu Pauliego [9]. Pierwszy empiryczny model uwzględniający odpychającą strukturę zaproponowany był przez Lennarda – Jonesa [10], który opisywał oddziaływania odpychające proporcjonalne do $1/R^{12}$. Innymi potencjałami często używanymi w opisie kompleksów vdW jest potencjał Morse'a [8], Maitlanda-Smitha [8] czy Halgrena [9].

Należy mieć jednak na uwadze, że granica między wiązaniem chemicznym a oddziaływaniem vdW jest niejednoznaczna. Przykładowo, analiza międzyjądrowej odległości równowagowej w stanie podstawowym molekuły Cd_2 wykazała, że między atomami, oprócz oddziaływań dyspersyjnych, występuje również domieszka wiązania kowalencyjnego [11]. Do

podobnych wniosków doprowadziły obliczenia *ab initio* dla stanów podstawowych molekuł Zn_2, Cd_2 i Hg_2 [12].

1.3 Stany rydbergowskie molekuł van der Waalsa

Stany rydbergowskie molekuł MeRg i Me_2 wykazują bardzo ciekawe właściwości, które po części zostały wyjaśnione dzięki obliczeniom *ab initio*. Przede wszystkim, PEC tych stanów często wykazują wielodołkową strukturę, która zazwyczaj wynika z kształtu modułu kwadratu funkcji falowej stanu rydbergowskiego atomu metalu [13]. Czasami jednak taka struktura ma związek ze sprzężeniem spinowo – orbitalnym. Dowodem na to jest fakt, że dwudołkowy kształt mogą wykazywać stany nie-rydbergowskie, np. stan $B^3 1(5^3P_1)$ w CdKr [14-16]. Taki charakter wynika z faktu, że przyczynek do potencjału $B^3 1$ wnoszą stany $^3\Pi$ oraz $^3\Sigma$, których minima są zlokalizowane dla różnych odległości międzyatomowych [14].

Z wielodołkową strukturą wiąże się inna ciekawa cecha molekuł w stanie rydbergowskim. Jest nią duża międzyjądrowa odległość równowagowa najdalszej studni [13]. która dla wysoko wzbudzonych stanów może dochodzić nawet do kilku mikrometrów [17-18]. Takie molekuły zostały szerzej omówione w podrozdziale 1.5.

Kolejną ciekawą właściwością, która charakteryzuje stany rydbergowskie jest stosunkowo mały przyczynek oddziaływań dyspersyjnych do kształtu potencjału. O ile dla stanów podstawowych w kompleksach MeRg oddziaływania dyspersyjne w obszarze dalekozasięgowym są dominujące, o tyle zostało pokazane, że molekułę CdAr w stanie rydbergowskim można w obliczeniach potraktować jako strukturę składającą się z: kationu Cd^+, atomu Ar i elektronu w stanie rydbergowskim, a kształt bariery potencjału oraz, częściowo, zewnętrznej studni można wytłumaczyć rozpraszaniem rydbergowskiego elektronu na atomie Ar [13]. Do podobnych wniosków doprowadziła analiza obliczeń *ab initio* molekuły ZnAr [19].

Tabela 1. Zestawienie badań nad molekułami van der Waalsa MeRg i Me_2 (gdzie Me=Zn,Cd,Hg, Rg=atom gazu szlachetnego).

Molekuła	Obliczenia *ab initio*	Eksperyment
	Zn	
ZnAr	Stany korelujące z asymptotami atomowymi: $5^3P_{0,1,2}$, 4^1D_2, $4^3D_{1,2,3}$, 5^1P_1, 6^3S_1, 6^1S_0 [C], [19]	$E^3\Sigma^+(5^3S_1)$ [20]
	Cd	
CdNe		$E^3\Sigma^+(6^3S_1)$ [E],[21]
CdAr	Stany korelujące z asymptotami atomowymi: 6^3S_1, 6^3S_0, $6^3P_{0,1,2}$, 5^1D_2, $5^3D_{1,2,3}$, 6^1P_1, 7^3S_1, 7^1S_0 wraz z dipolowymi momentami przejścia dla absorpcji ze stanu podstawowego [13]	$E^3\Sigma^+(6^3S_1)$: [A,E-F], [22-26]
CdKr		$E^3\Sigma^+(6^3S_1)$ [A], [24],[27-28]
Cd_2	$D^10_u^+$ (6^1S_0) [29] $F^31_u(6^3P_2)$ [29] $^31_g(6^3S_1)$ [30]	$D^10_u^+$ (6^1S_0) [29] $F^31_u(6^3P_2)$ [29] $^31_g(6^3S_1)$ [30]
	Hg	
HgNe	Stany $^30^-(7^3S_1)$, $^31(7^3S_1)$ oraz $^10^+(7^1S_0)$ wszystkich molekuł HgRg [31]	$^3\Sigma^+(n^3S_1)$, n=9-10 [32-33] $^1\Sigma^+(n^1S_0)$, n=7-9 [34]
HgAr		$E^3\Sigma^+(7^3S_1)$ [35] $^3\Sigma^+(8^3S_1)$ [33]

Tabela 1. pokazuje dotychczasowy stan badań nad stanami rydbergowskimi molekuł MeRg i Me_2. Do tej pory najlepiej przebadanym eksperymentalnie stanem jest $E^3\Sigma_1^+(6^3S_1)$ w CdAr. Wykazano, że posiada on dwudołkową strukturę [23-24] oraz wyznaczono kształt wewnętrznej $\mathbf{E^3\Sigma^+_{1in}}$ [26] i zewnętrznej $\mathbf{E^3\Sigma^+_{1\,out}}$ [25,F] studni potencjału. Niewątpliwie dużym osiągnięciem w tym zakresie było wyznaczenie kształtu potencjału obejmującego dwie studnie i barierę potencjału [F].

1.4 Metody eksperymentalne badań nad stanami rydbergowskimi molekuł van der Waalsa

Studnia potencjału molekuł vdW w stanie podstawowym jest zazwyczaj niezwykle płytka, w warunkach normalnych zbliżona do energii termicznej systemu. Dlatego większość

kompleksów vdW może być stabilna jedynie w układzie schłodzonym. W tej pracy zastosowano chłodzenie przez adiabatyczne rozprężanie gazu w wiązce naddźwiękowej [36]. W tej metodzie gaz jest w stanie nierównowagowym, a chłodzenie oscylacyjnych i rotacyjnych stopni swobody jest znacznie wydajniejsze, niż chłodzenie translacyjne [6].

Dużym wyzwaniem eksperymentalnym była budowa modułu źródła wiązki naddźwiękowej dla molekuł zawierających kadm i cynk. Otrzymanie par tych pierwiastków o ciśnieniu parcjalnym umożliwiającym formowanie molekuł vdW jest możliwe przez ablację laserową [37] lub podgrzewanie metalu do relatywnie wysokiej temperatury (odpowiednio ok. 650°C i 750°C). W niniejszej pracy została zastosowana druga z metod. Do badania molekuł CdRg i Cd_2 wykorzystano moduł źródła o pracy impulsowej, którego konstrukcja została opisana w [38]. Natomiast do spektroskopii kompleksów ZnRg i Zn_2, został zaprojektowany nowy moduł źródła o pracy ciągłej, którego konfiguracja, uruchomienie i testy wchodzą w skład niniejszej pracy [B]. Szczegóły dotyczące układu eksperymentalnego do badania molekuł Zn_2 oraz ZnRg, i zostały opisane w rozdziale 3.

Do badania struktury energetycznej kompleksów vdW zostały zastosowane metody spektroskopii laserowej przy użyciu impulsowych laserów barwnikowych o wysokiej energii. Zaletą laserów barwnikowych jest ich przestrajalność w szerokim zakresie energii, co pełni dwojaką funkcję:

- pozwala na eksplorację różnych stanów elektronowych przy zastosowaniu tych samych systemów laserowych,
- umożliwia realizację spektroskopii wzbudzenia w zakresie optycznym.

Główną metodą eksperymentalną stosowaną w niniejszej pracy jest spektroskopia wzbudzenia [A,B,E,F], jednak poczyniono również wysiłek w kierunku realizacji spektroskopii emisji [C,D]. Układ eksperymentalny używany do spektroskopii wzbudzeniowej molekuł Cd_2 i CdRg został pokazany na rys. 2a. W tej metodzie molekuły w wiązce naddźwiękowej są wzbudzane za pomocą przestrajalnych laserów, a całkowita indukowana laserowo emisja (ang. *Laser – Induced Fluorescence*, LIF) jest przedstawiana w funkcji zmierzonej liczby falowej wzbudzającego lasera. Do detekcji sygnału LIF używane są fotopowielacze.

Schemat układu umożliwiającego rejestrację widm emisji jest przedstawiony na rys. 2b. W tym przypadku lasery barwnikowe ustawione są na konkretne długości fali, odpowiadające dwóm przejściom o relatywie dużych dipolowych momentach przejścia (ang. *Transition Dipole*

Moment, TDM) w molekule, natomiast emisja jest analizowana z użyciem spektrometru i rejestrowana przez kamerę iCCD.

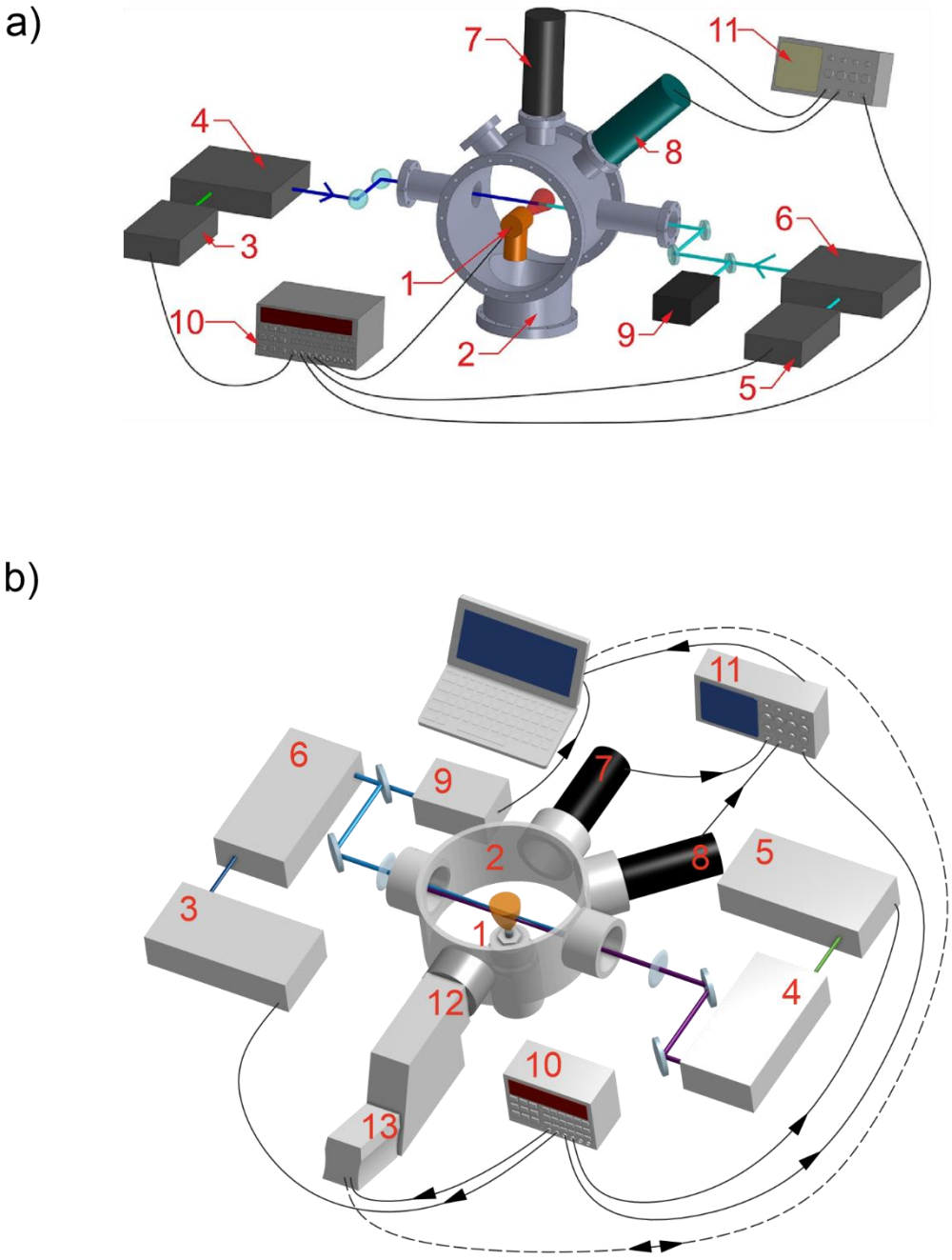

Rysunek 2. Schemat układu doświadczalnego służącego do badania widm: a) wzbudzenia [A], b) emisji [C] przy wzbudzeniu do stanów rydbergowskich metodą OODR. 1- moduł źródła wiązki naddźwiękowej, 2 – komora próżniowa, 3,5– impulsowy laser Nd:YAG pompujący laser barwnikowy, 4 – impulsowy laser barwnikowy (pompujący w OODR), 6 – impulsowy laser barwnikowy (próbkujący w OODR), 7 – fotopowielacz rejestrujący LIF z przejścia pompującego, 8 – fotopowielacz rejestrujący LIF przejścia próbkującego, 9 – falomierz, 10 – cyfrowy generator opóźnienia, 11 – oscyloskop, 12 – spektrometr, 13 – kamera iCCD.

Badanie stanów Rydbergowskich kompleksów vdW wymaga zastosowania energii wzbudzenia odpowiadającej próżniowemu UV. Przykładowo, energia wzbudzenia molekuły

CdAr ze stanu podstawowego do studni $E^3\Sigma^+_{1\,out}$ odpowiada długości fali ok. 194 nm. Aby uniknąć stosowania wiązek laserowych w zakresie próżniowego UV stwarzających duże trudności eksperymentalne ze względu na: ich absorpcję w powietrzu, niski próg zniszczenia elementów optycznych przez światło laserowe (ang. *laser damage threshold*) oraz bezpieczeństwo użytkowania, w niniejszych badaniach stosowany jest sekwencyjny (ang. *stepwise*) OODR [39]. Metoda ta polega na wzbudzeniu molekuły do wysokiego stanu elektronowego poprzez wybrany poziom oscylacyjny stanu pośredniego (rys. 3). Analogicznie do techniki *pump-and-probe* [40], przejście ze stanu podstawowego do pośredniego jest nazywane przejściem pompującym, natomiast wzbudzenie ze stanu pośredniego –przejściem próbkującym. Ściśle rzecz biorąc, sekwencyjny OODR nie jest jednak tożsamy z techniką *pump-and-probe*. Celem wykorzystania lasera próbkującego w sekwencyjnym OODR nie jest bezpośrednie zebranie informacji o próbce, jak w technice *pump-and-probe*, lecz wzbudzenie molekuły do poziomu oscylacyjno – rotacyjnego w wysokim stanie elektronowym. Stąd też wynika kolejna różnica: w *pump-and-probe* impuls próbkujący jest zwykle znacznie słabszy od impulsu pompującego, natomiast w sekwencyjnym OODR wykorzystywane są zwykle impulsy pompujący i próbkujący lasera o zbliżonej mocy.

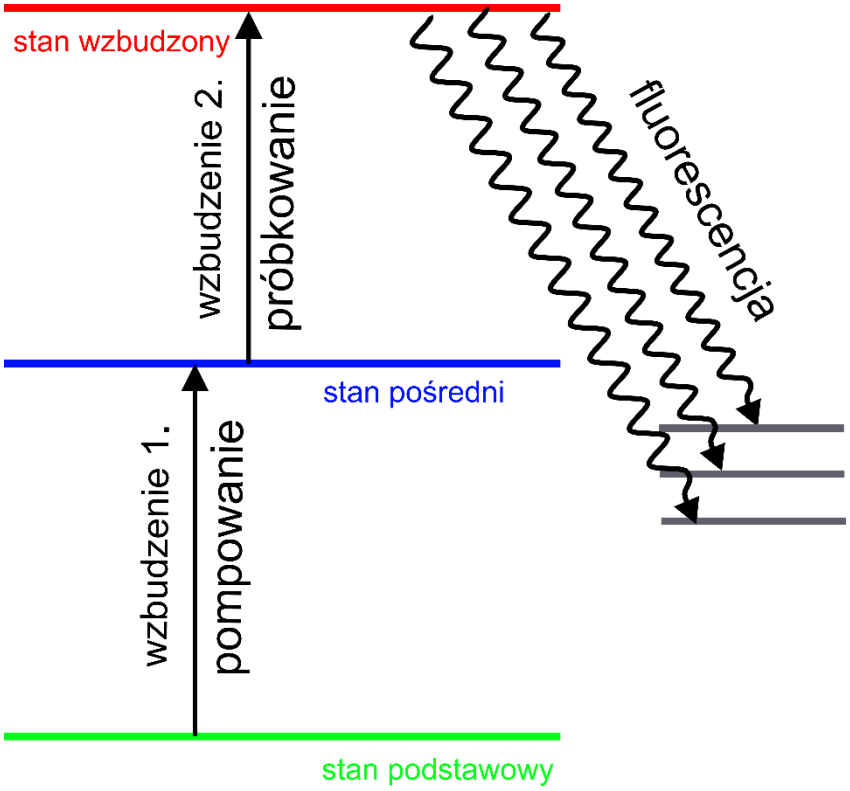

Rysunek 3. Schemat przejść w metodzie sekwencyjnego OODR [39] oraz powiązanie nazw przejść z nomenklaturą stosowaną w technice *pump-and-probe* [40].

1.5 Motywacja badań nad stanami rydbergowskimi molekuł van der Waalsa

Porównanie obliczeń *ab initio* oraz wyników eksperymentalnych PEC dla płytkich stanów $E^3 1_u(6^3P_2)$ oraz $F^3 0_u^+(6^3P_1)$ molekuły Hg_2 wykazało znaczne różnice między teorią a eksperymentem [41], choć zgodność ta była większa, niż w przypadku porównania tych samych wyników eksperymentalnych [42-43] ze wcześniejszymi obliczeniami *ab initio* [44-45]. Poprawa jakości obliczeń *ab initio* nastąpiła dzięki zastosowaniu nowych baz atomowych oraz użyciu szybszych komputerów umożliwiających uwzględnienie sprzężeń między większą ilością elektronów. Ponadto, wykorzystanie nowych metod symulacji widm, przy użyciu programów LEVEL [46] oraz PGOPHER [47] pozwoliło na ponowną analizę [41] wyników eksperymentalnych [42-43], uzyskując stałe spektroskopowe o większej precyzji i dokładności.

Powyższy przykład pokazuje, że fizyka kompleksów vdW wciąż pozostawia wiele pytań. Znalezienie kształtu PEC molekuły Hg_2 nawet dla niskich stanów elektronowych stanowi wyzwanie ze względu na znaczną liczbę elektronów, jaką należy uwzględnić w obliczeniach. Równie istotną problematyką jest badanie PEC stanów rydbergowskich molekuł vdW. Na przykład w analizie zawartej w [F] wchodzącej w zakres niniejszej pracy doktorskiej widoczna jest znaczna różnica między wynikami otrzymanymi z obliczeń *ab initio* a wynikami eksperymentalnymi dla kształtu potencjału $E^3\Sigma_1^+(6^3S_1)$ w CdAr. Szczególnie przejawia się ona w sporej rozbieżności w międzyjądrowej odległości równowagowej zewnętrznej studni oraz w kształcie bariery potencjału.

Dlaczego tak istotne jest udoskonalanie narzędzi badających i opisujących słabe oddziaływania dalekozasięgowe? Otóż pozwala to na zrozumienie i modelowanie wielu złożonych i istotnych zjawisk fizycznych i chemicznych. Kompleksy vdW można postrzegać jako stadium pośrednie pomiędzy izolowanymi atomami czy molekułami a fazą objętościową (ang. *bulk*), których właściwości skrajnie się różnią. Przykładowo, w dimerach Zn_2, Cd_2 i Hg_2 dominują oddziaływania dyspersyjne, podczas gdy cynk, kadm i rtęć w fazie objętościowej wykazują właściwości metaliczne. Ta rozbieżność została wyjaśniona dzięki analizie właściwości klastrów o zmiennej ilości atomów Zn_n [48], Cd_n [49] i Hg_n [50] ($n \geq 2$).

Kompleksy vdW stanowią również ciekawy obiekt badawczy w astronomii. Na przykład, dimery $(O_2)_2$ i $(H_2)_2$ zostały wykryte w atmosferze Jowisza i Saturna [51-53], natomiast kompleksy H_2-H_2O obecne w ośrodku międzygwiazdowym w gwiazdozbiorze

Cefeusza pełnią prawdopodobnie rolę ośrodka pompującego dla odkrytego w tym regionie masera wodnego [54]. Co ciekawe, w materii międzygwiazdowej zostały również wykryte pierwiastki Zn [55] i Cd [56], co w połączeniu ze sprzyjającymi warunkami termodynamicznymi pozwala wysunąć hipotezę, że kompleksy vdW pierwiastków Zn i Cd są w tej materii obecne i mogą stanowić stadium pośrednie w powstawaniu pyłu kosmicznego.

Stany rydbergowskie molekuł stanowią również bogatą rodzinę niezwykle ciekawych i złożonych systemów kwantowych. Kilkukrotnie pokazano istnienie stanów związanych między atomami o ekstremalnie długiej międzyjądrowej odległości równowagowej przekraczającej 1 μm, których pochodzenie zostało zidentyfikowane jako rezultat obecności nowego rodzaju wiązania pochodzącego od rozpraszania elektronu w stanie rydbergowskim na atomie lub molekule [57]. Takie molekuły, utworzone przez atomy rubidu, otrzymano przez stany związane na fali *s* (ang. *s-wave bound states*) [17], na fali *p* [58] oraz molekuły zawierające elektrony rydbergowskie o dużym momencie pędu – tzw. molekuły trylobitowe [59].

Podsumowując, wykonane badania nad stanami rydbergowskimi molekuł vdW wpisują się w dziedzinę fizyki fundamentalnej dążącej do doskonalenia narzędzi uwzględniających wpływ słabych oddziaływań międzyatomowych i międzymolekularnych na kwantowy opis systemu.

2. Spektroskopia wzbudzeniowa molekuł CdRg

W tym rozdziale zostanie omówiona spektroskopia wzbudzeniowa do stanu rydbergowskiego $E^3\Sigma_1^+(6^3S_1)$ molekuł CdAr, CdKr i CdNe uzyskana metodą OODR. W pracy poświęconej selekcji izotopologów molekuł CdAr i CdKr [A] doktorantka uczestniczyła w pomiarach widm wzbudzenia w molekule CdKr, co pozwoliło na naukę obsługi istniejącego już układu doświadczalnego używanego do wszystkich eksperymentów dotyczących spektroskopii Cd_2 i CdRg. Doktorantka wykonała również część grafik wchodzących do publikacji oraz brała udział w ostatecznej edycji tekstu publikacji. W pracy dotyczącej charakterystyki poziomów rotacyjnych stanu $E^3\Sigma_1^+$ w CdNe [E] doktoranta uczestniczyła w przygotowaniu układu doświadczalnego oraz w pomiarach wstępnych do omówionej w podrozdziale 2.2 spektroskopii molekuły CdNe.

Najważniejszym wkładem doktorantki w spektroskopię stanu $E^3\Sigma_1^+$ w CdRg było wyznaczenie kształtu potencjału $E^3\Sigma_1^+$ w CdAr uwzględniający barierę potencjału. Przeprowadziła ona wszystkie pomiary widm free←bound, a także wstępne pomiary widm bound←bound. Ponadto, wykonała ona analizę danych umożliwiającą wyznaczenie nowych stałych oscylacyjnych oraz nowej wartości międzyjądrowej odległości równowagowej na podstawie zmierzonych widm bound←bound. Brała również udział w analizie widm free←bound. Doktorantka jest autorką tekstu publikacji [F] dotyczącego wyników, dyskusji i podsumowania, a także większości rysunków.

2.1 Selektywne wzbudzenie izotopologów molekuł CdAr i CdKr z wykorzystaniem stanów rydbergowskich $E^3\Sigma_1^+(6^3S_1)$

W pracy [A] została pokazana metoda selektywnego wzbudzenia izotopologów do stanów rydbergowskich metodą OODR dla kompleksów CdAr i CdKr. Efekt ten jest możliwy dzięki zjawisku przesunięcia izotopowego, czyli różnicy energii przejścia oscylacyjnego dla poszczególnych izotopologów $\Delta\upsilon_{ij}$ [6]. Dla molekuł nierotujących, różnica ta między i-tym a j-tym izotopologiem przejścia oscylacyjnego $\upsilon' \leftarrow \upsilon''$ w przybliżeniu oscylatora anharmonicznego pierwszego rzędu jest równa

$$\Delta\upsilon_{ij} = (1-\rho_{ij})\left[\omega_e'\left(\upsilon'+\frac{1}{2}\right)-\omega_e''\left(\upsilon''+\frac{1}{2}\right)\right] - (1-\rho_{ij}^2)\left[\omega_e'x_e'\left(\upsilon'+\frac{1}{2}\right)^2-\omega_e''x_e''\left(\upsilon''+\frac{1}{2}\right)^2\right], \quad (14)$$

gdzie $\rho_{ij} = \sqrt{\frac{\mu_i}{\mu_j}}$, $\mu_{i(j)}$ – masa zredukowana i-tego (j-ego) izotopologu, ω_e – stała oscylacyjna, $\omega_e x_e$ – stała anharmoniczna 1. rzędu. Jak pokazuje równanie (14), przesunięcie izotopowe zależy od stosunku mas zredukowanych izotopologów.

W eksperymencie zastosowano kadm oraz gaz szlachetny o naturalnych abundancjach. Dla obydwu molekuł zastosowano schemat wzbudzenia $E^3\Sigma_1^+ \leftarrow A^3\Pi_{0^+} \leftarrow X^1\Sigma_{0^+}$.

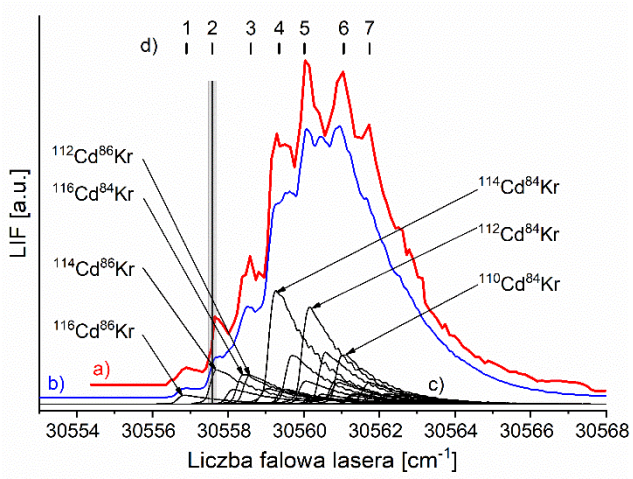

Rysunek 4. (a) Widmo eksperymentalne zarejestrowane z wykorzystaniem przejścia $A^3\Pi_{0^+}(\upsilon''=9) \leftarrow X^1\Sigma_{0^+}(\upsilon=0)$ w molekule CdKr. (b) Symulacja widma eksperymentalnego przy użyciu programów LEVEL [46] i PGOPHER [47]. (c) Przyczynki poszczególnych izotopologów do symulacji widma eksperymentalnego przedstawionego w (b) pochodzące od izotopologów o abundancji większej, niż 1%. Na każdy z przyczynków składa się struktura rotacyjna odpowiadająca temperaturze rotacyjnej $T_{rot} = 4$ K. (d) Pozycje lasera pierwszego wzbudzenia użyte do wzbudzenia w schemacie OODR $E^3\Sigma_1^+(\upsilon'=18) \leftarrow A^3\Pi_{0^+}(\upsilon''=9) \leftarrow X^1\Sigma_{0^+}(\upsilon=0)$ w CdKr, zrealizowane w pracy [A].

Idea selekcji izotopologów w schemacie OODR pokazana jest na rys. 4, na którym przedstawiono widmo zarejestrowane z wykorzystaniem przejścia $A^3\Pi_{0^+}(\upsilon''=9) \leftarrow X^1\Sigma_{0^+}(\upsilon=0)$ w CdKr. Wybrana linia oscylacyjna ma kształt odzwierciedlający strukturę izotopową, której poszczególne przyczynki pochodzące od izotopologów o największej abundancji zostały przedstawione na rys. 4c. Następnie, ustawiając laser 1. wzbudzenia (rys. 3) na jednym z siedmiu położeń, pokazanych na rys. 4d, zrealizowano przejście $E^3\Sigma_1^+(\upsilon'=18) \leftarrow A^3\Pi_{0^+}(\upsilon''=9)$. W zależności od energii lasera 1. wzbudzenia, dominujący wkład w widmo 2. wzbudzenia miał jeden (pozycje 1 i 2 na rys. 4d) lub wiele (pozycje 6 i 7 na rys. 4d) izotopologów. Analiza widm drugiego wzbudzenia wykonana w pracy [A] pokazała, że w celu

selekcji jednego izotopologu CdKr najlepszym wyborem jest energia pierwszego wzbudzenia równa 30 557.58 cm^{-1} (pozycja 2 na rys. 4d). Otrzymuje się wówczas wzbudzenie głównie izotopologu $^{114}Cd^{86}Kr$ z relatywnie dobrym stosunkiem sygnału do szumu.

Analogiczna analiza została wykonana dla kompleksu CdAr, w którym jednak przesunięcie izotopowe jest mniejsze z powodu mniejszej wartości masy zredukowanej, jak również niższej oscylacyjnej liczby kwantowej v'' użytej do analizy - $A^3\Pi_{0^+}(v''=6)$.

2.2 Charakterystyka poziomów rotacyjnych w rydbergowskim stanie $E^3\Sigma_1^+(6^3S_1)$ molekuły CdNe

Stan rydbergowski $E^3\Sigma_1^+(6^3S_1)$ kompleksu CdNe został dotychczas opisany tylko raz [21], z rozdzielczością pozwalającą jedynie na rozdzielenie struktury oscylacyjnej. W pracy [E] dokonano pierwszej analizy struktury rotacyjnej poziomów $v'=0$ oraz $v'=1$.

Przejścia zostały zrealizowane w schemacie OODR $E^3\Sigma_1^+(v',J'') \leftarrow A^3\Pi_{0^+}(v''=0,J'') \leftarrow X^1\Sigma_{0^+}(v=0,J)$. Przejście pompujące $A^3\Pi_{0^+}(v''=0,J'') \leftarrow X^1\Sigma_{0^+}(v=0,J)$ charakteryzuje się dobrze rozdzieloną strukturą rotacyjną, co umożliwiło uzyskanie przejścia próbkującego $E^3\Sigma_1^+(v',J'') \leftarrow A^3\Pi_{0^+}(v''=0,J'')$ z pojedynczego poziomu rotacyjnego. Widma zarejestrowane z wykorzystaniem przejść $E^3\Sigma_1^+(v',J'') \leftarrow A^3\Pi_{0^+}(v''=0,J'')$ wraz z przyporządkowaniem odpowiednich liczb rotacyjnych przedstawione są na rys. 5.

Analiza odległości między poszczególnymi komponentami rotacyjnymi pozwoliła na wyznaczenie stałych rotacyjnych $B'_{v=0}$ oraz $B'_{v=1}$, a także międzyjądrowej odległości równowagowej $R_e{}'$ studni potencjału stanu $E^3\Sigma_1^+$. Różnica między położeniem linii pochodzących z tego samego stanu J'' dla gałęzi P i Q, oznaczona jako Δ, jest w przybliżeniu równa

$$\Delta = 4B'_v \cdot J'' + 2B'_v. \qquad (15)$$

Równanie (15) pokazuje, że odległość ta jest liniową funkcją rotacyjnej liczby kwantowej J'', a współczynnik kierunkowy prostej pozwala na wyznaczenie stałych rotacyjnych $B'_{v=0}$ oraz $B'_{v=1}$. Wartości tych stałych zostały zamieszczone w tabeli 2.

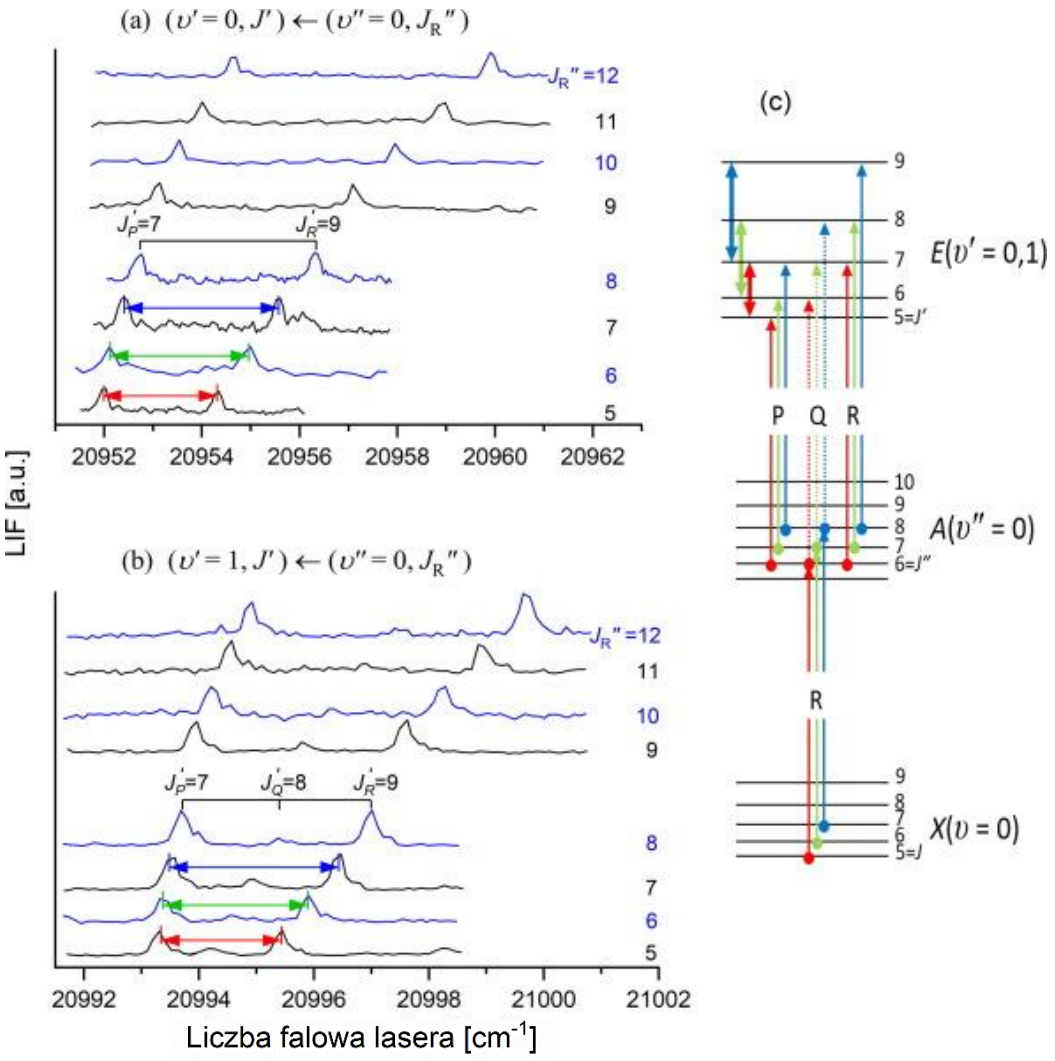

Rysunek 5. Widma eksperymentalne zarejestrowane z wykorzystaniem przejść $E^3\Sigma_1^+ \leftarrow A^3\Pi_{0^+}$ w CdNe dla przejść oscylacyjnych (a) $(\upsilon' = 0, J') \leftarrow \left(\upsilon'' = 0, J_R''\right)$ oraz (b) $(\upsilon' = 1, J') \leftarrow \left(\upsilon'' = 0, J_R''\right)$ [E]. (c) Struktura przejść rotacyjnych zrealizowanych w eksperymencie.

Wyznaczenie stałych $B'_{\upsilon=0}$ i $B'_{\upsilon=1}$ pozwoliło na obliczenie międzyjądrowej odległości równowagowej studni potencjału. Stałe rotacyjne mogą być wyrażone jako

$$B_\upsilon = B_e - \alpha_e\left(\upsilon + \frac{1}{2}\right), \tag{16}$$

gdzie B_e jest stałą rotacyjną w stanie równowagowym, a α_e jest poprawką anharmoniczną. Wobec tego

$$B_e = \frac{3B_{\upsilon=0} - B_{\upsilon=1}}{2}. \tag{17}$$

Międzyjądrową odległość równowagową można wyznaczyć korzystając z równania:

$$R_e = \sqrt{\frac{h}{8\pi^2 c\mu B_e}}, \qquad (18)$$

gdzie h - stała Plancka, c – prędkość światła, μ – masa zredukowana molekuły.

Tabela 2. Stałe rotacyjne oraz międzyjądrowa odległość równowagowa stanu $E^3\Sigma_1^+(6^3S_1)$ w kompleksie CdNe wyznaczone w [E].

$B'_{v=0}$ (cm^{-1})	$B'_{v=1}$ (cm^{-1})	B_e' (cm^{-1})	R_e' (Å)
0.106±0.001	0.095±0.001	0.112±0.002	2.98±0.06

2.3 Charakterystyka rydbergowskego stanu $E^3\Sigma_1^+(6^3S_1)$ molekuły CdAr

Stan $E^3\Sigma_1^+(6^3S_1)$ w CdAr wykazuje strukturę dwudołkową, co było wynikiem analizy w [23]. Do momentu publikacji [F] zbadano kształt głębokiej wewnętrznej $E^3\Sigma_{1\,in}^+$[24, A] lub płytkiej zewnętrznej $E^3\Sigma_{1\,out}^+$[24-25] studni tego potencjału, brakowało natomiast obrazu całościowego, łączącego oba obszary potencjału oddziaływania. Ponadto, choć podjęte zostały badania nad wyznaczeniem położenia i wysokości bariery potencjału [26], nie dawały one pełnej informacji o jej kształcie.

W pracy [F] po raz pierwszy został zaproponowany kompletny, dwudołkowy potencjał eksperymentalny stanu $E^3\Sigma_1^+(6^3S_1)$ w kompleksie CdAr uwzględniający również barierę potencjału między dwiema studniami. Jego kształt został zaprezentowany na rys. 6 ciągłą niebieską linią i porównany z potencjałami otrzymanymi w wyniku obliczeń *initio* [26] oraz we wcześniejszych eksperymentach [25].

Kształt studni $E^3\Sigma_{1\,out}^+$ został otrzymany przez analizę przejść bound ← bound zarejestrowanych metodą OODR $E^3\Sigma_{1\,out}^+ \leftarrow B^3\Sigma_1^+(v'') \leftarrow X^1\Sigma_{0^+}(v=0)$, gdzie v''=1-4. Przykładowe widmo zarejestrowane z wykorzystaniem przejścia $E^3\Sigma_{1\,out}^+ \leftarrow B^3\Sigma_1^+(v''=4)$ przedstawiono na rys. 7a. W porównaniu do poprzedniej analizy studni $E^3\Sigma_{1\,out}^+$ [25], zostały wyznaczone precyzyjniejsze stałe oscylacyjne ω_e' oraz $\omega_e' x_e'$ oraz międzyjądrowa odległość równowagowa R_e'. Wyznaczenie precyzyjniejszych wartości spektroskopowych studni $E^3\Sigma_{1\,out}^+$ stanowi bardzo istotny wkład do spektroskopowych badań stanu $E^3\Sigma_1^+$. Otóż, uzupełnienie poprzedniej analizy [25] o przejścia $E^3\Sigma_{1\,out}^+ \leftarrow B^3\Sigma_1^+(v'')$ z poziomów

oscylacyjnych $\upsilon'' = 2 - 4$ pozwoliło na poprawkę w przyporządkowaniu numeru poziomu oscylacyjnego do danej linii widmowej. Zielona strzałka na rys. 7a wskazuje linię oscylacyjną, która nie została zaobserwowana we wcześniejszym eksperymencie [25]. Wyniki nowo otrzymanych stałych zostały zawarte w tabeli 3.

Kształt bariery potencjału został odtworzony przez badanie widm free ← bound z wykorzystaniem przejść $\mathrm{E}^3\Sigma_1^+ \leftarrow \mathrm{B}^3\Sigma_1^+(\upsilon'')$, gdzie υ''= 0-4. Przykładowe widmo wykorzystujące jako pośredni poziom $\upsilon'' = 4$ przedstawiono na rys. 7b. Poszukiwania kształtu bariery rozpoczęto od potencjału otrzymanego w wyniku obliczeń *ab initio* [26] i przedstawionego w postaci zbioru punktów. Następnie zmodyfikowano położenie punktów tak, aby otrzymać maksymalną zgodność między widmami eksperymentalnymi a symulacjami wykonywanymi z wykorzystaniem programu BCONT [60]. Modyfikacja potencjału spowodowała powstanie punktów przegięcia po obu stronach bariery (rys. 6), z czego jeden z nich, po stronie studni $\mathrm{E}^3\Sigma_{1\,\mathrm{in}}^+$ został otrzymany w wyniku poprzedniej analizy [26] metodą odwróconego podejścia perturbacyjnego (ang. *Inverted Perturbativ Approach, IPA* [61]). W wyniku analizy przeprowadzonej w [F] oszacowano kształt bariery potencjału w postaci zbioru punktów oraz jej wysokość E_b (tabela 3).

Kształt wewnętrznej studni $\mathrm{E}^3\Sigma_{1\,\mathrm{in}}^+$ został otrzymany przez przesunięcie potencjału otrzymanego metodą IPA w [26] z widm bound ← bound z wykorzystaniem przejść $\mathrm{E}^3\Sigma_{1\,\mathrm{in}}^+ \leftarrow \mathrm{A}^3\Pi_{0^+}(5^3\mathrm{P}_1)$. Przesunięcie to było konieczne, aby możliwe było zszycie potencjału $\mathrm{E}^3\Sigma_{1\,\mathrm{in}}^+$ z potencjałem bariery. W [26] położenie maksimum bariery zostało oszacowane na ok. 5 Å, podczas gdy w wyniku nowej analizy [F] uzyskano wartość 7.235 Å (tabela 3), zatem różnica między poprzednią, a nową wartością wyniosła aż 1.235 Å.

Tabela 3. Stałe spektroskopowe stanu $\mathrm{E}^3\Sigma_{1\,\mathrm{out}}^+(6^3\mathrm{S}_1)$ w CdAr otrzymane w [F].

$\boldsymbol{\omega_e'}$ (cm^{-1})	$\boldsymbol{\omega_e' x_e'}$ (cm^{-1})	$\boldsymbol{R_e'}$(Å)	$\boldsymbol{E_b}$(cm^{-1})
4.36±0.05	0.207±0.005	7.235±0.121	27

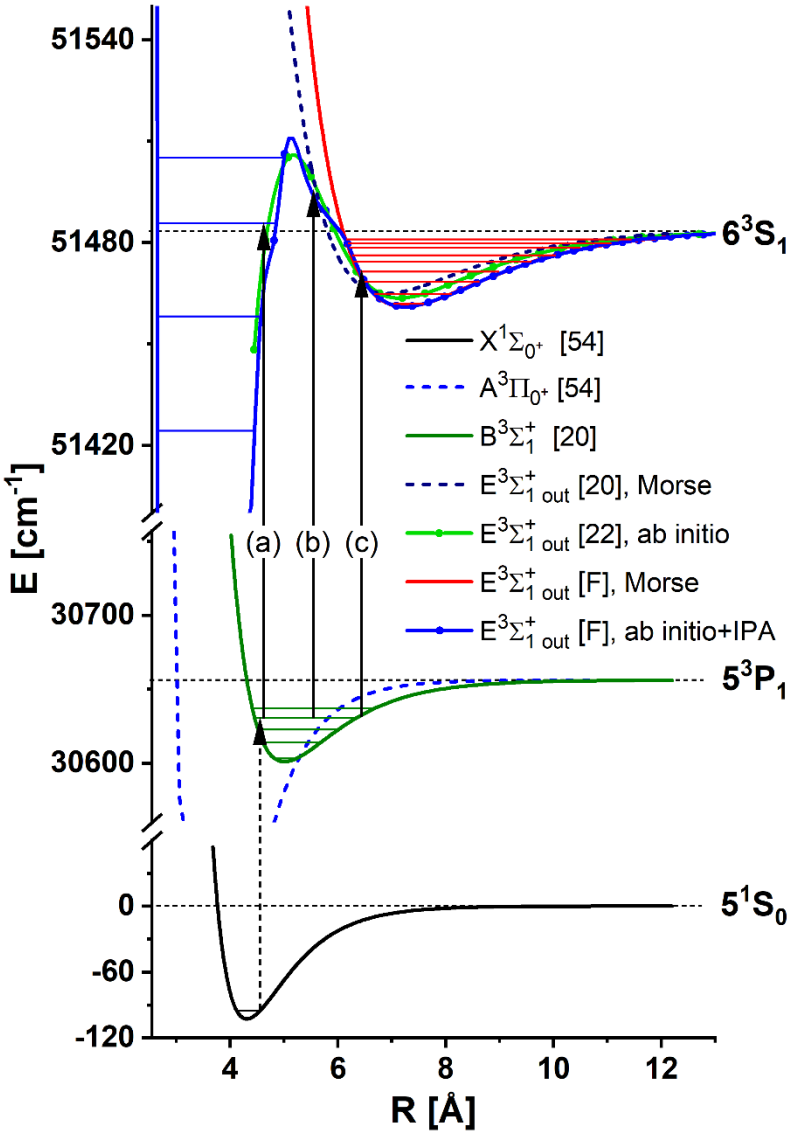

Rysunek 6. Potencjały międzyatomowe stanów elektronowych $X^1\Sigma_{0^+}$, $B^3\Sigma_1^+$ i $E^3\Sigma_1^+$ w CdAr biorących udział w procesie OODR przedstawionym w [F]. Przerywaną czarną strzałką zaznaczono schematycznie pierwszy proces wzbudzenia $B^3\Sigma_1^+(v'') \leftarrow X^1\Sigma_{0^+}(v = 0)$. Czarnymi ciągłymi strzałkami zaznaczono trzy możliwe drogi drugiego wzbudzenia $E^3\Sigma_1^+ \leftarrow B^3\Sigma_1^+(v'')$: (a) przejścia bound←bound do wewnętrznego dołka $E^3\Sigma_{1\,\mathrm{in}}^+$, (b) przejścia free←bound odzwierciedlające strukturę bariery oraz odpychającej części potencjału, oraz (c) przejścia bound←bound do płytkiego zewnętrznego dołka $E^3\Sigma_{1\,\mathrm{out}}^+$. Przerywaną niebieską linią zaznaczona jest pozycja stanu $A^3\Pi_{0^+}$.

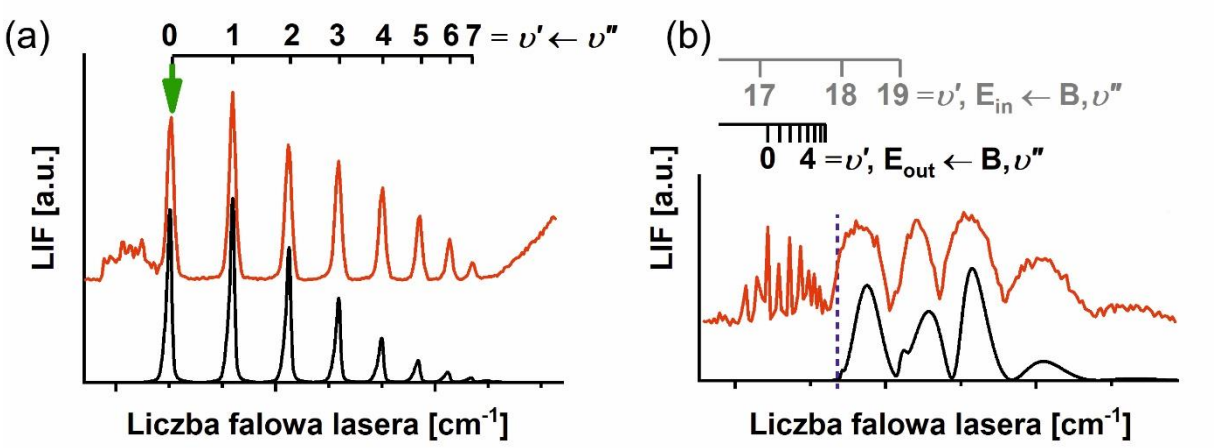

Rysunek 7. Przykładowe widma eksperymentalne (czerwona linia) oraz symulacje (czarna linia) (a) bound←bound oraz (b) free←bound przejścia $E^3\Sigma^+_{1\,out} \leftarrow B^3\Sigma^+_1(\upsilon'')$ otrzymane metodą OODR w CdAr. W tym przykładzie υ''=4. Powyżej, czarnymi liniami zaznaczone są położenia poziomów oscylacyjnych studni $E^3\Sigma^+_{1\,out}$, a szarymi – studni $E^3\Sigma^+_{1\,in}$. Zielona strzałka pokazuje położenie linii oscylacyjnej, która nie była obserwowana we wcześniejszym eksperymencie [25]. Wszystkie zarejestrowane widma bound←bound oraz free←bound używane do analizy kształtu potencjału $E^3\Sigma^+_1$ zostały zamieszczone w [F].

3. Dyspersyjna spektroskopia emisyjna

W tym rozdziale zostały zaprezentowane prace koncepcyjne nad spektroskopią emisyjną molekuł CdAr i ZnAr, które stanowią bardzo ważny wkład w dorobek doktorantki. Analiza widm emisji ze stanów rydbergowskich stwarza fascynującą możliwość eksploracji potencjałów, do których nie ma możliwości wzbudzenia ze stanu podstawowego. Obliczenia ab initio PEC stanów rydbergowskich w CdAr [13] i ZnAr [19] oraz TDM dla absorpcji ze stanów pośrednich umożliwiło wykonanie symulacji emisji ze stanów rydbergowskich. Symulacje te, opublikowane w [C], doktorantka wykonała w całości samodzielnie. Jest ona również autorką tekstu dotyczącego układu eksperymentalnego, wyników i wniosków oraz wszystkich rysunków w [C].

Projektowanie eksperymentu umożliwiającego rejestrację emisji ze stanów rydbergowskich w CdAr i ZnAr stanowiło inspirację dla stworzenia modelu szacowania liczby fotonów wpadających do detektora w wyniku emisji. Model ten, opublikowany w [D], został opracowany samodzielnie przez doktorantkę. Na podstawie zaproponowanego modelu wykonała ona również wszystkie obliczenia zawarte w [D]. Jest ona autorką wszystkich grafik oraz części tekstu dotyczącej liczby wzbudzonych molekuł i emitowanych fotonów.

3.1 Symulacja widm emisji ze stanów rydbergowskich molekuł CdAr i ZnAr

Wzbudzenie molekuł do stanów rydbergowskich stwarza możliwość eksploracji stanów niższych poprzez badanie widm emisji. W ten sposób możliwe jest badanie potencjałów niedostępnych we wzbudzeniu ze stanu podstawowego ze względu na małe wartości czynników Francka – Condona i/lub TDM. Szczególnie atrakcyjna wydaje się być perspektywa rejestracji widm emisji bound→free umożliwiającej badanie mało poznanych, krótkozasięgowych, odpychających części potencjału. Kształt tego fragmentu potencjału determinuje przebieg wielu ważnych procesów fizycznych, przede wszystkim procesu rozpraszania [62].

Ze względu na niskie koncentracje kompleksów wysoko wzbudzonych możliwe do uzyskania przez zastosowanie sekwencyjnego OODR w wiązce naddźwiękowej, eksperyment musi zostać dobrze zaprojektowany. Pomocne tutaj okazują się być obliczenia *ab initio* stanów

rydbergowskich oraz TDM z tych stanów, które umożliwiają symulację intensywności widm wzbudzenia i emisji oraz oszacowanie, czy obserwacja danego przejścia jest możliwa.

Korzystając z obliczeń *ab initio* stanów rydbergowskich w CdAr [13] oraz ZnAr [19] wykonano symulacje emisji ze stanów rydbergowskich w tych molekułach. Wyniki symulacji zostały przedstawione w [C].

Pierwszym krokiem była selekcja odpowiedniego stanu rydbergowskiego, z którego będzie rejestrowana emisja. W przypadku CdAr wybrano wielokrotnie badany stan $E^3\Sigma_1^+(6^3S_1)$ [A,E-F,19-26]. Dla ZnAr zdecydowano się na symulację emisji ze stanu $^1 1(4^1D_2)$ ze względu na intensywne przejście ze stanu $C^1 1(4^1P_1)$. Symulacja wzbudzenia $^1 1(4^1D_2) \leftarrow C^1 1(4^1P_1)$ z wykorzystaniem potencjału eksperymentalnego $C^1 1$ oraz wyniku obliczeń *ab initio* dla potencjału stanu $^1 1(4^1D_2)$ pokazała, że najintensywniejsze przejście zachodzi do stanu oscylacyjnego $\upsilon' = 13$. Dlatego do obserwacji widm emisji w ZnAr wybrano poziom oscylacyjny $\upsilon' = 13$ w stanie elektronowym $^1 1(4^1D_2)$.

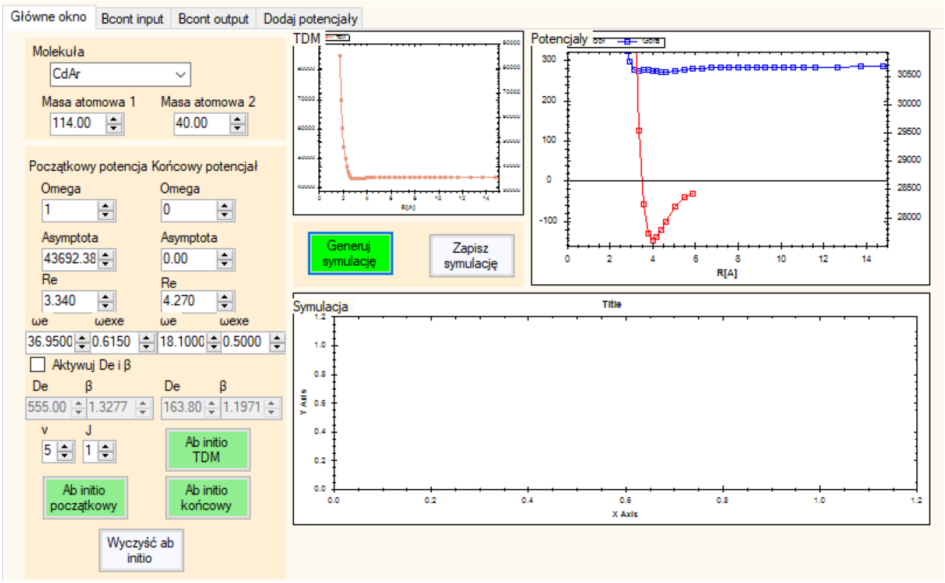

Rysunek 8. Główne okno programu *BCONTAdder* napisanego w języku C#. Program umożliwia korzystanie z programu BCONT [60] z interfejsem graficznym oraz sumowanie nakładających się na siebie widm.

Symulacje widm emisji bound→bound wykonano przy użyciu programów LEVEL [46] oraz PGOPHER [47]. Natomiast do symulacji widm emisji bound→free został wykorzystany program BCONT [60]. W celu stworzenia możliwości użycia programu BCONT z interfejsem graficznym, automatycznego połączenia widm bound→bound oraz bound→free, a także sumowania nakładających się widm emisji pochodzących z różnych stanów, doktorantka napisała program *BCONTAdder* w języku C# (rys. 8).

Symulacja widm emisji ze stanu $^1 1(4^1\mathrm{D}_2)(\upsilon' = 13)$ w ZnAr została przedstawiona na rys. 9. Wynika z niego, że istnieje możliwość detekcji widm bound→free do kilku stanów:

- do $\mathrm{D}^1 0^+(4^1\mathrm{P}_1)$ w obszarze 12 100 – 15 100 cm^{-1},
- do $\mathrm{c}^3 1(4^3\mathrm{P}_2)$ pokrywające się z widmem do $\mathrm{d}^3 0^-(4^3\mathrm{P}_2)$ w obszarze 29 600 – 32 300 cm^{-1},
- do $\mathrm{B}^3 1(4^3\mathrm{P}_1)$ w obszarze 29 600 – 29 900 cm^{-1}; choć widmo bound→free do $\mathrm{B}^3 1$ pokrywa się z widmami do $\mathrm{a}^3 0^-(4^3\mathrm{P}_0)$ oraz do $\mathrm{A}^3 0^+(4^3\mathrm{P}_1)$, intensywność tego pierwszego jest dominująca.

Podobna analiza emisji ze stanu $\mathrm{E}^3\Sigma_1^+(6^3\mathrm{S}_1)(\upsilon' = 2)$ CdAr wykazała, że możliwa jest detekcja widm bound→free do stanów $\mathrm{b}^3 2(5^3\mathrm{P}_2)$, $\mathrm{a}^3 0^-(5^3\mathrm{P}_0)$ oraz $\mathrm{A}^3 0^+(5^3\mathrm{P}_1)$. Szczegóły tej analizy zawarte są w [C].

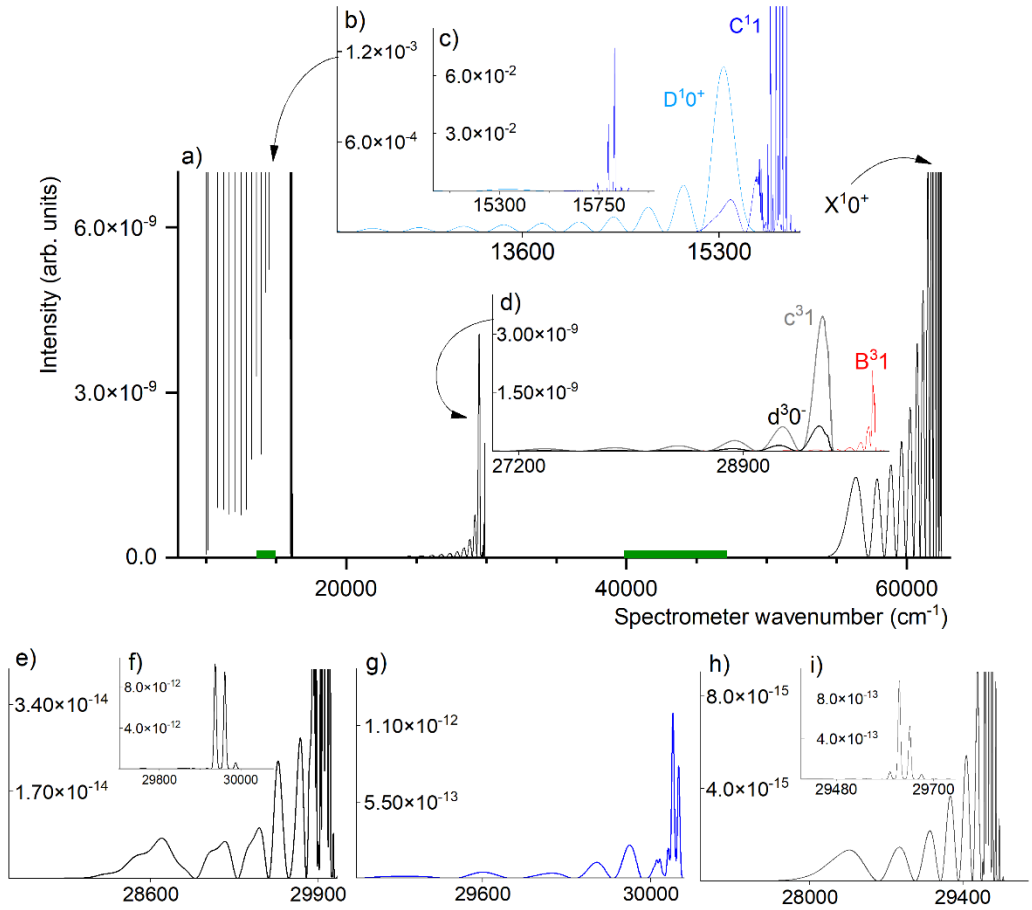

Rysunek 9. Symulacje wielokanałowej emisji bound→bound i bound→free ze stanu $^1 1(4^1\mathrm{D}_2), \upsilon' = 13$ w ZnAr [C]. Przejścia bound→bound zawierają zarówno strukturę oscylacyjną, jak i rotacyjną. Dwie zielone poziome linie przedstawiają obszar emisji ze stanu $\mathrm{C}^1 1, \upsilon' = 10$ używanego jako stan pośredni we wzbudzeniu OODR.

3.2 Model szacowania liczby fotonów emitowanych ze stanów rydbergowskich molekuł CdAr i ZnAr

Ważną informacją pozwalającą na ocenienie, czy dane przejście jest możliwe do rejestracji, jest liczba fotonów docierających do detektora podczas eksperymentu. Aby oszacować tę liczbę w emisji ze stanów $^1 1(4^1\mathrm{D}_2)$ w ZnAr i $\mathrm{E}^3\Sigma_1^+\left(6^3\mathrm{S}_1\right)$ w CdAr opisanych w podrozdziale 3.1, został zaproponowany model obliczeniowy uwzględniający: liczbę molekuł w stanie podstawowym powstałych w module źródła, rozprężanie gazu w wiązce molekularnej, przekrój czynny na absorpcję fotonu z wiązki lasera, oraz czas życia molekuł w stanie wzbudzonym. Szczegóły modelu zostały opisane w [D].

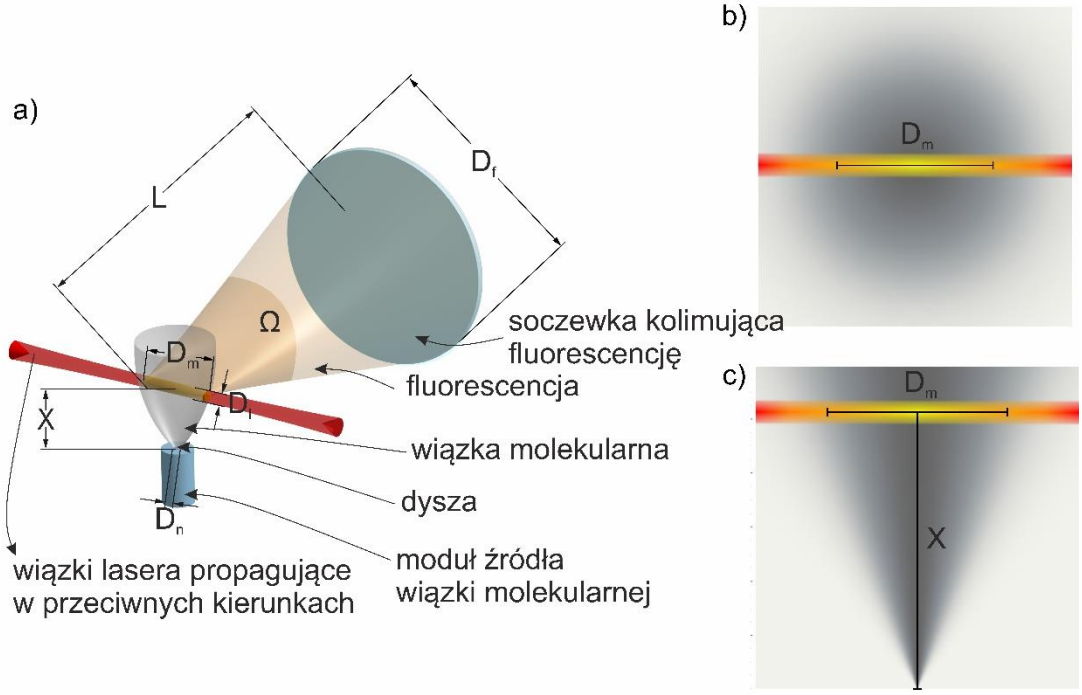

Rysunek 10. (a) Geometria eksperymentu rejestracji widma emisji ze stanów rydbergowskich molekuł ZnAr i CdAr chłodzonych w wiązce molekularnej [D]. (b) Rozkład gęstości molekuł w przekroju wiązki molekularnej prostopadłym do kierunku propagacji, zakładając rozkład gaussowski o odchyleniu standardowym $\sigma = \frac{D_m}{2}$. (c) Rozkład gęstości molekuł w wiązce molekularnej w płaszczyźnie symetrii wiązki wzdłuż kierunku propagacji. Założono liniowy wzrost odchylenia standardowego σ wzdłuż kierunku propagacji.

Rys. 10a przedstawia geometrię zastosowanego modelu. Cynk lub kadm w postaci stałej wewnątrz piecyka w module źródła są ogrzewane do temperatury T_0. W takiej temperaturze wytwarzają się pary metalu o ciśnieniu parcjalnym p_{Me}. Do modułu źródła dostarczany jest gaz nośny (argon) o ciśnieniu p_{Ar}, który po zmieszaniu z parami metalu przechodzi przez dyszę o

średnicy D_n i rozpręża się tworząc wiązkę molekularną. W odległości X od dyszy wiązka molekularna rozprężona do średnicy D_m jest oświetlona przez dwie wiązki lasera o średnicy D_l propagujące w przeciwnych kierunkach. W odległości L od wiązek laserowych znajduje się soczewka o średnicy D_f, kolimująca światło emisji zebrane z kąta bryłowego Ω. Za nią umieszczony jest układ optyczny skupiający sygnał do detektora (na rys. 10 nie pokazano).

Aby wyznaczyć początkową liczbę utworzonych molekuł MeRg, skorzystano z modelu Vigasina [63], zgodnie z którym stała reakcji

$$\mathrm{Me+Ar \rightleftharpoons MeAr}$$

zależy od temperatury i stałych spektroskopowych stanu podstawowego molekuły MeAr zgodnie z empirycznym równaniem:

$$K_p = \frac{18.86}{\omega_e B_\upsilon \chi T_0^{0.5} (\mu_{MeAr})^{1.5}} \left[e^{\frac{D_e}{T_0}} - \left(1 + \frac{D_e}{T_0}\right)\right], \qquad (19)$$

gdzie ω_e – stała oscylacyjna stanu podstawowego, B_υ – stała rotacyjna stanu podstawowego dla danego υ, χ – liczba określająca symetrię (dla molekuły heteroatomowej równa 1), T_0 – temperatura gazu w dyszy, μ_{MeAr} – masa zredukowana MeAr, D_e – głębokość studni stanu podstawowego w jednostkach [K].

Zakładając model stanu gazu doskonałego, można wyznaczyć początkową gęstość molekuł n_0.

Po rozprężeniu gęstość molekuł w wiązce wzdłuż osi propagacji maleje zgodnie z równaniem [64]:

$$n(X) = \frac{n_0}{\left[1 + \frac{1}{2}(\gamma - 1) M(X)^2\right]^{\frac{1}{\gamma - 1}}} \qquad (20)$$

Założono gaussowski rozkład gęstości molekuł w wiązce, oraz gaussowski rozkład energii w wiązce lasera. Przy oddziaływaniu wiązki molekularnej ze światłem z lasera populacja molekuł wzbudzonych $N_2^*(t)$ rośnie zgodnie z równaniem

$$N_2^*(t) = W_{12}^{abs} - W_{21}^{spont\ em} - W_{21}^{stim\ em} \qquad (21)$$

gdzie W_{12}^{abs} – współczynnik absorpcji, $W_{21}^{spont\ em}$ – współczynnik emisji spontanicznej, $W_{21}^{stim\ em}$ – współczynnik emisji wymuszonej. Wielkości występujące w (20) można wyrazić następująco:

$$W_{12}^{ab} = B_{12}\rho_{\omega}N_1^*,$$
$$W_{21}^{spont\ em} = A_{21}N_2^*, \qquad (22)$$
$$W_{21}^{stim\ em} = B_{21}\rho_{\omega}N_2^*.$$

B_{12}, A_{21}, B_{21} są policzonymi przez LEVEL [46] współczynnikami Einsteina na absorpcję, emisję spontaniczną i emisję wymuszoną, ρ_{ω} jest gęstością energii lasera na jednostkę częstości kołowej, $N_1(N_2)$ to liczba molekuł w stanie podstawowym (wzbudzonym).

Rozwiązanie równania (21) pozwala na wyznaczenie liczby wzbudzonych molekuł po zakończeniu pojedynczego impulsu lasera. W podobny sposób została wyznaczona liczba molekuł po drugim wzbudzeniu w schemacie OODR.

Założono, że jeden wzbudzony kompleks emituje jeden foton oraz że fotony emitowane są równomiernie w cały kąt bryłowy, $N_{phot\ tot} = N_2^*(t = 10\ \text{ns})$. Ponieważ soczewka kolimująca ma skończone rozmiary, liczba fotonów osiągająca detektor N_{phot} (bez uwzględniania strat na układzie optycznym) jest w przybliżeniu równa:

$$N_{phot} = \frac{\pi\left(\frac{D_f}{2}\right)^2}{4\pi L^2} N_{phot\ tot}. \qquad (23)$$

Obliczono, że liczba molekuł wzbudzonych do stanu rydbergowskiego wynosi: dla CdAr: $1.27 \cdot 10^8$ oraz dla ZnAr: $5.31 \cdot 10^7$. Odpowiada to liczbie fotonów docierających do soczewki: $2.08 \cdot 10^6$ dla CdAr i $3.8 \cdot 10^5$. Są to liczby pozwalające na obserwację widm emisji opisanych w podrozdziale 3.1. Wartości parametrów użytych do obliczeń zawarte są w [D].

3.3 Zarys kontynuacji badań nad spektroskopią emisji molekuł CdRg i ZnRg

We wcześniejszych eksperymentach widma emisji molekuł MeRg i Me_2 były rejestrowane przy użyciu fotopowielacza z monochromatorem [65-67]. Ponieważ jest to metoda niezwykle czasochłonna, jako detektora zaczęto używać spektrometru z kamerą CCD [68]. W ten sposób zostało wykazane, że ten typ detekcji może stanowić alternatywną do monochromatora z fotopowielaczem formę detekcji umożliwiającą rejestrację widm emisji molekuł chłodzonych w wiązce naddźwiękowej (zatem o niskich koncentracjach) i wzbudzanych laserowo.

Kolejny projekt realizowany w laboratorium zakłada budowę układu doświadczalnego, którego schemat został przedstawiony na rys. 2b, umożliwiającego rejestrację widm emisji ze stanów rydbergowskich, opisanych w podrozdziale 3.1. W tym celu został przetestowany spektrometr Mechelle 5000 z kamerą iStar DH334T. Aby zoptymalizować parametry pracy detektora, wykonano układ optyczny do rejestracji przejścia $B^3\Pi_{0u}^+(v' = 28) \rightarrow X^1\Sigma_g^+(v'')$ w molekule jodu I_2. Wstępne wyniki przedstawiono na rys. 11. Jednak, ze względu na dużą trudność napotkaną przy sprzęgnięciu sygnału emisji do światłowodu zrezygnowano z zastosowania spektrometru typu Echelle.

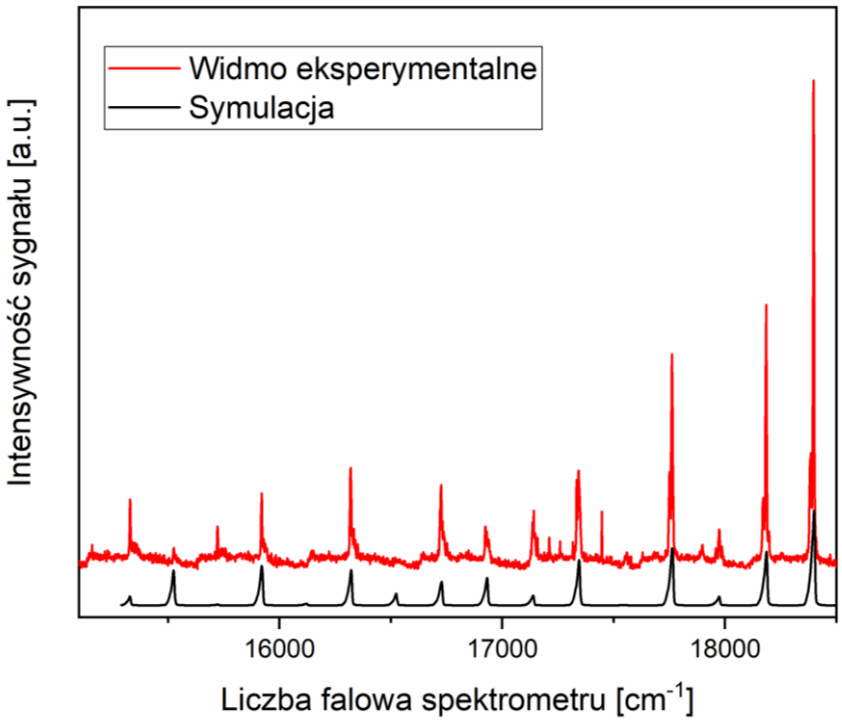

Rysunek 11. Widmo eksperymentalne (czerwona linia) i symulacja (czarna linia) emisji otrzymane z wykorzystaniem przejścia $B^3\Pi_{0u}^+(v' = 28) \rightarrow X^1\Sigma_g^+(v'')$ w molekule I_2 zarejestrowane z użyciem spektrometru Mechelle 5000 z kamerą iStar DH334T.

Przewiduje się, że rejestracja widma emisji ze stanu rydbergowskiego $E^3\Sigma_1^+(6^3S_1), v' = 2$ w CdAr jest znacznie bliższa realizacji, niż emisja z ZnAr, ponieważ widmo wzbudzenia tego stanu było już wielokrotnie otrzymywane w Laboratorium Spektroskopii Laserowej i Informacji Kwantowej Instytutu Fizyki UJ. Kolejnym zadaniem badawczym będzie zatem dostosowanie układu detekcji do rejestracji widma emisji.

Znacznie większe wyzwanie stanowi rejestracja widma emisji ze stanu rydbergowskiego $^1(4^1D_2)(v' = 13)$ w ZnAr. Jak dotąd, dla molekuł zawierających Zn nie zarejestrowano widm wzbudzenia otrzymanych z zastosowaniem metody OODR. Aby tego

dokonać, konieczna jest optymalizacja pracy modułu źródła wiązki molekularnej opisanego w rozdziale 4.

4. Nowy układ doświadczalny

Rozdział 4. traktuje o budowie nowego układu doświadczalnego wykorzystującego moduł źródła wiązki naddźwiękowej, zaprojektowanego we współpracy z firmą MeasLine i służący do spektroskopii molekuł Zn_2 i ZnAr. Doktorantka wykonała samodzielnie lub w dużej mierze samodzielnie wiele testów zmierzających do: optymalizacji temperatury pracy modułu źródła oraz ciśnienia gazu nośnego, znalezienia i wyeliminowania nieszczelności w module źródła i komorze próżniowej, dostosowania laserów barwnikowych do przejść w Zn_2, znalezienia położenia i szerokości wiązki lasera względem wiązki molekularnej umożliwiającego obserwację widm wzbudzenia, a także dostosowania pracy fotopowielacza do rejestracji LIF w Zn_2. Szczegóły dotyczące budowy modułu źródła, układu eksperymentalnego oraz rejestracji przejścia $b^3 0_u^+(4^3P_1), v' \leftarrow X^1 0_g^+(4^1S_0), v''$ w Zn_2 zostały opublikowane w [B]. Oprócz budowy układu doświadczalnego, doktorantka zrealizowała pomiary wzbudzenia $b^3 0_u^+, v' \leftarrow X^1 0_g^+, v''$ w Zn_2 i wykonała analizę danych umożliwiającą wyznaczenie nowych stałych spektroskopowych stanu $b^3 0_u^+$. Jest ona również autorką tekstu i rysunków w artykule.

4.1 Widma wzbudzenia molekuł Zn2 i ZnRg

Pośród innych pierwiastków 12. grupy UOP, Zn wyróżnia się ze względu na jego biologiczne i technologiczne znaczenie. Ciekawe na przykład jest zjawisko powstawania mostków cynkowych między ligandami organicznymi [69]. Znajomość potencjału oddziaływania między atomami Zn pozwala również na symulacje ważnych procesów technologicznych z użyciem cynku [70].

Jednocześnie, spośród wszystkich pierwiastków 12. grupy UOP, dimery vdW zawierające Zn są najmniej poznane. Przyczyną tego stanu rzeczy są poważne wyzwania technologiczne związane z wytwarzaniem wystarczająco wysokiego ciśnienia parcjalnego p_{Zn} par Zn, który charakteryzuje się stosunkowo wysoką temperaturą topnienia (419.53°C). Pary Zn są również wysoce reaktywne, powodując korozję stalowych elementów konstrukcyjnych.

We wcześniejszych badaniach nad dimerami Zn_2 i ZnRg stosowano ablację laserową [20], jednak ta metoda otrzymywania par metalu powoduje powstawanie dodatkowo w wiązce atomów oraz jonów w stanie wzbudzonym, co znacząco komplikuje, a czasem uniemożliwia interpretację danych spektroskopowych. Stosowano również metodę ogrzewania

rezystancyjnego w module źródła zawierającym elementy wykonane z molibdenu, który jest odporny na korozyjne działanie par cynku [65-66,71-72]. Jednak molibden jest materiałem bardzo trudnym w obróbce i spawaniu.

We współpracy z firmą MeasLine, w [B] zaproponowano konstrukcję modułu źródła wiązki naddźwiękowej dedykowanego dla pierwiastków korozyjnych o wysokiej temperaturze topnienia, szczególnie dla Zn. Schemat tego urządzenia pokazano na rys. 12. W zaprezentowanym module źródła, elementy mające styczność z parami cynku, tzn. tygiel i moduł dyszy wykonane są z grafitu. Materiał został wybrany w oparciu o kilka istotnych właściwości: wysoką temperaturę sublimacji (między 3620°C a 3745°C w warunkach normalnych [73]), wysoką odporność chemiczną w kontakcie z wieloma metalami w stanie ciekłym, m.in. Zn, Sn, Pb [74] oraz dobre właściwości mechaniczne. Talerz modułu dyszy, dociskany przez śruby, pełni również dodatkową funkcję uszczelniania stalowych elementów obudowy.

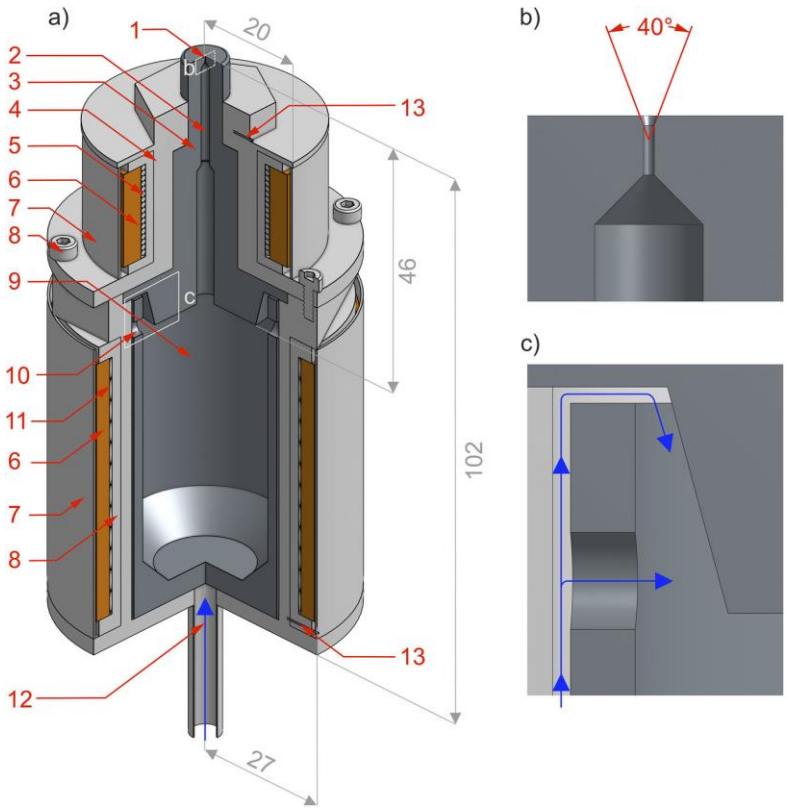

Rysunek 12. (a) Moduł źródła wiązki naddźwiękowej o pracy ciągłej dedykowanej dla pierwiastków korozyjnych [B]: (1) dysza, (2) przewód kapilarny w module dyszy, (3) grafitowy moduł dyszy, (4) stalowa obudowa, (5) górna grzałka, (6) warstwa ceramiczna, (7) osłona termiczna, (8) śruba dociskająca, (9) grafitowy tygiel, (10) otwór w tyglu - wlot gazu nośnego, (11) dolna grzałka, (12) wlot gazu nośnego, (13) termopara. (b) Przekrój przez profil dyszy. (c) Przekrój przez tygiel pokazujący szczegóły wlotu gazu nośnego (ścieżki przepływu gazu pokazane są niebieskimi strzałkami). Wszystkie wymiary podane są w milimetrach.

Tygiel wypełniany jest granulkami metalu, który podczas pracy urządzenia ogrzewany jest przez druty oporowe do temperatury mogącej osiągać 1300 K. Podczas eksperymentu, moduł dyszy jest podgrzewany do temperatury ok. 10 – 30 K wyższej, niż tygiel, aby zapobiec osadzaniu par metalu powodującemu zatykanie dyszy.

Gaz nośny jest wprowadzony stalową rurką zlokalizowaną u dołu modułu źródła. Gaz, którego maksymalne ciśnienie może wynosić 6 bar, wędruje w obszarze między stalową obudową a grafitowym tyglem, a następnie przez otwór w tyglu i od góry przemieszcza się do przewodu w module dyszy (rys. 12c). Mieszanina par metalu i gazu nośnego przechodzi przez dyszę o średnicy 0.2 mm i rozpręża się w komorze próżniowej tworząc wiązkę naddźwiękową.

Szczegóły budowy i funkcjonalności opisanego układu znajdują się w [B].

4.2 Test układu doświadczalnego

Przy użyciu nowego modułu źródła zarejestrowano widmo wzbudzenia z wykorzystaniem przejścia $\mathrm{b}^3\mathrm{0_u^+}(4^3\mathrm{P_1}), v' \leftarrow \mathrm{X}^1\mathrm{0_g^+}(4^1\mathrm{S_0}), v''$ w Zn_2. Do testu nowego układu doświadczalnego wybrano przejście, które było wykorzystane we wcześniejszych badaniach, w których rozdzielono strukturę oscylacyjną przy nierozdzieleniu struktury rotacyjnej [72].

Rys. 13a przedstawia widma eksperymentalne zarejestrowane przy użyciu nowego modułu źródła. W porównaniu z wcześniejszymi badaniami, wzbudzenia dokonano za pomocą lasera węższego spektralnie (0.1 cm^{-1} w porównaniu z 0.5 cm^{-1} w [72]), co pozwoliło na wyznaczenie stałych spektroskopowych z mniejszą niepewnością. Stałe oscylacyjne ω_e' i $\omega_e' x_e'$ wzbudzonego stanu $\mathrm{b}^3\mathrm{0_u^+}$ zostały otrzymane przy użyciu metody Birge – Sponer [75], a ich wartości znajdują się w tabeli 4.

Używając nowych stałych spektroskopowych stanu $\mathrm{b}^3\mathrm{0_u^+}$, przy użyciu programów LEVEL [46] i PGOPHER [47] wykonano symulacje przejść $\mathrm{b}^3\mathrm{0_u^+}, v' \leftarrow \mathrm{X}^1\mathrm{0_g^+}, v''$, pokazane na rys. 13b. Do opisu stanu $\mathrm{b}^3\mathrm{0_u^+}$ użyto funkcji Morse'a

$$E(R) = D_e\left\{1 - e^{-\beta(R-R_e)}\right\}^2 - D_e + E_{asympt,} \qquad (24)$$

gdzie $D_e = \frac{\omega_e^2}{4\omega_e x_e}$, $\beta = \sqrt{\frac{8\pi^2 c\mu\omega_e x_e}{h}}$, c – prędkość światła, h - stała Plancka, μ – masa zredukowana molekuły, R_e – międzyjądrowa odległość równowagowa.

Obecność przejść z wyższych poziomów oscylacyjnych stanu podstawowego, tzw. „gorących pasm” (zaznaczonych kolorem zielonym i czerwonym na rys. 13c) wskazuje na wysoką temperaturę oscylacyjną w wiązce. Przy założeniu boltzmanowskiego rozkładu obsadzenia poziomów oscylacyjnych, analiza natężeń „gorących pasm” pozwoliła na wyznaczenie temperatury oscylacyjnej molekuł w wiązce, która wynosiła $T_{osc} \approx 150$ K.

Użycie węższego spektralnie lasera pozwoliło również na częściowe rozdzielenie struktury izotopowej i rotacyjnej (rys. 13d,e), co umożliwiło oszacowanie temperatury rotacyjnej molekuł w wiązce. Z użyciem programu PGOPHER wykonano symulacje dla różnych wartości temperatur rotacyjnych, szukając najlepszej zgodności między symulacją a eksperymentem. Najlepszą zgodność stwierdzono dla $T_{rot} = 10$ K.

Szczegóły eksperymentu i analizy danych znajdują się w [B].

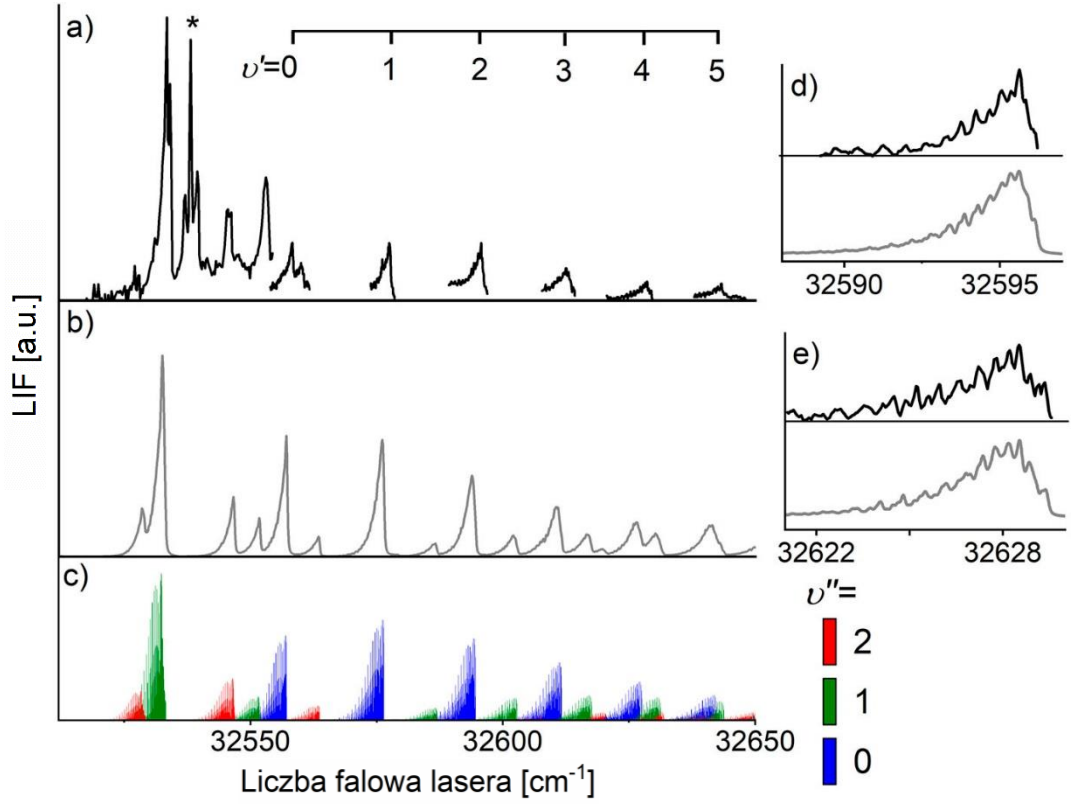

Rysunek 13. (a) Widma wzbudzenia zarejestrowane z wykorzystaniem przejścia $b^3 0_u^+(4^3P_1), \upsilon' \leftarrow X^1 0_g^+(4^1S_0), \upsilon''$ w Zn_2. Eksperyment wykonano przy użyciu nowego modułu źródła [B]. (b) Symulacja widma wykonana dla temperatur $T_{osc} = 150$ K i $T_{rot} = 10$ K. (c) Poszczególne przyczynki pochodzące od różnych izotopologów Zn_2 dla każdej składowej widma $\upsilon' \leftarrow \upsilon''$ składające się na profile przedstawione w (b). Po prawej stronie pokazano pasma z zarejestrowaną, częściowo rozdzieloną strukturą izotopowo – rotacyjną (d) $\upsilon' = 2 \leftarrow \upsilon'' = 0$ oraz (e) $\upsilon' = 4 \leftarrow \upsilon'' = 0$.

Tabela 4. Stałe spektroskopowe ω_e' i $\omega_e'x_e'$ stanu $b^3 0_u^+$otrzymane w [B] oraz wyznaczone temperatury: oscylacyjna T_{osc} i rotacyjna T_{rot}.

$\boldsymbol{\omega_e'}$ (cm^{-1})	$\boldsymbol{\omega_e'x_e'}$ (cm^{-1})	$\boldsymbol{T_{osc}}$ (K)	$\boldsymbol{T_{rot}}$ (K)
20.3±0.1	0.557±0.020	150	10

Podsumowanie

W rozprawie doktorskiej zaprezentowano wieloaspektowe podejście do problematyki niskich stanów rydbergowskich molekuł Me_2 i MeRg. Po pierwsze, została wzbogacona wiedza o kształtach krzywych potencjału oraz stałych spektroskopowych stanów rydbergowskich. Wyznaczono stałe oscylacyjne studni $E^3\Sigma_{1\,\mathrm{in}}^+$ w CdAr i CdKr [A], stałe oscylacyjne i międzyjądrową odległość równowagową studni $E^3\Sigma_{1\,\mathrm{out}}^+$ w CdAr [F] oraz stałe rotacyjne stanu $E^3\Sigma_1^+$w CdNe [E]. Nade wszystko, wyznaczono eksperymentalnie kompletny, dwudołkowy kształt potencjału $E^3\Sigma_1^+$ w CdAr uwzględniający również barierę [F], co stanowi najważniejszy wynik zaprezentowany w niniejszej rozprawie.

Ponadto, została wzbogacona metodologia badań eksperymentalnych nad niskimi stanami rydbergowskimi. Została pokazana możliwość selekcji izotopologów [A] oraz poziomów rotacyjnych [E] we wzbudzeniu OODR. Pokazano również, że detekcja widm free←bound może być pomocna w wyznaczeniu kształtu bariery potencjału [F]. Najważniejszym osiągnięciem doktorantki w tym zakresie jest zestawienie i przetestowanie nowego układu eksperymentalnego zawierającego moduł źródła wiązki naddźwiękowej zawierającej molekuły Zn_2 i ZnRg [B], co otwiera drogę do eksploracji ich stanów rydbergowskich.

Po trzecie, sprawdzono możliwość eksploracji niższych stanów molekularnych przez symulację widm wielokanałowej emisji z niskich stanów rydbergowskich w CdAr i ZnAr [C]. Możliwość realizacji eksperymentalnej została sprawdzona przez: uwzględnienie czynników Francka – Condona i TDM we wszystkich symulowanych przejściach [C] oraz oszacowanie liczby fotonów powstałych przez emisję, które mogą być zarejestrowane przez detektor [D]. Warto podkreślić, że symulacje te stanowią podwaliny dla eksperymentu rejestracji emisji z użyciem spektrometru z kamerą CCD, który jest intensywnie rozwijany w Laboratorium Spektroskopii Laserowej i Informacji Kwantowej Instytutu Fizyki UJ.

Bibliografia

[1] IUPAC. Compendium of Chemical Terminology, 2nd ed. (the "Gold Book"). Opracowane przez A. D. McNaught and A. Wilkinson. Blackwell Scientific Publications, Oxford (1997). https://doi.org/10.1351/goldbook

[2] C. J. van Oss, M. K. Chaudhury, R. J. Good, *Interfacial Lifshitz-van der Waals and polar interactions in macroscopic systems*, Chem. Rev. **88**, 927 (1988). https://doi.org/10.1021/cr00088a006

[3] B. R. Holstein, *The van der Waals interaction*, Am. J. Phys. **69**, 441 (2001). https://doi.org/10.1119/1.1341251

[4] F. London, *Zur theorie und systematik der molekularkräfte*, Z. Phys. **63**, 245 (1930). https://doi.org/10.1007/BF01421741

[5] H. B. G. Casimir, D. Polder, *The influence of retardation on the London – van der Waals force*, Phys. Rev. **73**, 360 (1948). https://doi.org/10.1103/PhysRev.73.360

[6] R. E. Leckenby, E. J. Robbins, *The observation of double molecules in gases*, Proc. R. Soc. London Ser. A **291**, 389 (1966). https://doi.org/10.1098/rspa.1966.0102

[7] B. L. Blaney, G. E. Ewing, *Van der Waals molecules*, Ann. Rev. Phys. Chem. **27**, 553 (1976). https://doi.org/10.1146/annurev.pc.27.100176.003005

[8] J. Koperski, *Van der Waals complexes in supersonic beams: Laser spectroscopy of neutral-neutral interactions*, Wiley-VCH, Weinheim (2003)

[9] J. A. Rackers, J. W. Ponder, *Classical Pauli repulsion: An anisotropic, atomic multipole model*, J. Chem. Phys. **150**, 084104 (2019). https://doi.org/10.1063/1.5081060

[10] J. E. Lennard – Jones, *Cohesion*, Proc. Phys. Soc. **43**, 461 (1931). https://doi.org/10.1088/0959-5309/43/5/301

[11] M. Strojecki, M. Ruszczak, M. Łukomski, J. Koperski, *Is Cd_2 truly a van der Waals molecule? Analysis of rotational profiles recorded at the $A0_u^+$, $B1_u \leftarrow X0_g^+$ transitions*, Chem. Phys. **340**, 171 (2007). https://doi.org/10.1016/j.chemphys.2007.08.016

[12] M. Yu, M. Dolg, *Covalent contributions to bonding in group 12 dimers M_2 (M=Zn, Cd, Hg)*, Chem. Phys. Lett. **273**, 329 (1997). https://doi.org/10.1016/S0009-2614(97)00609-X

[13] M. Krośnicki, A. Kędziorski, T. Urbańczyk, J. Koperski, *Rydberg states of the CdAr van der Waals complex*, Phys. Rev. A **99**, 052510 (2019). https://doi.org/10.1103/PhysRevA.99.052510

[14] J. Koperski, T. Urbańczyk, M. Krośnicki, M. Strojecki, *Free ← bound and bound ← bound profiles in excitation spectra of the $B^3\Pi \leftarrow X^1\Sigma^+$ transition in CdNg (Ng = noble gas) complexes*, Chem. Phys. **428**, 43 (2014). https://doi.org/10.1016/j.chemphys.2013.10.017

[15] E. Czuchaj, M. Krośnicki, H. Stoll, Q*uasirelativistic valence ab initio calculation of the potential-energy curves for Cd-rare gas atom pairs*, Theor. Chem. Acc. **105**, 219 (2001). https://doi.org/10.1007/s002140000206

[16] M. Łukomski, J. Koperski and M. Czajkowski, *Double-well potential energy curve of cadmium-krypton molecule in the B1(5^3P_1) state*, Spectrochim. Acta A: Mol. Biomol. Spectrosc. **58**, 1757 (2002). https://doi.org/10.1016/S1386-1425(01)00625-4

[17] V. Bendkowsky, B. Butscher, J. Nipper, J. P. Shaffer, R. Löw, T. Pfau, *Observation of ultralong-range Rydberg molecules*, Nature **458**, 1005 (2009). https://doi.org/10.1038/nature07945

[18] J. P. Shaffer, S. T. Rittenhouse, H. R. Sadeghpour, *Ultracold Rydberg molecules*, Nature Commun. **9**, 1965 (2018). https://doi.org/10.1038/s41467-018-04135-6

[19] A. Kędziorski, J. P. Zobel, M. Krośnicki, J. Koperski, *Rydberg states of ZnAr complex*, Mol. Phys. **120**, e2073282 (2022). https://doi.org/10.1080/00268976.2022.2073282

[20] R. R. Bennett, W. H. Breckenridge, *Spectroscopic characterization of the $\tilde{a}^3\Pi_{0^-}$, $\tilde{b}^3\Pi_2$, and $E^3\Sigma^+$ states of ZnAr*, J. Chem. Phys. **92**, 1588 (1990). https://doi.org/10.1063/1.458091

[21] J. Koperski, M. A. Czajkowski, *Spectroscopical characterization of CdNe van der Waals complex in the E1($^3\Sigma^+$) Rydberg state*, Chem. Phys. Lett. **357**, 119 (2002). https://doi.org/10.1016/S0009-2614(02)00464-5

[22] M. Czajkowski, R. Bobkowski, L. Krause, *Pomp-and-probe studies of the $\boldsymbol{E^1(6^3S_1)\leftarrow A0^+(5^3P_1)}$ excitation spectrum of CdAr in a supersonic beam*, Phys. Rev. A **45**, 6451 (1992). https://doi.org/10.1103/PhysRevA.45.6451

[23] J. Koperski, M. Czajkowski, *The structure of the lowest electronic Rydberg state of CdAr complex determined by laser double resonance method in a supersonic jet-expansion beam*,

Spectrochim. Acta A: Mol. Biomol. Spectrosc. **59**, 2435 (2003). https://doi.org/10.1016/S1386-1425(02)00396-7

[24] T. Urbańczyk, M. Strojecki, J. Koperski, *Structure of vibrational bands of the $E^3\Sigma^+(6^3S_1)$ ←$A^3\Pi_{0+}(5^3P_1)$, $B^3\Sigma_{1+}(5^3P_1)$ transitions in CdAr and CdKr studied by optical-optical double resonance method*, Chem. Phys. Lett., **503**, 18 (2011). https://doi.org/10.1016/j.cplett.2010.12.085

[25] T. Urbańczyk, J. Koperski, *The $E^3\Sigma^+(6^3S_1)$-state interatomic potential of CdAr in the long range region revisited: A new method for bond length adjustment*, Chem. Phys. Lett. **640**, 82 (2015). https://doi.org/10.1016/j.cplett.2015.10.013

[26] T. Urbańczyk, M. Krośnicki, A. Kędziorski, J. Koperski, *The $E^3\Sigma_1^+(6^3S_1)$← $A^3\Pi_{0+}(5^3P_1)$ transition in CdAr revisited: The spectrum and new analysis of the $E^3\Sigma_1^+$ Rydberg state interatomic potential*, Spectrochim. Acta A: Mol. Biomol. Spectrosc.**196**, 1386 (2018). https://doi.org/10.1016/j.saa.2018.01.075

[27] J. Koperski, M. Czajkowski, *Electronic structure of the CdKr lowest Rydberg state determined from laser-excitation spectra using supersonic beam and double optical resonance methods*, Phys. Rev. A **69**, 042509 (2004). https://doi.org/10.1103/PhysRevA.69.042509

[28] T. Urbańczyk, J. Koperski, *Spectroscopy of CdKr van der Waals complex using OODR process: New determination of the $E^3\Sigma_1^+(5s6s^3S_1)$ Rydberg state potential*, Chem. Phys. **525**, 110406 (2019). https://doi.org/10.1016/j.chemphys.2019.110406

[29] J. Koperski, M. Strojecki, M. Krośnicki, T. Urbańczyk, *Potentials of the $D^10_u^+$ (6^1S_0) and $F^31_u(6^3P_2)$ electronic Rydberg states of Cd_2 from ab initio calculations and laser-induced fluorescence excitation spectra*, J. Phys. Chem. A **115**, 6851 (2011). https://doi.org/10.1021/jp1112922

[30] T. Urbańczyk, M. Krośnicki, J. Koperski, *Observation of gerade Rydberg state of Cd_2 van der Waals complex cooled in free-jet expansion beam and excited using optical-optical double resonance method*, Spectrochim. Acta A: Mol. Biomol. Spectrosc. **253**, 119500 (2021). https://doi.org/10.1016/j.saa.2021.119500

[31] E. Czuchaj, M. Krośnicki, H. Stoll, *Quasirelativistic valence ab initio calculation of the potential energy curves for the Hg-rare gas atom complexes*, Chem. Phys. **263**, 7 (2001). https://doi.org/10.1016/S0301-0104(00)00344-X

[32] M. Okunishi, K. Yamanouchi, K. Onda, S. Tsuchiya, *Interatomic potential of the HgNe van der Waals complex in the E($^3\Sigma^+$) Rydberg state*, J. Chem. Phys. **98**, 2675 (1993). https://doi.org/10.1063/1.464149

[33] K. Onda, K. Yamanouchi, *Interatomic potentials of triplet s-Rydberg series of HgNe and HgAr van der Waals dimers*, J. Chem. Phys. **101**, 7290 (1994). https://doi.org/10.1063/1.468286

[34] K. Onda, K. Yamanouchi, *Interatomic potentials of singlet s-Rydberg series of a HgNe van der Waals dimer: Evidence for stabilization by superexchange interaction*, J. Chem. Phys. **102**, 1129 (1995). https://doi.org/10.1063/1.469171

[35] M.-C. Duval, O. B. D'Azy, W. H. Breckenridge, J. Jouvet, B. Soep, *The structure of several electronic states of the Hg–Ar complex as determined by laser double resonance in a supersonic jet*, J. Chem. Phys. **85**, 6324 (1986). https://doi.org/10.1063/1.451462

[36] H. Pauly, *Atom, Molecule and cluster beams I. Basic theory, production and detection of thermal energy beams*, Springer Series on Atomic, Optical and Plasma Physics **28**, G. F. Drake, G. Ecker, W. E. Baylis, R. N. Compton, M. R. Flannery, B. R. Judd, K. P. Kirby, P. Lambropoulos, G. Leuchs, P. Meystre, H. Walther (Eds.), Heidelberg, 2001. https://doi.org/10.1007/978-3-662-04213-7

[37] R. R. Bennett, J. G. McCaffrey, I. Wallace, D. J. Funk, A. Kowalski, W. H. Breckenridge, *A laser spectroscopic study of the $X^1\Sigma_0^+$-$C^1\Pi_1$ transition of MgAr: Evidence for Λ-type doubling*, J. Chem. Phys. **90**, 2139 (1989). https://doi.org/10.1063/1.456008

[38] T. Urbańczyk, J. Koperski, *High-temperature high-pressure all-metal pulsed source of van der Waals dimers: Towards the Einstein-Podolsky-Rosen experiment*, Rev. Sci. Instrum. **83**, 083114 (2012). https://doi.org/10.1063/1.4747274

[39] W. Demtröder, *Laser spectroscopy. Basic concepts and instrumentations*. Springer Series *Advanced texts in physics*, Heidelberg, 2003. https://doi.org/10.1007/978-3-662-05155-9

[40]A. Beeby, *Pump-probe laser spectroscopy* w Springer: *An Introduction to Laser Spectroscopy*, Boston 2002. https://doi.org/10.1007/978-1-4615-0727-7_4

[41] M. Krośnicki, M. Strojecki, T. Urbańczyk, A. Pashov, J. Koperski, *Interatomic potentials of the heavy van der Waals dimer Hg_2: A „test-bed" for theory-to-experiment agreement*, Phys. Rep. **591**, 1 (2015). https://doi.org/10.1016/j.physrep.2015.06.004

[42] J. Koperski, J. B. Atkinson, L. Krause, *The* $\mathbf{0_u^+(6^3P_1) \leftarrow X0_g^+}$ *spectrum of* Hg_2 *excited in a supersonic jet*, Chem. Phys. Lett. **219**, 161 (1994). https://doi.org/10.1016/0009-2614(94)87039-X

[43] J. Koperski, J. B. Atkinson, L. Krause, *Molecular beam spectroscopy of the* $\mathbf{1_u(6^3P_2) - X0_g^+}$ *and* $\mathbf{1_u(6^3P_1) - X0_g^+}$ *transitions in* Hg_2, Can. J. Phys. **72**, 1070 (1994). https://doi.org/10.1139/p94-139

[44] E. Czuchaj, F. Rebentrost, H. Stoll, H. Preuss, *Calculation of ground – and excited – state potential energy curves for the* Hg_2 *molecule in a pseudopotential approach*, Chem. Phys. **214**, 277 (1997). https://doi.org/10.1016/S0301-0104(96)00305-9

[45] O. Kullie, *A relativistic time-dependent density functional study of the excited states of the mercury dimer*, J. Chem. Phys. **140**, 024304 (2014). https://doi.org/10.1063/1.4859258

[46] R. J. Le Roy, *LEVEL: A computer program for solving the radial Schrödinger equation for bound and quasibound levels*, J. Quant. Spectrosc. Radiat. Transfer **186**, 167 (2017). https://doi.org/10.1016/j.jqsrt.2016.05.028

[47] C. M. Western, *PGOPHER: A program for simulating rotational, vibrational and electronic spectra*, J. Quant. Spectrosc. Radiat. Transfer **186,** 221 (2017). https://doi.org/10.1016/j.jqsrt.2016.04.010

[48] J. Wang, G. Wang, J. Zhao, *Nonmetal-metal transition in* Zn_n *(n=2-20) clusters*, Phys. Rev. A **68**, 013201 (2003). https://doi.org/10.1103/PhysRevA.68.013201

[49] J. Zhao, *Density-functional study of structures and electronic properties of Cd clusters*, Phys. Rev. A **64**, 043204 (2001). https://doi.org/10.1103/PhysRevA.64.043204

[50] G. E. Moyano, R. Wesendrup, T. Söhnel, P. Schwerdtfeger, *Properties of small- to medium-sized mercury clusters from a combined ab initio, density-functional, and simulated-annealing study*, Phys. Rev. Lett. **89**, 103401 (2002). https://doi.org/10.1103/PhysRevLett.89.103401

[51] A. R. W. McKellar, *Experimental vaerification of hydrogen dimers in the atmospheres of Jupiter and Saturn from Voyager IRIS far-infrared spectra*, Astroph. J. **326**, L75 (1988). https://doi.org/10.1086/185126

[52] L. M. Trafton, J. K. G. Watson, *Occurence of global-scale emissions on Jupiter: proposed identification of Jovian dimer* H_2 *emission*, Astroph. J. **385**, 320 (1992).

https://doi.org/10.1086/170941

[53] L. M. Trafton, S. J. Kim, T. R. Geballe, S. Miller, *Hydrogen dimer features in the 2-μm spectra of Saturn and Neptune*, Icarus **130**, 544 (1997). https://doi.org/10.1006/icar.1997.5825

[54] P. R. Rowland, R. J. Cohen, *Rapid variability of H_2O masers in Cepheus A*, Mon. Not. R. Astr. Soc. **220**, 233 (1986). https://doi.org/10.1093/mnras/220.1.233

[55] A. W. Harris, G. E. Bromage, J. C. Blades, *Zinc as a tracer of metallicity in the interstellar medium*, Mon. Not. R. Astr. Soc. **203**, 1225 (1983). https://doi.org/10.1093/mnras/203.4.1225

[56] U. J. Sofia, D. M. Meyer, J. A. Cardelli, *The abundance of interstellar tin and cadmium*, Astroph. J. **522**, L137 (1999). https://doi.org/10.1086/312240

[57] J. P. Shaffer, S. T. Rittenhouse, H. R. Sadeghpour, *Ultracold Rydberg molecules*, Nature Commun. **9**, 1 (2018). https://doi.org/10.1038/s41467-018-04135-6

[58] E. L. Hamilton, C. H. Greene, H. R. Sadeghpour, *Shape – resonance – induced long – range molecular Rydberg states*, J. Phys. B: At. Mol. Opt. Phys. **35**, L199 (2002). https://doi.org/10.1088/0953-4075/35/10/102

[59] C. H. Greene, A. S. Dickinson, H. R. Sadeghpour, *Creation of polar and nonpolar ultra-long-range Rydberg molecules*, Phys. Rev. Lett. **85**, 2458 (2000). https://doi.org/10.1103/PhysRevLett.85.2458

[60] R. J. LeRoy, G. T. Kraemer, BCONT 2.2, University of Waterloo Chemical Physics Research Report CP-650R2, 2004. http://scienide2.uwaterloo.ca/~rleroy/bcont

[61] A. Pashov, W. Jastrzębski, P. Kowalczyk, *Construction of potential curves for diatomic molecular states by the IPA method*, Comput. Phys. Commun. **128**, 622 (2000). https://doi.org/10.1016/S0010-4655(00)00010-2

[62] J. M. Pruneda, E. Artacho, *Short – range repulsive interatomic interactions in energetic processess in solids*, Phys. Rev. B **70**, 035106 (2004). https://doi.org/10.1103/PhysRevB.70.035106

[63] A. A. Vigasin, w *Weakly interacting molecular pairs: unconventional absorbers of radiation in the atmosphere* w Springer: *NATO Science Series (Series IV: Earth and Environmental Sciences)* **27**, Dordrecht 2003. https://doi.org/10.1007/978-94-010-0025-3_9

[64] R. E. Smalley, L. Wharton, D. H. Levy, *Molecular optical spectroscopy with supersonic beams and jets*, Acc. Chem. Res. **10**, 139 (1977). https://doi.org/10.1021/ar50112a006

[65] W. Kedzierski, J. B. Atkinson, L. Krause, *Laser – induced fluorescence of the Zn_2 excimer*. Opt. Lett. **14**, 607 (1989). https://doi.org/10.1364/OL.14.000607

[66] M. Ruszczak, M. Strojecki, M. Łukomski, J. Koperski, *Potential Energy curves for the $\boldsymbol{B^1 1_u}$ state and short – range part of the $\boldsymbol{X^1 0_g^+}$ state of Cd_2 determined from excitation and dispersed fluorescence spectra using the $\boldsymbol{B^1 1_u} \leftrightarrow \boldsymbol{X^1 0_g^+}$ transition*, J. Phys. B: At. Mol. Opt. Phys. **41**, 245101 (2008). https://doi.org/10.1088/0953-4075/41/24/245101

[67] M. Strojecki, J. Koperski, *LIF dispersed emission spectra and characterization of ZnRg (Rg=Ne, Ar, Kr) ground-state potentials*, Chem. Phys. Lett. **479**, 189 (2009). https://doi.org/10.1016/j.cplett.2009.08.019

[68] M. Strojecki, M. Krośnicki, P. Zgoda, J. Koperski, *Characterization of bound parts of the $\boldsymbol{b^3 0_u^+(5^3P_1)}$, $\boldsymbol{c^3 1_u(5^3P_2)}$ and $\boldsymbol{X^1 0_g^+}$ states of Cd_2 revisited: Bound – bound excitation and dispersed emission spectra*, Chem. Phys. Lett. **489**, 20 (2010). https://doi.org/10.1016/j.cplett.2010.02.039

[69] G. Parkin, *Zinc – zinc bonds: A new frontier*, Science **305**, 1117 (2004). https://doi.org/10.1126/science.1102500

[70] J. Qiao, L. Zhang, X. Hui, J. Lin, *Kinetic and thermodynamic properties of liquid zinc: An ab initio molecular dynamics study*, Comput. Mater. Sci. **141**, 180 (2018). https://doi.org/10.1016/j.commatsci.2017.09.034

[71] M. Strojecki, M. Krośnicki, J. Koperski, *Short-range repulsion in the $\boldsymbol{D^1\Sigma_{0^+}}$-state potential of the ZnRg (Rg = Ne, Ar, Kr) complexes determined from a direct free ← bound excitation at the $\boldsymbol{D^1\Sigma_{0^+} \leftarrow X^1\Sigma_{0^+}}$ transition*, Chem. Phys. Lett. **465,** 25 (2008). https://doi.org/10.1016/j.cplett.2008.09.051

[72] M. Strojecki, M. Ruszczak, M. Krośnicki, M. Łukomski, J. Koperski, *The $^3\boldsymbol{0_u^+(4^3P_1)}$ - state potential of Zn_2 obtained from excitation spectrum recorded at the $^3\boldsymbol{0_u^+} \leftarrow \boldsymbol{X^1 0_g^+}$ transition*, Chem. Phys. **327**, 229 (2006). https://doi.org/10.1016/j.chemphys.2006.04.008

[73] J. Abrahamson, *Graphite sublimation temperatures, carbon arcs and crystallite erosion*, Carbon **12**, 119 (1974). https://doi.org/10.1016/0008-6223(74)90019-0

[74] I. L. Shabalin, *Ultra – high temperature materials I: Carbon (Graphene/Graphite) and refractory metals*. Springer, Dordrecht 2014. https://doi.org/10.1007/978-94-007-7587-9

[75] R. T. Birge, H. Sponer, *The heat of dissociation of non-polar molecules*, Phys. Rev. **28**, 259 (1926). https://doi.org/10.1103/PhysRev.28.259

5. Przedruki publikacji

Journal of Quantitative Spectroscopy & Radiative Transfer 212 (2018) 32–38

Contents lists available at ScienceDirect

Journal of Quantitative Spectroscopy & Radiative Transfer

journal homepage: www.elsevier.com/locate/jqsrt

Isotopologue-selective excitation studied *via* optical-optical double resonance using the $E^3\Sigma_1^+(6^3S_1) \leftarrow A^3\Pi_{0^+}(5^3P_1) \leftarrow X^1\Sigma_{0^+}(5^1S_0)$ transitions in CdAr and CdKr van der Waals complexes

T. Urbańczyk*, J. Dudek, J. Koperski

Smoluchowski Institute of Physics, Jagiellonian University, ul. prof. Stanisława Łojasiewcza 11, Kraków 30-348, Poland

ARTICLE INFO

Article history:
Received 21 December 2017
Revised 3 March 2018
Accepted 14 March 2018
Available online 15 March 2018

ABSTRACT

A method of experimental selection of molecular isotopologues using optical-optical double resonance (OODR) scheme and supersonic beam source of van der Waals (vdW) complexes is presented. Due to an appropriately large isotopic shift, the proper choice of a wavenumber of a sufficiently narrowband laser in the first transition of OODR scheme can lead to a selective isotopologue excitation to the intermediate state. Thanks to this approach, it is possible to select some of the isotopologues which subsequently give a contribution to laser induced fluorescence (LIF) signal originated from the final state of OODR. In this article, results of tests of the proposed method that employs the $E^3\Sigma_1^+ \leftarrow A^3\Pi_{0^+} \leftarrow X^1\Sigma_{0^+}$ transitions in two vdW complexes, CdKr and CdAr, are presented and analysed.

1. Introduction

Isotope-selective laser excitation with subsequent photochemical reactions represent low-cost processes that have already been proved feasible in laboratory experiments devoted to the development of isotope-separation techniques. The increasing demands exist for fundamental research in physics and chemistry laboratories but also for the practical use of atom isotopes and molecular isotopologues in medicine, biology, geology, hydrology or nuclear power industry [1,2].

As already shown, the isotopologue-selective laser excitation of molecules can be based *e.g.*, on difference of rotational period between $^{79}Br_2$ and $^{81}Br_2$ as demonstrated by Akagi et al. [3] laser molecular alignment as proposed for $^{14}N_2$ and $^{15}N_2$ by Fleischer et al. [4], molecular spinning by a chiral train of short laser pulses as reported by Floss and Averbukh [5], or quantum control of the rovibrational excitation including both radial and angular motions as demonstrated theoretically for $^7Li^{37}Cl$ and $^7Li^{35}Cl$ mixture by Kurosaki and Yokoyama [6]. As far as the isotopologue-selective laser excitation is concerned, the process can also be simply demonstrated in the first step of optical-optical double resonance (OODR) scheme using the $E^3\Sigma_1^+(6^3S_1) \leftarrow A^3\Pi_{0^+}(5^3P_1) \leftarrow X^1\Sigma_{0^+}(5^1S_0)$ transitions in CdRg (Rg = Ar or Kr) van der Waals (vdW) complexes produced in a supersonic expansion beam. Subsequently, the effect of selective excitation can be examined using the second-step transition from the $A^3\Pi_{0^+}$ intermediate to the Rydberg $E^3\Sigma_1^+$ final state. The Rydberg electronic energy state $E^3\Sigma_1^+$ (*i.e.*, $E^3\Sigma^+$ or E^31 in Hund's case-a or case-c, respectively) correlating with the $5s6s^3S_1$ atomic cadmium asymptote was spectroscopically studied in CdAr and CdKr vdW complexes by several authors [7–12]. In both complexes, the $E^3\Sigma_1^+$-state potential possess a double-well structure (as concluded also from *ab initio* calculations [13]), with deeper (inner, E_{in}) and shallower (outer, E_{out}) wells. In order to demonstrate the isotopologue-selective laser excitation, it is essential to explore the energy structure of the $E^3\Sigma_1^+ \leftarrow A^3\Pi_{0^+}$ transition in both CdAr and CdKr.

Bennet and Breckenridge [7] studied the isotopic structure of five ($\upsilon' = 6-10$) vibrational profiles recorded in the $e^3\Sigma^+(\upsilon') \leftarrow b^3\Pi_2(\upsilon'' = 0)$ transition in CdAr (their $e^3\Sigma^+$ corresponds to the $E^3\Sigma_1^+$, in this article). However, in their investigation the lower $b^3\Pi_2$ state correlating with the $5s5p^3P_2$ asymptote was populated in a nonselective excitation what can be treated as a drawback of the method. As a result, spectroscopic constants for the $e^3\Sigma^+$-state inner well were reported.

Using pump-and-probe method in conjunction with a continuous supersonic expansion of CdAr, Czajkowski et al. [8] characterized the E^31-state inner well. In the excitation, as an intermediate they employed the A^30^+-state ($A^3\Pi$ in Hund's case-a) correlating with the $5s5p^3P_1$ asymptote. In the A^30^+ state, vibrational level $\upsilon'' = 5$ was used. Czajkowski et al. determined a distinct non-Morse behaviour of the E^31_{in} -state potential well close to the dissociation limit. The E^31_{out} -state well was omitted in the

* Corresponding author.
E-mail addresses: tomek.urbanczyk@uj.edu.pl, tomek_urbanczyk@op.pl (T. Urbańczyk).

https://doi.org/10.1016/j.jqsrt.2018.03.013
0022-4073/

analysis. Both, the $E^3 1$-state inner and outer wells were studied in CdAr by Koperski and Czajkowski [9] using the same experimental approach as in previous study [8]. In order to extend the $E^3 1$-state characterization, as additional intermediate they used the $B^3 1$ state ($B^3\Sigma^+$ in Hund's case-a) that correlates with the same $5s5p^3P_1$ asymptote as does the $A^3 0^+$, however, possessing longer bond length R_e'. The extended approach allowed for exploration (with a limited resolution though) of the vibrational energy structure in the $E^3 1_{out}$-state well. Neither isotopic nor rotational structure of the vibrational bands was resolved. Characterization of the $E^3 1$-state inner and outer wells, along with a position and height of the barrier, and long-range potential characteristics were determined. As the frequencies of the $E^3 1(\upsilon') \leftarrow A^3 0^+(\upsilon'' = 5)$ progression reported [9] did not correspond to those of Czajkowski et al. [8], and the $E^3 1_{in}$ -state dissociation energies D_0' (and well depths D_e') differed [7–9], additional investigations were carried out.

Urbańczyk et al. [10] partly extended exploration of the $E^3\Sigma^+{}_{in}$-state well in CdAr and investigated also the isotopic structure of three $(\upsilon', \upsilon'' = 5)$ vibrational bands in the $E^3\Sigma^+{}_{in} \leftarrow A^3\Pi$ transition. In their analysis, an influence of rotational energy structure of the studied bands was included. Several vibrational and rotational characteristics were determined. For the $E^3\Sigma^+{}_{out}$ -state well, isotopic structure of seven $(\upsilon', \upsilon'' = 1)$ vibrational bands in the $E^3\Sigma^+ \leftarrow B^3\Sigma^+$ transition were investigated improving characterization of the outer well.

Further studies of the $E^3\Sigma^+{}_{out}$ -state well in CdAr and new determination of its bond length R_e' by Urbańczyk and Koperski [11] provided its satisfactory characterization. On the contrary, in view of several inconsistencies between results of studies of the $E^3\Sigma^+_{1\,in}$ -state well, Urbańczyk et al. [12] performed revisited investigation of the $E^3\Sigma^+_{1\,in}(\upsilon') \leftarrow A^3\Pi_{0^+}(\upsilon'' = 6)$ transition in CdAr using both theoretical and experimental approach. Systematic detection of the $\upsilon' \leftarrow \upsilon'' = 6$ transition frequencies performed with higher accuracy and with spectrally narrower laser than in previous studies [8–10], extended and improved analysis of the spectrum and its simulation, and resulted in more consistent characterization of the $E^3\Sigma^+_{1\,in}$-state well with the help of inverse perturbation approach (IPA) methodology.

As far as CdKr is concerned, the $E^3\Sigma^+$-state inner and outer wells were studied by Koperski and Czajkowski [14] using the same experimental approach as that employed in the study of CdAr [9]. In order to perform the characterization as thorough as possible, both intermediate states *i.e.*, the $A^3 0^+(\upsilon'' = 9)$ and $B^3 1(\upsilon'' = 1)$ were used. The approach allowed for exploration (again with a limited resolution) a vibrational energy structure in the $E^3\Sigma^+$-state inner and outer wells. Neither isotopic nor rotational structure of the vibrational bands was resolved. Characterization of both $E^3\Sigma^+$-state potential wells, along with a position and height of the barrier, and long-range potential characteristics were proposed. Isotopic structure of the $E^3\Sigma^+_{1\,in}(\upsilon' = 21) \leftarrow A^3\Pi_{0^+}(\upsilon'' = 9)$ transition was investigated by Urbańczyk et al. [10] extending the $E^3\Sigma^+$-state characterization of the previous study [14].

2. Experimental

The experimental set-up for studying vdW complexes using OODR scheme is based on that used in our previous studies of CdRg complexes [15,16]. Here, we limit the description to necessary details. The scheme is presented in Fig. 1. In the experiment, CdRg (Rg = Kr or Ar) complexes were produced using a high-temperature, high-pressure pulsed source of the supersonic molecular beam [17]. The source was filled with cadmium pellets (purity 99.95%, natural abundance, Aldrich) and a carrier gas of high purity at a pressure from 3 bar to 6 bar was used (Ar or Kr, 99.999%, Linde Gas). In OODR scheme two laser systems are applied. First system, a frequency-doubled Nd^+:YAG-laser-pumped-dye-laser (YG981C-TDL90, Quantel) was employed to excite complexes in the beam from the ground $X^1\Sigma_{0^+}$ to the intermediate $A^3\Pi_{0^+}$ state.

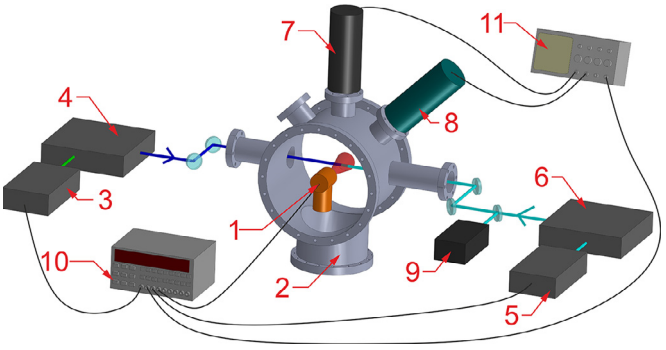

Fig. 1. Experimental scheme used in OODR experiment. (1) High-temperature, high-pressure, pulsed source of supersonic molecular beam. (2) Vacuum chamber. (3) YG981C pulsed Nd^+:YAG laser. (4) Frequency-doubled TDL90 tuneable dye laser (first-step excitation in OODR scheme). (5) Powerlite 7010 pulsed Nd^+:YAG laser. (6) TDL90 tuneable dye laser (second-step excitation in OODR). (7) R585 PM tube screened from the UV radiation and recording fluorescence from the final $E^3\Sigma^+_{1\,in}$ Rydberg state. (8) Auxiliary 9893QB/350 PM tube recording fluorescence from the intermediate $A^3\Pi_{0^+}$ state. (9) WSU30 wavemeter. (10) DG645 digital delay generator used for time synchronization of the pulsed beam source, Nd^+:YAG lasers and triggering of the oscilloscope. (11) TDS 2024B oscilloscope averaging signals from the PM tubes.

Second system, Nd^+: YAG-laser-pumped-dye-laser (Powerlite7010-TDL90, Continuum-Quantel), served for further excitation from the $A^3\Pi_{0^+}$ to the final $E^3\Sigma^+_{1\,in}$ state. Thanks to this approach, it was possible to excite the $E^3\Sigma^+_{1\,in}$ state which otherwise is difficult to reach using one-step excitation (in CdRg, excitation energy of the $E^3\Sigma^+_1$ state is about 50,000 cm^{-1} which corresponds to 200 nm). The two dye-laser beams were directed into a vacuum chamber (PREVAC) pumped with two rotary pumps (Trivac D25B, Oerlikon Leybold Vacuum) and two diffusion pumps (VHS-4, Varian). In the chamber, the laser beams intersected the molecular beam at a distance of 18 mm from the source nozzle (0.2 mm orifice diameter). To synchronize the pulsed beam source and the laser pulses, a digital delay generator was employed (DG645, Stanford Research Systems). Laser induced fluorescence (LIF) signals were registered using two photomultiplier (PM) tubes. For the auxiliary purposes, LIF signal resulting from the $A^3\Pi_{0^+} \leftarrow X^1\Sigma_{0^+}$ transition was monitored using first PM tube (9893QB/350, Electron Tubes) whereas that resulting from the $E^3\Sigma^+_{1\,in} \leftarrow A^3\Pi_{0^+}$ transition was recorded using second PM tube (R585, Hamamatsu), screened from the UV radiation. During OODR experiment, the wavenumbers of the first- and second-step excitation lasers were fixed and tuned (0.04–0.3-cm^{-1} steps), respectively. For each tuning step, the signal from the second PM was averaged over 64 laser pulses in oscilloscope (TDS 2024B, Tektronix) and the resulting averaged waveform was saved in a computer memory along with additional experimental parameters including wavenumbers of the second-step excitation laser measured by a precise wavemeter (WSU30, HighFinesse). To obtain the resulting spectrum from the collected waveforms, during data analysis process each registered waveform was integrated within a selected integration window (usually 2-μs wide, starting 1 μs after the second-step excitation laser pulse). Details of the integration process can be found elsewhere [18].

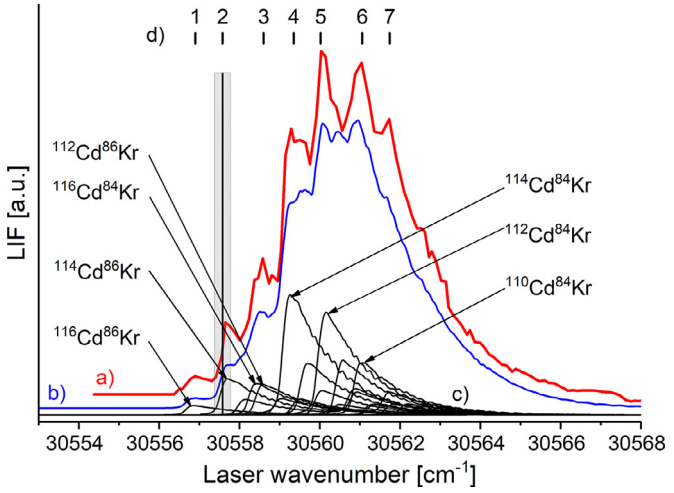

Fig. 2. (a) LIF excitation spectrum of the $A^3\Pi_{0^+}(\upsilon''=9) \leftarrow X^1\Sigma_{0^+}(\upsilon=0)$ transition in CdKr complex. (b) Simulation of the experimental spectrum performed using PGOPHER program and assuming $T_{rot}=4$K, Gauss and Lorentz broadenings: $\Delta_{GAUSS}=0.1\ cm^{-1}$ and $\Delta_{LOR}=0.1\ cm^{-1}$. Lower- and upper-state rotational constants B_υ and D_υ, and transition energies computed using LEVEL program for the $A^3\Pi_{0^+}$ and $X^1\Sigma_{0^+}$ -state potential characteristics (see Table 1). (c) Contributions to the simulation shown in (b) originating from different isotopologues with abundances $\alpha > 1\%$. (d) Positions of the first-step excitation laser wavenumbers E_l used in comparison presented in Fig. 3. Black vertical solid line and grey rectangle represent the laser wavenumber which is most suitable for one isotopologue excitation in the $A^3\Pi_{0^+}$ state (compare with Figs. 3 and 4) and the laser bandwidth ($\pm 0.1\ cm^{-1}$), respectively. (For interpretation of the references to colour in the text, the reader is referred to the web version of this article.)

3. Method of isotopologues selection

To understand the idea of isotopologues selection as well as shapes of LIF excitation spectra resulting from excitation of the final electronic energy state in OODR scheme (here, the $E^3\Sigma^+_{1\ in}$ state), one should examine the shape of LIF excitation spectrum resulting from the transition to the intermediate $A^3\Pi_{0^+}$ from the ground $X^1\Sigma_{0^+}$ state. Fig. 2 presents the experimental LIF excitation spectrum of the $A^3\Pi_{0^+}(\upsilon''=9) \leftarrow X^1\Sigma_{0^+}(\upsilon=0)$ transition in CdKr (red trace) and its simulation (blue trace) obtained with the help of LEVEL [19] and PGOPHER [20] programs (using parameters shown in caption of Fig. 2 and Table 1). Black traces show contributions to the simulation (b) originating from particular isotopologues (only these with abundance α larger than 1% were shown for clarity).

Positions of the first-step excitation laser (wavenumbers E_l) used during recording of the spectra presented in Fig. 3 are shown in Fig. 2(d) (vertical solid line and grey rectangle indicate laser wavenumber and bandwidth for position (2), respectively). From Fig. 2 it is obvious that each region of LIF excitation spectrum of the first-step $A^3\Pi_{0^+} \leftarrow X^1\Sigma_{0^+}$ transition can be associated with different group of $^{A_1}Cd^{A_2}Kr$ isotopologues. Particularly, in the low-wavenumber part of the spectrum the observed maxima in the experimental profile can be associated with excitation of few isotopologues only. For instance, the maximum near 30,557.6 cm^{-1} can be associated with excitation of mainly $^{114}Cd^{86}Kr$ isotopologue (see position 2 and vertical solid line in Fig. 2(d)). Due to the fact, that in OODR scheme the wavenumber of first-step excitation laser is fixed and the spectral bandwidth of this laser is relatively narrow (see grey rectangle depicting the assumed bandwidth $\pm 0.1\ cm^{-1}$) only a limited number of isotopologues can be excited to the intermediate $A^3\Pi_{0^+}$ state and contributes to LIF signal that results from the second-step $E^3\Sigma^+_{1\ in} \leftarrow A^3\Pi_{0^+}$ transition. In other words, selecting the first-step laser wavenumber of the $A^3\Pi_{0^+} \leftarrow X^1\Sigma_{0^+}$ transition, one can select isotopologues contributing to LIF signal

Table 1
Spectroscopic characteristics of the $X^1\Sigma_{0^+}$, $A^3\Pi_{0^+}$ and $E^3\Sigma^+_{1\ in}$ states in CdKr complex. All values are expressed in [cm^{-1}] except R_e and β which are expressed in [Å] and [$Å^{-1}$], respectively. For the $E^3\Sigma^+_{1\ in}$-state potential, due to a significant non-Morse behaviour near the dissociation limit, presented characteristics are valid only for υ' near the bottom of the potential well.

	$X^1\Sigma_{0^+}$	$A^3\Pi_{0^+}$	$E^3\Sigma^+_{1\ in}$
ω_e	18.1±0.5[a]	36.95±0.05[c]	91.1±0.50[e] 90.97±1.00[c]
$\omega_e x_e$	0.5±0.01[a]	0.615±0.005[c]	1.42±0.04[e] 1.374±0.030[c]
R_e	4.27[a]	3.34±0.03[c]	2.99±0.05[c]
D_e	163.8±5.0[b]	555.0±0.5[c]	1461.1±9.0[e]
β	1.1971[b]	1.3277[d]	2.0174[e]
Morse potential asymptote	0	30663.8[f]	51321.8[f]

[a] Ref. [21].

[b] Obtained using formulas $D_e = \frac{\omega_e^2}{4\omega_e x_e}$ and $\beta = \sqrt{\frac{8\pi^2 c\mu\omega_e x_e}{h}}$, and characteristics from Ref. [21].

[c] Ref. [10].

[d] Obtained using formulas from "b" and characteristics from Ref. [10]

[e] This work, based on experimental data; vibrational constants obtained using agreement plot [11,12] for 8 vibrational components υ' (from range $\upsilon' = 0$–18) which were recorded applying selective excitation of $^{114}Cd^{86}Kr$ isotopologue.

[f] This work, based on experimental data; the obtained asymptotes are different (by +7.7 cm^{-1} and −162.2 cm^{-1} for the $A^3\Pi_{0^+}$ and $E^3\Sigma^+_{1\ in}$ states, respectively) from the atomic asymptotes [24] due to a non-Morse behaviour of their interatomic potentials near the asymptotes; the energy shifts were adjusted to obtain agreement between simulations and absolute energies of the observed vibrational components.

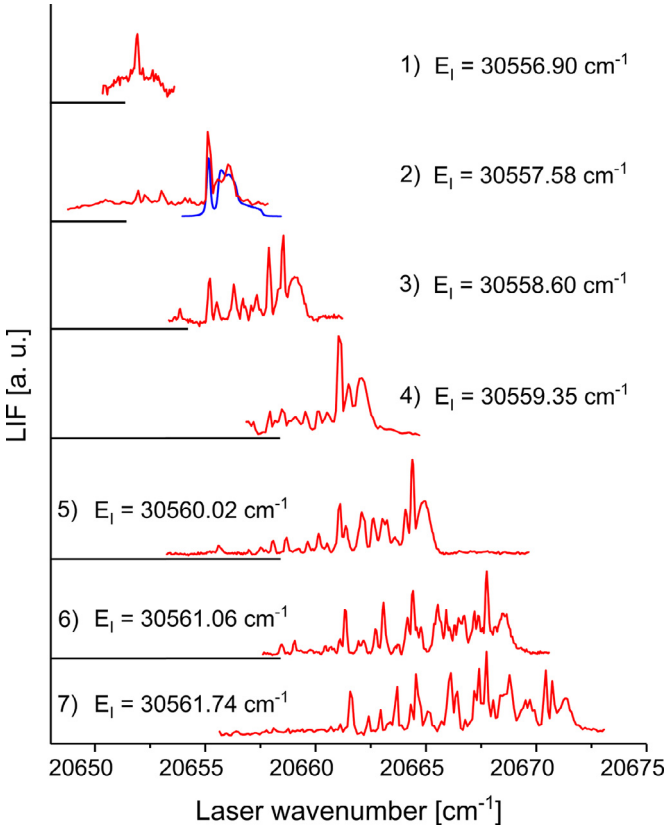

Fig. 3. Experimental LIF excitation spectra (red traces) of the $E^3\Sigma^+_{1\ in}(\upsilon'=18) \leftarrow A^3\Pi_{0^+}(\upsilon''=9)$ transition in CdKr recorded using OODR scheme for different laser wavenumbers (E_l) of the first-step excitation $A^3\Pi_{0^+}(\upsilon''=9) \leftarrow X^1\Sigma_{0^+}(\upsilon=0)$. Numbers adjacent to the E_l's correspond to the positions depicted in Fig. 2(d) where the E_l's are shown with respect to the experimental LIF excitation spectrum of the $A^3\Pi_{0^+}(\upsilon''=9) \leftarrow X^1\Sigma_{0^+}(\upsilon=0)$ transition. Simulation shown in part (2) (blue trace) is described in detail in Fig 4. (For interpretation of the references to colour in this figure legend, the reader is referred to the web version of this article.)

Table 2
List of isotopologues $^{A_1}Cd^{A_2}Kr$ with abundances α larger than 1%. Reduced mass μ and α are expressed in [atomic mass units] and [%], respectively.

A_1	A_2	A_1+A_2	α	μ
110	82	192	1.45	46.933
111	82	193	1.48	47.115
110	83		1.44	47.260
112	82	194	2.80	47.294
111	83		1.47	47.444
110	84		7.12	47.582
113	82	195	1.42	47.472
112	83		2.77	47.626
111	84		7.29	47.769
114	82	196	3.33	47.648
113	83		1.41	47.806
112	84		13.75	47.953
110	86		2.16	48.218
114	83	197	3.30	47.985
113	84		6.96	48.136
111	86		2.21	48.410
114	84	198	16.37	48.317
112	86		4.17	48.600
113	86	199	2.11	48.787
116	84	200	4.27	48.673
114	86		4.96	48.973
116	86	202	1.29	49.339

resulting from the $E^3\Sigma^+_{1\ in} \leftarrow A^3\Pi_{0^+}$ transition. It has to be emphasized that the isotopologues selection has a tremendous impact on the shape of the observed excitation spectra. It is clearly visible in Fig. 3, which shows shapes of LIF profiles recorded using the $E^3\Sigma^+_{1\ in} \leftarrow A^3\Pi_{0^+}$ transition for seven different first-step laser wavenumbers E_I (for more details see Section 4.1). The method of isotopologues selection may be applied to other complexes with rich isotopic structure. The only requirement is an existence of an appropriately large isotopic shift that can be resolved using laser with sufficiently small bandwidth in the first-step of OODR scheme.

4. Results and discussion

4.1. CdKr

In CdKr complex reduced mass μ is relatively large and the strongest vibrational component in υ'-progression of the $A^3\Pi_{0^+}(\upsilon'') \leftarrow X^1\Sigma_{0^+}(\upsilon = 0)$ transition occurs for the $\upsilon'' = 9$.

As the isotopic shift increases with increasing υ'', the magnitude of the isotopic shift in LIF excitation spectrum of this transition is sufficiently large. Moreover, due to the fact that CdKr complex has a significant number of isotopologues (*i.e.*, 22 with abundance $\alpha > 1\%$, compare with Table 2), the CdKr is a good candidate to apply the isotopologue selection method using OODR scheme. Fig. 3 presents LIF excitation spectra of the $E^3\Sigma^+_{1\ in}(\upsilon' = 18) \leftarrow A^3\Pi_{0^+}(\upsilon'' = 9)$ transition in CdKr recorded for different laser wavenumbers E_I of the $A^3\Pi_{0^+}(\upsilon'' = 9) \leftarrow X^1\Sigma_{0^+}(\upsilon = 0)$ first-step transition of OODR scheme (compare positions from 1 to 7 in Fig. 3 with those in Fig. 2(d)). From Fig. 3 one can conclude that the laser wavenumber E_I has a large impact on the shape of the recorded LIF excitation spectrum originating from OODR final state. The complexity of the spectrum increases with increasing E_I. The reason for this is the fact, that with increasing E_I larger number of isotopologues is excited to the $A^3\Pi_{0^+}$ state contributing to the complexity of the LIF spectrum. From Fig. 2 one can infer that most preferable separation of isotopologues occurs for $E_I = 30{,}556.90\ cm^{-1}$ (see position 1). In this case, only $^{116}Cd^{86}Kr$ is excited to the $A^3\Pi_{0^+}$ state. Unfortunately, the abundance of $^{116}Cd^{86}Kr$ isotopologue in the molecular beam is small ($\alpha = 1.3\%$, see Table 2), thus, the signal-to-noise ratio (SNR) in the spectrum of the $E^3\Sigma^+_{1\ in}(\upsilon' = 18) \leftarrow A^3\Pi_{0^+}(\upsilon'' = 9)$ transition is also low (refer to position 1 in Fig. 3). For $E_I = 30{,}557.58\ cm^{-1}$ (position 2 in Fig. 3), $^{114}Cd^{86}Kr$ and $^{116}Cd^{86}Kr$, with relatively small admixture of $^{113}Cd^{86}Kr$, are excited to the $A^3\Pi_{0^+}$ state. However, due to a large abundance ($\alpha = 5.0\%$), $^{114}Cd^{86}Kr$ dominates in the spectrum. Concluding, to record the spectrum for primarily one isotopologue with reasonable SNR, $E_I = 30{,}557.58\ cm^{-1}$ should be considered as the most appropriate option.

Further increase of E_I usually leads to more complex spectra. For example, for $E_I = 30{,}561.06\ cm^{-1}$ (position 6 in Figs. 2 and 3) several abundant isotopologues make a significant contribution to the spectrum. One exception from the presented rule occurs for $E_I = 30{,}559.35\ cm^{-1}$ (position 4 in Figs. 2 and 3) when the contribution from $^{114}Cd^{84}Kr$ is much stronger than that from other isotopologues.

Simplification of LIF excitation spectrum by reducing number of excited isotopologues greatly simplifies further simulation. In some cases it might also allow to partially resolve the rotational structure of a vibrational component, which would be difficult (or even impossible) without the isotopologues selection, due to the overlap of the spectra originating from different isotopologues. Using spectrally narrowband laser in the first-step excitation has also an impact on a distribution of the populations of intermediate-state rotational levels. In other words, if the first-step excitation laser is sufficiently narrow only a selected group of rotational levels J in the $A^3\Pi_{0^+}$ state is populated. It is evident that by narrowing the spectral bandwidth of the first-step excitation laser, one can restrict the range of J in the intermediate state without manipulating of rotational temperature T_{rot}. Therefore, also LIF spectrum originated from the $E^3\Sigma^+_{1\ in}$ state contains contribution only from the selected range of J.

Red traces (a) in Fig. 4 present experimental LIF excitation spectra with partially resolved rotational structure recorded for three vibrational components ($\upsilon' = 0$, $\upsilon' = 3$ and $\upsilon' = 18$) of the $E^3\Sigma^+_{1\ in}(\upsilon') \leftarrow A^3\Pi_{0^+}(\upsilon'' = 9)$ transition recorded with the selection of $^{114}Cd^{86}Kr$ isotopologue ($E_I = 30{,}557.58\ cm^{-1}$, position 2 in Fig. 2). Simulations of these profiles (black traces) were obtained using LEVEL [19] and PGOPHER [20] programs, under assumption that interatomic potentials of the $E^3\Sigma^+_{1\ in}$ and $A^3\Pi_{0^+}$ states are represented with Morse functions (parameters in Table 1), $T_{rot} = 4.5K$ (for $\upsilon' = 0$ and $\upsilon' = 3$), $T_{rot} = 15K$ (for $\upsilon' = 18$), Gauss and Lorentz broadenings: $\Delta_{GAUSS} = 0.1\ cm^{-1}$ and $\Delta_{LOR} = 0.1\ cm^{-1}$, and minimum and maximum rotational quantum numbers considered in the simulation $J_{min} = 0$, $J_{max} = 15$ (for $\upsilon' = 0$ and $\upsilon' = 3$) and $J_{min} = 7$, $J_{max} = 20$ (for $\upsilon' = 18$). The rotational constants $B_{\upsilon'}$ and $D_{\upsilon'}$ for several low-lying υ' levels of the $E^3\Sigma^+_{1\ in}$ state are collected in Table 3. The determined rotational constants, that improved characteristics of the $E^3\Sigma^+_{1\ in}$ state in

Table 3
Rotational characteristics (all expressed in [cm^{-1}]) of several lowest υ' levels in the $E^3\Sigma^+_{1\ in}$-state inner potential well of $^{114}Cd^{86}Kr$ isotopologue, obtained using of LEVEL program [19] under an assumption that the $E^3\Sigma^+_{1\ in}$-state potential is represented using constants from Table 1 (see footnote[e]).

υ'	$B_{\upsilon'}$	$D_{\upsilon'} \times 10^{-7}$
0	0.03828	0.2980
1	0.03782	0.3081
2	0.03736	0.3189
3	0.03689	0.3305

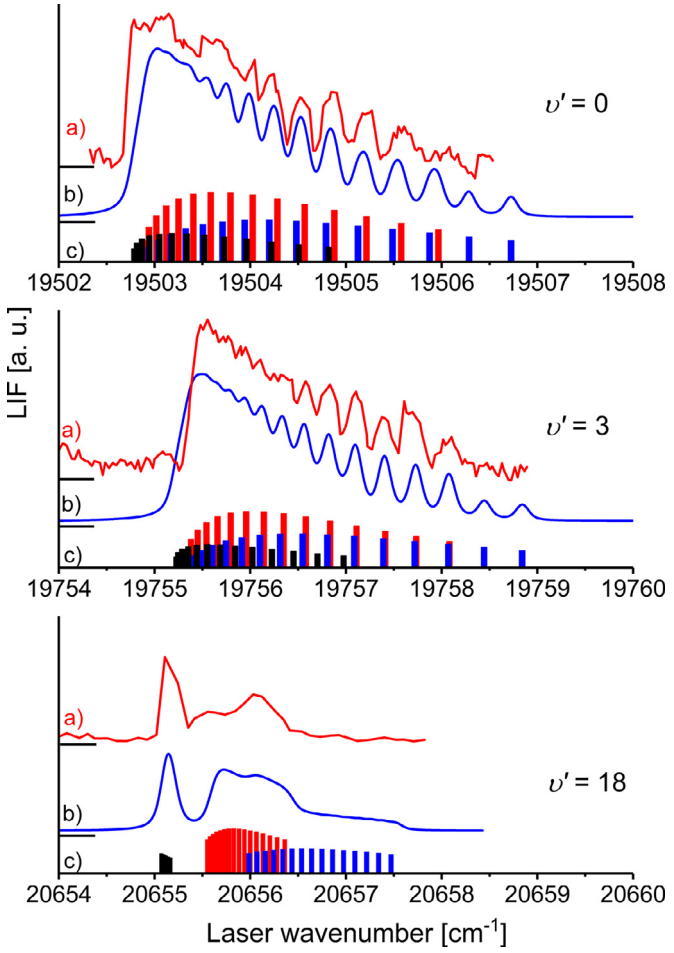

Fig. 4. (a) Experimental LIF excitation spectra (red traces) of the $E^3\Sigma^+_{1\ in}(\upsilon') \leftarrow A^3\Pi_{0^+}(\upsilon''=9)$ transition recorded for $\upsilon' = 0$ (upper part), $\upsilon' = 3$ (middle part) and $\upsilon' = 18$ (lower part) in $^{114}Cd^{86}Kr$ isotopologue ($E_I = 30{,}557.58$ cm^{-1}, position 2 in Fig. 2). For $\upsilon' = 18$ compare also part (2) in Fig. 3). (b) Simulations (blue traces) performed using PGOPHER program assuming lower- and upper-state rotational constants B_υ and D_υ, and transitions energies obtained using LEVEL program based on characteristics of the $E^3\Sigma^+_{1\ in}$ and $A^3\Pi_{0^+}$ state potentials from Table 1, and assuming $T_{rot} = 4.5$ K ($\upsilon' = 0$ and $\upsilon' = 3$), $T_{rot} = 15$ K ($\upsilon' = 18$), $J_{min} = 0$, $J_{max} = 15$ ($\upsilon' = 0$ and $\upsilon' = 3$) and $J_{min} = 7$, $J_{max} = 20$ ($\upsilon' = 18$). For all simulations: $\Delta_{GAUSS} = 0.1$ cm^{-1} and $\Delta_{LOR} = 0.1$ cm^{-1}. (c) Simulated distributions of P-, Q- and R-branch components represented by black, red and blue bars, respectively. For the sake of comparison, for all υ' the range of horizontal axis was unified (6 cm^{-1}). (For interpretation of the references to colour in this figure legend, the reader is referred to the web version of this article.)

comparison to Ref. [10], were obtained using LEVEL program based on representation of the interatomic potential with constants from Table 1.

4.2. CdAr

The isotopologue selection can also be observed in CdAr complex. In comparison with CdKr, naturally abundant CdAr expanding in the beam consists of smaller number of $^{A_1}Cd^{A_2}Ar$ isotopologues (7 instead of 22 with $\alpha > 1\%$, see Table 4).

However, due to smaller μ and lower $\upsilon' = 6$, for the $A^3\Pi_{0^+}(\upsilon') \leftarrow X^1\Sigma_{0^+}(\upsilon = 0)$ transition, the isotopic shift is smaller than for analogous transition in CdKr (refer to Fig. 5). Red trace in Fig. 5 shows experimental LIF excitation spectrum of the $A^3\Pi_{0^+}(\upsilon'' = 6) \leftarrow X^1\Sigma_{0^+}(\upsilon = 0)$ transition while blue trace presents a simulation of the spectrum performed using PGOPHER program (with spectroscopic parameters shown in figure

Table 4
List of isotopologues $^{A_1}Cd^{A_2}Ar$ with abundances α larger than 1%. Reduced mass μ and α are expressed in [atomic mass units] and [%], respectively.

A_1	A_2	A_1+A_2	α	μ
106	40	146	1.25	29.014
110	40	150	12.44	29.306
111	40	151	12.75	29.377
112	40	152	24.03	29.447
113	40	153	12.17	29.515
114	40	154	28.62	29.583
116	40	156	7.46	29.717

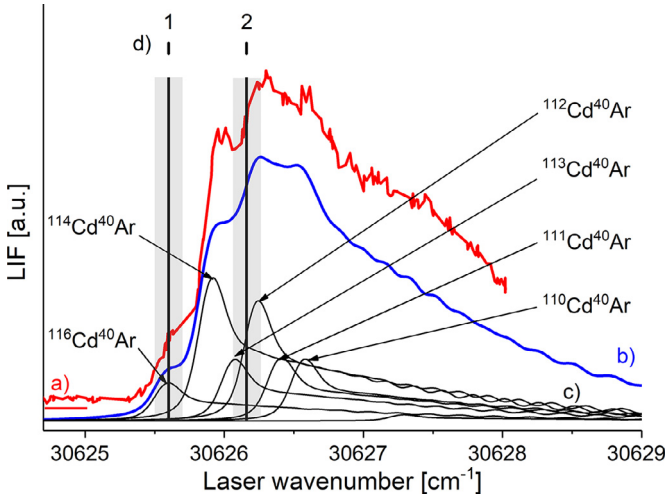

Fig. 5. (a) LIF excitation spectrum of the $A^3\Pi_{0^+}(\upsilon'' = 6) \leftarrow X^1\Sigma_{0^+}(\upsilon = 0)$ transition in CdAr complex. (b) Simulation of the experimental spectrum performed using PGOPHER program and assuming $T_{rot} = 5$ K, Gauss and Lorentz broadenings: $\Delta_{GAUSS} = 0.1$ cm^{-1} and $\Delta_{LOR} = 0.15$ cm^{-1}. Lower- and upper-state rotational constants B_υ and D_υ, and transition energies computed using LEVEL program for the $A^3\Pi_{0^+}$ and $X^1\Sigma_{0^+}$ -state potential characteristics (see Table 3). (c) Contributions to the simulation shown in (b) originating from different isotopologues with abundances $\alpha > 1\%$. (d) Positions of the first-step excitation laser wavenumbers E_I used in comparison presented in Fig. 6. Black vertical solid lines and grey rectangle represent the first-step laser wavenumbers used in OODR scheme and laser bandwidth (±0.1 cm^{-1}), respectively.

caption). Black traces on the bottom part of the figure show contributions to the simulation from particular $^{A_1}Cd^{A_2}Ar$ isotopologues.

Black vertical lines and grey rectangles in Fig. 5(d) show laser wavenumbers of the first-step excitation in OODR scheme that were used during the experiment and the assumed laser bandwidth (±0.1 cm^{-1}), respectively. For the first-step wavenumber $E_I = 30{,}625.60$ cm^{-1} (position 1 in Fig. 5(d)), $^{116}Cd^{40}Ar$ with small admixture of $^{114}Cd^{40}Ar$ is excited to the $A^3\Pi_{0^+}$ intermediate state. For $E_I = 30{,}626.16$ cm^{-1} (position 2 in Fig. 5(d)), three isotopologues ($^{114}Cd^{40}Ar$, $^{112}Cd^{40}Ar$ and $^{113}Cd^{40}Ar$) can be efficiently excited. For the same E_I, three other isotopologues ($^{116}Cd^{40}Ar$, $^{111}Cd^{40}Ar$ and $^{110}Cd^{40}Ar$) are possible to be excited but the efficiency of this process is significantly smaller, especially for $^{111}Cd^{40}Ar$ and $^{110}Cd^{40}Ar$ (refer to Fig. 5(c)). Thus, one can foresee, that for $E_I = 30{,}626.16$ cm^{-1} the spectrum originated from the final state of OODR should be more complex than these recorded upon the first-step excitation using $E_I = 30{,}625.6$ cm^{-1}.

The prediction was confirmed experimentally and the result is presented in Fig. 6. Red traces show experimental LIF excitation spectra of the $E^3\Sigma^+_{1\ in}(\upsilon' = 2, 6, 13) \leftarrow A^3\Pi_{0^+}(\upsilon'' = 6)$ transitions recorded for $E_I = 30{,}626.16$ cm^{-1} (position 2 in Fig. 5(d)) whereas black traces present spectra recorded for $E_I = 30{,}625.60$ cm^{-1} (position 1 in Fig. 5(d)). Simulations of the

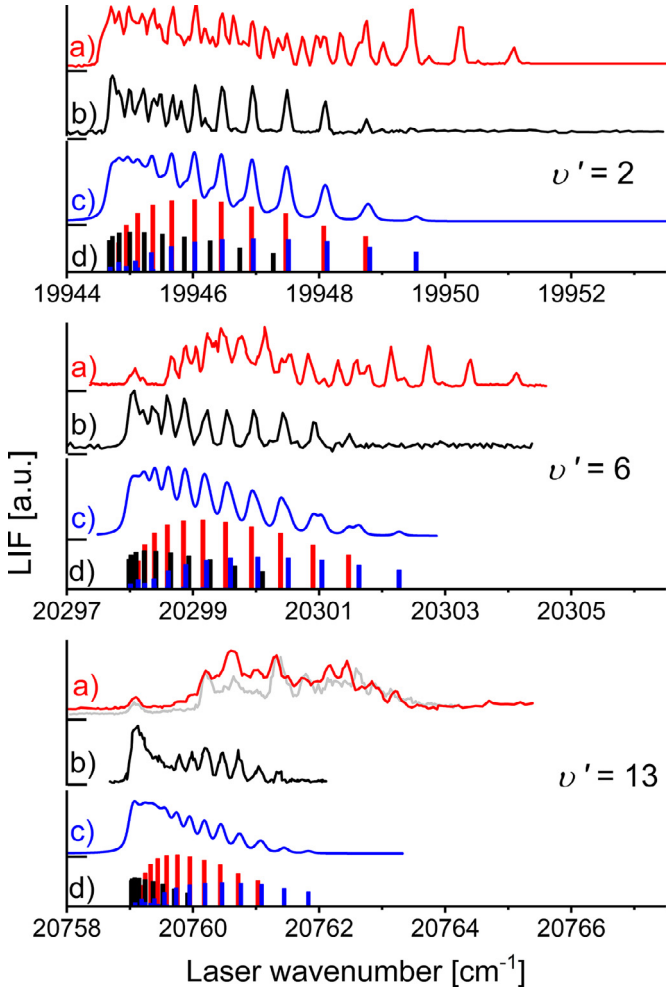

Fig. 6. (a) and (b) Experimental LIF excitation spectra of the $E^3\Sigma^+_{1\ in}(\upsilon' = 2, 6, 13) \leftarrow A^3\Pi_{0^+}(\upsilon'' = 6)$ transitions in CdAr recorded using OODR scheme. For spectra in (a) (red traces) the first-step laser excitation wavenumber: $E_I = 30{,}626.16\ cm^{-1}$ (position 2 in Fig. 5(d)) resulting in excitation to the $A^3\Pi_{0^+}$ state mainly $^{114}Cd^{40}Ar$, $^{112}Cd^{40}Ar$ and $^{113}Cd^{40}Ar$ with small admixture of $^{116}Cd^{40}Ar$. For spectra in (b) $E_I = 30{,}625.60\ cm^{-1}$ (position 1 in Fig. 5(d)) resulting in excitation mainly $^{116}Cd^{40}Ar$ with small admixture of $^{114}Cd^{40}Ar$. In case of the $\upsilon' = 13 \leftarrow \upsilon'' = 6$ transition, the spectrum of the $\upsilon' = 13 \leftarrow \upsilon'' = 5$ transition collected using a continuous beam source [10] is shown for comparison (grey trace). The spectrum was rescaled by 3.12% to compensate the difference in isotopic shift due to a different υ'' and shifted along horizontal axis to compensate the difference between energies of $\upsilon'' = 6$ and $\upsilon'' = 5$ levels in the $A^3\Pi_{0^+}$ state. (c) Simulations of the experimental spectra shown in (b) performed using PGOPHER program and assuming lower- and upper-state rotational constants B_υ and D_υ and transitions energies computed using LEVEL for the $A^3\Pi_{0^+}$ -state potential characteristics (see Table 3) and $E^3\Sigma^+_{1\ in}$-state potential as result of IPA method [12]. All simulations were performed assuming: $T_{rot} = 4.5$ K, $\Delta_{GAUSS} = 0.1\ cm^{-1}$, $\Delta_{LOR} = 0.1\ cm^{-1}$ and $J_{max} = 10$. (d) Simulated distributions of P-, Q- and R-branch components represented by black, red and blue bars, respectively. For the sake of comparison, for all υ' the range of horizontal axis was unified ($9.5\ cm^{-1}$). (For interpretation of the references to colour in this figure legend, the reader is referred to the web version of this article.)

spectra shown in traces (b) were performed using LEVEL and PGOPHER programs and are shown with blue traces. In the simulations, the $A^3\Pi_{0^+}$ -state potential characteristics from Table 5 were employed. Note: for the $E^3\Sigma^+_{1\ in}$ state, potential obtained using IPA method was used [12], whereas in Table 5 for the $E^3\Sigma^+_{1\ in}$ state Morse potential characteristics are collected, which can be treated as approximation (the characteristics were used to construct initial potential used in IPA method). Comparison of the experimental spectra in Fig. 6, recorded for two different E_I used in the first-step excitation (traces (a) and (b)), illustrates that

Table 5
Spectroscopic characteristics of the $X^1\Sigma_{0^+}$, $A^3\Pi_{0^+}$ and $E^3\Sigma^+_{1\ in}$ states in CdAr complex. All values are expressed in [cm^{-1}] except R_e and β which are expressed in [Å] and [$Å^{-1}$], respectively. For the $E^3\Sigma^+_{1\ in}$ -state potential, due to a significant non-Morse behaviour near the dissociation limit, presented characteristics are valid only for υ' near the bottom of the potential well.

	$X^1\Sigma_{0^+}$	$A^3\Pi_{0^+}$	$E^3\Sigma^+_{1\ in}$
ω_e	19.8[a]	37.51±0.30[c]	106.5±0.3[e]
$\omega_e x_e$	0.93[a]	1.098±0.020[c]	2.16±0.02[e]
R_e	4.31±0.02[a]	3.51±0.03[c]	2.850±0.005[e]
D_e	102.8±0.4[b]	320.4±5.0[d]	1312.8±14.2[f]
β	1.2775[d]	1.3881[d]	1.9469[f]
Morse potential asymptote	0	30656.13	51538.25[g]

[a] Ref. [22].
[b] Ref. [23].
[c] Ref. [12].
[d] Obtained using formulas $D_e = \frac{\omega_e^2}{4\omega_e x_e}$ and $\beta = \sqrt{\frac{8\pi^2 c\mu\omega_e x_e}{h}}$, and characteristics from Ref. [12].
[e] Ref. [10].
[f] Obtained using formulas from [b] and characteristics from Ref. [10].
[g] This work, based on experimental data; the obtained asymptote is different (by $+54.25\ cm^{-1}$) from the atomic asymptote [24] due to a non-Morse behaviour of its interatomic potential near the asymptote; the energy shift was adjusted to obtain agreement between simulation and absolute energies of the observed vibrational components.

for all three υ' there is an evidence of $^{116}Cd^{40}Ar$ excitation for both E_I. However, in case of excitation using $E_I = 30{,}625.60\ cm^{-1}$ (traces (b)), $^{116}Cd^{40}Ar$ strongly dominates the spectrum, whereas in case of $E_I = 30{,}626.16\ cm^{-1}$ (traces (a)), the intensity of LIF signal associated with $^{116}Cd^{40}Ar$ is significantly smaller (compare with Fig. 5(c)). It is also worth to mention, that the shape of spectrum (a) for $\upsilon' = 13$ is in an agreement with previous result from our laboratory [10] (see Fig. 3 (I) there). The agreement should be noted despite the 20-cm^{-1} shift associated with different selection of υ'' in the intermediate $A^3\Pi_{0^+}$ state (6 in this work and 5 in [10]) and more precise determination of laser wavenumbers than that done previously [10]. For the comparison, in the lowest part of Fig. 6, an additional trace was added (in grey) which presents the experimental spectrum of the $(\upsilon' = 13) \leftarrow (\upsilon'' = 5)$ transition reported in [10] for CdAr. To compensate the difference in isotopic shift due to different υ'', presented spectrum was rescaled by 3.12%. The spectrum was also shifted along horizontal axis to compensate the difference between energies of the $\upsilon'' = 6$ and $\upsilon'' = 5$ levels in the $A^3\Pi_{0^+}$ state.

5. Conclusions

In this article we presented a method of experimental selection of molecular isotopologues using optical-optical double resonance (OODR) scheme applied to CdRg (Rg=rare gas) van der Waals (vdW) complexes expanded in a supersonic beam. The isotopologue selection was realised at the first-step transition but revealed itself in LIF excitation spectra recorded using transition of the second-step of OODR. Due to the isotopic shift between different isotopologues of the studied CdRg complexes, by employing laser with sufficiently small spectral bandwidth, using transition between the ground and intermediate state of OODR scheme one can excite only selected isotopologues present in the molecular beam. The method was demonstrated using the $E^3\Sigma^+_{1\ in} \leftarrow A^3\Pi_{0^+} \leftarrow X^1\Sigma_{0^+}$ transitions in CdKr and CdAr complexes. In Fig. 3 we demonstrated an influence of selection of a wavenumber of the first-step excitation laser (which was used to excite complexes from the $X^1\Sigma_{0^+}$ to the intermediate $A^3\Pi_{0^+}$ state) on LIF excitation spectrum recorded using the $E^3\Sigma^+_{1\ in} \leftarrow A^3\Pi_{0^+}$ transition in CdKr complex. Limiting the number of isotopologues participating in the LIF signal leads to simplification of the ob-

served spectra and consequently, simplifies the simulation process which was presented in Fig. 6.

The benefits of isotopologues selection are also clearly visible by comparison of results of this work with results of our previous analysis of the $E^3\Sigma^+_{1\ in} \leftarrow A^3\Pi_{0^+}$ transition in CdRg molecules [10]. Due to employing of the isotopologues selection method, spectra presented in this work were collected with partially resolved rotational structure (see traces c) and d) in Figs. 4 and 6, respectively), whereas in Ref. [10] only the isotopic structure was resolved and the rotational structure manifested itself in the shapes of observed spectra only. The spectra presented in Ref. [10] were collected using the first-step excitation laser with considerably wider bandwidth than in case of this study. In the previous experiment [10], we set the frequency of first-step excitation laser at the frequency of the bandhead of the first-excitation transition. Neglecting the fact, that in Ref. [10] and in this study we used different υ'' in the intermediate state ($\upsilon'' = 6$ and $\upsilon'' = 5$, respectively), one can assume that the method of first-step excitation used in Ref. [10] is similar to this of setting the first-step laser to position 5 in Fig. 2 (CdKr) and position 2 in Fig. 5 (CdAr) in the present study (in a sense of the first-step laser frequency with respect to a shape of the profile resulting from the first OODR transition). LIF spectra originated from the $E^3\Sigma^+_{1\ in}$ state which were presented in Ref. [10] contain contributions from a larger number of isotopologues. The comparison of the previous results with these of the present study shows that the recorded spectra are similar in character. It is presented in the lower part of Fig. 6(a) for the $E^3\Sigma^+_{1\ in}(\upsilon' = 13) \leftarrow A^3\Pi_{0^+}$ transition in CdAr molecule.

Acknowledgments

This work was supported by the National Science Centre Poland under grant number UMO-2015/17/B/ST4/04016. The research was carried out with the equipment purchased thanks to the financial support of the European Regional Development Fund in the framework of the Polish Innovation Economy Operational Program (contract no. POIG.02.01.00-12-023/08).

References

[1] Aldridge JP, Birley JH, Cantrell CD, Cartwright DC. Experimental studies of laser isotope separation. Laser photochemistry, tunable lasers. Jacobs SE, Sargent SM, Scully MO, Walker CT, editors. Reading, MA: Addison-Wesley; 1976.
[2] Jensen RJ, Judd OP, Sullivan JA. Separating isotopes with lasers. Los Alamos Sci 1982;4:2–33. http://la-science.lanl.gov/lascience04.shtml.
[3] Akagi H, Ohba H, Yokoyama K, Yokoyama A, Egashira E, Fujimura Y. Rotational-coherence molecular laser isotope separation. Appl Phys B 2009;95:17–21. https://doi.org/10.1007/s00340-009-3453-8.
[4] Fleischer S, Averbukh ISh, Prior Y. Isotope-selective laser molecular alignment. Phys Rev A 2006;74 041403(R)-1-4 https://doi.org/10.1103/PhysRevA.74.041403.
[5] Floss J, Sh Averbukh I. Molecular spinning by a chiral train of short laser pulses. Phys Rev A 2012;86 063414-1-11 https://doi.org/10.1103/PhysRevA.86.063414.
[6] Kurosaki Y, Yokoyama K. Quantum optimal control of the isotope-selective rovibrational excitation of diatomic molecules. Chem Phys 2017;493:183–93. https://doi.org/10.1016/j.chemphys.2017.07.003.
[7] Bennett RB, Breckenridge WH. Van der Waals bonding in the lowest electronic states of MgAr, ZnAr, CdAr, and HgAr: spectroscopic characterization of the $b^3\Pi_2$ and $e^3\Sigma^+$ states of the CdAr molecule. J Chem Phys 1992;96:882–90. http://dx.doi.org/10.1063/1.462108.
[8] Czajkowski M, Bobkowski R, Krause L. Pump-and-probe studies of the $E1(6^3S_1) \leftarrow A0^+(5^3P_1)$ excitation spectrum of CdAr in a supersonic beam. Phys Rev A 1992;45:6451–8. https://doi.org/10.1103/PhysRevA.45.6451.
[9] Koperski J, Czajkowski M. The structure of the lowest electronic Rydberg state of CdAr complex determined by laser double resonance method in a supersonic jetexpansion beam. Spectrochim Acta A 2003;59:2435–48. https://doi.org/10.1016/S1386-1425(02)00396-7.
[10] Urbańczyk T, Strojecki M, Koperski J. Structure of vibrational bands of the $E^3\Sigma^+_1(6^3S_1) \leftarrow A^3\Pi_{0^+}(5^3P_1)$,$B^3\Sigma^+_1(5^3P_1)$ transitions in CdAr and CdKr studied by optical– optical double resonance method. Chem Phys Lett 2011;503:18–24. https://doi.org/10.1016/j.cplett.2010.12.085.
[11] Urbańczyk T, Koperski J. The $E^3\Sigma^+(6^3S_1)$-state interatomic potential of CdAr in the long range region revisited: a new method for bond length adjustment. Chem Phys Lett 2015;640:82–6. https://doi.org/10.1016/j.cplett.2015.10.013.
[12] Urbańczyk T, Krośnicki M, Kędziorski A, Koperski J. The $E^3\Sigma_1{}^+$ $(6^3S_1) \leftarrow A^3\Pi_{0+}(5^3P_1)$ transition in CdAr revisited: the spectrum and new analysis of the $E^3\Sigma_1{}^+$ Rydberg state interatomic potential. Spectrochim Acta A 2018;196:58–66. https://doi.org/10.1016/j.saa.2018.01.075.
[13] Czuchaj E, Krośnicki M, Stoll H. Quasirelativistic valence ab initio calculation of the potential-energy curves for Cd–rare gas atom pairs. Theor Chem Acc 2001;105:219–26. https://doi.org/10.1007/s002140000206.
[14] Koperski J, Czajkowski M. Electronic structure of the CdKr lowest Rydberg state determined from laser-excitation spectra using supersonic beam and double optical resonance methods. Phys Rev A 2004;69 042509-1-9 https://doi.org/10.1103/PhysRevA.69.042509.
[15] Urbańczyk T, Koperski J. Rotational profiles of vibrational bands recorded at the $B^31(5^3P_1) \leftarrow X^10^+(5^1S_0)$ transition in CdAr complex. Chem Phys Lett 2014;591:64–8. https://doi.org/10.1016/j.cplett.2013.11.009.
[16] Urbańczyk T, Koperski J. Rotational profiles in the excitation spectrum recorded for the $B^31(5^3P_1) \leftarrow X^10^+(5^1S_0)$ transition in CdNe van der Waals complex. Chem Phys Lett 2016;644:231–4. https://doi.org/10.1016/j.cplett.2015.11.051.
[17] Urbańczyk T, Koperski J. High-temperature high-pressure all-metal pulsed source of van der Waals dimers: towards the Einstein-Podolsky-Rosen experiment. Rev Sci Instrum 2012;83:083114. http://doi.org/10.1063/1.4747274.
[18] Urbańczyk T, Koperski J. Profiles of $(\upsilon';\upsilon'';=0)$ bands recorded in excitation spectra using $b^30^+_u \leftarrow X^10^+_g$ transitions in Cd_2 and $B^31 \leftarrow X^10^+$ transitions in CdAr. Mol Phys 2014;112:2486–94. http://dx.doi.org/10.1080/00268976.2014.933901.
[19] Le Roy RJ. LEVEL: a computer program for solving the radial Schrödinger equation for bound and quasibound levels. J Quant Spectrosc Radiat Transf 2017;186:167–78. http://dx.doi.org/10.1016/j.jqsrt.2016.05.028.
[20] Western CM. PGOPHER: a program for simulating rotational, vibrational and electronic spectra. J Quant Spectrosc Radiat Transf 2017;186:221–42. http://dx.doi.org/10.1016/j.jqsrt.2016.04.010.
[21] Koperski J, Łukomski M, Czajkowski M. Laser spectroscopy of CdKr molecules in ultraviolet region. Spectrochim Acta A 2002;58:2709–24. https://doi.org/10.1016/S1386-1425(02)00027-6.
[22] Koperski J, Kiełbasa S, Czajkowski M. Interatomic potentials of cadmium-argon $B1(^3\Sigma^+)$ and $X0^+(^1\Sigma^+)$ states based on near-dissociation expansion and 'hot' bands observed in the $B1 \leftarrow X0^+$ excitation spectrum. Spectrochim Acta A 2000;56:1613–26. https://doi.org/10.1016/S1386-1425(00)00213-4.
[23] Koperski J, Urbańczyk T, Krośnicki M, Strojecki M. Free ← bound and bound ← bound profiles in excitation spectra of the $B^31 \leftarrow X^10^+$ transition in CdNg (Ng = noble gas) complexes". Chem Phys 2014;428:43–52. https://doi.org/10.1016/j.chemphys.2013.10.017.
[24] NIST Atomic Spectra Database Levels Data, https://physics.nist.gov/PhysRefData/ASD/levels_form.html (27.11.2017).

Review of Scientific Instruments ARTICLE scitation.org/journal/rsi

High-temperature continuous molecular beam source for aggressive elements: An example of zinc

Cite as: Rev. Sci. Instrum. 90, 115109 (2019); doi: 10.1063/1.5127809
Submitted: 13 September 2019 • Accepted: 24 October 2019 •
Published Online: 12 November 2019

J. Dudek, K. Puczka, T. Urbańczyk, and J. Koperski[a)]

AFFILIATIONS

Smoluchowski Institute of Physics, Jagiellonian University, Łojasiewicza 11, 30-348 Krakow, Poland

[a)]Author to whom correspondence should be addressed: ufkopers@cyf-kr.edu.pl

ABSTRACT

Expansion of Zn_2 or ZnRg (Rg = rare gas atom) in a molecular supersonic beam constitutes a considerable technical challenge due to the high zinc melting point and high zinc reactivity with stainless steel at high temperatures. In order to overcome these difficulties and meet the requirements for spectroscopy of van der Waals molecules containing zinc, a high-temperature source-module of the supersonic molecular beam for aggressive elements was designed. The module was tested in the laser-induced fluorescence excitation spectroscopy experiment using the $b^3 0_u^+(4^3P_1) \leftarrow X^1 0_g^+(4^1S_0)$ bound ← bound transitions in Zn_2. The new source-module can be used for other aggressive elements for which a laser-vaporization technique has been used to date.

I. INTRODUCTION

Laser spectroscopy of metal-containing dimers or clusters in supersonic expansion beams requires production of metal-vapor at a sufficient partial pressure. In the past, three approaches have been used: (i) heating of a metal sample at temperatures considerably higher than its melting point to provide sufficient metal-vapor partial pressure,[1] (ii) metal vaporization by irradiation with a high-power pulsed laser before expansion,[2] and (iii) photolysis of a metal-containing larger complex by an excimer pulsed laser downstream of the source orifice.[3] However, the first technique allows production of molecules or clusters only in their ground state. It considerably simplifies the laser excitation schemes and, what is more important, facilitates the interpretation and analysis of the spectroscopic data.

Stainless steel is an inexpensive material widely used in the production of molecular beam source-modules. It is easy to weld and mechanically machine. However, there exist metal elements that in melted form, due to the high reactivity of their vapors, lead to a rapid degradation of stainless steel construction elements. Thus, the manufacture of the beam source-module for those "reactive" metals requires using materials with appropriate chemical resistance and compatibility.

Another problem is high temperature that has to be applied to achieve a sufficient metal-vapor partial pressure. In molecular spectroscopy, induction heating is not an option due to the presence of an inhomogeneous magnetic field causing undefined shifts of molecular spectral lines. Another method is an electron-beam heating, but it is not proposed here. The option that is used in our laboratory is a resistance heating. In this case, a small size of heated elements, and thus a small area for winding of resistance wires, determines a requirement for well-designed geometry and precise construction of the beam source-module.

Zinc is subjected to both criteria of the difficulty mentioned above: stainless-steel high-temperature degradation while in contact with zinc vapor and considerably high melting point (692.7 K) as compared with two other 12-group metal elements (Cd and Hg with their 594.2 K and 234.3 K melting points, respectively). As a 12-group metal, zinc is characterized by closed-shell electronic configuration, and along with 18-group rare-gas elements (Rg = He, Ne, Ar, Kr, and Xe), it is a good candidate to form van der Waals (vdW) molecules. However, due to the above-mentioned experimental difficulties, vdW molecules such as Zn_2 and ZnRg have been less intensively investigated as compared with Hg_2[4] and Cd_2,[5] or CdRg[1] and HgRg.[1] Nevertheless, in the previous studies of

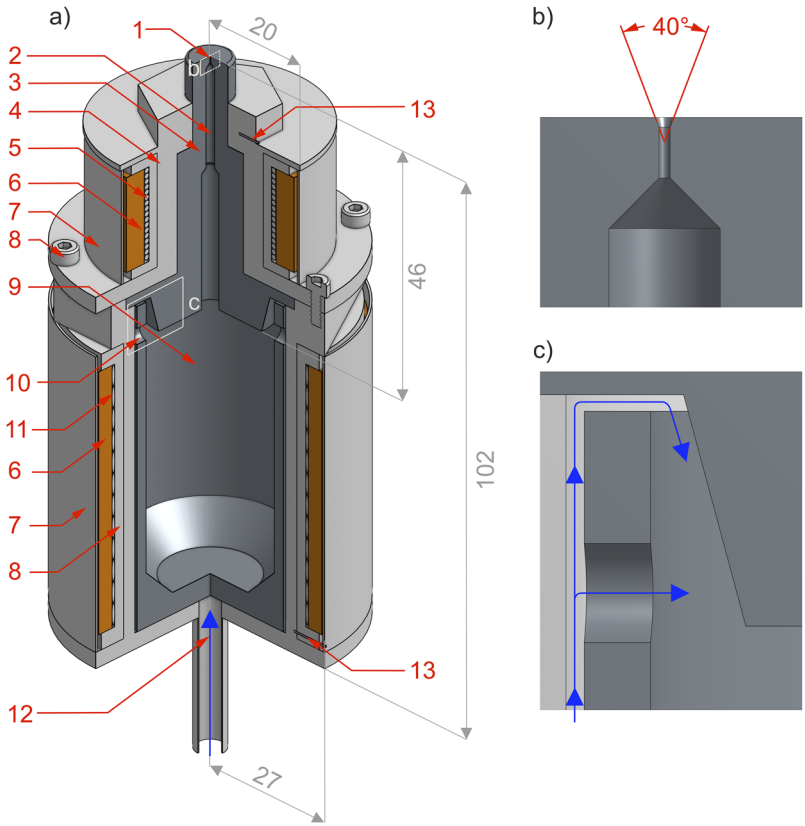

FIG. 1. (a) High-temperature source-module of the continuous supersonic molecular beam designed for aggressive elements: (1) nozzle, (2) capillary passage in the nozzle-cap, (3) graphite nozzle-cap, (4) stainless steel casing, (5) upper heater, (6) ceramic layer, (7) thermal shield, (8) tightening screw, (9) graphite zinc reservoir (crucible), (10) carrier-gas inlet-hole, (11) lower heater, (12) carrier-gas inlet pipe, and (13) thermocouple. Insets show cross section details of (b) the nozzle profile and (c) carrier-gas inlet to the crucible (the carrier-gas flow is marked with blue arrows). Overall dimensions are in millimeters.

complexes containing zinc, to overcome difficulties associated with stainless steel degradation, a molybdenum source-module was applied in, e.g., an investigation of laser-induced fluorescence (LIF) excitation spectra of the $C^1 1(4^1P_1) \leftarrow X^1 0^+(4^1S_0)$ transition in ZnNe,[6] the $D^1\Sigma_0^+(4^1P_1) \leftarrow X^1\Sigma_0^+(4^1S_0)$ transition in ZnRg (Rg = Ne, Ar, Kr),[7] and the $b^3 0_u^+(4^3P_1) \leftarrow X^1 0_g^+(4^1S_0)$ transition in Zn_2,[8] and LIF emission spectra recorded using the $C^1 1(4^1P_1)$, $v' = 10 \rightarrow X^1 0^+(4^1S_0)$ transition in ZnAr.[9] However, due to difficulties associated with a necessity of machining and welding, molybdenum was temporarily abandoned as a material for the source-module production. Instead, other researchers employed a laser vaporization technique in the investigation of LIF excitation spectra of the $C^1\Pi_1 \leftarrow X^1\Sigma_0^+$ transitions in ZnAr,[10] ZnKr,[11] and ZnNe,[12] as well as the $D^1\Sigma_0^+ \leftarrow X^1\Sigma_0^+$ transition in ZnXe,[13] stumbling with ambiguities in spectra interpretation and analysis, however.

A preferable material suitable for the production of the supersonic molecular-beam source-module for aggressive and high-temperature-melting metal elements is graphite. It is due to its several advantages: (i) high sublimation temperature—between 3895 K and 4020 K under 1.013 bars (1 atm) pressure,[14] (ii) low thermal expansion, and thus high thermal shock resistance,[15] (iii) good chemical compatibility with numerous melted metals,[16] e.g., Zn, Sn, and Pb, (iv) very good machining properties, and (v) relatively high thermal conductivity[17] that allows for an efficient heat transfer. A variety of graphite sources were used by other researchers in their studies[18–21] to produce Cl_2,[18,19] Br_2,[18,19] and I_2[19] molecular halogen beams including supersonic beams[19] with rare gas carriers under several-bars pressure, Br and Br_2 effusive beams[20] or serving as an evaporation source for the Al beam.[21] However, in the last example, melting of Al in a graphite reservoir leads to its slow gradual degradation and caused the formation of unwanted aluminum carbide Al_4C_3. In other cases, graphite can dissolve in some liquid metals, e.g., Fe.[22] Very recently, porous graphite was used both as a resistive heater and a heat exchanger in the high enthalpy source for the temperatures reaching 2000 K.[23]

In this article, we present a high-temperature source-module for the supersonic molecular beam that is devoted to highly aggressive elements. The components that are exposed to the molten aggressive metal, i.e., the reservoir (crucible) and nozzle-cap (see Fig. 1), are made of graphite, which ensures chemical resistance. Because of the inability of welding, a new method for mixing the carrier gas and metal vapor inside the graphite crucible is proposed. The source-module was tested in LIF excitation spectroscopy using the $b^3 0_u^+ \leftarrow X^1 0_g^+$ bound $\leftarrow$ bound transitions in Zn_2.

II. DESIGN OF THE SOURCE-MODULE

An overall view with the partial cross section of the source-module is presented in Fig. 1. Both reservoir (crucible) [(9), see Fig. 1(a)] and nozzle-cap (3) that are exposed to a molten aggressive

metal element (here, zinc) and its vapor are made of graphite. Casing of the source-module (4) that is not exposed to the aggressive metal is made of stainless steel. The crucible is filled with metallic zinc and placed in the casing, which is heated with a ribbon-shaped resistance heater [Kanthal® D (11)]. The nozzle-module itself is heated separately with a round-shaped heater made of tantalum (5). The two-part heating system allows us to control the source-module temperature during the experiment; hence, the upper part (with the nozzle) remains 10–30 K hotter than the lower part. It secures the nozzle orifice against clogging. Temperatures of the upper and lower parts of the source-module are controlled with two thermocouples (13). Using the heating system, temperatures reaching 1300 K are possible to obtain. The shape of the nozzle-cap was designed to maximize the area available for mounting the heating tantalum wire and, at the same time, to minimize the volume of the heated part. Thus, the middle part of the graphite nozzle-cap (15 mm in diameter) is taller than the top part (8 mm in diameter). The source-module is sealed-up mechanically by pressing the graphite flange on the bottom part of the nozzle-cap (38 mm in diameter) against the stainless steel flange of the casing using 6 Allen screws (8) located on the module's upper wall. All screws are tightened using 4.5-N m torque that ensures sufficient sealing and does not damage the fragile graphite flange.

Both the upper and lower heaters are mechanically stabilized with a ceramic layer (6) made of sodium silicate, which simultaneously forms a barrier that stops transferring the heat outside the module. In addition, in order to further minimize the radiative heat transfer, the source is surrounded by a thin metal sheet (7) made of C16 stainless steel.

A 5-mm-inner-diameter stainless steel carrier-gas inlet pipe (12) is welded to the bottom of the casing. The carrier-gas fills the empty space between the casing and the crucible and then enters into the crucible through four holes, 3 mm in diameter, located symmetrically in the top part of the crucible wall (10). The maximum pressure of the carrier-gas is limited by mechanical resistance of the nozzle-cap graphite flange and cannot exceed 6 bars. The carrier-gas mixed with zinc vapor expands through the two-part capillary passage (4 mm and 2 mm in diameter) in the nozzle-cap (2) and enters into the vacuum chamber through the 0.2-mm nozzle orifice (1) drilled in its 1-mm-thick front wall. The nozzle is equipped with an additional 40° conical opening [see Fig. 1(b)], which, according to Even,[24] provides an optimal well-defined shape of the beam.

Although maintaining the temperature gradient could prevent the hotter nozzle orifice from clogging, it was observed that occasional formation of zinc oxide at the surface of the congealed zinc and inside the nozzle-cap long capillary passage may lead to the loss of the intensity of the recorded signal in the spectroscopy test experiment. The zinc oxide can be easily removed by immersing the contaminated parts in 10% acetic acid. In order to avoid clogging of the nozzle orifice and contaminating the heated source-module with air (and oxygen), the following shutdown sequence was ensured: (i) switching-off the bottom heater power supply, (ii) waiting until the temperature gradient reaches 100 K, (iii) reducing the upper heater power supply, (iv) waiting until the crucible is cooled down below the zinc melting point, (v) switching-off the upper heater power supply, and (vi) turning-off the valve on the carrier-gas inlet pipe and the carrier gas supply.

III. DIAGNOSTICS AND TESTS OF THE SOURCE-MODULE

Using the new source-module, LIF excitation spectrum of the $b^3 0_u^+(4^3P_1), v' \leftarrow X^1 0_g^+(4^1S_0), v''$ transitions in Zn_2 was recorded and analyzed. The scheme of the experimental setup is shown in Fig. 2. The crucible was filled with zinc pellets (Alfa Aesar, 99.99% purity, natural abundance). The upper and lower heaters were supplied with 163 W and 216 W of electric power, respectively. It enabled to heat the parts with the crucible and the nozzle-cap up to about 1000 K and 1020 K, respectively, and resulted in 125 mbar of zinc vapor partial pressure.[25] Argon as a carrier-gas at 5-bars backing pressure was delivered to the source. The background pressure inside the vacuum chamber, 0.03 mbar and 0.25 mbar without and with the carrier-gas delivery system off and on, respectively, was obtained using a Roots pump (RUVAC WAU501, Leybold) backed by a rotary pump (SOGEVAC SV200, Leybold). In the vacuum chamber, the source-module was surrounded with a water-shield, which acted as a protection against the chamber overheating. At a distance of 8 mm from the nozzle, Zn_2 molecules in the beam were irradiated with a frequency-doubled output of a tunable pulsed dye-laser (TDL90, Quantel) with a dye-mixture of Rh640 and DCM in methanol. The dye-laser was pumped with a second-harmonic output of the Nd^+:YAG laser (YG981C, Quantel). The resulting LIF signal from the beam was monitored at right angles to the plane containing the crossed molecular and laser beams. The LIF signal was focused at the photocathode of a photomultiplier (9893QB/350, Electron Tubes), recorded with a digital oscilloscope (TDS 2024B, Tektronix), and stored in a computer. The frequency of the fundamental dye-laser beam was monitored with a wavemeter (WSU-30, High Finesse).

Both experimental and simulated LIF excitation spectra of the $b^3 0_u^+, v' \leftarrow X^1 0_g^+, v''$ transitions are shown in Fig. 3. The excited-state vibrational frequency (ω_e') and anharmonicity ($\omega_e' x_e'$) were determined using a Birge-Sponer (B-S) plot method[26] and were somewhat different from those obtained previously.[8] Uncertainties of the intersect with the vertical axis and the slope of the linear regression of the B-S plot were used to determine uncertainties of the ω_e'

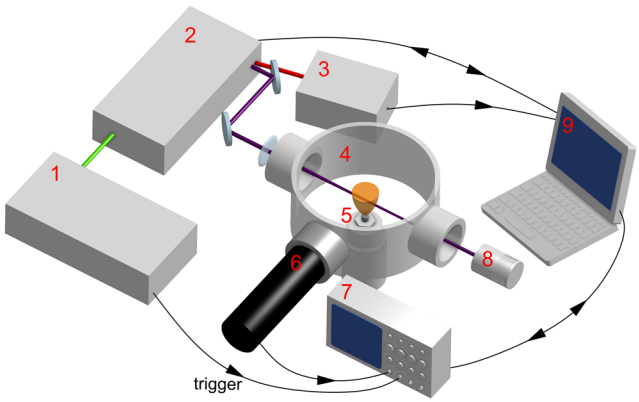

FIG. 2. Experimental setup of LIF excitation spectroscopy of Zn_2 produced in the supersonic molecular beam. (1)The pulsed Nd^+:YAG laser, (2) dye laser, (3) wavemeter, (4) vacuum chamber, (5) source-module, (6) photomultiplier tube, (7) oscilloscope, (8) beam-dump, and (9) computer.

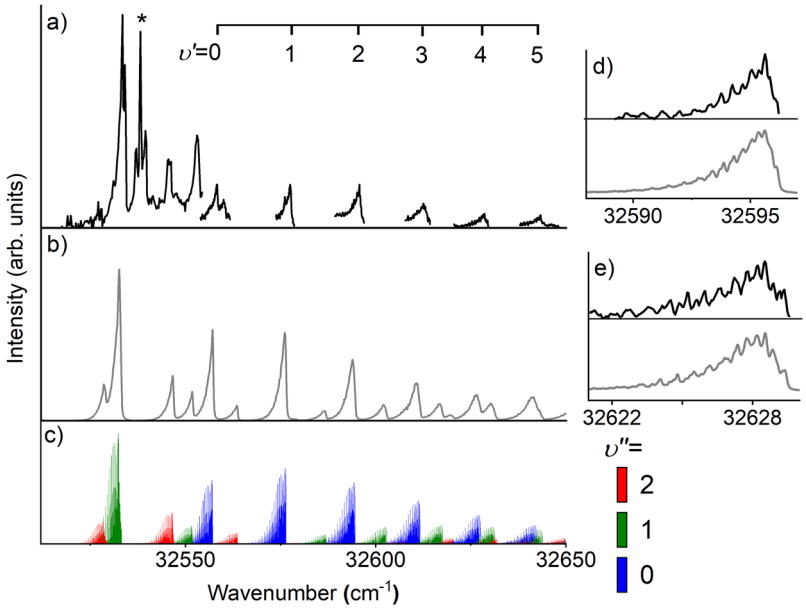

FIG. 3. (a) Experimental LIF excitation spectra of the $b^3 0_u^+(4^3P_1) \leftarrow X^1 0_g^+(4^1S_0)$ transition in Zn_2 recorded using the new source-module. (b) Simulations of the $b^3 0_u^+, v' \leftarrow X^1 0_g^+, v''$ transitions obtained with parameters: T_{vib} = 150 K, T_{rot} = 10 K, Morse-function representation for the excited- and ground-state potentials (see details in text), and 0.1-cm^{-1} (FWHM) Gaussian and Lorentzian convolutions for every rotational transition. (c) Intensities of all individual Zn_2 isotopologue components within each of the $v' \leftarrow v''$ vibrational band (see the color legend), which constitute shaded profiles in (b). Insets: experimental (black) and simulated (gray) rotational-isotopologue structures of (d) $v' = 2 \leftarrow v'' = 0$ and (e) $v' = 4 \leftarrow v'' = 0$ components. The unidentified spectral component in (a) marked with an asterisk originates most likely from the $B^3 1(4^3P_1) \leftarrow X^1 0^+(4^1S_0)$ transition in ZnAr.

and $\omega_e' x_e'$, respectively (see Table I). In comparison with the previous study,[8] better accuracy of the laser-frequency measurement (0.03 cm^{-1}) allowed to obtain positions of the vibrational components with better accuracy (compared with 0.5 cm^{-1} of Strojecki *et al.*[8]).

Simulations of the experimental LIF excitation spectra were performed using LEVEL[27] and PGOPHER[28] programs, with a Morse function representing the excited- and ground-state interatomic potentials, using potential parameters obtained in this analysis and by Strojecki *et al.*,[8] for the excited and ground states, respectively. Comparing experimental spectra with these simulated for different vibrational (T_{vib}) and rotational (T_{rot}) temperatures, T_{vib} and T_{rot} were estimated to be 150 K and 10 K, respectively. For $v' \leftarrow v'' = 0$ transitions, a distinct rotational shading can be observed [see details of $v' = 2 \leftarrow v'' = 0$ and $v' = 4 \leftarrow v'' = 0$ components in Figs. 3(d) and 3(e), respectively]. The presence of $v' \leftarrow v'' = 1$ and $v' \leftarrow v'' = 2$ progressions in the spectrum suggests T_{vib} higher than that reported by Strojecki *et al.* (T_{vib} = 30 K).[8]

TABLE I. The $b^3 0_u^+(4^3P_1)$ and $X^1 0_g^+(4^1S_0)$-state interatomic potential parameters in Zn_2.

	$b^3 0_u^+(4^3P_1)$	$X^1 0_g^+(4^1S_0)$
ω_e (cm^{-1})	20.3 ± 0.1[a] 20.6 ± 0.1[b]	25.90 ± 0.45[b]
$\omega_e x_e$ (cm^{-1})	0.557 ± 0.020[a] 0.58 ± 0.01[b]	0.69 ± 0.03[b]
D_e (cm^{-1})	185.0 ± 0.5[a] 182.6 ± 0.5[b]	242 ± 1[b]
R_e (Å)	4.58 ± 0.01[b]	4.19 ± 0.01[b]

[a]This work.
[b]Strojecki *et al.*[8]

IV. CONCLUSIONS

The high-temperature source-module of the supersonic molecular beam for aggressive elements was designed and constructed. Its operation was tested in the experiment with detection and analysis of the $b^3 0_u^+(4^3P_1) \leftarrow X^1 0_g^+(4^1S_0)$ transition in Zn_2. The occurrence of spectroscopic components originating from $v'' = 1, 2$ suggests a relatively high T_{vib} vibrational temperature of Zn_2 molecules in the beam (approximately 150 K). As compared to other source-modules that had been used to produce supersonic molecular beams containing zinc,[6–9] two innovative solutions were introduced: graphite as a material for metal reservoir (crucible) and a nozzle cap with an orifice, as well as a new carrier-gas distribution system inside the source module that can be applied for source modules containing a crucible made of nonweldable materials.

ACKNOWLEDGMENTS

This project was financed by the National Science Centre Poland under Contract No. UMO-2015/17/B/ST4/04016. The authors appreciate the expertise of MeasLine.

REFERENCES

[1]J. Koperski, Phys. Rep. **369**, 177 (2002), and references therein.
[2]T. G. Dietz, M. A. Duncan, D. E. Powers, and R. E. Smalley, J. Chem. Phys. **74**, 6511 (1981).
[3]C. Tao and P. J. Dagdigian, J. Chem. Phys. **118**, 1242 (2003).
[4]M. Krośnicki, M. Strojecki, T. Urbańczyk, A. Pashov, and J. Koperski, Phys. Rep. **591**, 1 (2015), and references therein.
[5]T. Urbańczyk, M. Strojecki, M. Krośnicki, A. Kędziorski, P. S. Żuchowski, and J. Koperski, Int. Rev. Phys. Chem. **36**, 541 (2017), and references therein.
[6]J. Koperski and M. Czajkowski, Phys. Rev. A **62**, 012505 (2000).

[7]M. Strojecki, M. Krośnicki, and J. Koperski, Chem. Phys. Lett. **465**, 25 (2008).
[8]M. Strojecki, M. Ruszczak, M. Krośnicki, M. Łukomski, and J. Koperski, Chem. Phys. **327**, 229 (2006).
[9]J. Koperski and M. Czajkowski, J. Mol. Spectrosc. **212**, 162 (2002).
[10]I. Wallace, R. R. Bennett, and W. H. Breckenridge, Chem. Phys. Lett. **153**, 127 (1988).
[11]I. Wallace, J. Ryter, and W. H. Breckenridge, J. Chem. Phys. **96**, 136 (1992).
[12]J. G. McCaffrey, D. Bellert, A. W. K. Leung, and W. H. Breckenridge, Chem. Phys. Lett. **302**, 113 (1999).
[13]I. Wallace, J. G. Kaup, and W. H. Breckenridge, J. Phys. Chem. **95**, 8060 (2005).
[14]J. Abrahamson, Carbon **12**, 111 (1974).
[15]P. Hidnert and W. T. Sweeney, Technol. Pap. Bur. Stand. **21**, 223 (1927).
[16]I. L. Shabalin, *Ultra-High Temperature Materials I: Carbon (Graphene/Graphite) and Refractory Metals* (Springer, Dordrecht, 2014).
[17]Engineering ToolBox, Thermal conductivity of common materials and gases, 2003, available at https://www.engineeringtoolbox.com/thermal-conductivity-d_429.html; accessed 19 October 2019.
[18]Y. T. Lee, J. D. McDonald, P. R. LeBreton, and D. R. Herschbach, Rev. Sci. Instrum. **40**, 1402 (1969).
[19]J. J. Valentini, M. J. Coggiola, and Y. T. Lee, Rev. Sci. Instrum. **48**, 58 (1977).
[20]L. Holmlid and A. Sigurdsson, J. Appl. Phys. **57**, 1102 (1985).
[21]Y. A. Folz, J. S. Hickmann, L. F. M. Braun, and R. E. Francke, J. Vac. Sci. Technol. A **8**, 151 (1990).
[22]E. te Sligte, R. C. M. Bosch, B. Smeets, P. van der Straten, H. C. W. Beijerinck, and K. A. H. van Leeuwen, Proc. Natl. Acad. Sci. U. S. A. **99**(Suppl. 2), 6509 (2002).
[23]R. Georges, J. Thiévin, A. Benidar, S. Carles, B. Amyay, M. Louviot, V. Boudon, and J. Vander Auwera, Rev. Sci. Instrum. **90**, 093103 (2019).
[24]U. Even, Adv. Chem. **2014**, 636042-1–636042-11.
[25]See https://www.iap.tuwien.ac.at/www/surface/vapor_pressure to see Zn in T = 1000 K; accessed 4 September 2019.
[26]R. T. Birge and H. Sponer, Phys. Rev. **28**, 259 (1926).
[27]R. J. Le Roy, J. Quant. Spectrosc. Radiat. Transfer **186**, 167 (2017).
[28]C. M. Western, J. Quant. Spectrosc. Radiat. Transfer **186**, 221 (2017).

Journal of Molecular Structure 1222 (2020) 128840

Contents lists available at ScienceDirect

Journal of Molecular Structure

journal homepage: http://www.elsevier.com/locate/molstruc

Bound→free and bound→bound multichannel emission spectra from selectively excited Rydberg states in the ZnAr and CdAr van der Waals complexes

J. Dudek [a, *], A. Kędziorski [b], J.P. Zobel [c], M. Krośnicki [d], T. Urbańczyk [a], K. Puczka [a], J. Koperski [a]

[a] Smoluchowski Institute of Physics, Faculty of Physics, Astronomy and Applied Computer Science, Jagiellonian University, Łojasiewicza 11, 30-348, Kraków, Poland
[b] Institute of Physics, Faculty of Physics, Astronomy and Informatics, Nicolaus Copernicus University, Grudziądzka 5/7, 87-100, Toruń, Poland
[c] Institute of Theoretical Chemistry, Faculty of Chemistry, University of Vienna, Währinger Straße 17, A-1090, Vienna, Austria
[d] Institute of Theoretical Physics and Astrophysics, Faculty of Mathematics, Physics and Informatics, University of Gdansk, Wita Stwosza 57, 80-308, Gdańsk, Poland

ARTICLE INFO

Article history:
Received 3 March 2020
Received in revised form
2 June 2020
Accepted 5 July 2020
Available online 15 July 2020

Keywords:
Potential energy curve
Ab initio potential
Fluorescence spectrum
Emission spectrum
van der Waals molecule
Diatomic molecule

ABSTRACT

Multichannel dispersed emission spectra originated upon a selective excitation of Rydberg electronic energy states in the ZnAr and CdAr van der Waals (vdW) complexes are simulated and analysed as a proof-of-concept of the future experimental approach. Simulations of the emission spectra are based on *ab-initio* calculated interatomic potentials and transition dipole moments (TDMs), that for ZnAr were newly calculated. Experimental set-up that is under construction along with the experimental procedure are discussed.

1. Introduction

Bound→free and bound→bound laser induced fluorescence (LIF) emission (also called fluorescence) spectra emitted after a selective excitation of Rydberg states of diatomic van der Waals (vdW) complexes are a source of information, mainly on repulsive part, but also on potential well of the lower-lying electronic state potentials that are not accessible in the excitation from the ground state. Modelling of the dispersed emission spectra provides a direct information on the steepness of the short-range branch of the potential at which the emission terminates – information that is hard to access from LIF excitation spectra.

The selective excitation to the Rydberg states can be realized using different methods. If the transition from the ground to the Rydberg state is allowed, a direct excitation can be implemented. This way, for complexes such as *e.g.*, the Rg_2 (Rg = rare gas atom), pulsed synchrotron radiation has been used to perform a state-selective excitation of the Ar_2, Kr_2 and Xe_2 complexes to their $30_u^+(^3P_1)$ or $31_u(^3P_1)$ lower-lying excited states at 106.8–108.8 nm, 124–126.5 nm and 148–151.5 nm wavelength ranges, respectively [1]. Following the excitation, oscillatory bound→free continua, also called Condon internal diffraction (CID) patterns [2], were observed using time-resolved emission in 130–180 nm, 150–200 nm and 175–230 nm spectral ranges, respectively.

Beside high-energy UV synchrotron radiation beam, a more convenient method for exciting molecular Rydberg states is optical-optical double resonance (OODR) method that simply uses two laser beams, both in the VIS and/or UV range. Also, OODR allows to excite a molecule to the electronic energy states to which transitions from the ground state are forbidden as well as using different intermediate electronic states to access and probe different parts of the ro-vibrational energy structure in the final Rydberg-state

* Corresponding author.
E-mail address: joanna.b.dudek@doctoral.uj.edu.pl (J. Dudek).

https://doi.org/10.1016/j.molstruc.2020.128840
0022-2860/

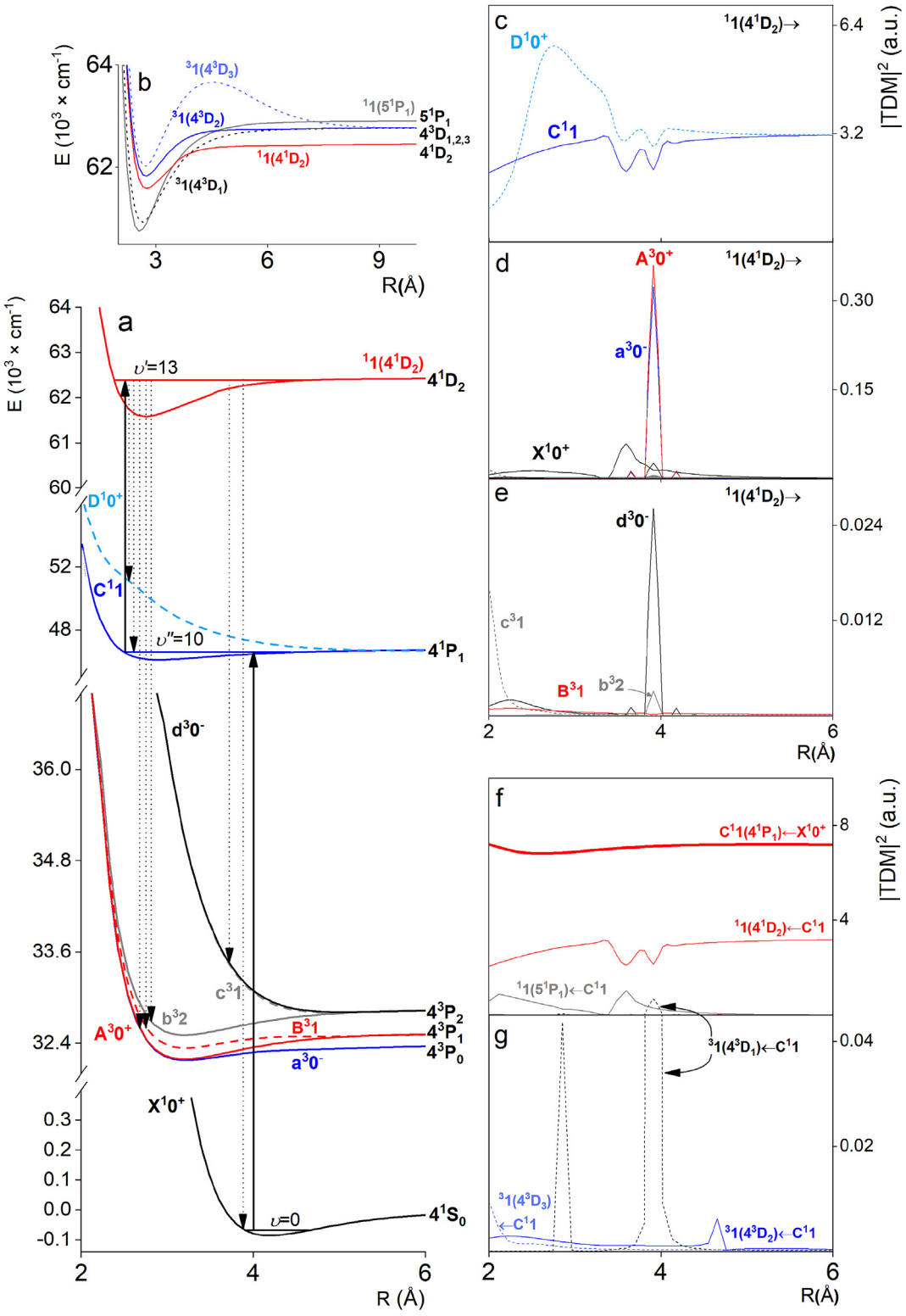

Fig. 1. (a) *Ab initio* interatomic potentials for electronic states of the ZnAr used in simulation of multichannel emission from the $^1 1\left(4^1D_2\right)$, $\upsilon' = 13$. The $^1 1\left(4^1D_2\right), \upsilon' = 13 \leftarrow C^1 1, \upsilon'' = 10 \leftarrow X^1 0^+, \upsilon = 0$ excitation in OODR process is depicted with vertical solid arrows whereas allowed emission channels are shown with vertical dashed arrows. (b) *Ab initio* interatomic potentials intersecting with the $^1 1\left(4^1D_2\right)$ emitting state (only these with $\Omega = 1$ are shown). (c), (d), (e) Values of $|TDM|^2$ for an emission from the $^1 1\left(4^1D_2\right)$ state to the states correlating with the 4^1P_1, 4^3P_J, and 4^1S_0 atomic asymptotes. (f), (g) Values of $|TDM|^2$ for the $C^1 1\left(4^1P_1\right) \leftarrow X^1 0^+\left(4^1S_0\right)$ excitation (thick solid line) and the excitation from the $C^1 1$ (thin solid and dotted lines) to several Rydberg states in ZnAr.

potential. Employing OODR, a number of Rydberg electronic states in the MRg (M = Cd, Hg) heteroatomic complexes has been reached, among them, as first, the $C^3 1(7^3S_1)$ double-well Rydberg state in the HgAr that was excited *via* the $A^3 0^+(6^3P_1)$ or $B^3 1(6^3P_1)$ intermediate states [3,4], and studied recording LIF excitation spectra. The same intermediates were used to excite to and record excitation spectra from the triplet Rydberg series of the $^3\Sigma^+(n^3S_1,\ n = 7-10)$ states in HgNe [5,6], the $^3\Sigma^+\left(8^3S_1\right)$ Rydberg state in HgAr [6] and the singlet Rydberg series of the $1\Sigma^+(n^1S_0,\ n = 7-9)$ states in HgNe [7].

As far as the CdRg (Rg = Ne, Ar, Kr) complexes are concerned, OODR *via* the lower-lying $A^3 0^+(5^3P_1)$ and $B^3 1(5^3P_1)$ intermediates was employed to investigate a complex double-well structure of the $E^3 1(6^3S_1)$ Rydberg state in CdNe [8], CdAr [9–15] and CdKr [12,14,16,17] using LIF excitation spectra.

Regarding the ZnRg complexes, only the $E^3\Sigma^+(5^3S_1)$ state in ZnAr has been investigated, however, using excitation *via* vaporization-optical (VO) method [18]. In general, VO relies on utilizing a vaporization laser pulse in the first-step of the excitation. It produces a number of atoms in long-lived metastable intermediate states. Characterisation of the $E^3\Sigma^+$ state has been performed using LIF excitation spectra recorded using the second-step $E^3\Sigma^+ \leftarrow a^3\Pi_{0^-}\left(4^3P_0\right)$, $b^3\Pi_2(4^3P_2)$ transitions.

As concerns the M_2 (M = Zn, Cd, Hg) homoatomic complexes, by employing OODR it was possible for the first time to excite a *gerade* Rydberg state in Cd_2 *via* the $b^3 0_u^+(5^3P_1)$ intermediate and record a pronounced $v' \leftarrow v'' = 0, 3$ progressions showing their isotopologue structure [19].

It has to be emphasized however, that in any of the above Rydberg-state studies emission spectra in MRg complexes have not been observed, except one investigation. For the HgAr, Duval et al. [4] recorded dispersed emission bound→bound spectra using the $C^3 1(7^3S_1), v' = 3 \rightarrow A^3 0^+(6^3P_1), v''$, $C^3 1, v' = 14, 19 \rightarrow a^3 0^-(6^3P_0), v''$ and $C^3 1, v' = 2, 4, 14 \rightarrow b^3 2\left(6^3P_2\right)$, $c^3 1\left(6^3P_2\right)$, $d^3 0^-\left(6^3P_2\right), v''$ transitions, as well as long bound→free undulated CID *reflection* [20] patterns using the $C^3 1$, $v' = 3, 11 \rightarrow a^3 0^-$, $C^3 1, v' = 2, 10 \rightarrow A^3 0^+$, $B^3 1$ and $C^3 1, v' = 3, 14 \rightarrow b^3 2$, $c^3 1$, $d^3 0^-$ transitions; it allowed to probe and determine lower-lying state potentials including their repulsive branches.

In this article, we propose a scheme for excitation of the ZnAr complex to the $^1 1(4^1D_2)$ Rydberg state *via* the $C^1 1(4^1P_1)$ intermediate using OODR and detection of a dispersed emission from the $^1 1(4^1D_2)$ state to the lower-lying electronic states (see Fig. 1a). The goal is to analyse the $^1 1\left(4^1D_2\right) \rightarrow a^3 0^-\left(4^3P_0\right)$, $A^3 0^+\left(4^3P_1\right)$, $B^3 1\left(4^3P_1\right)$, $b^3 2\left(4^3P_2\right)$, $c^3 1\left(4^3P_2\right)$, $d^3 0^-\left(4^3P_2\right)$, $C^1 1\left(4^1P_1\right)$, $D^1 0^+\left(4^1P_1\right)$ emission channels taking into account newly calculated *ab initio* ZnAr interatomic potentials and transition dipole moments (TDMs) for transitions between the emitting and lower electronic energy states.

Along with the analysis for the ZnAr, we present also a similar consideration for detection of dispersed emission spectra in the CdAr complex after a selective excitation of the $E^3 1(6^3S_1)$ Rydberg state (see Fig. 2). The analysis is based on *ab-initio* calculated interatomic potentials obtained in our laboratory and recently published by Krośnicki et al. [21].

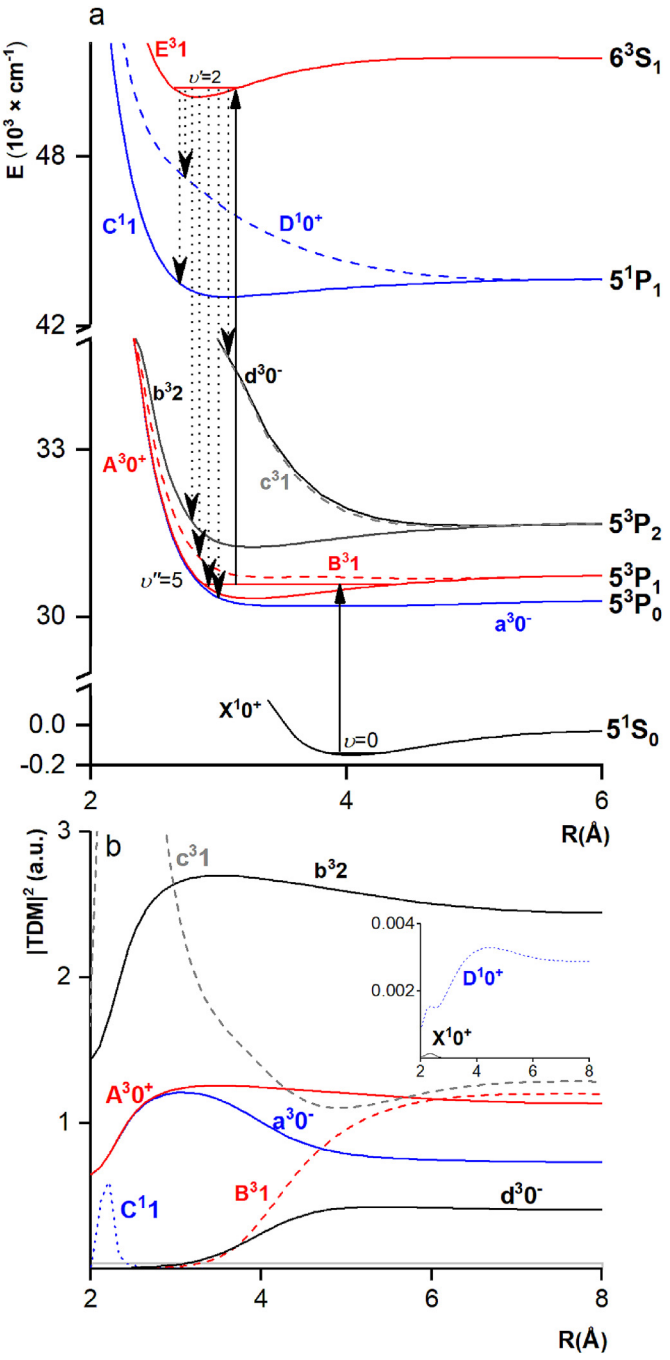

Fig. 2. (a) *Ab initio* interatomic potentials for electronic states of the CdAr [21] used in simulation of multichannel emission from the $E^3 1\left(6^3S_1\right), v' = 2$. The $E^3 1, v' = 2 \leftarrow A^3 0^+\left(5^3P_1\right), v'' = 5 \leftarrow X^1 0^+\left(5^1S_0\right), v = 0$ excitation in OODR process is depicted with vertical solid arrows whereas allowed emission channels are shown with vertical dashed arrows. (b) Values of $|TDM|^2$ for emission from the $E^3 1$ state to the states correlating with the 5^1P_1, 5^3P_J and 5^1S_0 atomic asymptotes. Inset shows two smallest $|TDM|^2$.

2. *Ab initio* calculations

Ab initio potentials of electronic states of ZnAr complex up to Zn 6^1S_0 asymptote have been calculated within three-step approach. Firstly, the state-average complete active space self-consistent field method has been applied (SA-CASSCF) [22,23] for the active space, in which two electrons are distributed on the molecular orbitals of

the predominant Zn 4s, 4p, 4d, 5s, 5p, 6s character. Calculations were performed in C_{2v} symmetry. State averaging was performed over the following sets of states: seven states of $^1A_1$ symmetry, six of $^3A_1$, three of $^1B_1$ $^3B_1$ $^1B_2$, $^3B_2$ and one of $^1A_2$ and $^3A_2$ symmetries.

Secondly, the multi-state second-order CAS perturbation theory method (MS-CASPT2) has been used [24]. Finally, the spin-orbit interaction has been taken into account by means of restricted active space state interaction method (RASSI-SO) [25]. Scalar relativistic effects have been accounted for within Douglas-Kroll-Hess second-order Hamiltonian [26,27]. We used new ANO-type (ANO = atomic natural orbitals) basis for Zn atom within general contraction scheme (23s17p12d6f4g2h)/[11s9p7d4f2g], which is modified and extended Zn basis from Ref. [28]; discussion on the construction of new Zn ANO basis set can be found in Supporting Information of Ref. [29]. For Ar, we used (17s12p5d4f2g)/[8s7p5d4f2g] ANO basis set [30]. Additionally, we used mid-bond basis applying (8s4p3d1f)/[6s4p3d1f] Hydrogen ANO basis [31]. *Ab initio* calculations of ZnAr were performed for the following grid of points of internuclear distances (in bohr): range 3.4–9.6 with step 0.2; 9.6–24.0 with step 0.4; 24–30 with step 1; 30–40 with step 2; 40–60 with step 4; 60–100 with step 10. Details of new Zn basis and of the computational aspects are presented elsewhere [29,32]. TDMs have been calculated within SA-CASSCF/MS-CASPT2/RASSI-SO approach, where the initial and final states are the linear combinations of the SA-CASSCF states. All the calculations were performed with Molcas 8.2 [33].

Details of *ab initio* calculations of electronic states and TDMs of CdAr complex are presented in Ref. [21].

3. Experiment – a prospective set-up

There are two experimental methods devoted to detection of LIF dispersed emission spectra with the use of: i) a tuneable monochromator in front of a photocathode of a photomultiplier tube (PMT) - the method which is limited by a considerable time consumption during the experiment, especially when a large spectral range is scanned over (see *e.g.* Ref. [36]), or ii) a spectrometer fitted with an iCCD camera (see *e.g.* Refs. [37]) - the method in which the whole spectrum is recorded at once without a necessity of executing the time-consuming scans.

Fig. 3 presents experimental set-up for excitation of the ZnAr to the selected Rydberg state using OODR method, followed by detection of a dispersed emission that occurs to the lower-lying electronic energy states. Description of a continuously operating source-module of a molecular beam containing zinc and description of a molecular single excitation were included elsewhere [34]. Both crucible and cap with the source nozzle are made of graphite that is chemically resistant to numerous melted aggressive metals and metal vapours. ZnAr complexes in the beam are excited by UV laser radiation produced by a pulsed dye laser (TDL90, Quantel) pumped with a Nd^+:YAG laser (YG981C, Quantel). To perform OODR excitation, a second dye laser (TDL90, Quantel) pumped with another Nd^+:YAG laser (Powerlite 7010, Continuum) is employed. Total LIF emission from the first and the second excitation-step is controlled by two photomultipliers (R375, Hamamatsu and 9893QB/350, Electron Tubes) and recorded with a digital oscilloscope (TDS 2024B, Tektronix). Emission from the Rydberg state is focused on the entrance slit of an echelle spectrometer (ME5000, Andor), dispersed with a spectral resolution $\frac{\lambda}{\Delta\lambda} = 5000$ and operating wavelength range 200–975 nm, and detected by iCCD camera (334T, iStar). The lasers, oscilloscope and camera are triggered by a

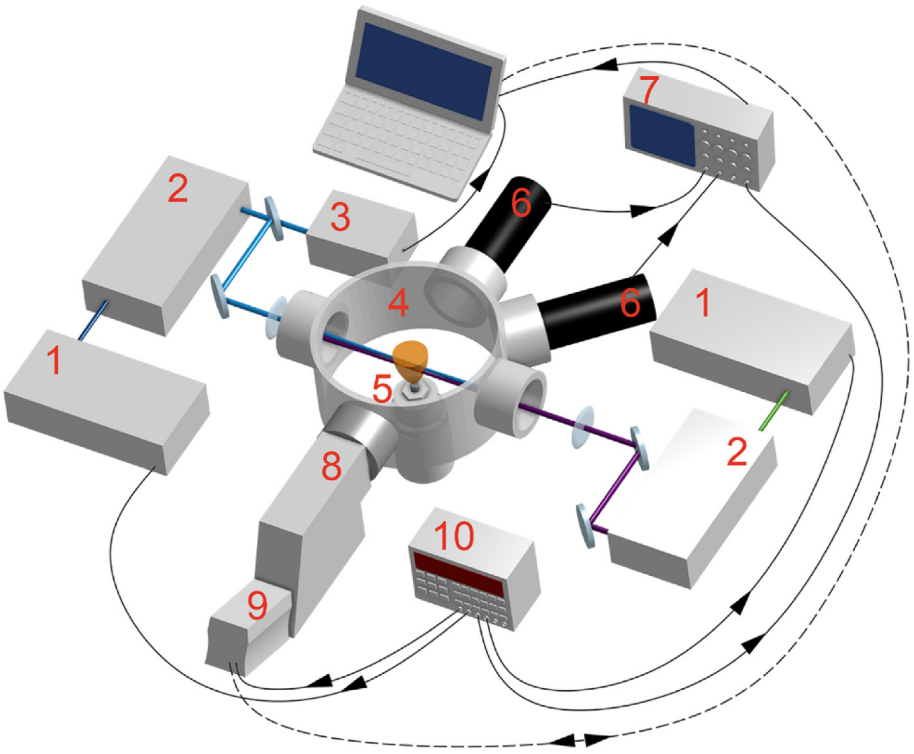

Fig. 3. Scheme of experimental set-up for excitation of the ZnAr complexes to the $^1 1\left(4^1D_2\right)$ Rydberg state using OODR method followed by detection of a dispersed emission to lower-lying electronic energy states (under construction in our laboratory). 1 - Pulsed Nd^+:YAG lasers, 2 - dye lasers, 3 - wavemeter, 4. - vacuum chamber, 5 - continuously operating source-module of the molecular beam, 6 – photomultipliers, 7- oscilloscope, 8 - spectrometer, 9 - iCCD camera, 10 - digital delay generator.

digital delay generator (DDG) (DG645, Stanford Research Systems).

The experimental set-up for excitation of vdW complexes containing cadmium atoms using OODR method was used in our previous studies [14]. In the experiment, a molecular beam was produced with high-temperature, high-pressure pulsed molecular beam-module [35]. For the CdAr, as in the case of the ZnAr, spectrometer fitted with iCCD camera triggered with DDG is planned to be installed to record emission from the Rydberg state.

4. Results

For both ZnAr and CdAr complexes, LEVEL Fortran code [38] for vibrational spectra, and PGOPHER [39] for rotational spectra, were used to simulate all bound↔bound transitions in OODR excitations and subsequent emissions. To simulate bound→free CID patterns in emission, BCONT program [40] was used. The initial states (the $^1 1(4^1D_2)$ and $E^3 1(6^3S_1)$ in ZnAr and CdAr, respectively) from which emission was originated were selected to assure the allowed emission channels. Indeed, the projection of the total electronic angular momentum represented by Ω quantum number (Hund's case c) equals 1 for both the $^1 1(4^1D_2)$ and $E^3 1(6^3S_1)$ emitting states, and thus transitions to the lower-lying states with Ω = 0,1 and 2 are allowed.

4.1. ZnAr

Analysis of $|TDM(R)|^2$ functions for the excitation from the ground $X^1 0^+$, $v = 0$ reveals that the excitation to the $C^1 1(4^1P_1)$ state can be chosen for being the intermediate step in OODR. Experimental spectrum of the $C^1 1, v'' \leftarrow X^1 0^+, v = 0$ transition [41,42] reveals the $v'' = 10 \leftarrow v = 0$ as the most intensive vibrational

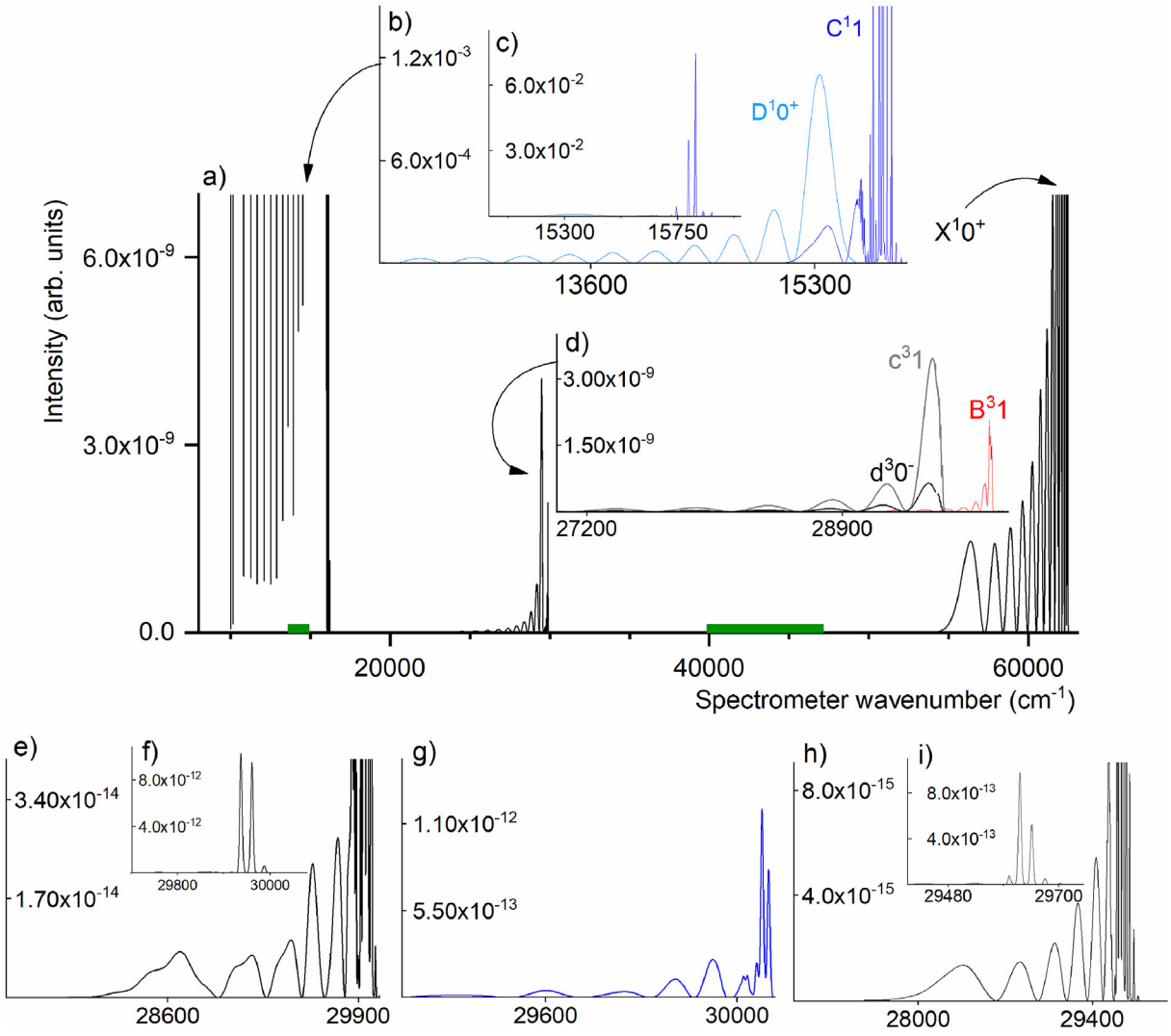

Fig. 4. a) Simulation [38–40] of multichannel bound→bound and bound→free transitions in emission from the $^1 1(4^1D_2), v' = 13$ in ZnAr to the electronic states correlating with the 4^1P_1, 4^3P_J and 4^1S_0 atomic asymptotes. Bound→bound transitions include both vibrational and rotational components, Gaussian convolution (FWHM) corresponds to the spectrometer resolution, *i.e.* $\frac{\lambda}{\Delta\lambda} = 5000$. Two green bars on the energy axis in part a) show a location of the expected emission spectrum from the $C^1 1, v' = 10$ intermediate level which is used in OODR excitation (based on [43] and simulation). Arrows depict contributions to the total emission spectrum originating from single-channel emissions shown in insets. b) Bound→free emission channels to the $C^1 1$ (dark blue) and $D^1 0^+$(light blue) states. c) Single bound→bound emission channel to the $C^1 1$ state. d) Both bound→bound and bound→free emission channels to the $d^3 0^-$ (black), $c^3 1$ (gray) and $B^3 1$ (red) states. The lowest-intensity spectra are shown below. e) Bound→free and f) bound→bound emission channel to the $A^3 0^-$. g) Bound→bound and bound→free emission channel to the $a^3 0^-$ state. h) Bound→free and i) bound→ bound emission channels to the $b^3 2$ state.

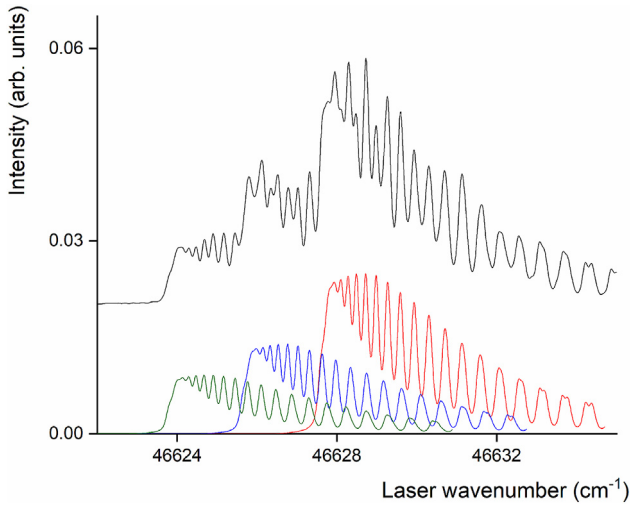

Fig. 5. Simulation [38,39] of the $C^1 1(4^1P_1), v" = 10 \leftarrow X^1 0^+, v = 0$ vibrational transition in the excitation spectrum of ZnAr where rotational profiles of three most abundant isotopologues: $^{64}Zn^{40}Ar$ (red line), $^{66}Zn^{40}Ar$ (blue line), $^{68}Zn^{40}Ar$ (green line) along with the resulting profile (black line) are revealed. The simulation was performed using PGOPHER [39] with parameters: T_{rot} = 10 K and 0.1 cm^{-1} (FWHM) Gaussian convolution.

transition. Therefore, the $C^1 1, v" = 10$ was chosen for first-step excitation in OODR. In the previous realization of the $C^1 1 \leftarrow X^1 0^+$ excitation [41], frequency-doubled output of a dye laser working with Stilbene 3 dye was used, but a frequency-tripling with DCM dye can be applied as well. Due to wide-separation of the isotopologue components in the $v" = 10 \leftarrow v = 0$ transition (Fig. 5), an isotopologue-selective OODR [14] is possible to apply. Thus, the $^1 1(4^1D_2) \leftarrow C^1 1, v" = 10$ can be realized mostly for the $^{64}Zn^{40}Ar$ isotopologue.

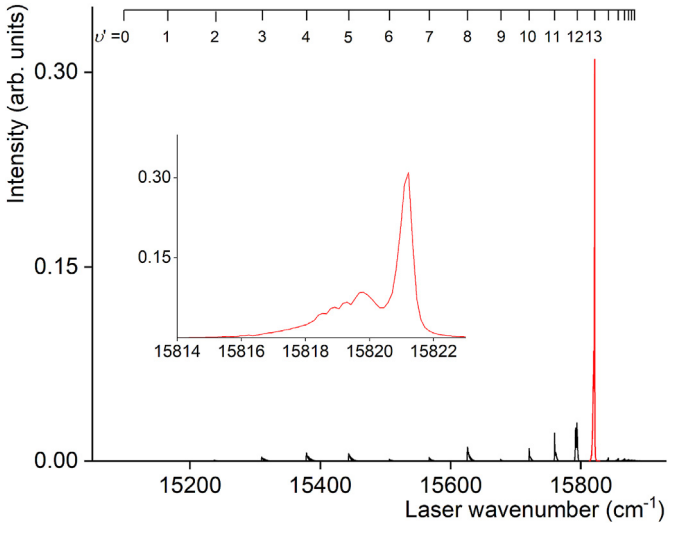

Fig. 6. Simulation of the $^1 1(4^1D_2), v' \leftarrow C^1 1(4^1P_1), v" = 10$ transition in excitation spectrum of ZnAr that is planned for realization of OODR scheme. The simulation was performed for the $^{64}Zn^{40}Ar$ isotopologue, with parameters: T_{rot} = 10 K and 0.2 cm^{-1} (FWHM) Gaussian convolution. Inset shows the spectrum of the $v' = 13 \leftarrow v" = 10$ transition with partly resolved rotational structure.

For the final state in OODR, the $^1 1(4^1D_2)$ electronic state was chosen not only to assure all transition channels in the subsequent emission to be allowed, but also to assure the excitation frequencies from dye lasers available in our lab. Realization of the $^1 1(4^1D_2), v' \leftarrow C^1 1, v" = 10$ transition requires frequencies in the range of 15,200–15,850 cm^{-1} (it is ensured by using *e.g.*, DCM dye pumped with a second harmonic of Nd^+:YAG laser). Although several intersecting potentials with $\Omega = 1$ are accessible in the energy region: $^1 1(4^1D_2)$, $^3 1(4^3D_1)$, $^3 1(4^3D_2)$, $^3 1(4^3D_3)$ and $^1 1(5^1P_1)$ (see Fig. 1b), the $^1 1(4^1D_2) \leftarrow C^1 1(4^1P_1), v" = 10$ transition has the highest intensity. It is due to the high value of $|TDM|^2$ (see Fig. 1f) and the same multiplicity of the initial and final states. Simulation of the $^1 1(4^1D_2), v' \leftarrow C^1 1, v" = 10$ for the $^{64}Zn^{40}Ar$ isotopologue (Fig. 6) includes rotational transitions with the rotational temperature T_{rot}=10 K and Gaussian convolution FWHM = 0.2 cm^{-1}, that are typical values for excitation experiments realized in our laboratory. The strongest $v' = 13$ vibrational component was chosen to simulate emission from.

In the emission from the $^1 1(4^1D_2), v' = 13$, parameters used in the simulation of bound→bound transitions correspond to the conditions that are most likely to be realized in the planned experiment, *i.e.* rotational temperature T_{rot} = 10 K and spectral broadening of bound → bound components that corresponds to the spectrometer resolution ($\frac{\lambda}{\Delta\lambda} = 5000$).

The total multichannel emission (bound→free along with bound→bound transitions) from the $^1 1(4^1D_2), v' = 13$ (see Fig. 4 and Table 1) encompasses three main energy regions: (i) 10,000-15,900 cm^{-1} where relatively intensive emission to the states correlating with the 4^1P_1 atomic asymptote is expected; (ii) 27,100-30,000 cm^{-1} with much weaker spin-forbidden emission to triplet states correlating with the 4^3P_J asymptotes; (iii) emission to the ground $X^1 0^+$ state that is beyond of the range of the spectrometer (see Sec. 3).

According to the simulation (Fig. 4 and Table 1), there is a possibility of detection of strong bound→free emission to the $D^1 0^+(4^1P_1)$ state which within the 12,100-15,100 cm^{-1} energy range is not influenced by other emission channels. Only the first maximum within the 15,100-15,600 cm^{-1} overlaps with residual bound→free emission from the $^1 1(4^1D_2), v' = 13$ emitting state.

Bound→free transitions to the $c^3 1(4^3P_2)$ and $d^3 0^-(4^3P_2)$ states overlap in the energy region 29,600-32,300 cm^{-1}. A higher value of $|TDM|^2$ for the $^1 1(4^1D_2) \rightarrow c^3 1$ transition below R = 3 Å results in a considerably higher intensity of the emission to the $c^3 1$ state.

Within the 29,600-29,900 cm^{-1} range, a combination of bound→bound and bound→free transitions to the $a^3 0^-(4^3P_0)$, $A^3 0^+(4^3P_1)$ and $B^3 1(4^3P_1)$ states is located, with a significant

Table 1
Energy range and fraction of integrated fluorescence of all simulated emission channels originating from the $^1 1(4^1D_2), v' = 13$ state in ZnAr molecule. Only the simulated emission channels were included in the integration of total fluorescence.

Final state	Energy range (cm^{-1})	Fraction of integrated fluorescence
$X^1 0^+$	62,507–54,685	$2.12\ 10^{-5}$
$A^1 0^+$	30,170–27,950	$1.44 \cdot 10^{-10}$
$B^3 1$	30,028–27,775	$7.67 \cdot 10^{-8}$
$C^1 1$	16,269–15,078	$6.23 \cdot 10^{-1}$
$D^1 0^+$	15,628–10,000	$3.76 \cdot 10^{-1}$
$a^3 0^+$	30,190–27,589	$4.70 \cdot 10^{-11}$
$b^3 2$	29,855–27,940	$1.26 \cdot 10^{-11}$
$c^3 1$	29,688–21,881	$6.30 \cdot 10^{-7}$
$d^3 0^-$	29,685–17,839	$1.38 \cdot 10^{-7}$

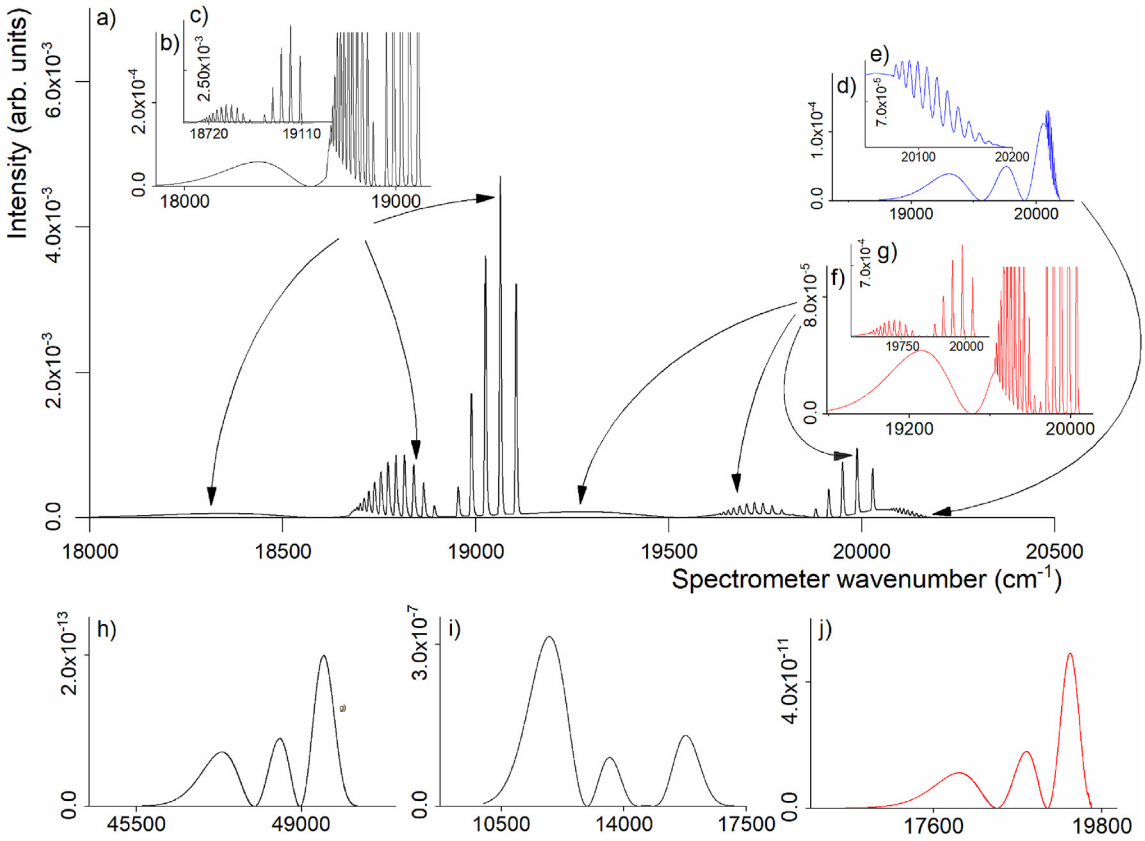

Fig. 7. a) Simulation [38–40] of multichannel bound→bound and bound→free transitions in emission from the $E^3 1(6^3S_1), \upsilon' = 2$ in CdAr to the electronic states correlating with the 5^3P_J and 5^1S_0 atomic asymptotes. Bound→bound transitions include vibrational and rotational components, Gaussian convolution (FWHM) corresponds to the spectrometer resolution, *i.e.* $\frac{\lambda}{\Delta\lambda} = 5000$. Arrows depict contributions to the total emission spectrum originating from single-channel emissions shown in insets. b) Bound→free and c) bound→bound single emission channels to the $b^3 2$ state. d) Bound→bound and bound→free, and e) zoom in of the bound→bound single emission channel to the $a^3 0^-$ state. f) Bound→bound and bound→free, and g) zoom in of the bound→bound emission to the $A^3 0^-$ state. The lowest-intensity spectra are shown below: bound→free transitions to the h) $X^1 0^+$, i) $c^3 1$ and j) $B^3 0^+$ states.

domination of these to the $B^3 1$ state. Although resolution of the spectrometer is too low to resolve the bound→bound $^1 1(4^1D_2)$→$B^3 1$ emission spectrum (below 1 cm^{-1} is required), the bound→-free continuum could be detectable.

It has to be noted, that the emission from the intermediate $C^1 1$, $\upsilon' = 10$ used in OODR to the states correlating with the 4^3P_J atomic asymptotes occurs within the 13,500-14,000 cm^{-1} range, so, it could overlap with the bound→free $^1 1(4^1D_2), \upsilon' = 13 \rightarrow D^1 0^+$ transition. However, change of the multiplicity in former transitions suppress the intensity of their spectra. According to Koperski and Czajkowski [43], strong $C^1 1, \upsilon'' = 10 \rightarrow X^1 0^+$ emission occurs within the 39,900-47,000 cm^{-1} range, therefore, does not overlap with any emission channels from the $^1 1(4^1D_2)$ (see green bar in Fig. 4).

Estimated number of photons originating from the emission occurring from the $^1 1(4^1D_2), \upsilon' = 13$ per one laser pulse is equal to 5.08 x 10^8 which corresponds to 3.67 x 10^6 photons focused on a slit of the spectrometer [44]. The estimations were performed based on simplified model of equilibrium constant of formation of ZnAr molecules [45] and Einstein coefficients calculated by LEVEL [38].

4.2. CdAr

In case of the CdAr, excitation from the ground to the double-well $E^3 1(6^3S_1)$Rydberg state using OODR scheme, through $\upsilon'' = 5$ level in the $A^3 0^+(5^3P_1)$ intermediate state, has been recently recorded and re-analysed [15]. To simulate emission from the $E^3 1$ state, $\upsilon' = 2$, situated near the bottom of the $E^3 1$-state inner well, was chosen as the $E^3 1, \upsilon' = 2 \leftarrow A^3 0^+, \upsilon'' = 5$ transition possess a relatively large intensity. It also allowed to avoid an influence of the $E^3 1$-state outer-well vibrational levels on those in the inner-well as far as calculation of their wave functions and energies was

Table 2
Energy range and fraction of integrated fluorescence of all simulated emission channels from the $E^3 1\left(6^3S_1\right), \upsilon' = 2$ state in CdAr molecule. Only the simulated emission channels were included in the integration of total fluorescence.

Final state	Energy range (cm^{-1})	Fraction of integrated fluorescence
$X^1 0^+$	50,609–45,172	$9.52 \cdot 10^{-10}$
$A^1 0^+$	20,082–18,450	$1.80 \cdot 10^{-1}$
$B^3 1$	19,820–16,365	$1.21 \cdot 10^{-7}$
$a^3 0^+$	20,283–18,600	$1.65 \cdot 10^{-1}$
$b^3 2$	19,163–17,736	$6.32 \cdot 10^{-1}$
$c^3 1$	18,864–10,000	$2.62 \cdot 10^{-3}$
$d^3 0^-$	18,860–10,053	$2.07 \cdot 10^{-2}$

concerned.

In the emission from the $E^3 1\ v' = 2$ (see Fig. 7), T_{rot} and spectral broadening used in the simulation of bound→bound transitions are the same as in case of the ZnAr analysed above. For the CdAr, the most intense emission spectra extend within the 18,000-20,200 cm^{-1} range (see Table 2). According to the simulation, the most intensive $E^3 1,\ v' = 2 \rightarrow b^3 2(5^3P_2)$, $a^3 0^-(5^3P_0)$ and $A^3 0^+(5^3P_1)$ channels are generally well separated. Only the bound→free transitions in emission to the $a^3 0^-$ and bound→-bound transitions to the $A^3 0^+$ states overlap. Taking into account the experimental determination of the $A^3 0^+$-state potential that was based on the $A^3 0^+, v'' \leftarrow X^1 0^+,\ v = 0$ vibrational structure [15] and that the overlapped transitions represent different character (discrete and continuous), both spectra would be able to separate. However, a particularly valuable observation from the simulation of the emission spectra, that would extend possible characterization of CdAr electronic energy states, is well-resolved vibrational structure in the $b^3 2$ and $a^3 0^-$ states, as their excitation from the ground state is forbidden.

Using the same model applied to ZnAr, the estimated number of CdAr molecules excited to the $E^3 1(6^3S_1), v' = 2$ is estimated to equal $2.33 \cdot 10^9$ that corresponds to $1.63 \cdot 10^7$ photons focused on a slit of the spectrometer [44].

5. Conclusions

Multichannel emission spectra from $v' = 13$ level in the $^1 1(4^1D_2)$ and $v' = 2$ level in the $E^3 1(5^3S_1)$ Rydberg states in ZnAr and CdAr, respectively, were simulated based on *ab-initio* calculated potentials and transition dipole moment (TDM) functions for ZnAr [32] and CdAr [21]. For ZnAr, newly-calculated potentials were used for the first time. An experimental realization of the detection of the emission spectra presently prepared in our laboratory was proposed and discussed. Because an excitation of the $^1 1(4^1D_2)$ Rydberg state in ZnAr has never been reported, OODR excitation *via* the previously reported [41,42] $C^1 1(4^1P_1)$ intermediate was simulated as well.

Simulation of emission spectra from the $^1 1(4^1D_2), v' = 13$ in ZnAr reveals a promising prospect for recording bound→free transitions to the $D^1 0^+(4^1P_1)$, $c^3 1(4^3P_2)$ and $B^3 1(4^3P_1)$ states that would allow determine a shape of short-range repulsive parts of the potentials at which emission terminates, and/or explore potentials of lower-lying electronic states that are not accessible in the excitation from the ground state.

In case of emission from the $E^3 1, v' = 2$ state in CdAr, according to the simulation, bound→bound and bound→free transitions to the $b^3 2(5^3P_2)$, $a^3 0^-(5^3P_0)$ and $A^3 0^+(5^3P_1)$ are well−separated or easy to be separated in detection. It offers prospects for determination of the shape of both repulsive part and the potential well in one experiment.

CRediT authorship contribution statement

J. Dudek: Methodology, Software, Investigation, Formal analysis, Writing - original draft. **A. Kędziorski:** Methodology, Formal analysis, Data curation, Writing - original draft. **J.P. Zobel:** Methodology, Data curation. **M. Krośnicki:** Methodology, Data curation. **T. Urbańczyk:** Software, Validation, Writing - review & editing. **K. Puczka:** Visualization. **J. Koperski:** Conceptualization, Validation, Writing - original draft, Writing - review & editing, Supervision, Project administration.

Declaration of competing interest

The authors declare that they have no known competing financial interests or personal relationships that could have appeared to influence the work reported in this paper.

Acknowledgements

The project was financed by the National Science Centre Poland under Contract No. UMO-2015/17/B/ST4/04016. A partial support from Polish Ministry of Science and Higher Education through grants 7150/E-338/M/2018 and 7150/E-338/M/2019 is acknowledged.

Appendix A. Supplementary data

Supplementary data to this article can be found online at https://doi.org/10.1016/j.molstruc.2020.128840.

References

[1] T. Möller, J. Stapelfeldt, M. Beland, G. Zimmerer, Oscillatory structures in bound-free fluorescence spectra of Xe_2, Kr_2 and Ar_2, Chem. Phys. Lett. 117 (1985) 301−306, https://doi.org/10.1016/0009-2614(85)80225-6.
[2] E.U. Condon, Nuclear motions associated with electron transitions in diatomic molecules, Phys. Rev. 32 (1928) 858−872, https://doi.org/10.1103/PhysRev.32.858.
[3] W.H. Breckenridge, M.C. Duval, C. Jouvet, B. Soep, Laser double-resonance studies of Rydberg states of HgAr, Chem. Phys. Lett. 122 (1985) 181−184, https://doi.org/10.1016/0009-2614(85)80559-5.
[4] M.-C. Duval, O.B. D'Azy, W.H. Breckenridge, C. Jouvet, B. Soep, The structure of several electronic states of the Hg-Ar complex as determined by laser double resonance in a supersonic jet, J. Chem. Phys. 85 (1986) 6324−6334, https://doi.org/10.1063/1.451462.
[5] M. Okuishi, K. Yamanouchi, K. Onda, S. Tsuchiya, Interatomic potential of the HgNe van der Waals complex in the $E(^3\Sigma^+)$ Rydberg state, J. Chem. Phys. 98 (1993) 2675−2681, https://doi.org/10.1063/1.464149.
[6] K. Onda, K. Yamanouchi, M. Okunishi, S. Tsuchiya, Interatomic potentials od triplet s-Rydberg series of HgNe and HgAr van der Waals dimers, J. Chem. Phys. 101 (1994) 7290−7299, https://doi.org/10.1063/1.468286.
[7] K. Onda, K. Yamanouchi, Interatomic potentials of singlet s-Rydberg series of a HgNe van der Waals dimer: evidence for stabilization by superexchange interaction, J. Chem. Phys. 201 (1995) 1129−1140, https://doi.org/10.1063/1.469171.
[8] J. Koperski, M.A. Czajkowski, Spectroscopical characterization of CdNe van der Waals complex in the $E1(^3\Sigma^+)$ Rydberg state, Chem. Phys. Lett. 357 (2002) 119−125, https://doi.org/10.1016/S0009-2614(02)00464-5.
[9] R.R. Bennett, W.H. Breckenridge, Van der Waals bonding in the lowest electronic states of MgAr, ZnAr, CdAr and HgAr: spectroscopic characterization of the $b^3\Pi_2$ and $e^3\Sigma^+$ states of the CdAr molecule, J. Chem. Phys. 96 (1992) 882−890, https://doi.org/10.1063/1.462108.
[10] M. Czajkowski, R. Bobkowski, L. Krause, Pump-and-probe studies of the $E1(6^3S_1) \leftarrow A0^+(5^3P_1)$ excitation spectrum of CdAr in a supersonic beam, Phys. Rev. A 45 (1992) 6451−6458, https://doi.org/10.1103/PhysRevA.45.6451.
[11] J. Koperski, M. Czajkowski, The structure of the lowest electronic Rydberg state of CdAr complex determined by laser double resonance method in a supersonic jet-expansion beam, Spectrochim. Acta 59 (2003) 2435−2448, https://doi.org/10.1016/S1386-1425(02)00396-7.
[12] T. Urbańczyk, M. Strojecki, J. Koperski, Structure of vibrational bands of the $E^3\Sigma^+(6^3S_1) \leftarrow A^3\Pi_{0+}(5^3P_1)$, $B^3\Sigma_1^+(5^3P_1)$ transitions in CdAr and CdKr studied by optical-optical double resonance method, Chem. Phys. Lett. 503 (2011) 18−24, https://doi.org/10.1016/j.cplett.2010.12.085.
[13] T. Urbańczyk, J. Koperski, The $E^3\Sigma^+(6^3S_1)$-state interatomic potential of CdAr in the long range region revisited: a new method for bond length adjustment, Chem. Phys. Lett. 640 (2015) 82−86, https://doi.org/10.1016/j.cplett.2015.10.013.
[14] T. Urbańczyk, J. Dudek, J. Koperski, Isotopologue-selective excitation studied *via* optical-optical double resonance using the $E^3\Sigma_1^+(6^3S_1) \leftarrow A^3\Pi_{0+}(5^3P_1) \leftarrow X^1\Sigma_{0+}(5^1S_0)$ transitions in CdAr and CdKr van der Waals complexes, J. Quant. Spectrosc. Radiat. Transf. 212 (2018) 32−38, https://doi.org/10.1016/j.jqsrt.2018.03.013.
[15] T. Urbańczyk, M. Krośnicki, A. Kędziorski, J. Koperski, The $E^3\Sigma_1^+(6^3S_1) \leftarrow A^3\Pi_{0+}(5^3P_1)$ transition in CdAr revisited: the spectrum and new analysis of the $E^3\Sigma_1^+$ Rydberg state interatomic potential, Spectrochim. Acta 196 (2018) 58−66, https://doi.org/10.1016/j.saa.2018.01.075.
[16] J. Koperski, M. Czajkowski, Electronic structure of the CdKr lowest Rydberg state determined from laser-excitation spectra using supersonic beam and double optical resonance methods, Phys. Rev. A 69 (2004), 042509, https://

doi.org/10.1103/PhysRevA.69.042509.
[17] T. Urbańczyk, J. Koperski, Spectroscopy of CdKr van der Waals complex using OODR process: new determination of the $E^3\Sigma_1^+(5s6s\ ^3S_1)$ Rydberg state potential, Chem. Phys. 525 (2019), 110406, https://doi.org/10.1016/j.chemphys.2019.110406.
[18] R.R. Bennett, W.H. Breckenridge, Spectroscopic characterization of the $a^3\Pi_{0-}$, $b^3\Pi_2$, and $E^3\Sigma^+$ states of ZnAr, J. Chem. Phys. 92 (1990) 1588–1597, https://doi.org/10.1063/1.458091.
[19] T. Urbańczyk, J. Koperski, First-time observation of transitions to the gerade electronic energy Rydberg state in Cd2 using OODR method, (to be published).
[20] J. Tellinghuisen, The franck-condon principle in bound-free transitions, in: K.P. Lawley (Ed.), Photodissociation and Photoionization, vol. 60, 1985, pp. 229–369, https://doi.org/10.1002/9780470142844.ch7. Adv. Chem. Phys.
[21] M. Krośnicki, A. Kędziorski, T. Urbańczyk, J. Koperski, Rydberg states of the CdAr van der Waals complex, Phys. Rev. A 99 (2019), 052510, https://doi.org/10.1103/PhysRevA.99.052510.
[22] B.O. Roos, P.R. Taylor, P.E.M. Siegbahn, A complete active space SCF method (CASSCF) using a density matrix formulated super-CI approach, Chem. Phys. 48 (1980) 157–173, https://doi.org/10.1016/0301-0104(80)80045-0.
[23] B.O. Roos, The complete active space self-consistent field method and its applications in electronic structure calculations, in: K.P. Lawley (Ed.), *Ab Initio* Methods in Quantum Chemistry Part II, Volume 69 of Advances in Chemical Physics, John Wiley & Sons, Hoboken, NJ, USA, 1987, pp. 399–445.
[24] J. Finley, P.-Å. Malmqvist, B.O. Roos, L. Serrano-Andres, The multi-state CASPT2 method, Chem. Phys. Lett. 288 (1998) 299–306, https://doi.org/10.1016/S0009-2614(98)00252-8.
[25] P.-Å. Malmqvist, B.O. Roos, B. Schimmelpfennig, The restricted active space (RAS) state interaction approach with spin–orbit coupling, Chem. Phys. Lett. 357 (2002) 230–240, https://doi.org/10.1016/S0009-2614(02)00498-0.
[26] M. Douglas, N.M. Kroll, Quantum electrodynamical corrections to the fine structure of helium, Ann. Phys. 82 (1974) 89–155, https://doi.org/10.1016/0003-4916(74)90333-9.
[27] B.A. Hess, Relativistic electronic-structure calculations employing a two-component no-pair formalism with external-field projection operators, Phys. Rev. A 33 (1986) 3742–3748, https://doi.org/10.1103/PhysRevA.33.3742.
[28] B.O. Roos, R. Lindh, P.-Å. Malmqvist, V. Veryazov, P.-O. Widmark, New relativistic ANO basis sets for transition metal atoms, J. Phys. Chem. 109 (2005) 6575–6579, https://doi.org/10.1021/jp0581126.
[29] J.P. Zobel, P.-O. Widmark, V. Veryazov, The ANO-R basis set, J. Chem. Theor. Comput. 16 (2020) 278–294, https://doi.org/10.1021/acs.jctc.9b00873.
[30] B.O. Roos, R. Lindh, P.-Å. Malmqvist, V. Veryazov, P.-O. Widmark, Main group Atoms and dimers studied with a new relativistic ANO basis set, J. Phys. Chem. 108 (2004) 2851–2858, https://doi.org/10.1021/jp031064+.
[31] P.-O. Widmark, P.-Å. Malmqvist, B.O. Roos, Density matrix averaged atomic natural orbital (ANO) basis sets for correlated molecular wave functions, Theor. Chim. Acta 77 (1990) 291–306, https://doi.org/10.1007/BF01120130.
[32] A. Kędziorski et al., (in preparation).
[33] F. Aquilante, et al., Molcas 8: new capabilities for multiconfigurational quantum chemical calculations across the periodic table, J. Comput. Chem. 37 (2016) 506–541, https://doi.org/10.1002/jcc.24221.
[34] J. Dudek, T. Urbańczyk, K. Puczka, J. Koperski, High – temperature continuous molecular beam source for aggressive elements: an example of zinc, Rev. Sci. Instrum. 90 (2019) 115109, https://doi.org/10.1063/1.5127809.
[35] T. Urbańczyk, J. Koperski, High-temperature high-pressure all-metal pulsed source of van der Waals dimers: towards the Einstein-Podolsky-Rosen experiment, Rev. Sci. Instrum. 83 (8) (2012), 083114, https://doi.org/10.1063/1.4747274.
[36] D.J. Funk, A. Kvaran, W.H. Breckenridge, Spectroscopic characterization of the lowest singlet sates of CdNe, CdAr, and CdKr, J. Chem. Phys. 90 (1989) 2915–2926, https://doi.org/10.1063/1.455943.
[37] M. Strojecki, J. Koperski, LIF dispersed emission spectra and characterization of ZnRg (Rg = Ne, Ar, Kr) ground-state potentials, Chem. Phys. Lett. 479 (2009) 189–194, https://doi.org/10.1016/j.cplett.2009.08.019.
[38] R.J. Le Roy, LEVEL: a computer program for solving the radial Schrödinger equation for bound and quasibound levels, J. Quant. Spectrosc. Radiat. Transf. 186 (2017) 167–178, https://doi.org/10.1016/j.jqsrt.2016.05.028.
[39] C.M. Western, PGOPHER: a program for simulating rotational, vibrational and electronic spectra, J. Quant. Spectrosc. Radiat. Transf. 186 (2017) 221–242, https://doi.org/10.1016/j.jqsrt.2016.04.010.
[40] R.J. LeRoy, G.T. Kraemer, BCONT 2.2, University of Waterloo Chemical Physics Research Report CP-650R2, 2004. The source code: http://www.leroy.uwaterloo.ca.
[41] M. Strojecki, M. Krośnicki, J. Koperski, Short-range repulsion in the $D^1\Sigma_0^+$ - state potential of the ZnRg (Rg=Ne,Ar,Kr) complexes determined from a direct free ← bound excitation at the $D^1\Sigma_0^+ \leftarrow X^1\Sigma_0^+$ transition, Chem. Phys. Lett. 465 (2008) 25–30, https://doi.org/10.1016/j.cplett.2008.09.051.
[42] I. Wallace, R.R. Bennett, W.H. Breckenridge, Spectroscopic characterization of the $X^1\Sigma_0$ and $C^1\Pi_1$ states of the ZnAr van der Waals molecule, Chem. Phys. Lett. 153 (1988) 127–132, https://doi.org/10.1016/0009-2614(88)85199-6.
[43] J. Koperski, M. Czajkowski, Short-range characterization of the MeAr (Me=Zn, Cd) ground – state potentials from fluorescence spectra, J. Mol. Spectrosc. 212 (2002) 162–170, https://doi.org/10.1006/jmsp.2002.8550.
[44] J. Dudek, T. Urbańczyk, J. Koperski, (to be published).
[45] A.A. Vigasin, Equilibrium constants for the formation of weakly bound dimers, in: C. Camy-Peyret, A.A. Vigasin (Eds.), Weakly Interacting Molecular Pairs: Unconventional Absorbers of Radiation in the Atmosphere, NATO Science Series (Series IV: Earth and Environmental Sciences), vol. 27, Springer, Dordrecht, 2003, https://doi.org/10.1007/978-94-010-0025-3_9.

MOLECULAR PHYSICS e2024614
https://doi.org/10.1080/00268976.2021.2024614

Taylor & Francis
Taylor & Francis Group

L. WOLNIEWICZ SPECIAL ISSUE

Optical–optical double resonance process in free-jet supersonic expansion of van der Waals molecules: characteristics of the expansion, number of excited molecules and emitted photons

Joanna Sobczuk, Tomasz Urbańczyk and Jarosław Koperski

Marian Smoluchowski Institute of Physics, Jagiellonian University Kraków, Poland

ABSTRACT

Basic characteristics of a free-jet supersonic expansion beam are presented along with an estimation of a number of expanding CdAr and ZnAr molecules that are excited in the free-jet in the optical–optical double resonance process. The estimation is demonstrated for laser excitation from the ground, *via* respective $A^3 0^+(5^3P_1)$ or $C^1 1(4^1P_1)$ intermediate, to the $E^3 1(6^3S_1)$ or $^1 1(4^1D_2)$ Rydberg state of CdAr or ZnAr, respectively. A number of subsequently emitted and collected photons is also predicted.

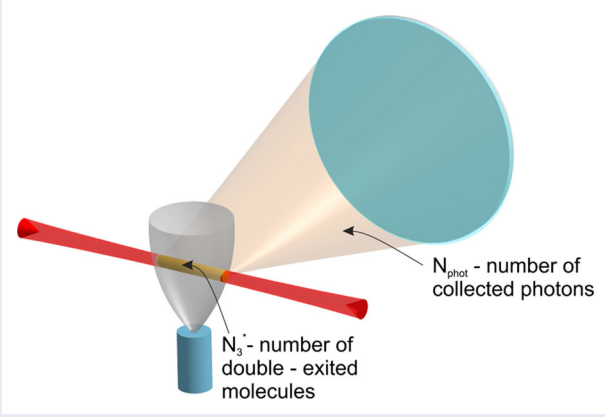

ARTICLE HISTORY
Received 5 November 2021
Accepted 28 December 2021

KEYWORDS
Free-jet supersonic expansion; number density of molecules; Mach number; optical–optical double resonance; Rydberg molecular state

1. Introduction

For experiments in physics and chemistry, pioneering applications of molecular beams were those in Stern-Gerlach [1] and the maser [2] experiments. In those works, so-called effusive beams were used, however, they were limited to low number densities and relatively high temperatures, as particles were emitted in free-molecular flow. Supersonic molecular beams [3] introduced denser beams of ro-vibrationally colder molecules, leading to advances in fields of research such as nanomaterials [4], atom interferometry [5], reaction studies [6] and high-resolution molecular spectroscopy [7]. Later, supersonic beams have been employed as sources for molecular decelerators [8,9], applied toward molecular evaporative cooling [10,11] and in molecular interferometry experiments [12].

Free-jet (i.e. skimmerless) supersonic expansion beams [13] have been frequently combined with laser excitation and subsequent observation of laser-induced fluorescence (LIF) excitation or emission spectra. They consist a well-established experimental technique for studies of molecular electronic, vibrational and rotational energy structures [13,14]. Usually, to excite molecules propagating in the beam, one- or two-step laser excitation is employed to transfer a molecular-level population from the ground to a lower or higher lying (Rydberg) electronic energy state. Then, sweeping the laser frequency or spectrometer wavelength, LIF excitation or emission spectra

CONTACT Joanna Sobczuk joanna.b.dudek@doctoral.uj.edu.pl Marian Smoluchowski Institute of Physics, Jagiellonian University, S. Łojasiewicza 11, 30–348 Kraków, Poland

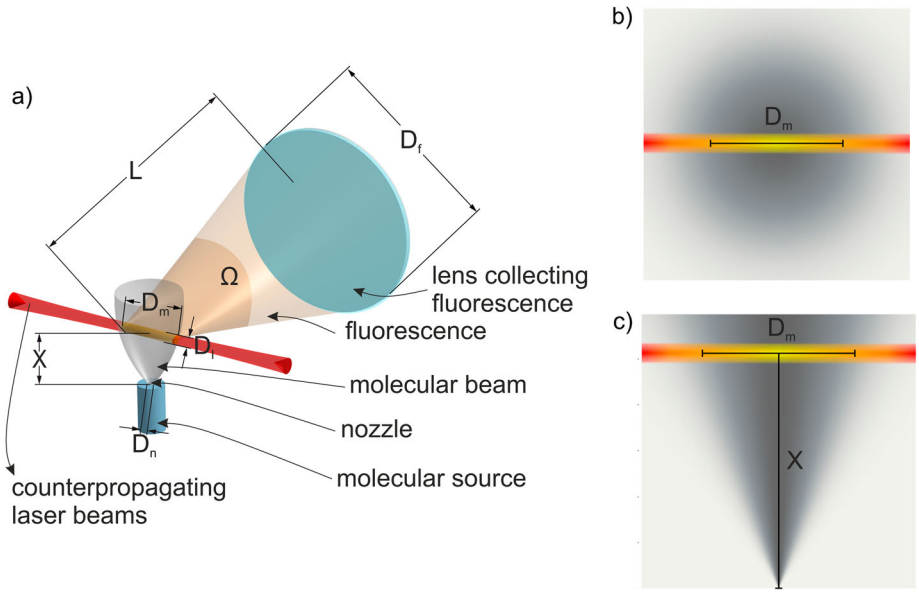

Figure 1. (a) Geometry of the experiment with CdAr or ZnAr vdW molecules excited in a molecular free-jet using OODR process. Two laser beams overlap in the interaction region with the molecular free-jet. A lens is used to collect LIF from the interaction region. To acquire the excitation spectrum, LIF is recorded by the detector (CCD camera or photomultiplier) as a function of frequency of the second-step excitation laser. To observe the emission spectrum, LIF is dispersed using spectrograph situated in front of the detector (not shown). (b) An approximate molecular density distribution in a cross-section of the molecular free-jet perpendicular to its direction of propagation; a Gaussian distribution of the molecular density with $\sigma = \frac{D_m}{2}$ standard deviation has been assumed. (c) As in (b) but in a cross-section of the molecular free-jet along its direction of propagation. In this model, a linear increase of standard deviation σ of the molecular density along X is assumed.

are observed, respectively. In both processes, but particularly in the process of excitation of Rydberg states *via* optical–optical double resonance (OODR), a final number of excited molecules in the free-jet appears to be a crucial parameter for assessing whether LIF signal would be strong enough to be detected with e.g. a CCD camera or a photomultiplier.

In experiments devoted to studies of CdRg or ZnRg (Rg = rare gas atom) van der Waals (vdW) molecules that are performed in our laboratory [15], cadmium or zinc pellets are heated in a molecular source crucible (see Figure 1) to the temperature T_0 (equal to the source nozzle stagnation temperature [16]) that results in p_{Me} cadmium or zinc vapour partial pressure (ME = Cd or Zn). A carrier gas (argon), under the pressure p_{Ar}, is delivered to the crucible causing a mixture of metal vapour and argon to expand through the source nozzle (diameter D_n) into a vacuum chamber. In OODR process, at the distance X from the nozzle, two counterpropagating resonant laser beams (each of diameter D_l) excite molecules. At X, the molecular free-jet has diameter D_m. After the excitation, LIF signal is collected from a solid angle Ω using a lens (diameter D_f) located at the distance$L$ from the interaction region ($L \gg D_m$).

The goal of this article is to estimate a number of excited molecules and number of consequently emitted photons in the total emission per one laser pulse. It is realised in the environment of a free-jet supersonic expansion for laser excitation from the ground, *via* respective $A^30^+(5^3P_1)$ or $C^11(4^1P_1)$ intermediate, to the $E^31(6^3S_1)$ or $^11(4^1D_2)$ Rydberg state of CdAr or ZnAr, respectively. Besides few characteristics of the free-jet supersonic expansion that are crucial to the analysed problem, several quantities are evaluated: an equilibrium constant of formation of MeAr molecules, a number density of MeAr at the distance X from the nozzle, a number of excited MeAr based on Einstein coefficients calculated using LEVEL Fortran code [17] and number of emitted photons.

2. OODR processes in CdAr or ZnAr

A scheme of OODR process that is realised to excite Rydberg electronic energy states in CdAr or ZnAr is shown in Figure 2. It has been described in detail in [15]. Generally, two laser beams in the VIS and/or UV region are used in the process. They are employed to excite molecules to the electronic states to which transitions from the ground state are forbidden or not possible in one-step excitation. Moreover, OODR can involve different intermediate electronic states to access and probe different parts of the ro-vibrational energy structure in the final Rydberg-state potential well(s).

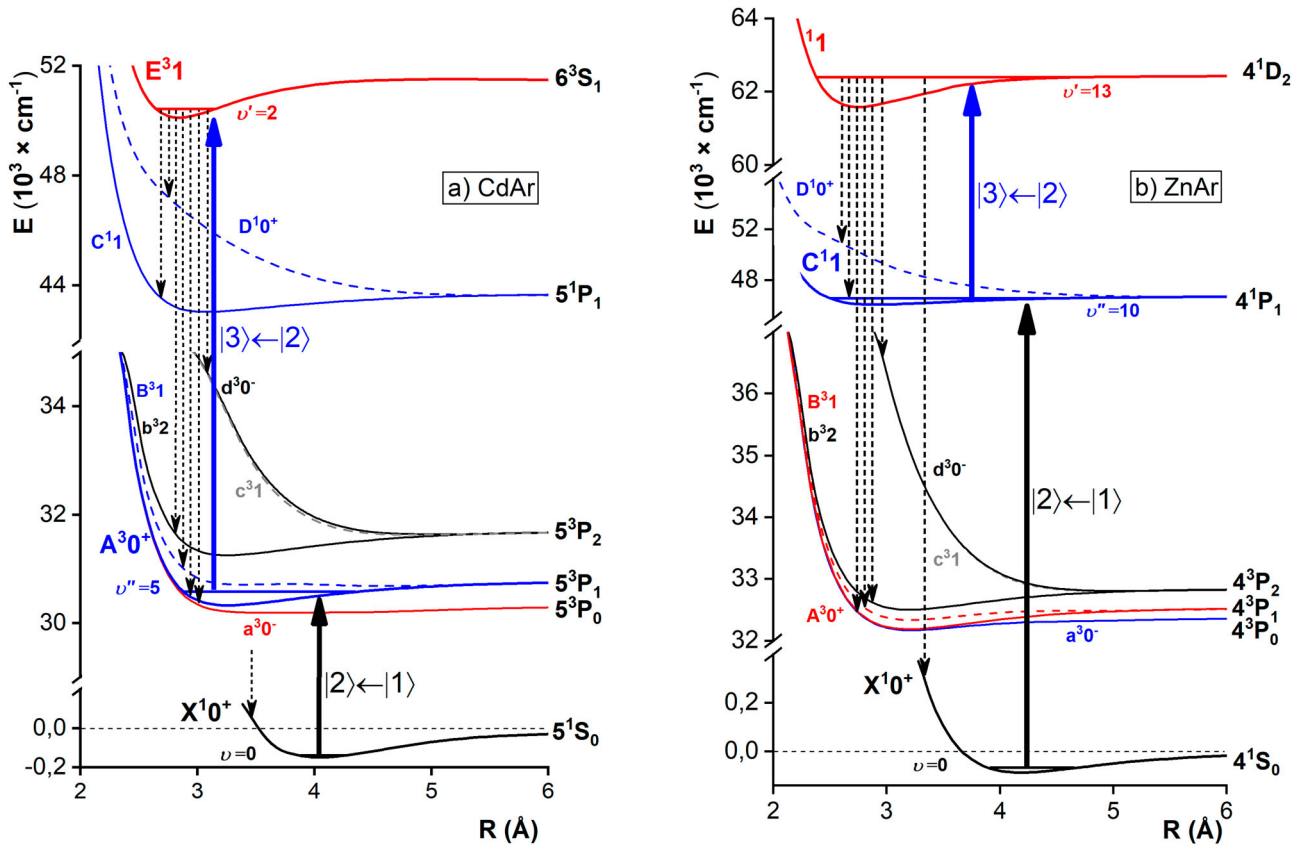

Figure 2. Ab-initio calculated interatomic potentials of electronic states in (a) CdAr [18] and b) ZnAr [15] molecules. A scheme of OODR process is shown (solid vertical arrows) for excitation of (a) the $E^3 1(6^3S_1)$, $\upsilon' = 2$ and (b) the $^1 1(4^1D_2)$, $\upsilon' = 13$ levels in Rydberg states (level $|3\rangle$) from $\upsilon = 0$ of the ground state (level $|1\rangle$) using (a) the $A^3 0^+(5^3P_1)$, $\upsilon'' = 5$ and (b) the $C^1 1(4^1P_1)$, $\upsilon'' = 10$ intermediates (level $|3\rangle \leftarrow |2\rangle$). Possible channels of the allowed emission analysed in [15] are shown with dashed vertical arrows. 350 × 200 mm (300 × 300 DPI)

Detection of dispersed emission from a Rydberg state can be used in determination of those parts of lower lying state potential that are not accessible in the excitation from the ground state. As shown in [15], it can be applied for CdAr or ZnAr molecules by collecting fluorescence from molecules previously excited to the $E^3 1(6^3S_1)$ or $^1 1(4^1D_2)$ Rydberg states *via* the $A^3 0^+(5^3P_1)$ or $C^1 1(4^1P_1)$ intermediates, respectively (see Figure 2). However, to effectively realise OODR process, one must ensure that the chosen molecular transitions guarantee efficient vibrational-level population transfer from the $|1\rangle$ground to the $|3\rangle$ Rydberg state. Except for sufficiently intense resonant laser pulses and adequately 'dense' molecular free-jet (in the sense of molecular number density), one has to choose transitions for which transition dipole moments (TDMs) have satisfactory large values. Figure 3 presents $|\mathrm{TDM}|^2(R)$, where R is an internuclear separation, for (a) the $E^3 1 \leftarrow A^3 0^+ \leftarrow X^1 0^+(5^1S_0)$ and (b) the $^1 1 \leftarrow C^1 1 \leftarrow X^1 0^+(4^1S_0)$ transitions for CdAr and ZnAr, respectively. As one can see, for ZnAr, as both transitions are singlet←singlet transitions, are appreciably large, which is not the case for the first triplet←singlet transition in CdAr that is characterised by $|\mathrm{TDM}|^2$ which is three orders of magnitude smaller. Fortunately, despite the fact, the $A^3 0^+ \leftarrow X^1 0^+$ transition in CdAr has been experimentally realised in several laboratories as reported, e.g. in [13] and [19].

3. Number density of ground-state MeAr molecules in free-jet supersonic expansion

Let us consider a process of formation of diatomic molecules (here MeAr from Me and Ar atoms), in a thermal equilibrium bath which takes place in the source nozzle

$$\mathrm{Me} + \mathrm{Ar} \rightleftharpoons \mathrm{MeAr}$$

According to Vigasin [20], near the bottom of the molecular potential that is well approximated by a truncated harmonic oscillator, K_p equilibrium constant can be

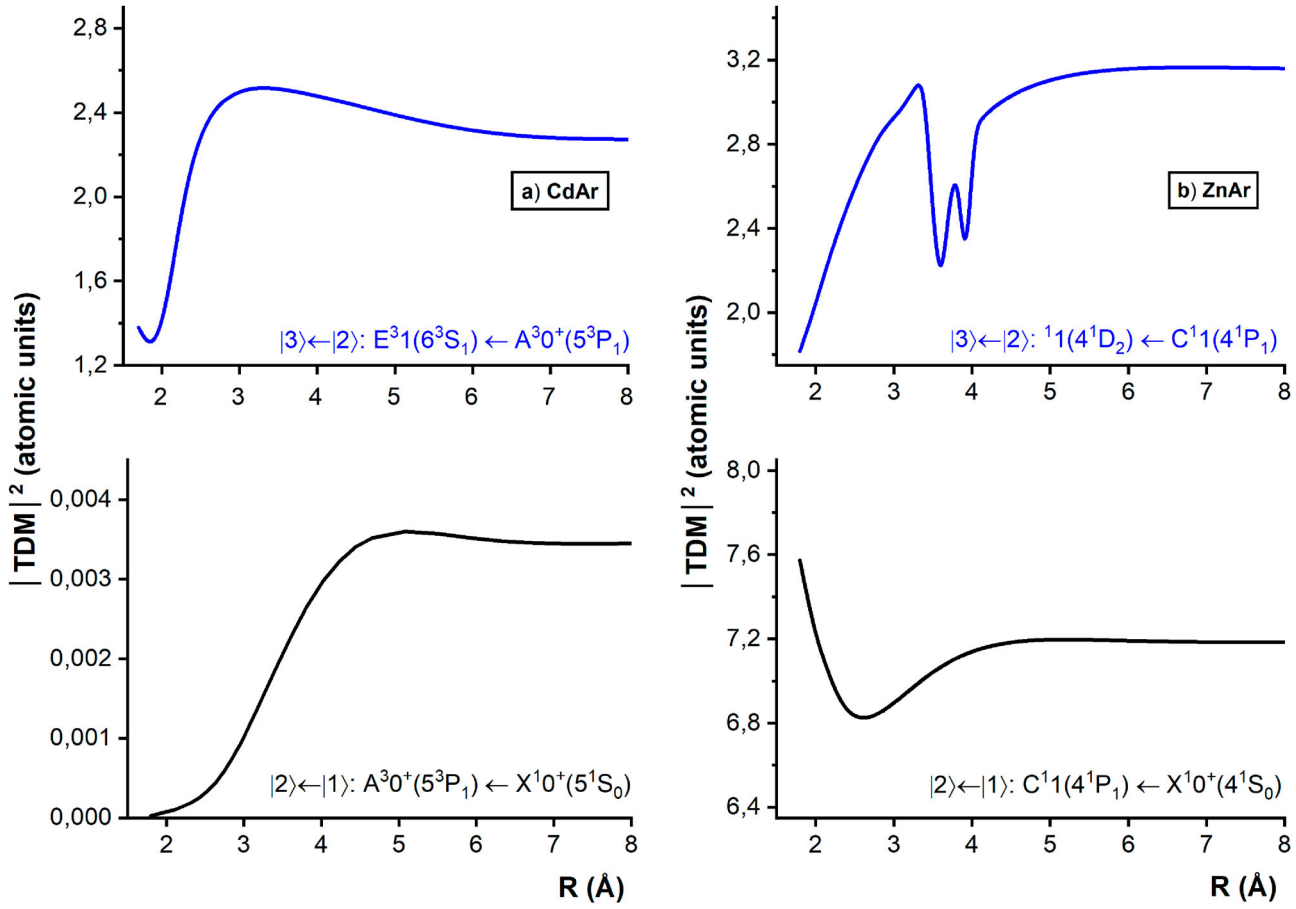

Figure 3. Ab-initio calculated transition dipole moments $|\,\mathrm{TDM}\,|^2$ for electronic transitions in (a) CdAr [18] and (b) ZnAr [15] molecules shown in Figure 2 for which OODR process is performed. 289 × 202 mm (300 × 300 DPI)

expressed in (atm^{-1}) as

$$K_p = \frac{18.86}{\omega_e B_v \chi T_0^{0.5} \mu_{MeAr}^{1.5}} \left[e^{\frac{D_e}{T_0}} - \left(1 + \frac{D_e}{T_0}\right) \right], \quad (1)$$

where ω_e is a harmonic vibrational constant and B_v is a rotational constant for a given υ, both in (cm^{-1}), χ is the symmetry number (equal to 1 for heteronuclear molecule), T_0 is a nozzle stagnation temperature (equal to the temperature of a gas mixture in the crucible) in (K), μ_{MeAr} is a reduced mass of MeAr in (atomic units) and D_e is MeAr ground-state potential depth in (K).

Having K_p, one can write the formula

$$K_p = \frac{p_{MeAr}}{p_{Me} p_{Ar}} \quad (2)$$

which is valid only if $K_p \ll 1$ (it means only a small fraction of Me and Ar atoms forms MeAr molecules which is a realistic approximation in free-jet supersonic expansion) and where p_{MeAr} is a partial vapour pressure of MeAr in the source nozzle where the molecules are formed due to collisions. Using Equations (1) and (2), p_{MeAr} and then number density n_0 of the ground-state MeAr in the nozzle can be calculated assuming an ideal gas approximation

$$n_0 = \frac{p_{MeAr}}{k_B T_0} \quad (3)$$

where k_B is the Boltzmann constant.

For an isentropic flow in free-jet supersonic expansion, after travelling the distance X, number density $n(X)$ of MeAr along with the central axis of free-jet propagation decreases according to the formula [7]

$$n(X) = \frac{n_0}{\left[1 + \frac{1}{2}(\gamma - 1) M(X)^2\right]^{\frac{1}{\gamma - 1}}} \quad (4)$$

where $\gamma = \frac{c_p}{c_v}$ and $c_{p(v)}$ is the heat capacity at a constant pressure (volume), and the decrease of n in Equation (4) is due to the increasing of $M(X)$ local Mach number that satisfies the equation [7]

$$M(X) = A \left(\frac{X}{D_n} \right)^{\gamma - 1} \quad (5)$$

where A is a constant. Here, we discuss so-called seeded molecular free-jet which consists of Me atoms with small

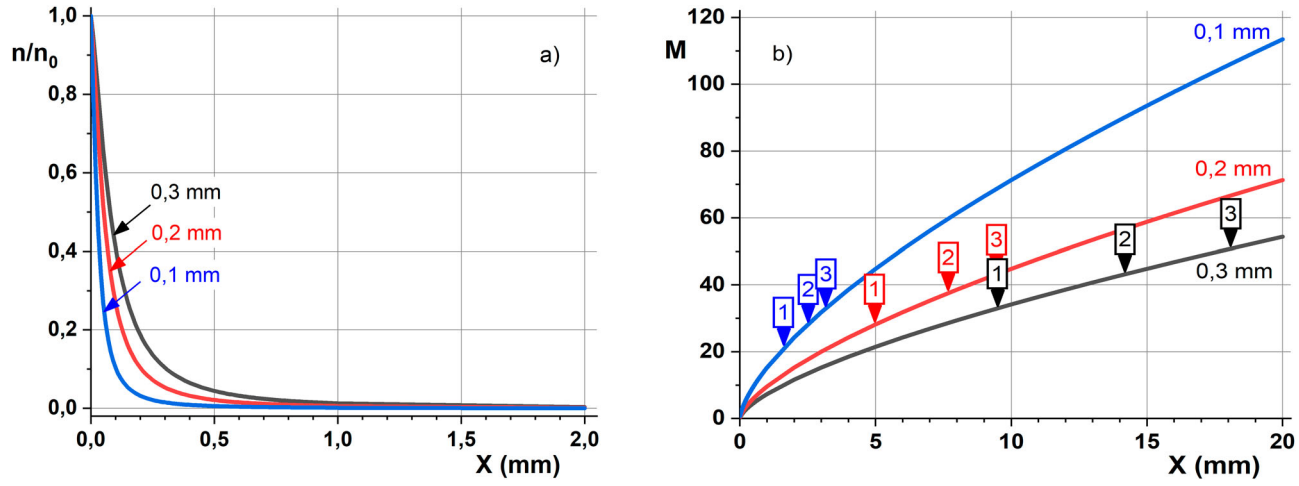

Figure 4. (a) Relative number density $\frac{n}{n_0}$ of MeAr along the central axis of free-jet supersonic expansion and (b) Mach numbers M plotted against distance X, both for molecular source nozzle diameters $D_n = 0.1$, 0.2 and 0.3 mm—according to (a) Equation (4) and (b) Equation (5). 540 × 208 mm (300 × 300 DPI)

number density in a cold 'bath' of carrier gas Ar atoms; for monoatomic gas $\gamma = 5/3$ and $A = 3.26$. (Note: M corresponds to $\frac{\upsilon_{Ar}}{\upsilon_s}$ ratio of υ_{Ar}, the local velocity of the carrier gas in the free-jet, to υ_s, the local velocity of sound, and as $\upsilon_s \sim \sqrt{T}$, T drops along with the central axis of expansion while M increases).

Figure 4 shows (a) $\frac{n}{n_0}(X)$ and (b) $M(X)$ dependencies that illustrate relations expressed with Equations (4) and (5), respectively, and are derived for three different D_n nozzle diameters, typical in our experiments. It is evident that number density n of the ground-state molecules along with the central axis of free-jet supersonic expansion decreases quickly with X and, for experimental conditions of present consideration, the decrease is approx. from 5 to 6 orders of magnitude at $X = 20$ mm (Note: in Figure 4(a) only X from 0 to 2 mm is shown).

It is interesting to examine $M(X)$ for different D_n with respect to M_T terminal Mach number beyond which no further cooling of molecular internal degrees of freedom is taking place and particles travel in the molecular free-jet in so-called zone of silence without collisions. Here, M_T for monoatomic gas is given by the phenomenological formula [7,21]

$$M_T = 133(p_{Ar}D_n)^{0.4} \tag{6}$$

where p_{Ar} and D_n are expressed (atm) and (cm), respectively, and — as M_T depends on D_n and p_{Ar} — it is worthwhile to estimate M_T for typical experimental parameters. In Figure 4(b), several values of M_T were depicted with arrows numbered according to increased p_{Ar}: (1), (2) and (3) for 1, 2 and 3 atm, respectively. Along with the central axis of free-jet propagation, the distance X_T from the nozzle at which M_T occurs (and origin of 'zone of silence' starts) can be estimated using the formula [16]

$$X_T = D_n\left(\frac{M_T}{3.26}\right)^{1.5} \tag{7}$$

and one can see that for all D_n and p_{Ar} available in the experiment M attain their M_T terminal values for X smaller than 20 mm.

The analysis presented above allows to formulate a conclusion: with increasing D_n the number density n of molecules along with the central axis of free-jet expansion increases as well; however, for larger D_n the drop of n along with the central axis is slower than that for smaller D_n. For larger D_n, conditions for ro-vibrational cooling become worse. The best cooling conditions are reached for smaller D_n, and larger p_{Ar} and X.

Finally, according to a thermodynamic description of free-jet supersonic expansion, M at particular X expressed by Equation (5) allows to estimate an average flow velocity [21,22]

$$\upsilon_{aver}(X) = M(X)\left(\frac{\gamma k_B T(X)}{\mu_{MeAr}}\right)^{0.5}, \tag{8}$$

where T along with the central axis of propagation is governed by the formula [7,21]

$$T(X) = \frac{T_0}{1 + \frac{1}{2}(\gamma - 1)M(X)^2}. \tag{9}$$

Figure 5 shows (a) $\upsilon_{aver}(X)$ and (b) $T(X)$ dependencies for ZnAr expanding in the free-jet as expressed by Equations (8) and (9), respectively. It is evident that for experimental parameters of this analysis υ_{aver} increases sharply at the beginning of the expansion (say, first 0.5–1

mm) and the larger D_n the smaller is υ_{aver}. As far as T is concerned, it drops very fast from its T_0 starting value at first 1–2 mm of the expansion and its drop is faster the smaller is D_n. Using Equations (8) and (9), one can show that assuming typical experimental conditions realised in our laboratory, *i.e.* $D_n = 0.2$ mm, $T_0 = 913$ K and $T_0 = 1073$ K for CdAr and ZnAr, respectively, one can arrive at $\upsilon_{aver}(X_{exp} = 10\,\text{mm}) = 1131\ \text{m s}^{-1}$ and $\upsilon_{aver}(X_{exp} = 7\,\text{mm}) = 1343\ \text{m s}^{-1}$ for CdAr and ZnAr, respectively.

4. Number of excited MeAr molecules

To realise the first-step transition of OODR process, at distance X_{exp}, the molecular free-jet is illuminated by a pulsed laser beam that emits pulses of duration t_p, spectral bandwidth $\Delta\omega_{las}$ ($=2\pi\,\Delta\nu_{las}$) and a total energy per pulse E_p. The pulses have spectral energy density distribution $\rho(\omega)$ which is a function of angular frequency ω and is given by the formula

$$\rho(\omega) = \rho_0 \frac{1}{\sqrt{2\pi}\sigma} \exp\left[\frac{(\omega - \omega_{las})^2}{2\sigma^2}\right], \tag{10}$$

where ρ_0 is energy density per laser pulse ($\rho_0 = \frac{E_p}{2\pi\,(D_l/2)^2 c t_p}$, c is the speed of light), $\sigma = \frac{1}{2\sqrt{2\ln 2}}\Delta\omega_{las}$, and ω_{las} is an average laser frequency. Let us assume ω_{las} is tuned to ω_{21} resonance frequency of the molecular transition between $|1\rangle$ lower and $|2\rangle$ upper state ro-vibrational energy levels: $\omega_{las} = \omega_{12}$, and the transition natural linewidth $\Delta\omega_{nat} \ll \Delta\omega_{las}$. Then, the total rate of absorption W_{12}^{abs} expressed in (s^{-1}) is equal [23]

$$W_{12}^{abs} = B_{12}\rho_\omega N_1 \tag{11}$$

where B_{12} is Einstein coefficient for absorption in $\left(\frac{\text{m}^3\cdot\text{rad}\cdot\,\text{s}^{-1}}{\text{J}\cdot\text{s}}\right)$, ρ_ω is energy density per unit of angular frequency expressed as $\rho_\omega = \frac{1}{\sqrt{2\pi}}\frac{\rho_0}{\sigma}$ in $\left(\frac{\text{J}\cdot\text{m}^{-3}}{\text{rad}\cdot\text{s}^{-1}}\right)$ and N_1 is an initial number of absorbing molecules in level $|1\rangle$ (see Equation (17)) Assuming a Gaussian distribution of molecular number density along with the direction of the laser beam with a variance σ satisfying the condition $D_m = 2\sigma$ (D_m can be determined experimentally [24]), N_1 can be approximated by

$$N_1 = n(X)(2\pi)^{\frac{3}{2}}\left(\frac{D_m}{2}\right)\left(\frac{D_l}{2}\right)^2, \tag{12}$$

where $n(X)$ is given by Equation (4).

Together with an increasing N_2 number of the excited molecules in level $|2\rangle$, spontaneous and stimulated emissions with $W_{21}^{spont\ em}$ and $W_{21}^{stim\ em}$ rates, respectively, occur and

$$W_{21}^{spont\ em} = A_{21}N_2, \tag{13}$$

$$W_{21}^{stim\ em} = B_{21}\rho_\omega N_2, \tag{14}$$

where A_{21} and B_{21} are Einstein coefficients for spontaneous and stimulated emissions to the lower level expressed in (s^{-1}) and $\left(\frac{\text{m}^3\cdot\text{rad}\cdot\,\text{s}^{-1}}{\text{J}\cdot\text{s}}\right)$, respectively. Here, for the sake of simplicity, we assume spontaneous emission only to one lower level. A_{21} coefficients were calculated by LEVEL program [17] taking into account interatomic potentials of the electronic states involved in the transitions and respective TDMs as a function of R, with one exception: In case of the $A^3 0^+$, $\upsilon'' = 5 \leftarrow X^1 0^+$, $\upsilon = 0$ transition in CdAr, the A_{21} coefficient has been assumed as that determined experimentally [25]. Mutual relations between Einstein coefficients are as follows [23]:

$$B_{21} = \left(\frac{2\pi^3 c^3}{h\omega_{21}^3}\right) A_{21}, \tag{15}$$

$$B_{12} = \left(\frac{g_2}{g_1}\right) B_{21} \tag{16}$$

where h is the Planck constant and $g_{2(1)}$ is degeneracy of the upper (lower) level.

The N_1 and N_2 numbers of molecules are time dependent, thus $N_1 \Rightarrow N_1^*(t)$ and $N_2 \Rightarrow N_2^*(t)$. In general, ρ_ω is also time dependent due to absorption (emission) of photons and non-rectangular shape of the laser pulse in time domain. However, in case of considered transitions, the number of absorbed photons is negligible as compared to the total number of photons in the laser beam. Moreover, for the sake of simplicity as shown above, in time domain, we assumed a rectangular shape of the laser pulse. In such a case, ρ_ω is constant. With the above assumptions, the population transfer $N_2(t) \leftarrow N_1^*(t)$ occurs and $N_2^*(t)$ is given by the equation

$$\frac{dN_2^*}{dt} = W_{12}^{abs} - W_{21}^{spont\ em} - W_{21}^{stim\ em} = B - AN_2^*(t), \tag{17}$$

where $A = B_{12}\rho_\omega + B_{21}\rho_\omega + A_{21}$ and $B = B_{12}\rho_\omega N_1$. With the boundary condition $N_2^*(t=0) = 0$, solution of Equation (17) is

$$N_2^*(t) = \frac{B}{A}(1 - e^{-At}). \tag{18}$$

Excitation in the second-step of OODR process is analogous to that in the first-step, with the exception that in the second-step the $N_3^*(t) \leftarrow N_2^*(t)$ population transfer occurs and emission from level $|3\rangle$ is recorded.

In this study, it is approximated that there is no delay τ between the two excitation pulses in OODR process. This

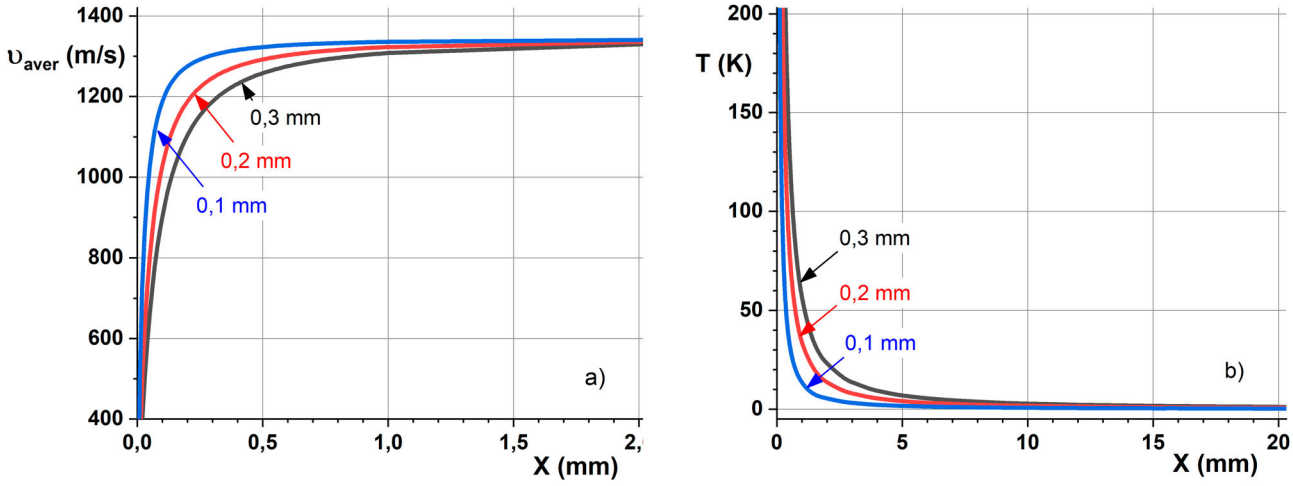

Figure 5. (a) Average flow velocity υaver and (b) temperature T along the central axis of free-jet supersonic expansion plotted against distance X for ZnAr, and for source nozzle diameters $D_n =$ 0.1, 0.2 and 0.3 mm—according to (a) Equation (8) and (b) Equation (9).

Table 1. Parameters of the experiment with OODR excitation process of CdAr and ZnAr molecules from the ground to the $E^3 1(6^3S_1)$ and $^1 1(4^1D_2)$ Rydberg states, respectively.

Parameter	Unit	Description	CdAr	ZnAr
Initial parameters of the free-jet supersonic expansion				
T_0	K	Nozzle stagnation temperature = temperature of a gas mixture in the crucible	913	1073
p_{Me}	bar	Metal vapour pressure in the crucible [28]	0.220	0.335
p_{Ar}	bar	Argon pressure in the crucible	5	7
Geometry of the experiment				
D_n	mm	Diameter of the nozzle	0.2	0.2
D_m	mm	Diameter of the molecular free-jet at X_{exp}	5	4
D_l	mm	Diameter of the laser beam at the intersection with the molecular free-jet	2	2
D_f	mm	Diameter of the collecting lens	51	51
X_{exp}	mm	Distance between the nozzle and the laser beam	10	7
L	mm	Distance between the intersection of the laser beams and molecular free-jet, and the collecting lens	100	150
Parameters of laser beams in OODR process				
E_{p1}	mJ	Energy per pulse of the first excitation	3	1.5
E_{p2}	mJ	Energy per pulse of the second excitation	1.5	1.5
t_p	ns	Laser pulse duration	10	10
$\Delta\nu_{las}$	cm^{-1}	Spectral bandwidth of the laser pulse	0.2	0.2
Parameters of the molecular electronic ground-state				
υ	—	Vibrational quantum number	0	0
ω_e	cm^{-1}	Harmonic vibrational constant [13,29]	19.8	19.8
$B_{v=0}$	cm^{-1}	Rotational constant for $\upsilon = 0$ [17]	0.046	0.034
D_e	K	Potential well depth [13,29],	146.88	116.73

is because after τ of few tens of ns (in the experiment $\tau \approx$ 50 ns) molecules in the free-jet travel approx. 60–70 μm which is a negligible distance as compared with D_m and D_l that are of few mm each (see Table 1). Thus, the loss of molecules from the interaction region is also negligible and $\tau = 0$ ns is justified to be assumed.

5. Number of emitted and collected photons

As excited energy level $|3\rangle$ in both Rydberg states of CdAr and ZnAr possess a limited lifetime, so in our model one can assume that one photon from each excited molecule in the first-step LIF is emitted. Secondary LIF events are not taken into consideration. Thus, the number of emitted photons is equal to the number of excited molecules: $N_{phottot} = N_2^*(t)$. Moreover, in this study, an idealised detection system is described. It is affected neither by scattering from the collecting lens nor efficiency of the detector. Although photons are emitted in full solid angle, only these that reach the collecting lens can be detected (see Figure 1). Thus, a number of photons collected by the lens approximately equals

$$N_{phot} = \frac{\pi (D_f/2)^2}{4\pi L^2} N_{phot\ tot}. \tag{19}$$

Table 2. Calculated parameters of the experiment of OODR process and subsequent emission from the $E^3 1(6^3S_1)$ and $^1 1(4^1D_2)$ Rydberg states of CdAr and ZnAr molecules, respectively.

Parameter	Unit	Description	CdAr	ZnAr
Free-jet supersonic expansion				
K_p	atm^{-1}	Equilibrium constant of MeAr formation in the ground state, Equation (1)	$8.9 \cdot 10^{-5}$	$4.3 \cdot 10^{-5}$
n_0	m^{-3}	Number density of MeAr molecules in the source nozzle (Equation (3))	$7.7 \cdot 10^{20}$	$6.7 \cdot 10^{20}$
n	m^{-3}	Number density of MeAr molecules at X along the axis of molecular free-jet, Equation (4)	$4.6 \cdot 10^{16}$	$8.2 \cdot 10^{16}$
M	—	Mach number at X, Equation (5)	44.8	35.3
T	K	Temperature at X, Equation (9)	1.5	2.6
υ_{aver}	$m\,s^{-1}$	Average velocity of molecules at X, Equation (8)	1131	1343
First-step excitation in OODR process (transition $\|2\rangle \leftarrow \|1\rangle$)				
A_{21}	s^{-1}	Einstein coefficient for spontaneous emission [15,22]	$3.7 \cdot 10^5$	$1.26 \cdot 10^8$
B_{12}	$\frac{m^3 \cdot rad \cdot s^{-1}}{J \cdot s}$	Einstein coefficient for absorption, Equation (16)	$1.95 \cdot 10^{19}$	$1.87-10^{21}$
B_{21}	$\frac{m^3 \cdot rad \cdot s^{-1}}{J \cdot s}$	Einstein coefficient for stimulated emission, Equation (15)	$9.73 \cdot 10^{18}$	$9.36-10^{20}$
ω_{12}	$rad\,s^{-1}$	Resonant angular frequency	$5.77 \cdot 10^{15}$	$8.79 \cdot 10^{15}$
N_2^*	—	Number of MAr excited molecules after laser pulse ($t = 10ns$) first excitation, Equation (18)	$1.2 \cdot 10^9$	$1.7 \cdot 10^9$
Second-step excitation in OODR process (transition $\|3\rangle \leftarrow \|2\rangle$)				
A_{32}	s^{-1}	Einstein coefficient for spontaneous emission [15]	$2.42 \cdot 10^5$	$1.35 \cdot 10^6$
B_{23}	$\frac{m^3 \cdot rad \cdot s^{-1}}{J \cdot s}$	Einstein coefficient for absorption, Equation (16)	$1.59 \cdot 10^{18}$	$1.29 \cdot 10^{20}$
B_{32}	$\frac{m^3 \cdot rad \cdot s^{-1}}{J \cdot s}$	Einstein coefficient for stimulated emission, Equation (15)	$7.95 \cdot 10^{17}$	$1.29 \cdot 10^{21}$
ω_{23}	$rad\,s^{-1}$	Resonance angular frequency	$3.75 \cdot 10^{15}$	$2.98 \cdot 10^{15}$
N_3^*	—	Number of MAr excited molecules after laser pulse ($t = 10ns$) second excitation, Equation (18)	$4.0 \cdot 10^8$	$1.1 \cdot 10^8$
N_{phot}	—	Number of photons collected by lens per one laser pulse (transition $\|3\rangle \rightarrow \|2\rangle$), Equation (20)	$6.5 \cdot 10^6$	$8.0 \cdot 10^5$

6. Conclusions

Basic characteristics of a free-jet supersonic expansion along with its central axis such as: Mach number $M(X)$, terminal Mach number M_T, number density $n(X)$ of molecules, average flow velocity $\upsilon_{aver}(X)$ and temperature $T(X)$ were analysed along with an estimation of N_3^*, the number of expanding CdAr and ZnAr molecules that are excited in the free-jet in OODR process. The estimation was demonstrated for laser excitation from the ground, *via* intermediate, to the $E^3 1(6^3S_1)$ or $^1 1(4^1D_2)$ Rydberg state for CdAr or ZnAr, respectively. A number of subsequently collected photons, N_{phot}, in the detection system was also evaluated.

Table 1 collects parameters of the experiment with OODR excitation process of CdAr and ZnAr molecules from the ground to the $E^3 1$ and $^1 1$ Rydberg states, respectively. It encloses initial parameters of the free-jet supersonic expansion, parameters describing the geometry of the experiment, laser beams and molecular electronic ground-state. Table 2 collects calculated parameters of free-jet supersonic expansion, two steps of excitation in OODR process and subsequent emission from the $E^3 1$ and $^1 1$ Rydberg states in both molecules.

It was shown that for both CdAr and ZnAr, the number of Rydberg-state excited molecules N_3^* ($1.27 \cdot 10^8$ and $5.31 \cdot 10^7$, respectively) as well as subsequently emitted photons N_{phot} ($2.08 \cdot 10^6$ and $3.8 \cdot 10^5$, respectively) may ensure detection of ZnAr in the free-jet supersonic expansion after excitation of the $^1 1$ Rydberg state. This is because LIF emission from the $E^3 1$ state in CdAr has been readily detected not only in our laboratory [26,27] while N_{phot} in the case of ZnAr is only approx. 5.4 times smaller than that of CdAr.

Acknowledgements

This research was funded by the Priority Research Area SciMat under the program *Excellence Initiative—Research University* at the Jagiellonian University in Krakow, Poland. Partial support of the National Science Centre Poland under grant number UMO-2015/17/B/ST4/04016 is also appreciated.

Disclosure statement

No potential conflict of interest was reported by the author(s).

Funding

This research was funded by the Priority Research Area SciMat under the program *Excellence Initiative—Research University* at the Jagiellonian University in Krakow, Poland. Partial support of the National Science Centre Poland [grant number UMO-2015/17/B/ST4/04016] is also appreciated.

ORCID

Joanna Sobczuk http://orcid.org/0000-0001-8978-2878
Tomasz Urbańczyk http://orcid.org/0000-0002-9515-3426
Jarosław Koperski http://orcid.org/0000-0002-6414-9651

References

[1] W. Gerlach and O. Stern, Z. Phys. 9, 349 (1922). doi:10.1007/BF01326983.

[2] J.P. Gordon, H.J. Zeiger and C.H. Townes, Phys. Rev. 99, 1264 (1955). doi:10.1103/PhysRev.99.1264.

[3] A. Kantrowitz and J. Grey, Rev. Sci. Instrum. 22, 328 (1951). doi:10.1063/1.1745921.

[4] H.W. Kroto, J.R. Heath, S.C. O'Brien, R.F. Curl and R.E. Smalley, Nature. 318, 162 (1985). doi:10.1038/318162a0.

[5] D.W. Keith, C.R. Ekstrom, Q.A. Turchette and D.E. Pritchard, Phys. Rev. Lett. 66, 2693 (1991). doi:10.1103/PhysRevLett.66.2693.

[6] D.R. Herschbach, *Advances in Chemical Physics: Molecular Beams* (John Wiley, 2009). Vol. 10, pp. 319–393. doi:10.1002/9780470143568.ch9.

[7] R.E. Smalley, L. Wharton and D.H. Levy, Acc.Chem. Res. 10, 139 (1977). doi:10.1021/ar50112a006.

[8] J.R. Bochinski, E.R. Hudson, H.J. Lewandowski, G. Meijer and J. Ye, Phys. Rev. Lett. 91, 243001 (2003). doi:10.1103/PhysRevLett.91.243001.

[9] S.Y.T. van de Meerakker, H.L. Bethlem, N. Vanhaecke and G. Meijer, Chem. Rev. 112, 4828 (2012). doi:10.1021/cr200349r.

[10] B.K. Stuhl, M.T. Hummon, M. Yeo, G. Quéméner, J.L. Bohn and J. Ye, Nature. 492, 396 (2012). doi:10.1038/nature11718.

[11] Y. Segev, M. Pitzer, M. Karpov, N. Akerman, J. Narevicius and E. Narevicius, Nature. 572, 189 (2019). doi:10.1038/s41586-019-1446-2.

[12] P. Haslinger, N. Dörre, P. Geyer, J. Rodewald, S. Nimmrichter and M. Arndt, Nat. Phys. 9, 144 (2013). doi:10.1038/nphys2542.

[13] J. Koperski, Phys. Reports. 369, 177 (2002). doi:10.1016/S0370-1573(02)00200-4.

[14] W. H. Breckenridge, C. Jouvet and B Soep, in *Advances in Metal and Semiconductor Clusters*, edited by M. Duncan (AI Press Inc., Greenwich, 1995), pp. 1–83.

[15] J. Dudek, A. Kędziorski, J.P. Zobel, M. Krośnicki, T. Urbańczyk, K. Puczka and J. Koperski, J. Mol. Struct. 1222, 128840 (2020). doi:10.1016/j.molstruc.2020.128840.

[16] R. Campargue, J. Phys. Chem. 88, 4466 (1984). doi:10.1021/j150664a004.

[17] R.J. Le Roy, J. Quant. Spectrosc. Radiat. Transf. 186, 167 (2017). doi:10.1016/j.jqsrt.2016.05.028.

[18] M. Krośnicki, A. Kędziorski, T. Urbańczyk and J. Koperski, Phys. Rev. A. 99, 052510 (2019). doi:10.1103/PhysRevA.99.052510.

[19] A. Kvaran, D.J. Funk, A. Kowalski and W.H. Breckenridge, J. Chem. Phys. 89, 6069 (1988). doi:10.1063/1.455422.

[20] A. A. Vigasin, in *Weakly Interacting Molecular Pairs: Unconventional Absorbers of Radiation in the Atmosphere. NATO Science Series (Series IV: Earth and Environmental Sciences)*, edited by C. Camy-Peyret and A. A. Vigasin (Springer, Dordrecht, 2003). vol. 27. doi:10.1007/978-94-010-0025-3_9.

[21] D.M. Lubman, C.T. Rettner and R.N. Zare, J. Phys. Chem. 86, 1129 (1982). doi:10.1021/j100396a017.

[22] H. Haberland, U. Buck and M. Tolle, Rev. Sci. Instrum. 56, 1712 (1985). doi:10.1063/1.1138129.

[23] R.C. Hilborn, Am. J. Phys. 50, 982 (1982). doi:10.1119/1.12937.

[24] Y. Segev, N. Bibelnik, N. Akerman, Y. Shagam, A. Luski, M. Karpov, J. Narevicius and E. Narevicius, Sci. Adv. 3, e1602258 (2017). doi:10.1126/sciadv.1602258.

[25] R. Bobkowski, M. Czajkowski and L. Krause, Phys. Rev. A. 41, 243 (1990). doi:10.1103/PhysRevA.41.243.

[26] M. Czajkowski, R. Bobkowski and L. Krause, Phys. Rev. A. 45, 6451 (1992). doi:10.1103/PhysRevA.45.6451.

[27] R.R. Benett and W.H. Breckenridge, J. Chem. Phys. 96, 882 (1992). doi:10.1063/1.462108.

[28] Institute für Angewandte Physik, Vapor Pressure Calculator. < https://www.iap.tuwien.ac.at/www/surface/vapor_pressure > (Accessed 24 Sept. 2021).

[29] J. Koperski, T. Urbańczyk, M. Krośnicki and M. Strojecki, Chem. Phys. 428, 43 (2014). doi:10.1016/j.chemphys.2013.10.017.

Spectrochimica Acta Part A: Molecular and Biomolecular Spectroscopy 264 (2022) 120248

Contents lists available at ScienceDirect

Spectrochimica Acta Part A: Molecular and Biomolecular Spectroscopy

journal homepage: www.elsevier.com/locate/saa

Rotational characterization of the $E^3\Sigma_1^+(5s6s\ ^3S_1)$ Rydberg state of CdNe van der Waals complex *via* selective *J*-excitation in OODR process

Tomasz Urbańczyk *, Joanna Sobczuk, Jarosław Koperski

Smoluchowski Institute of Physics, Faculty of Physics, Astronomy and Applied Computer Science, Jagiellonian University, Łojasiewicza 11, 30-348 Kraków, Poland

HIGHLIGHTS

- *J*-selective excitation of CdNe complex to the $E^3\Sigma_1^+$ state in OODR process.
- Determination of the B_e, $B_{\upsilon=0}$ and $B_{\upsilon=1}$ rotational constants of the $E^3\Sigma_1^+$ state.
- Determination of new $E^3\Sigma_1^+$ - state R_e bond length.

GRAPHICAL ABSTRACT

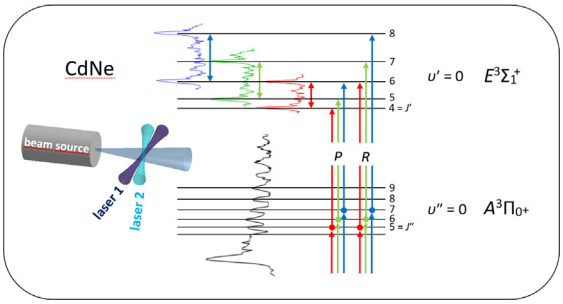

ARTICLE INFO

Article history:
Received 2 May 2021
Accepted 1 August 2021
Available online 8 August 2021

Keywords:
van der Waals molecule
CdNe complex
Free-jet expansion beam
Optical–optical double resonance
Rotational energy structure

ABSTRACT

Spectroscopic rotational characterization of two $\upsilon' = 0$ and $\upsilon' = 1$ vibrational components of the $E^3\Sigma_1^+(5s6s\ ^3S_1)$ Rydberg state of CdNe van der Waals (vdW) complex has been performed using specially designed approach. In optical–optical double resonance (OODR) process, a selective *J*-excitation has been realized using the $E^3\Sigma_1^+ \leftarrow A^3\Pi_{0^+}(5s5p\ ^3P_1)$ transition, with $\upsilon'' = 0$ level of the $A^3\Pi_{0^+}$ state as an intermediate in the excitation from $\upsilon = 0$ of the $X^1\Sigma_{0^+}(5s^2\ ^1S_0)$ state. As a result, $B'_{\upsilon=0}$ and $B'_{\upsilon=1}$ rotational constants have been determined as well as the R'_e equilibrium internuclear separation in the $E^3\Sigma_1^+$ - state potential well.

1. Introduction

Studies of lower-lying Rydberg electronic energy states of 12-group metal (M = Zn,Cd,Hg) and rare gas (Rg = Ne,Ar,Kr) MRg van der Waals (vdW) complexes have been conducted employing laser spectroscopy in supersonic beams. To excite the Rydberg states, one of the two techniques has been explored: a selective optical–optical double resonance (OODR) process where the Rydberg state is reached from the ground state by applying two consecutive laser pulses *via* an intermediate state, or less-selective vaporization-optical (VO) process that utilizes a vaporization laser pulse in the first-step excitation and produces a number of atoms in metastable states that form complexes in the intermediate electronic states for the second-step excitation.

The OODR process has been employed for HgRg in an investigation of the lowest-lying triplet $E^3\Sigma^+(6sns\ ^3S_1, n = 7-10)$ [1,2] and singlet $^1\Sigma^+(6sns\ ^1S_0, n = 7-9)$ Rydberg states [3] in HgNe, and the $E^3\Sigma^+(6s7s\ ^3S_1)$ [4] and $E^3\Sigma^+(6s8s\ ^3S_1)$ states in HgAr [2]. In case of CdRg, the $E^3\Sigma_1^+(5s6s\ ^3S_1)$ state in CdNe [5], CdAr [6] and CdKr [7] have been studied. In turn, the VO process has been applied in studies of the $e^3\Sigma^+(5s6s\ ^3S_1)$ state in CdAr [8] and $E^3\Sigma^+(4s5s\ ^3S_1)$ state in ZnAr [9].

The lower-lying Rydberg state $E^3\Sigma_1^+$ in CdNe has been investigated spectroscopically only once [5] and with vibrational resolu-

* Corresponding author.
E-mail address: tomek.urbanczyk@uj.edu.pl (T. Urbańczyk).

https://doi.org/10.1016/j.saa.2021.120248
1386-1425/

tion only. In that study, two intermediate energy states, the $A^3\Pi_{0^+}(5s5p\ ^3P_1)$ and $B^3\Sigma_1^+(5s5p\ ^3P_1)$ have been used to independently probe the $E^3\Sigma_1^+$ state potential in a widest possible range of R internucelar separations. As a result, $\upsilon' = 0,1,2 \leftarrow \upsilon'' = 0,1$ bound ← bound excitation spectra of the $E^3\Sigma_1^+ \leftarrow A^3\Pi_{0^+}$ transition were recorded. From that study, spectroscopical parameters of the $E^3\Sigma_1^+$ - state potential well were determined. In the excitation spectrum of the $E^3\Sigma_1^+ \leftarrow B^3\Sigma_1^+$ transition, a nodal structure of free ← bound transitions was observed and described as a projection of the $B^3\Sigma_1^+$ - state vibrational wave-function onto the $E^3\Sigma_1^+$ - state potential barrier, in accordance with the prediction of *ab initio* calculations [10,11]. Studies with rotational resolution have never been performed. Here, we propose to fill this gap in a specially designed experimental approach that in its nature overcomes limitation associated with spectral resolution imposed by our lasers.

2. Experimental set-up

The experimental set-up is similar to that employed in our previous studies of CdRg molecules using OODR method [12,13] so here, we limit the description only to necessary details. The source of supersonic beam with CdNe complexes was filled with cadmium pellets (purity 99.95%, natural abundance). The high purity neon (99.999%) carrier gas was delivered to the source at the pressure of 8–9 bars. The frequency-doubled pulsed dye laser (TDL90, Quantel, with a dye mixture of LDS and DCM in methanol) pumped with a 2nd harmonic of Nd:YAG laser (YG981C, Quantel) was used to first-step excitation of CdNe from the ground $X^1\Sigma_{0^+}(\upsilon = 0,J)$ to the specified ro-vibrational level in the intermediate $A^3\Pi_{0^+}(\upsilon'' = 0,J'')$ state. Second-step excitation from the $A^3\Pi_{0^+}$ to the $E^3\Sigma_1^+(\upsilon',J')$ state was realized using the second-step dye laser (TDL90, Quantel, with Coumarin 102 in methanol) pumped with a 3rd harmonic of Nd:YAG laser (Powerlite 7010, Continuum). With the help of a wavemeter (WSU30, High Finesse), the spectral bandwidth of both dye lasers was estimated to be 0.1 cm^{-1}(-FWHM). The pulses of two Nd:YAG lasers were synchronized with the pulsed molecular beam source with the help of the digital delay generator (DG645, Stanford Research Systems). Both counter-propagating laser beams intersected the molecular beam at the distance of 19 mm from the source nozzle. During the experiment, the wavenumber of the first-step excitation laser was fixed, whereas the second-step excitation laser was tuned with a 0.05–0.15 cm^{-1} step. The laser induced fluorescence (LIF) signals associated with both OODR transitions were registered by two photomultipliers (PMT) oriented perpendicularly to the direction of molecular beam. Details of the detection procedure as well as the integration and data accumulation processes can be found in [14].

3. Results

3.1. Determination of rotational constants $B'_{\upsilon=0}$ and $B'_{\upsilon=1}$

Fig. 1a) presents the profile of vibrational component in LIF excitation spectrum recorded using the $A^3\Pi_{0^+}(\upsilon'' = 0,J'') \leftarrow X^1\Sigma_{0^+}(\upsilon = 0,J)$ transition in which the rotational structure was partly resolved. The spectrum was reported, *e.g.* by Kvaran *et al.* [15] and Funk *et al.* [16]. The characteristics of the $X^1\Sigma_{0^+}$ and $A^3\Pi_{0^+}$ - state potentials, as well as of the $E^3\Sigma_1^+$ - state, are collected in Table 1.

Due to the narrow spectral bandwidth of the first-step excitation laser (compare with blue vertical bars in Fig. 1), for each chosen laser wavenumber, CdNe complexes were excited to one J'' rotational level in the $A^3\Pi_{0^+}(\upsilon'' = 0)$ component (compare with Table 2). Fig. 2 presents LIF excitation spectra recorded using the $E^3\Sigma_1^+(\upsilon' = 0,1) \leftarrow A^3\Pi_{0^+}(\upsilon'' = 0)$ transitions in CdNe for second-step excitations starting from different J'' selectively excited in the first step of OODR process (see Fig. 1). Each spectrum contains two distinctive lines with increasing distance between them as J'' increases. The lines in the spectra can be identified as belonging to two rotational P- and R- branches which correspond to the excitation associated with the change the initial J'' by −1 and +1, respectively. Due to the selection rules, the spectra should contain three rotational P-,Q- and R- branches. However, Okunishi *et. al.* [1] showed, that in case of analogous HgNe complex the intensity of Q-branch can be significantly lower than, *e.g.* P- branch (compare the intensities of bandheads in Fig. 4 of Ref. [1]). In fact, in few cases of spectra registered in our experiment, there exists an additional line with low intensity located between two more intense lines assigned to P- and R- branches (compare with Fig. 2(b)).

Measuring separations between P- and R- branch lines shown in Fig. 2 allows for determination of the $E^3\Sigma_1^+$- state rotational constant B'_υ for a particular vibrational level υ'. Limiting the reasoning to the first order of approximation in the expression for the E'_{rot} rotational energy component in the total energy, we define

$$E'_{rot} = B'_\upsilon J'(J'+1). \tag{1}$$

During the excitation from J'' rotational level, $J'_R = J'' + 1$ and $J'_P = J'' - 1$ for R- and P- branches, respectively. Consequently, we obtain

$$\begin{aligned} E'_{rot\,R} &= B'_\upsilon(J''+1)(J''+2), \\ E'_{rot\,P} &= B'_\upsilon J''(J''-1), \end{aligned} \tag{2}$$

which leads to Δ defined as the difference between energies of two rotational lines originating from the same J'' and associated with P- and R- branches. It can be expressed as

$$\Delta = E'_{rot\,R} - E'_{rot\,P} = 4B'_\upsilon \cdot J'' + 2B'_\upsilon. \tag{3}$$

According to Eq. (3), the separation Δ increases linearly with J'', which here, due to the first-step selective excitation, is J''_R. The rotational constants B'_υ can be determined from the slope $(4B'_\upsilon)$ of the linear regression of $\Delta(J''_R)$ dependency as well as from its intersection with the vertical axis $(2B'_\upsilon)$. Fig. 3 shows the linear regression of $\Delta(J''_R)$ plotted for $\upsilon' = 0$ and $\upsilon' = 1$ according to the experimental data presented in Figs. 2(a) and 2(b), respectively. The determined $B'_{\upsilon=0}$ and $B'_{\upsilon=1}$ rotational constants for the $E^3\Sigma_1^+$ Rydberg state are collected in Table 3.

It should be noticed that the isotopic structure of CdNe has not been resolved in the experiment due to small υ' in the recorded transitions. Consequently, we assumed the obtained vibrational constants as these corresponding to the most abundant CdNe isotopologue, *i.e.* $^{114}Cd^{20}Ne$. Simulation shows that for CdNe isotopologues with abundances larger than 3% the isotopic shifts between the most separated isotopologues (*i.e.* $^{110}Cd^{20}Ne$ and $^{116}Cd^{20}Ne$) are equal 0.042 cm^{-1} for the intermediate $A^3\Pi_{0^+}(\upsilon'' = 0)$, and 0.096 cm^{-1} (υ'= 0) or 0.181 cm^{-1} (υ'= 1) for the final $E^3\Sigma_1^+$ states. For the same isotopologues, isotopic shifts simulated for the observed transitions $E^3\Sigma_1^+(\upsilon') \leftarrow A^3\Pi_{0^+}(\upsilon'' = 0)$ are even smaller: 0.054 cm^{-1} and 0.14 cm^{-1} for υ' = 0 and υ' = 1, respectively.

3.2. Simulation of profile of the $\upsilon' = 1 \leftarrow \upsilon'' = 0$ vibrational component

To verify the correctness of the obtained $E^3\Sigma_1^+$- state rotational constants, we recorded the profile of the $\upsilon' = 1 \leftarrow \upsilon'' = 0$ vibrational component of the $E^3\Sigma_1^+ \leftarrow A^3\Pi_{0^+}$ transition with the first-

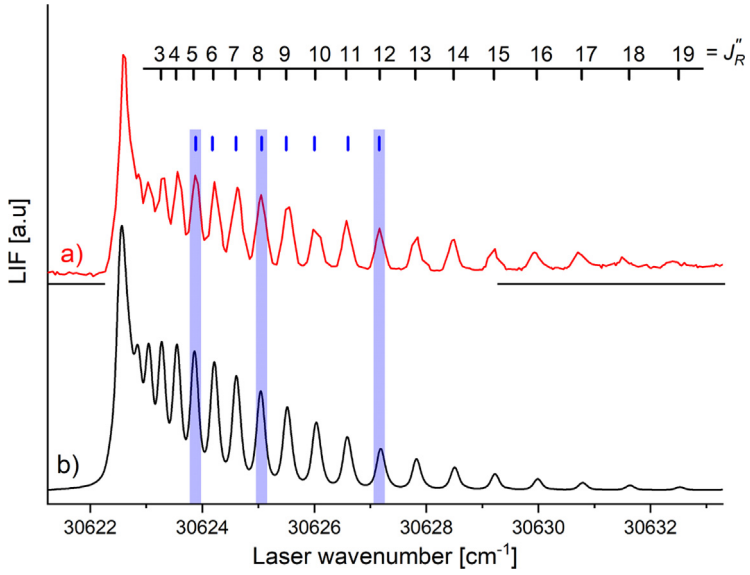

Fig. 1. Profile of the vibrational component of LIF excitation spectrum of the $A^3\Pi_{0^+}(\upsilon''=0,J''_R) \leftarrow X^1\Sigma_{0^+}(\upsilon=0,J)$ transition in CdNe complex (a) recorded in experiment and (b) simulated. The simulation was made using Level [18] and Pgopher [19] programs assuming: $T_{rot}=5\ K$ rotational temperature, $\Delta_{Gauss}=\Delta_{Lorentz}$=0.1 cm $^{-1}$ Gaussian (responsible for a residual Doppler broadening associated with the transversal divergence of the molecular beam) and Lorentzian (responsible for a bandwidth of the laser beam) broadenings, and a Morse - function representations of the $X^1\Sigma_{0^+}$ and $A^3\Pi_{0^+}$ states with characteristics from Table 1. The assignment of J''_R quantum numbers in the resolved rotational structure of the *R*-branch is shown above the spectra. Rotational levels used as intermediate in OODR process (blue tics, compare with Fig. 2) and and three vertical bars representing the laser bandwidth (±0.1 cm^{-1}) are also depicted.

Table 1
Spectroscopic characteristics of the $E^3\Sigma_1^+(6^3S_1)$, $A^3\Pi_{0^+}(5^3P_1)$ and $X^1\Sigma_{0^+}(5^1S_0)$ states in CdNe. All parameters are expressed in (cm^{-1}), except the R_e which is expressed in (Å).

	$E^3\Sigma_1^+$	$A^3\Pi_{0^+}$	$X^1\Sigma_{0^+}$
ω_e	56.6 ± 3.0[a]	22.6[b]	13.2[d]
$\omega_e x_e$	8.8 ± 0.4[a]	1.6[b]	1.15[d]
R_e	3.21 ± 0.05[a]	3.62[b]	4.26[b]
	3.04 ± 0.07[e]		
	2.86 ± 0.07[f]		
	3.00 ± 0.07[g]		
	2.98 ± 0.06[h]		
D_e	91.0 ± 4.0[a]	79.8[c]	37.9[c]

[a] Ref. [5].
[b] Ref. [15].
[c] $D_e \approx \frac{\omega_e^2}{4\omega_e x_e}$.
[d] Ref. [16].
[e] Ref. [11], *ab initio* result, the R_e uncertainty determined as a half of difference between *R* of neighbouring points.
[f] Ref. [10], *ab initio* result, the R_e uncertainty determined as in [e].
[g] Ref. [17], *ab initio* result, the R_e uncertainty determined as in [e].
[h] This work, determined from $B'_{\upsilon=0}$ and $B'_{\upsilon=1}$ (recommended value).

Table 2
The excited rotational levels of the $A^3\Pi_{0^+}(\upsilon''=0)$ vibrational component in CdNe for different laser wavenumbers in (cm^{-1}) used in the $A^3\Pi_{0^+}(\upsilon''=0,J''_R) \leftarrow X^1\Sigma_{0^+}(\upsilon=0,J)$ transition.

Laser wavenumber	Excited J''_R
30623.9	5
30624.2	6
30624.6	7
30625.1	8
30625.5	9
30626.0	10
30626.6	11
30627.2	12

step excitation laser set at the band-head of the $A^3\Pi_{0^+}(\upsilon''=0) \leftarrow X^1\Sigma_{0^+}(\upsilon=0)$ transition (ν= 30622.6 cm^{-1}). The recorded profile along with its simulation is shown in Fig. 4. In this case, not a single but several lower-lying rotational levels J'' are excited in the $A^3\Pi_{0^+}$ - state $\upsilon''=0$ level. The simulation performed using Level [18] and Pgopher [19] programs, employing potential parameters (Table 1) and and rotational constants obtained here (Table 3), shows a very good agreement with the experimental profile confirming reliability of results obtained in this study.

3.3. Determination of the R'_e for the $E^3\Sigma_1^+$ state

The rotational constants B_υ can be expressed as

$$B_\upsilon = B_e - \alpha_e\left(\upsilon+\frac{1}{2}\right), \tag{4}$$

where B_e is a rotational constant at the equilibrium internuclear distance ($R=R_e$) and α_e is a constant. Having determined the $B_{\upsilon=0}$ and $B_{\upsilon=1}$, one can express rotational constant B_e as

$$B_e = \frac{3B_{\upsilon=0} - B_{\upsilon=1}}{2}. \tag{5}$$

The constant B_e is related with the R_e using formula:

$$R_e = \sqrt{\frac{h}{8\pi^2 c\mu B_e}}, \tag{6}$$

where h, c and μ are Planck constant, the speed of light and CdNe reduced mass, respectively. Using the $B'_{\upsilon=0}$ and $B'_{\upsilon=1}$ determined in this work, we calculated B'_e=0.112±0.002 cm^{-1} which lead to $R'_e = 2.98 \pm 0.06$ Å for the $E^3\Sigma_1^+$ Rydberg state of CdNe. As one can see in Table 1, R'_e obtained in this work agrees more with results of *ab initio* calculation of [11,10,17] than with previous result [5] obtained from the analysis of intensities of vibrational components.

3.4. Conclusions

We presented a direct experimental rotational characterization of two $\upsilon'=0$ and $\upsilon'=1$ vibrational components of the $E^3\Sigma_1^+$ (6^3S_1) Rydberg state of CdNe vdW complex. It relied on a selective *J*-level

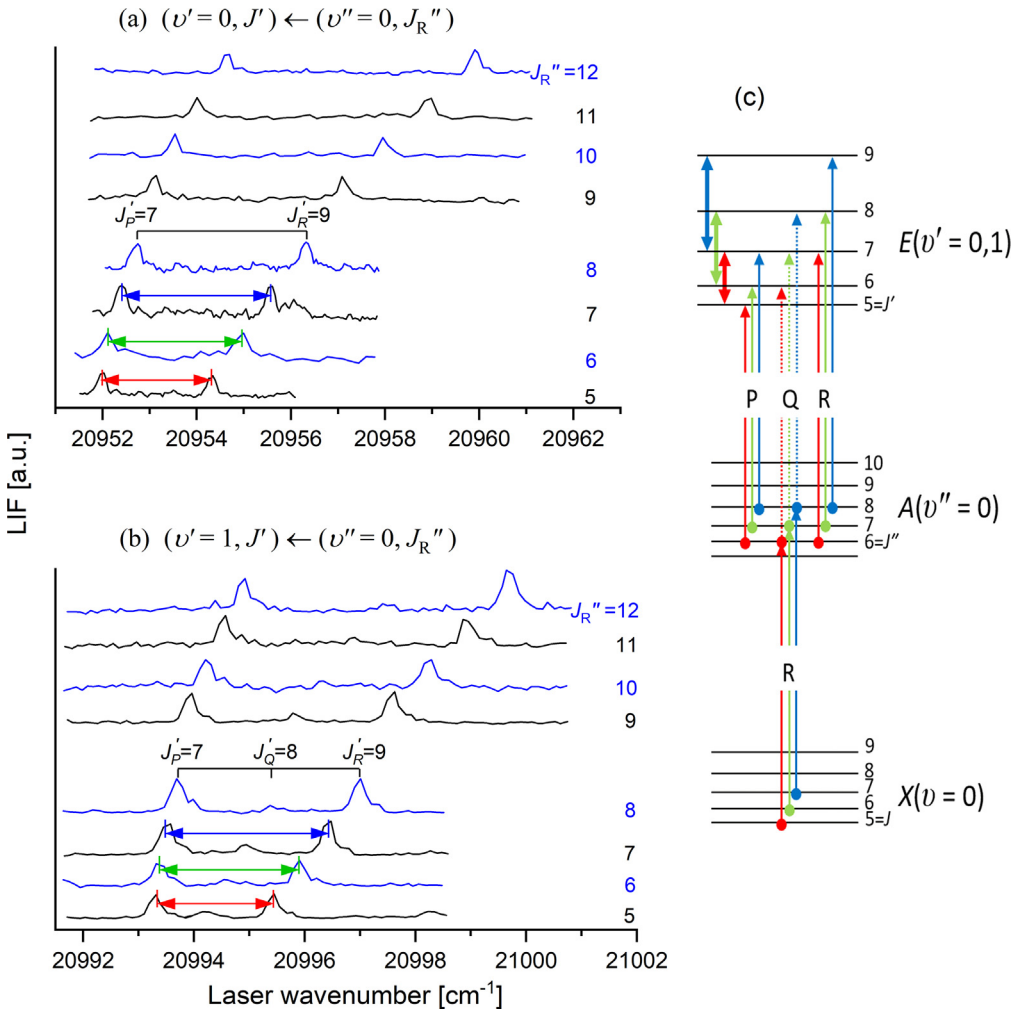

Fig. 2. The experimental LIF excitation spectra recorded using the $E^3\Sigma_1^+ \leftarrow A^3\Pi_{0^+}$ transition in CdNe for (a) $(\upsilon' = 0, J') \leftarrow (\upsilon'' = 0, J_R'')$ and (b) $(\upsilon' = 1, J') \leftarrow (\upsilon'' = 0, J_R'')$. For $(\upsilon' = 0, J_R'' = 8)$ and $(\upsilon' = 1, J_R'' = 8)$, assignment of J' belonging to rotational branches is shown. (c) Rotational energy structure of the vibrational components involved in the analyzed selective J' excitation. Details in text.

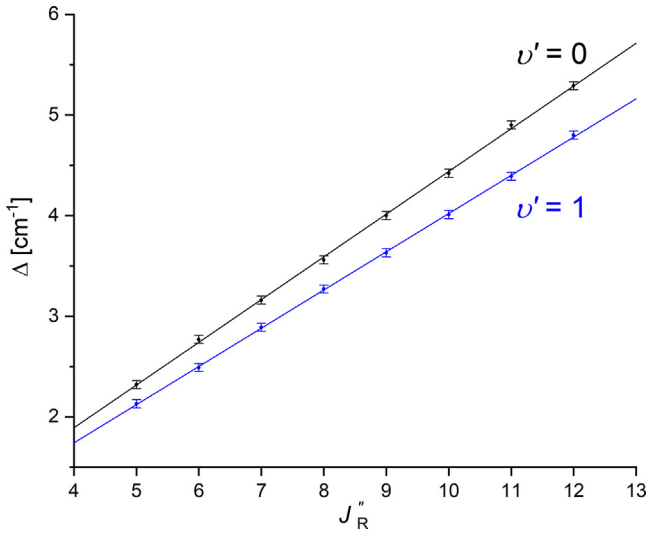

Fig. 3. Experimental separations $\Delta(J_R'')$ between energies of rotational transitions belonging to $P(J_R'' - 1)$ and $R(J_R'' + 1)$ branches (compare with Fig. 2 and Eq. 3). Results for $\upsilon' = 0 \leftarrow \upsilon'' = 0$ and $\upsilon' = 1 \leftarrow \upsilon'' = 0$ vibrational components of the $E^3\Sigma_1^+ \leftarrow A^3\Pi_{0^+}$ transition are shown. Rotational constants $B'_{\upsilon=0}$ and $B'_{\upsilon=1}$ obtained from the linear regression of the plot are collected in Table 3. Details in text.

Table 3
Rotational characteristics of the $E^3\Sigma_1^+(6^3S_1)$ Rydberg state in CdNe determined in this study. B'_υ and B'_e are expressed in (cm^{-1}).

$B'_{\upsilon=0}$	$B'_{\upsilon=1}$	B_e
0.106±0.001[a]	**0.095± 0.001**[a]	0.112±0.002[c]
0.092[b]	0.080[b]	

[a] From a slope of the linear regression of $\Delta(J_R'')$ plot, recommended value.
[b] Obtained using Level program [18] from characteristics of the $E^3\Sigma_1^+$ - state potential (see Table 1).
[c] This work (see Eq. 5).

excitation realized using the $E^3\Sigma_1^+ \leftarrow A^3\Pi_{0^+}(5^3P_1)$ transition, with $\upsilon'' = 0$ level of the $A^3\Pi_{0^+}$ state as an intermediate in the excitation from $\upsilon = 0$ of the $X^1\Sigma_{0^+}(5^1S_0)$ state in OODR process. The study resulted in $B'_{\upsilon=0}$ and $B'_{\upsilon=1}$ rotational constants as well as the R'_e equilibrium internuclear separation for the $E^3\Sigma_1^+$- state potential well.

Declaration of Competing Interest

The authors declare that they have no known competing financial interests or personal relationships that could have appeared to influence the work reported in this paper.

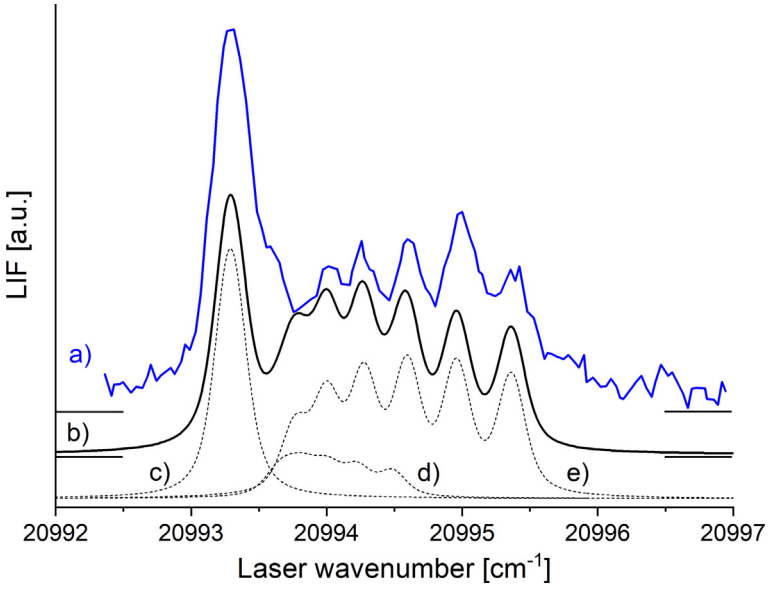

Fig. 4. (a) LIF excitation spectrum recorded using the $E^3\Sigma_1^+(v'=1) \leftarrow A^3\Pi_{0^+}(v''=0)$ transition in CdNe with first-step excitation of lower-lying J'' levels in the $A^3\Pi_{0^+}(v''=0)$. (b) Simulation of rotational *P*-, *Q*- and *R*- branches for CdNe isotopologues with abundances larger than 3%, performed using Pgopher [19] program, with potential parameters from Table 1 and rotational constant from Table 3, for $J''_{max}=6$, rotational temperature T_{rot}=5 K, and $\Delta_{Gauss}=\Delta_{Lorentz}$=0.15 cm^{-1} Gaussian and Lorentzian broadenings. (c), (d) and (e) Contributions from *P*-,*Q*- and *R*- branches, respectively. Intensity of the *Q*-branch was adjusted according to these of *P*- and *R*- branches as observed in the experiment (see Fig. 2b). All simulations take into account an isotopic shift between considered CdNe isotopologues as approximately one order of magnitude smaller than their rotational structure.

Acknowledgement

The research was financed by the National Science Centre Poland (UMO-2015/17/B/ST4/04016).

References

[1] M. Okunishi, K. Yamanouchi, K. Onda, S. Tsuchiya, Interatomic potential of the HgNe van der Waals complex in the E($^3\Sigma^+$) Rydberg state, J. Chem. Phys. 98 (1993) 2675–2681, https://doi.org/10.1063/1.464149.

[2] K. Onda, K. Yamanouchi, M. Okunishi, S. Tsuchiya, Interatomic potentials of triplet s-Rydberg series of HgNe and HgAr van der Waals dimers, J. Chem. Phys. 101 (1994) 7290–7299, https://doi.org/10.1063/1.468286.

[3] K. Onda, K. Yamanouchi, Interatomic potentials of singlet s-Rydberg series of a HgNe van der Waals dimer: Evidence for stabilization by superexchange interaction, J. Chem. Phys. 102 (1995) 1129–1140, https://doi.org/10.1063/1.469171.

[4] M. Duval, O.B. D'Azy, W.H. Breckenridge, C. Jouvet, B. Soep, The structure of several electronic states of the Hg–Ar complex as determined by laser double resonance in a supersonic jet, J. Chem. Phys. 85 (1986) 6324–6334, https://doi.org/10.1063/1.451462.

[5] J. Koperski, M. Czajkowski, Spectroscopical characterization of CdNe van der Waals complex in the E^1($^3\Sigma^+$) Rydberg state, Chem. Phys. Lett. 357 (2002) 119–125, https://doi.org/10.1016/S0009-2614(02)00464-5.

[6] J. Koperski, M. Czajkowski, The structure of the lowest electronic Rydberg state of CdAr complex determined by laser double resonance method in a supersonic jet-expansion beam, Spectrochim. Acta A 59 (2003) 2435–2448, https://doi.org/10.1016/S1386-1425(02)00396-7.

[7] J. Koperski, M. Czajkowski, Electronic structure of the CdKr lowest Rydberg state determined from laser-excitation spectra using supersonic beam and double optical resonance methods, Phys. Rev. A 69 (2004) 042509, https://doi.org/10.1103/PhysRevA.69.042509.

[8] R.R. Bennett, W.H. Breckenridge, Van der Waals bonding in the lowest electronic states of MgAr, ZnAr, CdAr, and HgAr: Spectroscopic characterization of the b$^3\Pi_2$ and e$^3\Sigma^+$ states of the CdAr molecule, J. Chem. Phys. 96 (1992) 882–890, https://doi.org/10.1063/1.462108.

[9] R.R. Bennett, W.H. Breckenridge, Spectroscopic characterization of the $a^3\Pi_0^-, b^3\Pi_2, and E^3\Sigma^+$ states of ZnAr, J. Chem. Phys. 92 (1990) 1588–1597, https://doi.org/10.1063/1.458091.

[10] E. Czuchaj, H. Stoll, Calculation of ground- and excited-state potential energy curves for the Cd-rare gas complexes, Chem. Phys. 248 (1999) 1–16, https://doi.org/10.1016/S0301-0104(99)00247-5.

[11] E. Czuchaj, M. Krośnicki, H. Stoll, Quasirelativistic valence ab initio calculation of the potential-energy curves for Cd–rare gas atom pairs, Theor. Chem. Acc. 105 (2001) 219–226, https://doi.org/10.1007/s002140000206.

[12] T. Urbanczyk, J. Dudek, J. Koperski, Isotopologue-selective excitation studied via optical-optical double resonance using the $E^3\Sigma_1^+(6^3S_1) \leftarrow A^3\Pi_0^+(5^3P_1) \leftarrow X^1\Sigma_{0^+}(5^1S_0)$ transitions in CdAr and CdKr van der Waals complexes, J. Quant. Spectrosc. Radiat. Transf. 212 (2018) 32–38, https://doi.org/10.1016/j.jqsrt.2018.03.013.

[13] T. Urbańczyk, M. Krośnicki, A. Kędziorski, J. Koperski, The $E^3\Sigma_1^+(6^3S_1) \leftarrow A^3\Pi_{0+}(5^3P_1)$ transition in CdAr revisited: The spectrum and new analysis of the $E^3\Sigma_1^+$ Rydberg state interatomic potential, Spectrochim. Acta A 196 (2018) 58–66, https://doi.org/10.1016/j.saa.2018.01.075.

[14] T. Urbańczyk, J. Koperski, Profiles of $(v';v''=0)$ bands recorded in excitation spectra using $b^3 0_u^+ \leftarrow X^1 0_g^+$ transitions in $Cd_2 and B^3 1 \leftarrow X^1 0^+$ transitions in CdAr, Mol. Phys. 112 (2014) 2486–2494, https://doi.org/10.1080/00268976.2014.933901.

[15] A. Kvaran, D.J. Funk, A. Kowalski, W.H. Breckenridge, Spectroscopic characterization of the $X(^1 0^+)$ and $A(^3 0^+)$ states of CdNe, CdAr, CdKr, and CdXe, J. Chem. Phys. 89 (1988) 6069–6080, https://doi.org/10.1063/1.455422.

[16] D.J. Funk, A. Kvaran, W.H. Breckenridge, Spectroscopic characterization of the lowest singlet states of CdNe, CdAr, and CdKr, J. Chem. Phys. 90 (1989) 2915–2926, https://doi.org/10.1063/1.455943.

[17] M. Krośnicki, Numerical data of adiabatic potential energy curves and transition dipole moments for diatomic molecules, http://iftia9.univ.gda.pl/kroch/b4_b5/CdNe/CdNe_symmetry_2_as_final.dat, accessed: 2021-04-30.

[18] R.J. Le Roy, LEVEL: A computer program for solving the radial Schrödinger equation for bound and quasibound levels, J. Quant. Spectrosc. Radiat. Transf. 186 (2017) 167–178, https://doi.org/10.1016/j.jqsrt.2016.05.028.

[19] C.M. Western, PGOPHER: A program for simulating rotational, vibrational and electronic spectra, J. Quant. Spectrosc. Radiat. Transf. 186 (2017) 221–242, https://doi.org/10.1016/j.jqsrt.2016.04.010.

Spectrochimica Acta Part A: Molecular and Biomolecular Spectroscopy 282 (2022) 121655

Contents lists available at ScienceDirect

Spectrochimica Acta Part A:
Molecular and Biomolecular Spectroscopy

journal homepage: www.journals.elsevier.com/spectrochimica-acta-part-a-molecular-and-biomolecular-spectroscopy

The lowest-lying Rydberg state of CdAr van der Waals complex: The improved characterization of the interatomic potential

J. Sobczuk *, T. Urbańczyk, J. Koperski

Smoluchowski Institute of Physics, Faculty of Physics, Astronomy and Applied Computer Science, Jagiellonian University, Łojasiewicza 11, 30-348 Kraków, Poland

HIGHLIGHTS

- Shape of the shallow outer well and potential barrier of the double-well $E^3\Sigma_1^+ 6^3S_1$ state in CdAr molecule experimentally determined.
- υ'-assignment of the $E^3\Sigma_{1out}^+\upsilon' \leftarrow B^3\Sigma_1^+\upsilon''$ transitions corrected and new values of vibrational constants for the outer well determined.
- Determination of the $E^3\Sigma_{1out}^+$ - state outer-well $R_{e'out}$ equilibrium distance improved.
- Height E_b, position R_b, and shape of the potential barrier of the $E^3\Sigma_1^+$ state estimated based on free ← bound $E^3\Sigma_1^+ \leftarrow B^3\Sigma_1^+\upsilon''$ excitation spectra.

GRAPHICAL ABSTRACT

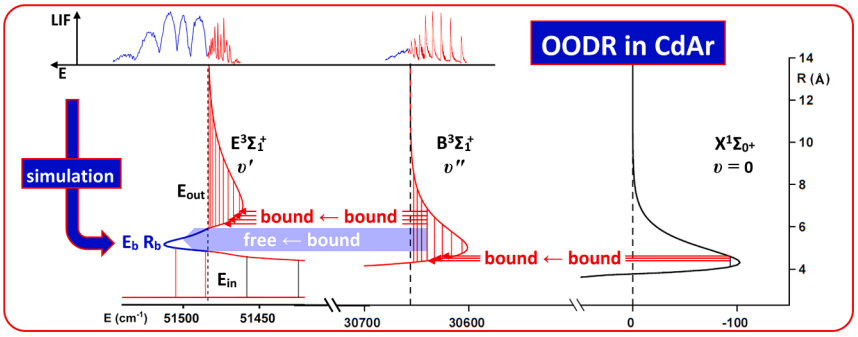

ARTICLE INFO

Keywords:
Optical-optical double resonance (OODR)
van der Waals CdAr complex
Rydberg electronic state
Potential barrier
Vibrational characterization
Free - bound transitions

ABSTRACT

Previous characterization of the double-well $E^3\Sigma_1^+(6^3S_1)$ - Rydberg state outer potential well $(E^3\Sigma_{1\ out}^+)$ in CdAr van der Waals (vdW) complex has been based on detection of the $E^3\Sigma_1^+ \leftarrow B^3\Sigma_1^+(5^3P_1)$ (υ''=0–2) transitions only. In this study, the gap in the limited characterization of the $E^3\Sigma_{1\ out}^+$ shallow well and the neighbouring potential barrier has been filled by recording bound (υ') ← bound (υ''=1–4) and free ← bound (υ''=0–4) excitation spectra. The result, spectroscopic description of the $E^3\Sigma_{1\ out}^+$ well along with the potential barrier have been concluded from simulations of the recorded spectra. The results were compared with those published previously.

1. Introduction

In different branches of atomic and molecular physics there is rapidly growing interest in long-range forces acting between atoms interacting in variety of traps, in experiments of matter-wave interferometry and photo-association of cold molecules [1]. The recent advances in laser cooling and optical trapping techniques as well as two- and three-step photo-association processes of cold molecules have been largely responsible for the renewed interest in the studies of the long-range region of internuclear separations R [2,3]. Knowledge of the complex shape of the interatomic potentials facilitates an optimum design of the photo-association schemes. Among the various available techniques, diatomic molecular spectroscopy has proved to be the most effective and precise way to obtain information about the interaction between the two entities *e.g.*, M and M in M_2, or M and Ng in MNg complexes (M and Ng are metal and noble gas atoms, respectively) [1] in the experimentally

* Corresponding author.
E-mail address: joanna.b.dudek@doctoral.uj.edu.pl (J. Sobczuk).

https://doi.org/10.1016/j.saa.2022.121655
Received 31 March 2022; Received in revised form 14 July 2022; Accepted 17 July 2022
Available online 21 July 2022

available range of R.

A double-well structure of the lowest-lying Rydberg $E^3\Sigma_1^+(6^3S_1)$-state interatomic potential of CdAr has been predicted by Czuchaj and Stoll and Czuchaj and co-workers in their *ab initio* calculations of potential energy curves (PECs) of the CdRg complexes (Rg-rare gas atom) [4,5]. However, the early laser spectroscopy experiments [6,7] have not supported this prediction as they were focused on the characterization of the inner (deeper) $E^3\Sigma_1^+$-state potential well only. That picture had been maintained until Koperski and Czajkowski concluded in their experimental study [8] that the $E^3\Sigma_1^+$-state potential does indeed possess a double-well structure. According to their work, the inner $(E^3\Sigma_{1\ in}^+)$ and the outer $(E^3\Sigma_{1\ out}^+)$, 1309.5-cm^{-1} and 24.2-cm^{-1} deep potential wells, respectively, have been separated by a potential barrier 48.0 cm^{-1} in height with respect to the 6^3S_1 atomic asymptote. They have also found that the deeper and shallower wells, and the barrier were located at R estimated as 2.85 Å, 5.60 Å and 4.70 Å, respectively. After that, there has been a series of investigations that focused at more detailed characterization of the $E^3\Sigma_{1\ in}^+$ [9–10] and $E^3\Sigma_{1\ out}^+$ [9,12] potential wells, and those studies were reasonably accurate with respect to the former [8], however, they left considerable uncertainty concerning characterization of the $E^3\Sigma_{1\ out}^+$ as well as determination of the position R_b and height of the potential barrier E_b.

Till now, as far as the characterization of the $E^3\Sigma_{1\ out}^+$ is concerned, it has been based on detection and simulation of the $E^3\Sigma_{1\ out}^+ \leftarrow B^3\Sigma_1^+(5^3P_1)$ bound(v') ← bound(v''=0–2) transitions or not-simulated free ← bound (v''=0–2) transitions only. The characterization has not exhausted other intermediate v'' vibrational levels sufficiently populated in the $B^3\Sigma_1^+ \leftarrow X^1\Sigma_{0^+}(5^1S_0)$ first-step transition in optical–optical double resonance (OODR) process applied in the studies. From those studies, new values for $R_e'_{out}$ (7.63 Å [9], 6.90 Å [12]) and $D_e'_{out}$ (19.14 cm^{-1} [9], 19.10 cm^{-1} [12]) have been obtained. Moreover, new estimation of the height of the potential barrier E_b between 21.1 cm^{-1} and 39.4 cm^{-1} resulted from the recorded $v' \leftarrow v''$=6 progression using the $E^3\Sigma_{1\ in}^+ \leftarrow A^3\Pi_{0^+}(5^3P_1)$ transition [11], but more accurate description of the shape of the outer-well has not been performed.

From the theoretical point of view, previous [5,13] and new [14] *ab initio* calculations performed by Czuchaj *et al.*, Strojecki *et al.*, and Krośnicki *et al.*, respectively, provided values of 7.94 Å [5], 7.67 Å [13] and 7.36 Å [14] for the $R_e'_{out}$, 15.5 cm^{-1} [5], 17 cm^{-1} [13] and 16 cm^{-1} [14] for the $D_e'_{out}$, as well as 4.96 Å and 46 cm^{-1} [14] for the R_b and E_b, respectively.

In this article, we have taken on filling the gap in the limited characterization of the $E^3\Sigma_1^+$-state outer potential well and the potential barrier, and have also used more available bound (v') ← bound (v''=1–4) and free ← bound (v''=0–4) LIF excitation spectra recorded using the $E^3\Sigma_{1\ out}^+ \leftarrow B^3\Sigma_1^+$ transition. As a result, more reliable and consistent description of the $E^3\Sigma_{1\ out}^+$ along with the potential barrier has been derived from simulations of the recorded spectra. Together with our previous determination of the $E^3\Sigma_{1\ in}^+$ [11], a consistent PEC of the whole $E^3\Sigma_1^+$ state has been derived experimentally.

2. Experimental set-up

An experimental set-up is similar to that used in OODR studies of CdRg (Rg = Ne, Ar, Kr) complexes previously reported from our laboratory [10–12,15]. Here, we limit the description to necessary details.

The CdAr complexes were produced using a high-temperature, high-pressure pulsed source for the supersonic molecular beam [16]. The source was filled with cadmium pellets (purity 99.95 %, natural abundance) and a carrier gas of high purity argon (99.999 %) at a pressure of 2–5 bar. Operation of the source was synchronized with two pulsed laser systems that were used to excite CdAr molecules to the $E^3\Sigma_1^+$ state from the $X^1\Sigma_{0^+}$ state *via* intermediate $B^3\Sigma_1^+$ state. Synchronization between the pulsed source and the laser systems was realized using a digital delay generator.

The first-step excitation laser system consisted of a frequency-doubled Nd:YAG laser (YG981C, Quantel)-pumped-dye laser (TDL90, Quantel) which used a dye mixture of LDS (33 %) and DCM (67 %) in ethanol. It was used to excite CdAr from the ground $X^1\Sigma_{0^+}(v=0)$ to the specified v'' vibrational level in the $B^3\Sigma_1^+$ state. The frequency of the second-step excitation from the $B^3\Sigma_1^+$ (v'') was swept over a profile of the v' vibrational components in the $E^3\Sigma_1^+$ final state or over an undulated structure of the free ← v'' transitions. The second laser system consisted of a Nd:YAG laser (Powerlite 7010, Continuum)-pumped-dye laser (TDL90, Quantel) which used Coumarin 102 in methanol to cover the range of studied spectra. The dye laser output was tuned over the range from 20800 cm^{-1} to 21000 cm^{-1} (approx. 476–480 nm) in 0.04–0.3-cm^{-1} steps. According to the measurement with a wavemeter (WSU30, HighFinesse), linewidths of fundamental frequencies of both TDL90 lasers were about 0.07 cm^{-1} and 0.1 cm^{-1} for the first- and second-step lasers, respectively.

The two dye-laser outputs were directed in opposite directions into a vacuum chamber where they intersected the molecular beam at a distance of 18 mm from the source nozzle (0.2 mm orifice diameter). During the experiment, LIF signal from the $B^3\Sigma_1^+$ (v'') ← $X^1\Sigma_{0^+}(v=0)$ transitions was monitored using first photomultiplier (PM) tube (9893QB/350, Electron Tubes) whereas LIF signal from the $E^3\Sigma_1^+ \leftarrow B^3\Sigma_1^+(v'')$ transitions was recorded using second PM tube (R585, Hamamatsu). The PM tubes were oriented at 45- and 90-degree angles to the direction of the laser beams and perpendicular to the molecular beam. The second PM tube was screened using a UV-absorbing filter to remove strong emission induced by the first excitation process. For each second-dye-laser tuning step, LIF signals that corresponded to 64 dye-laser shots were averaged using a digital oscilloscope (TDS 2024B, Tektronix). The resulting average waveforms were saved in a computer memory along with parameters describing the corresponding tuning step including the dye-laser frequency and its bandwidth measured with the wavemeter.

3. Results and discussion

3.1. Bound ← bound LIF excitation spectra

3.1.1. New v'-assignment and correction to vibrational characteristics

The bound ← bound part of LIF excitation spectra of the $E^3\Sigma_{1\ out}^+(v') \leftarrow B^3\Sigma_1^+(v''=1,2,3,4)$ transitions are presented (see Fig. 1a) with respect to the position of the $X^1\Sigma_{0^+}$ ground-state asymptote. Detection of the $v' \leftarrow v''$ transitions originating from higher vibrational states (v''=3,4) led to a significant change (as compared to the earlier studies [12]) in the description of the $E^3\Sigma_{1\ out}^+$. For v''=3 and 4, a distinct additional component, that previously had not been taken into consideration, has been observed (see green vertical arrow in Fig. 1a). The component has been assigned to v'=0 ← v'' transition since its position follows the linearity of Birge-Sponer (B-S) plot presented in Fig. 2. Using the B-S plot and new v' - assignment, new vibrational characteristics of the $E^3\Sigma_{1\ out}^+$ have been determined and collected in Table 1. It was assumed that due to the shallow character of the $E^3\Sigma_{1\ out}^+$, a formula $D_e \approx \omega_e^2/4\omega_e x_e$, which results from linearity of B-S plot will accurately approximate the outer-well depth, and a Morse function in the form:

$$E(R) = D_e\left\{1 - e^{-\beta(R-R_e)}\right\}^2 - D_e + E_{asympt} \quad (1)$$

will give a good representation of the $E^3\Sigma_{1\ out}^+$ potential.

3.1.2. New estimate for the $R_e'_{out}$ equilibrium distance of the $E^3\Sigma_1^+$-state outer well

Determination of the $E^3\Sigma_{1\ out}^+$ - well equilibrium distance $R_e'_{out}$ was

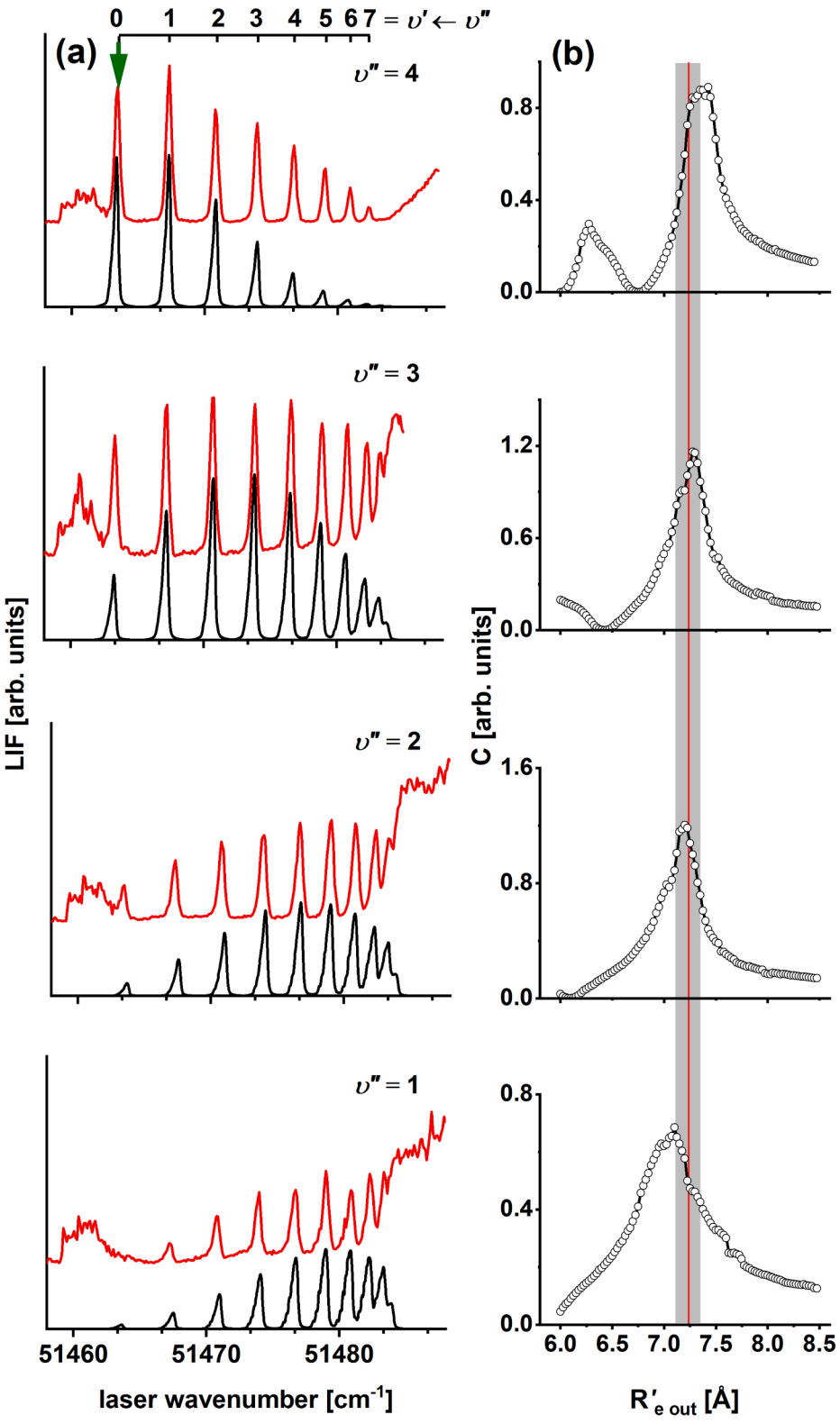

Fig. 1. (a) Experimental LIF excitation spectra of the $E^3\Sigma_{1\ out}^+(v')\leftarrow B^3\Sigma_1^+(v'')$ bound ← bound transitions in CdAr recorded for v''=1,2,3,4 (red lines), and their simulations [18,19] (black lines). Horizontal axis wavenumbers are given with respect to the $X^1\Sigma_{0+}$ ground-state asymptote. Position of the v'=0 ← v'' component that has not been previously recorded [12] is depicted with green arrow. The $E^3\Sigma_{1\ in}^+(v'=17)\leftarrow B^3\Sigma_1^+(v'')$ vibrational component is located at approx. 51460 cm^{-1}. (b) The agreement coefficient C (see Eq. (2)) plotted as a function of $R_{e\ out}'$. It describes agreement between experimental and simulated intensities of the vibrational components in the $E^3\Sigma_{1\ out}^+(v')\leftarrow B^3\Sigma_1^+(v'')$ transitions. Position of the determined equilibrium distance and its uncertainty $R_{e\ out}' = 7.235 \pm 0.121$ Å is depicted by red line and grey margin, respectively. See text for details.

based on analysis a Franck-Condon (F-C) envelope of $v'\leftarrow v''$ vibrational components observed in the $E^3\Sigma_{1\ out}^+\leftarrow B^3\Sigma_1^+$ transition, *i.e.* on their recorded relative intensities. The respective procedure that was applied in the current study had been described in detail in Ref. [12]. For v'' = 1,2,3 and 4, intensities of the vibrational components recorded in the experiment were compared with the simulated ones. Similarly to the analysis performed in Ref. [12], the simulation was iterated through values of $R_{e\ out}'$ within the range 6.0 Å–8.5 Å with 0.025-Å step. So-called agreement coefficient C was calculated according to the formula:

$$C\left(R_{e\ out}'\right) = \frac{1}{\sum_i \left[I_{exp}^i - I_{sim}^i\left(R_{e\ out}'\right)\right]^2} \quad (2)$$

where $I_{\exp}^i$ and $I_{sim}^i\left(R_{e\ out}'\right)$ are normalized experimental and simulated

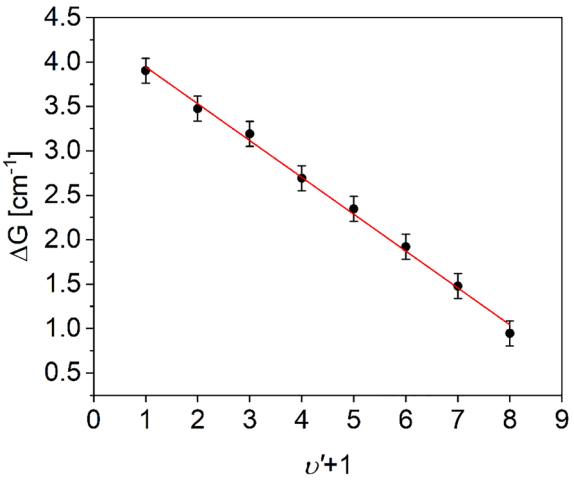

Fig. 2. Birge - Sponer plot for $\upsilon' \leftarrow \upsilon''=4$ vibrational progression recorded in the $E^3\Sigma_{1\ out}^+(\upsilon') \leftarrow B^3\Sigma_1^+(\upsilon'')$ transition in CdAr. Linear fit (red solid line) determines vibrational constants $\omega_e' = 4.36 \pm 0.05\ cm^{-1}$ and $\omega_e' x_e' = 0.207 \pm 0.005\ cm^{-1}$. Uncertainty of ΔG originates mainly from the laser bandwidth as well as rotational and isotopologue structure of the line, and is estimated to be $\pm 0.14\ cm^{-1}$.

intensities of the *i* th vibrational component.

To increase the accuracy of the simulated intensities, parameters of the simulation have to be carefully chosen. The intensity of each simulated vibrational component depends mainly on several effects: F-C factor calculated using LEVEL program [18], corresponding rotational structure calculated using PGOPHER program [19] (unresolved in this experiment), transition dipole moment function, adopted here from Ref. [14], and CdAr isotopologue structure.

The last effect results in increasing of the intensity of lower υ' vibrational components as compared to the higher ones. It is due to the increasing of the isotopologue separation with υ'. Simulations were performed assuming natural CdAr isotopologue abundances with 3 % threshold. Both, the $B^3\Sigma_1^+$ - state potential well and the $E^3\Sigma_{1\ out}^+$ are represented with Morse functions, the former using parameters from Ref. [12] and the latter with newly-determined vibrational constants of this study. Simulations were performed applying a 0.1-cm^{-1} (FWHM) Gaussian and Lorentzian convolutions for each rotational component within every simulated vibrational profile, and rotational temperature $T_{rot} = 2$ K. Moreover, since the $E^3\Sigma_{1\ out}^+ \leftarrow B^3\Sigma_1^+$ transition is the second-step excitation of OODR process, only several rotational transitions, selected in the $B^3\Sigma_1^+ \leftarrow X^1\Sigma_{0^+}$ first-step excitation, were taken into consideration, here $J'' = 0$–7. This is illustrated in Fig. 3a where partly-rotationally-resolved profile of the $B^3\Sigma_1^+(\upsilon''=2) \leftarrow X^1\Sigma_{0^+}(\upsilon=0)$ vibrational band recorded (red line) and simulated (black line) are shown. The rotational structure of the band is shown in Fig. 3b in which P-, Q- and R-branches are represented with black, red and blue vertical bars, respectively. From Fig. 3 it is obvious that with the first-step excitation laser, which frequency was set at that corresponding to the vicinity of the vibrational band-head (see grey vertical bar), only $J'' < 8$ rotational levels can be effectively excited. Only those J'' participated in the second-step excitation.

The agreement coefficient $C(R_e'_{out})$ for each υ'' employed in the second-step excitation is presented in Fig. 1b. The meaning of the *C* coefficient can be understood in such a way that the higher *C* value, the better agreement between simulation and experiment. Values of the $R_e'_{out}$ for which the best agreement (highest *C*) were obtained are presented in Table 2. As one can see, the value of the $R_e'_{out}$ slightly increases with υ''. This surprising observation can be attributed to the fact that relative intensity of vibrational components in LIF excitation spectrum depends on the transition dipole moment function which was calculated using *ab initio* method [14] and may differ from the real one.

Table 1
Spectroscopic characteristics of the $B^3\Sigma_1^+(5^3P_1)$- and $E^3\Sigma_{1\ out}^+(6^3S_1)$-state potentials of CdAr complex.

	$B^3\Sigma_1^+(5^3P_1)$[f]	$E^3\Sigma_{1\ out}^+(6^3S_1)$
ω_e (cm^{-1})	11.1 ± 0.1	**4.36 ± 0.05**[a] 4.4 ± 0.2[e] 4.15 ± 0.05[f] 4.15 ± 0.10[g]
$\omega_e x_e$ (cm^{-1})	0.56 ± 0.01	**0.207 ± 0.005**[a] 0.20 ± 0.01[e] 0.225 ± 0.005[f] 0.225 ± 0.010[g]
D_e (cm^{-1})	55.0 ± 2.0	**22.96 ± 0.76**[a] 24.2 ± 1.0[e] 19.14 ± 0.63[f] 19.10 ± 1.30[g] 15.5[i] 17[j] 16[k]
R_e (Å)	5.01 ± 0.05	**7.235 ± 0.121**[b] 5.60 ± 0.05[e] 7.63 ± 0.05[f] 6.90 ± 0.15[g] 7.94[i] 7.67[j] 7.36[k]
β ($Å^{-1}$)	0.991 ± 0.018	**0.603 ± 0.015**[a] 0.628 ± 0.014[f] 0.628 ± 0.028[g]
R_b (Å)		**5.15**[c] 4.70[e] 4.89[j] 4.96[k]
E_b (cm^{-1})[d]		**27**[c] 48[e] 21.1–39.4[h] 70[j] 46[k]
E_{asympt} (cm^{-1})[l]	30656.087 ± 0.002	51483.980 ± 0.002

[a] This work, from linear Birge – Sponer plot and Morse-function representation (recommended value).
[b] This work, from intensity distribution in bound ← bound excitation spectra (recommended value).
[c] This work, from simulation of free ← bound excitation spectra (recommended value).
[d] With respect to the 6^3S_1 atomic asymptote.
[e] Ref. [8].
[f] Ref. [9].
[g] Ref. [12].
[h] Ref. [11], from analysis of the $E^3\Sigma_1^+ \leftarrow A^3\Pi_{0^+}(5^3P_1)$ transition.
[i] Ref. [5], ab initio calculations.
[j] Ref. [13], ab initio calculations; also: iftia9.univ.gda.pl/~kroch/potentials.html.
[k] Ref. [14], ab initio calculations.
[l] Ref. [17].

The final estimation of the $R_e'_{out}$ was calculated as an average of the $R_e'_{out}$ values collected in Table 2, with uncertainty as a sample standard deviation. Thus, $R_e'_{out} = 7.235 \pm 0.121$ Å. The simulated spectra are presented in Fig. 1a (black lines) and compared with the experimental results (red lines). Table 3 collects registered and simulated transition frequencies, ν_{expt} and ν_{sim}, respectively. As one can see, the simulated spectra are in good agreement in relation to positions, relative intensities and line shapes, particularly for transitions to lower-lying υ'. For the highest observed $\upsilon'=7$ the intensity of bound ← bound transitions is affected by proximity of free ← bound spectra. Due to the significant laser bandwidth (approximately 0.1 cm^{-1}), for the laser frequency close to the dissociation energy, both free ← bound and bound ← bound transitions can be excited.

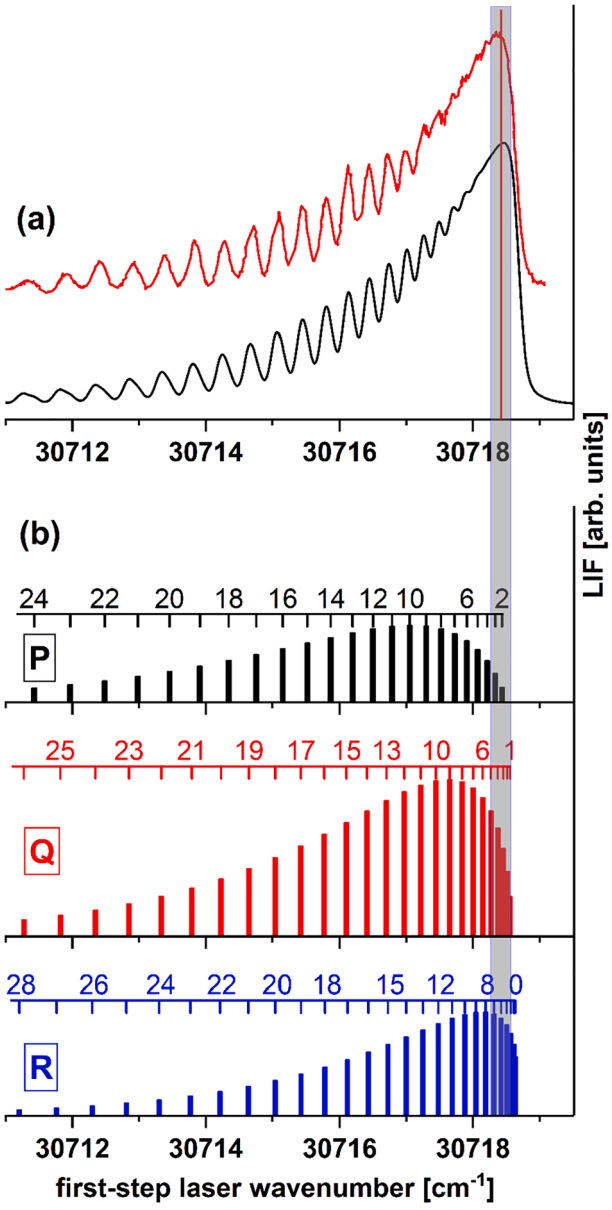

Fig. 3. (a) Partly-rotationally-resolved profile of the $B^3\Sigma_1^+(v''=2)\leftarrow X^1\Sigma_{0^+}(v=0)$ vibrational band recorded (red line) and simulated [19] (black line). (b) Rotational structure of the band showing P-, Q- and R-branches represented with black, red and blue vertical bars, respectively. First-step laser excitation of the J"<8 levels at the band-head (±0.15 cm^{-1}) is illustrated with grey vertical bar).

Table 2
Values of the $R_e'_{out}$ equilibrium distance of the $E^3\Sigma_1^+$ - state outer well that were used in simulation of the $E^3\Sigma_{1\ out}^+(v')\leftarrow B^3\Sigma_1^+(v'')$ transitions in CdAr (Fig. 1a).

v''	1	2	3	4
$R_e'_{out}$ (Å)	7.10	7.20	7.25	7.39

3.2. Free ← bound LIF excitation spectra

Location of the $E^3\Sigma_1^+$ - state potential along with its potential barrier with respect to the $B^3\Sigma_1^+$ - state potential allowed to excite free ← bound transitions that originated from a chosen v'' and terminated on both: the repulsive part of the potential barrier above the dissociation limit and the $E^3\Sigma_1^+$ - state repulsive branch above the barrier. As it can be seen in Fig. 4, the recorded free ← bound spectra of the $E^3\Sigma_1^+\leftarrow B^3\Sigma_1^+$ ($v''=0,1,2,3,4$) transitions (red lines) do not correspond strictly to the rule of the reflection structure described by Tellinghuisen [20] according to which it conserves the peak and node count of the initial v'' - level wavefunction. We interpreted the fact similarly to the explanation by Duval *et al.* [21] who reported analogous transitions recorded for HgAr complex. They argued that the extraneous oscillations in the spectra might be a product of an interference structure resulting from occurrence of a barrier in the $E^3\Sigma_1^+$ - state potential.

Table 3
Transition frequencies ν_{expt} in [cm^{-1}] recorded in OODR process upon the $E^3\Sigma_{1\ out}^+(v')\leftarrow B^3\Sigma_1^+(v''=3)$ excitation in CdAr. To obtain values shown in Fig. 1, energy of the first-step excitation with respect to the ground-state asymptote must be added (*i.e.* 30632.8 cm^{-1}).

v'	ν_{expt}	ν_{sim}	$\nu_{expt}-\nu_{sim}$
0	20830.0	20830.0	0.0
1	20833.9	20833.9	0.0
2	20837.4	20837.5	−0.1
3	20840.6	20840.6	0.0
4	20843.3	20843.3	0.0
5	20845.6	20845.6	0.0
6	20847.4	20847.4	0.1
7	20848.9	20848.9	0.1
8	20850.0	20849.9	0.1
9	–	20850.5	–

To simulate the recorded free ← bound spectra shown in Fig. 4, a pointwise model potential of the $E^3\Sigma_1^+$ state was constructed; it consisted of three parts that corresponded to different regions of the $E^3\Sigma_1^+$ - state potential (solid blue curve in Fig. 5).

The shape of the $E^3\Sigma_{1\ in}^+$ deeper well (for R up to 4.56 Å) was adopted being a result obtained from inverted perturbation approach (IPA) method [11]. The potential barrier (four points within the range from R = 4.82 Å to R = 5.91 Å) was constructed by modification of *ab-initio*-calculated potential without basis set superposition error (BSSE) correction [14] (solid light green points and curve in Fig. 5). Finally, for R > 6.38 Å, the $E^3\Sigma_{1\ out}^+$ shallower well was represented by a Morse function with newly-obtained vibrational characteristics and $R_e'_{out}$ of this study (the analytical potential was converted to the pointwise form). To unify the whole $E^3\Sigma_1^+$ - state representation, the three curves were combined using a cubic spline method. To obtain smoother spline line (especially in the regions where the potential barrier is joined with respective parts representing the inner and outer wells) as well as for better agreement of BCONT simulation with free ← bound experimental spectrum (compare with Fig. 4), a modification of the potential was introduced. It consisted of the 0.01-Å shift along the R axis of all *ab-initio* points used to construct the barrier, as well as the 0.16-Å shift in R of the IPA-based $E^3\Sigma_{1\ in}^+$ - state potential.

It is worth commenting on the existence of a shelf feature that occurs on either side of the barrier (there exist inflection points of the potential function near the barrier). The similar structure on the left-hand side of the barrier occurred also as a result of IPA method presented in [11]. In this work, we tried to eliminate this structure by broadening the potential barrier (the part of potential above the atomic asymptote). Unfortunately, such modification led to significant increase in discrepancy between experiment and simulation for the free ← bound spectra and has been rejected. However, this shelf structure is quite unusual and requires further verification. In this context, an observation of bound → free fluorescence spectra originating from the $E^3\Sigma_{1\ in}^+$ - state vibrational levels above the dissociation limit (v' = 18,19) can be particularly valuable as they can reveal additional information about the shape of the v' wave function in the region of interest.

Results of the simulation, performed using BCONT [22] program, are presented in Fig. 4 (black lines) and compared with experimental spectra showing an overall agreement. As can be seen, the undulating

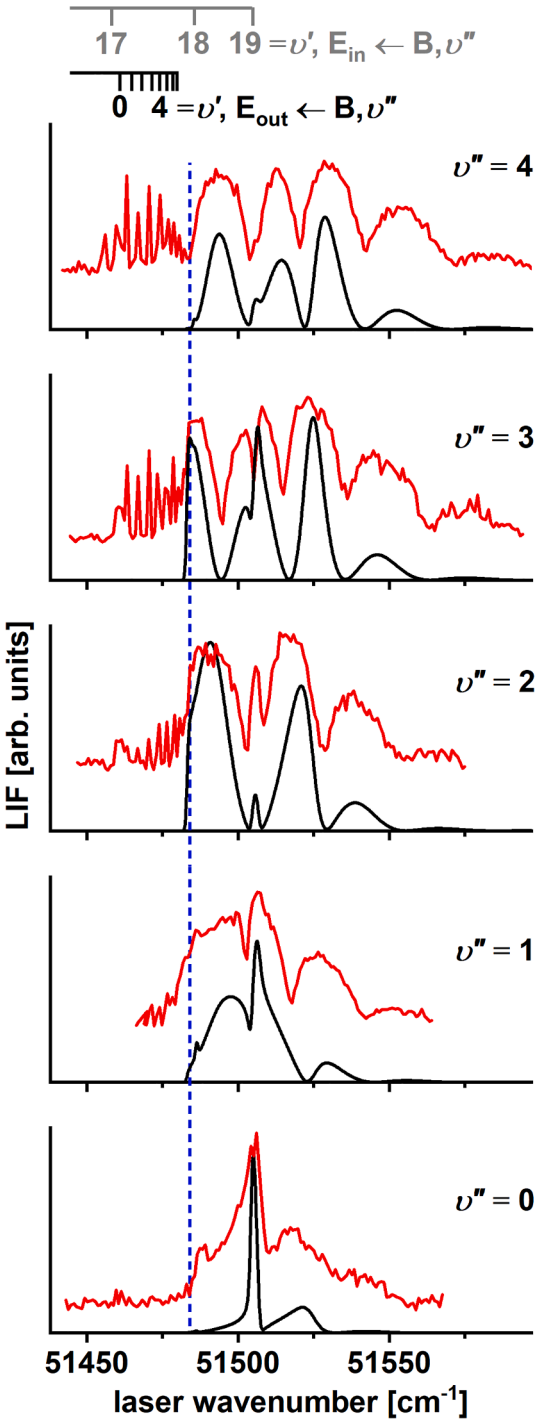

Fig. 4. Experimental LIF excitation spectra of the $E^3\Sigma_1^+ \leftarrow B^3\Sigma_1^+(v'')$ free ← bound transitions in CdAr recorded for v''=0,1,2,3,4 (red lines), and their simulations [22] (black lines). Horizontal axis wavenumbers are given with respect to the $X^1\Sigma_{0^+}$ ground-state asymptote. Positions of the $E^3\Sigma_{1\ in}^+(v') \leftarrow B^3\Sigma_1^+(v'')$ and $E^3\Sigma_{1\ out}^+(v') \leftarrow B^3\Sigma_1^+(v'')$ bound ← bound transitions are marked on the top with grey and black lines, respectively. The energy of the 6^3S_1 atomic asymptote is depicted with blue dashed line.

structure of the spectra corresponding to free ← bound transitions overlap with bound ← bound transitions from v'' of the $B^3\Sigma_1^+$ state to two $v' = 18$ and 19 supported by the $E^3\Sigma_{1\ in}^+$ well *above* the dissociation limit. Their positions were marked on the top of Fig. 4.

Simulating free ← bound spectra, we attempted a direct determination of E_b height of the energy barrier and R_b internuclear distance at

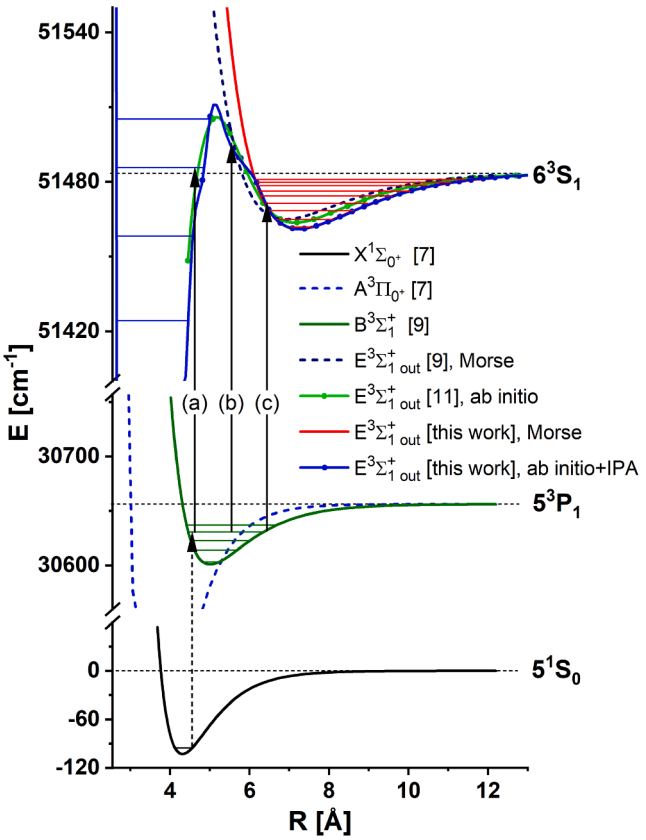

Fig. 5. Interatomic potentials of the $X^1\Sigma_{0^+}$, $B^3\Sigma_1^+$ and $E^3\Sigma_1^+$ electronic energy states of CdAr involved in OODR process. First-step $B^3\Sigma_1^+(v'') \leftarrow X^1\Sigma_{0^+}(v = 0)$ transition is illustrated with dashed black arrow. Three possible ways to realize the $E^3\Sigma_1^+ \leftarrow B^3\Sigma_1^+(v'')$ transitions: (a) bound ← bound to the $E^3\Sigma_{1\ in}^+$ inner well, (b) free ← bound terminating at the potential barrier and at the repulsive branch of the $E^3\Sigma_1^+$ -state potential above the potential barrier, and (c) bound ← bound to the $E^3\Sigma_{1\ out}^+$ outer well are shown with black solid arrows. Position of the $A^3\Pi_{0^+}$ - state potential (dashed blue line) is also shown.

which the barrier occurs. The values of E_b and R_b in Table 1 are quoted without their uncertainties. The reason is that the position and shape of the simulated free ← bound profiles strongly depend not only on the E_b and R_b but also on the $R_e'_{in}$ and $R_e'_{out}$ whose values are determined with relatively significant uncertainties *i.e.*, ±0.005 Å and ± 0.121 Å, respectively.

4. Conclusions

In this article, a long-time undetermined shape of outer well and potential barrier of the $E^3\Sigma_1^+(6^3S_1)$ double-well state in CdAr molecule was proposed based on experimental evidence and simulations. We presented analysis of both bound ← bound and free ← bound parts of LIF excitation spectra recorded using the $E^3\Sigma_{1\ out}^+ \leftarrow B^3\Sigma_1^+(v'')$ transitions in CdAr. Concerning bound ← bound part, a new v'-assignment was proposed and, consequently, new vibrational constants characterizing the outer well of the $E^3\Sigma_1^+$ state potential were determined (see Table 1). Furthermore, comparison of experimental intensities of bound ← bound transitions and their simulated counterparts enabled to make a correction to the $R_e'_{out}$ equilibrium distance in the $E^3\Sigma_{1\ out}^+$. The newly-estimated value of the $R_e'_{out} = 7.235$ Å is by 0.395 Å smaller and by 0.335 Å larger than those obtained previously in Refs. [9] and [12], respectively. Moreover, the value of $R_e'_{out}$ obtained here is very close to the newest *ab initio* value (7.36 Å) obtained by Krośnicki *et al.* [14]. It must be strongly emphasized that intensities of vibrational components

depend not only on corresponding F-C factors, but also on the transition dipole moment which is function of R. Thus, to determine the $R_e'_{\text{out}}$ with better accuracy, it is necessary to resolve rotational structure which requires the use of lasers with narrower spectral bandwidth. If the value of $R_e'_{\text{out}}$ is obtained with this method, determination of a shape of transition dipole moment function based on the presented bound ← bound spectra will be possible allowing its confrontation with result of ab-initio calculation [14]. Here, in conjunction with our previous determination of the shape of the $E^3\Sigma_1^+{}_{\text{in}}$ using IPA method [11], a consistent and reliable PEC of the whole $E^3\Sigma_1^+(6^3S_1)$ state in CdAr complex was first-time derived experimentally (compare with Fig. 5).

CRediT authorship contribution statement

J. Sobczuk: Investigation, Writing – original draft, Formal analysis, Visualization. **T. Urbańczyk:** Investigation, Writing – original draft, Formal analysis, Visualization, Software. **J. Koperski:** Conceptualization, Validation, Supervision, Funding acquisition, Project administration, Writing – original draft.

Declaration of Competing Interest

The authors declare that they have no known competing financial interests or personal relationships that could have appeared to influence the work reported in this paper.

Data availability

Data are included in supplementary material.

Acknowledgements

This work was supported by the National Science Centre Poland under grant number UMO-2015/17/B/ST4/04016.

Appendix A. Supplementary material

Supplementary data to this article can be found online at https://doi.org/10.1016/j.saa.2022.121655.

References

[1] P.D. Lett, P.S. Julienne, W.D. Phillips, Photoassociative spectroscopy of laser-cooled atoms, Ann. Rev. Phys. Chem. 46 (1995) 423–452, https://doi.org/10.1146/annurev.pc.46.100195.002231.

[2] D. Comparat, C. Drag, B. Laburthe Torla, A. Fioretti, P. Pillet, A. Crubellier, O. Dullieu, F. Masnou-Seeuws, Formation of cold Cs_2 ground state molecules through photoassociation in the 1_u pure long-range state, Eur. Phys. J. D 11 (2000) 59–71, https://doi.org/10.1007/s100530070105.

[3] M.-L. Almazor, O. Dulieu, F. Masnou-Seeuws, R. Beuc, G. Pichler, Formation of ultracold molecules via photoassociation with blue detuned laser light, Eur. Phys. J. D 15 (2001) 355–363, https://doi.org/10.1007/s100530170152.

[4] E. Czuchaj, H. Stoll, Calculation of ground- and excited-state potential energy curves for the Cd-rare gas complexes, Chem. Phys. 248 (1999) 1–16, https://doi.org/10.1016/S0301-0104(99)00247-5.

[5] E. Czuchaj, M. Krośnicki, H. Stoll, Quasirelativistic valence ab initio calculation of the potential-energy curves for Cd-rare gas atom pairs, Theor. Chem. Acc. 105 (2001) 219–226, https://doi.org/10.1007/s002140000206.

[6] R.R. Bennett, W.H. Breckenridge, Van der Waals bonding in the lowest electronic states of MgAr, ZnAr, CdAr and HgAr: Spectroscopic characterization of the $b^3\Pi_2$ and $e^3\Sigma^+$ states of the CdAr molecule, J. Chem. Phys. 96 (1992) 882–890, https://doi.org/10.1063/1.462108.

[7] M. Czajkowski, R. Bobkowski, L. Krause, Pump-and-probe studies of the $E1(6^3S_1)\leftarrow A0^+(5^3P_1)$ excitation spectrum of CdAr in a supersonic beam, Phys. Rev. A 45 (1992) 6451–6458, https://doi.org/10.1103/PhysRevA.45.6451.

[8] J. Koperski, M. Czajkowski, The structure of the lowest electronic Rydberg state of CdAr complex determined by laser double resonance method in a supersonic jet-expansion beam, Spectrochim. Acta A 59 (2003) 2435–2448, https://doi.org/10.1016/S1386-1425(02)00396-7.

[9] T. Urbańczyk, M. Strojecki, J. Koperski, Structure of vibrational bands of the $E^3\Sigma^+(6^3S_1)\leftarrow A^3\Pi_{0^+}(5^3P_1)$, $B^3\Sigma_1^+(5^3P_1)$ transitions in CdAr and CdKr studied by optical-optical double resonance method, Chem. Phys. Lett. 503 (2011) 18–24, https://doi.org/10.1016/j.cplett.2010.12.085.

[10] T. Urbańczyk, J. Dudek, J. Koperski, Isotopologue-selective excitation studied via optical-optical double resonance using the $E^3\Sigma^+(6^3S_1)\leftarrow A^3\Pi_{0^+}(5^3P_1)\leftarrow X^1\Sigma_{0^+}(5^1S_0)$ transitions in CdAr and CdKr van der Waals complexes, J. Quant. Spectrosc. Radiat. Transf. 212 (2018) 32–38, https://doi.org/10.1016/j.jqsrt.2018.03.013.

[11] T. Urbańczyk, M. Krośnicki, A. Kędziorski, J. Koperski, The $E^3\Sigma_1^+(6^3S_1)\leftarrow A^3\Pi_{0^+}(5^3P_1)$ transition in CdAr revisited: the spectrum and new analysis of the Rydberg state interatomic potential, Spectrochim. Acta A 196 (2018) 58–66, https://doi.org/10.1016/j.saa.2018.01.075.

[12] T. Urbańczyk, J. Koperski, The $E^3\Sigma^+(6^3S_1)$-state interatomic potential of CdAr in the long range region revisited: a new method for bond length adjustment, Chem. Phys. Lett. 640 (2015) 82–86, https://doi.org/10.1016/j.cplett.2015.10.013.

[13] M. Strojecki, M. Krośnicki, J. Koperski, Repulsive and bound parts of the interatomic potentials of the lowest singlet electronic energy states of the MeRg complexes (Me=Zn, Cd; Rg=He, Ne, Ar, Kr, Xe), J. Mol. Spectrosc. 256 (1) (2009) 128–134, https://doi.org/10.1016/j.jms.2009.03.005.

[14] M. Krośnicki, A. Kędziorski, T. Urbańczyk, J. Koperski, Rydberg states of the CdAr van der Waals complex, Phys. Rev. A 99 (5) (2019), https://doi.org/10.1103/PhysRevA.99.052510.

[15] T. Urbańczyk, J. Sobczuk, J. Koperski, Rotational characterization of the $E^3\Sigma_1^+(5s6s\,^3S_1)$ Rydberg state of CdNe van der Waals complex *via* selective *J*-excitation in OODR process, Spectrochim. Acta A: Mol. Biomol. Spectrosc. 264 (2022), 120248, https://doi.org/10.1016/j.saa.2021.120248.

[16] T. Urbańczyk, J. Koperski, High-temperature high-pressure all-metal pulsed source of van der Waals dimers: towards the Einstein-Podolsky-Rosen experiment, Rev. Sci. Instrum. 83 (8) (2012) 083114, https://doi.org/10.1063/1.4747274.

[17] A. Kramida, Yu. Ralchenko, J. Reader, NIST ASD Team, 2021. NIST Atomic Spectra Database (version 5.9), [Online]. Available from: <https://physics.nist.gov/asd> [Fri Jun 10 2022]. National Institute of Standards and Technology, Gaithersburg, MD. https://doi.org/10.18434/T4W30F.

[18] R.J. Le Roy, LEVEL: a computer program for solving the radial Schrödinger equation for bound and quasibound levels, J. Quant. Spectrosc. Radiat. Transfer **186** (2017) 167–178, https://doi.org/10.1016/j.jqsrt.2016.05.028.

[19] C.M. Western, PGOPHER: a program for simulating rotational, vibrational and electronic spectra, J. Quant. Spectrosc. Radiat. Transfer **186** (2017) 221–242, https://doi.org/10.1016/j.jqsrt.2016.04.010.

[20] J. Tellinghuisen, Reflection and interference structure in diatomic Franck – Condon distributions, J. Mol. Spectrosc. 103 (1984) 455–465, https://doi.org/10.1016/0022-2852(84)90068-7.

[21] M.-C. Duval, O.B. D'Azy, W.H. Breckenridge, C. Jouvet, B. Soep, The structure of several electronic states of the Hg-Ar complex as determined by laser double resonance in supersonic jet, J. Chem. Phys. 85 (1986) 6324–6334, https://doi.org/10.1063/1.451462.

[22] R.J. LeRoy, G.T. Kraemer, BCONT 2.2, University of Waterloo Chemical Physics Research Report CP-650R2, 2004; the source code: Available from: <http://scienide2.uwaterloo.ca/~rleroy/bcont>.